DISSERTATION

submitted to the
Combined Faculty of Mathematics, Engineering and Natural Sciences
of Heidelberg University, Germany
for the degree of
Doctor of Natural Sciences

Put forward by

Friderike Katharina Longarino

born in: Heidelberg, Germany

Oral examination: November 14, 2023

Dual-energy computed tomography for predicting range in particle therapy

Dual-energy computed tomography for predicting range in particle therapy

Radiotherapy with protons or light ions is a highly precise form of cancer treatment. In treatment planning for particle therapy, ion stopping power ratio (SPR) maps of patient tissues are used to predict particle ranges and calculate dose distributions. To more accurately calculate dose distributions and minimize irradiating healthy tissue, it is crucial to improve SPR prediction. To this end, this thesis investigated dual-layer spectral computed tomography, a dual-energy CT (DECT) technique, as an alternative to conventional single-energy CT (SECT). The SECT-based method relies on converting CT numbers to SPR, yet CT numbers acquired from photon attenuation cannot be used to accurately predict energy loss by ions, which makes the approach indirect and heuristic. The DECT-based method, however, uses measurements of relative electron density and effective atomic number to directly and patient-specifically predict SPR. SPR prediction using DECT was evaluated in tissue-equivalent materials, anthropomorphic phantoms, and non-tissue materials; clinically analyzed in a retrospective patient study; and experimentally investigated for patients with dental materials. DECT-based SPR prediction improved dose calculation accuracy in particle therapy compared to SECT with a remaining range uncertainty of about 1% in controlled experimental scenarios. DECT may thus substantially improve range prediction for highly accurate particle therapy.

This thesis is presented in a cumulative format and includes three peer-reviewed publications.

Zwei-Spektren-Computertomographie für die Reichweitevorhersage in der Partikeltherapie

Die Strahlentherapie mit Protonen oder leichten Ionen stellt eine sehr präzise Therapieform in der Krebsbehandlung dar. Bei der Bestrahlungsplanung für die Partikeltherapie werden Karten des Ionenbremsvermögens (SPR) des Patientengewebes zur Vorhersage der Partikelreichweiten und zur Berechnung der Dosisverteilungen verwendet. Die Verbesserung der SPR-Vorhersage ist für eine genauere Berechnung der Dosisverteilungen und die Minimierung der Bestrahlung von gesundem Gewebe entscheidend. Zu diesem Zweck wurde in dieser Arbeit die Dual-Layer Spektral-Computertomographie, eine Zwei-Spektren-CT (DECT)-Technik, als Alternative zur konventionellen Ein-Spektren-CT (SECT) untersucht. Die SECT-basierte Methode beruht auf der Umwandlung von CT-Zahlen in SPR. Die aus der Photonen-Abschwächung gewonnenen CT-Zahlen können jedoch nicht zur genauen Vorhersage von Energieverlusten von Ionen verwendet werden, wodurch der Ansatz indirekt und heuristisch ist. Die DECT-basierte Methode hingegen nutzt Messungen der relativen Elektronendichte und der effektiven Ordnungszahl, um das SPR direkt und patientenspezifisch vorherzusagen. Die SPR-Vorhersage mittels DECT wurde in gewebeäquivalenten Materialien, anthropomorphen Phantomen und nicht-gewebeäquivalenten Materialien evaluiert, in einer retrospektiven Patientenstudie klinisch analysiert und für Patienten mit Dentalmaterialien experimentell untersucht. Die DECT-basierte SPR-Vorhersage verbesserte die Genauigkeit der Dosisberechnung in der Partikeltherapie im Vergleich zu SECT mit einer verbleibenden Reichweiteunsicherheit von etwa 1% in kontrollierten experimentellen Szenarien. DECT könnte somit die Reichweitevorhersage für eine hochgenaue Partikeltherapie erheblich verbessern.

Die vorliegende kumulative Dissertation umfasst drei von Experten begutachtete Veröffentlichungen.

Contents

List of Figures

List of Tables

List of Abbreviations

CSDA	Continuous slowing down approximation
CT	Computed tomography
CTN	CT number
CTV	Clinical target volume
DICOM	Digital Imaging and Communications in Medicine
DECT	Dual-energy computed tomography
DLCT	Dual-layer spectral computed tomography
DNA	Deoxyribonucleic acid
DSCT	Dual-source computed tomography
EAN	Effective atomic number
FOV	Field-of-view
GTV	Gross tumor volume
HLUT	Hounsfield look-up table
HU	Hounsfield unit
ICRU	International Commission on Radiation Units and Measurements
IMPT	Intensity-modulated particle therapy
KVSCT	Fast kVp-switching computed tomography
LET	Linear energy transfer
MAR	Metal artifact reduction
MRI	Magnetic resonance imaging
NTCP	Normal tissue complication probability
OAR	Organ-at-risk
PET	Positron emission tomography
PMMA	Polymethyl methacrylate
PTV	Planning target volume
RBE	Relative biological effectiveness
RED	Electron density relative to water
ROI	Region-of-interest
SACT	Sequential acquisition computed tomography
SECT	Single-energy computed tomography
SFCT	Split-filter computed tomography
SOBP	Spread-out Bragg peak
SPR	Stopping power ratio relative to water
TCP	Tumor control probability
TPS	Treatment planning system
TRD	Tissue retraction device

1
Introduction

1.1 Radiotherapy as a treatment modality for cancer

Cancer is the second leading cause of death worldwide [1], accounting for nearly one in six deaths today [2]. With the rapid growth and aging of the global population, cancer incidence and mortality are expected to continue to increase [2, 3]. The generic term cancer refers to a large group of diseases that can affect any part of the body [4]. A defining characteristic of cancer is the rapid formation of abnormal cells that grow beyond their normal boundaries and then may invade adjacent parts of the body and spread to other organs, a process that is also known as metastasis [4]. For more than 150 years, researchers have been investigating the causes of cancer, identifying risk factors, developing prevention strategies, searching for diagnostic tools, and exploring treatment options [5]. Today, many types of cancer can be cured if they are detected early and treated effectively [6]. Treatment usually includes surgery, radiotherapy, and/or systemic therapy (e.g., chemotherapy, targeted biological therapy, hormonal therapy, immunotherapy) [4, 7].

Radiotherapy is currently used in more than half of all tumor patients, whether as the sole primary therapy, in multimodal therapy, or in the later course of the disease to treat tumor recurrence or metastases [8]. In radiotherapy, ionizing radiation is used to exploit its properties therapeutically as it passes through tissue, inducing deoxyribonucleic acid (DNA) damage in proliferating tumor cells [8]. Radiation therapy has demonstrated the potential to cure tumors by eliminating cancer stem cells and has considerable potential to advance the effectiveness of precision medicine in oncology [9].

The fundamental goal of modern radiotherapy consists in delivering a prescribed radiation dose to maximize the tumor control probability while minimizing the dose to healthy surrounding tissues or organs [8]. Particle therapy, which utilizes beams of protons or light ions for irradiation, is widely regarded as one of the most precise and advanced forms of radiotherapy, thanks to the favorable energy deposition of charged particles [10, 11]. Compared to conventional photon-based radiotherapy, particle therapy is biologically more effective; it also has the potential to reduce adverse side effects in normal tissues, because it can deliver highly conformal dose distributions to solid tumors [9, 10]. These advantages are particularly important for tumors close to vital tissues (e.g., the brain stem, optic nerve, or intestine), for deep-seated tumors, and for re-irradiation of tumors; they are also important for sensitive patients, such as children [12].

Over the past six decades, the availability of and demand for particle therapy has grown exponentially [11]. The increasing number of particle therapy facilities made it possible for approximately 360,000 patients worldwide to be treated with particle therapy by the end of 2022 [13]. There are currently over 110 particle therapy centers in operation in 22 countries [14]. Yet the long-term projected availability of such therapy is still very limited [15]. Less than 1% of all radiation therapy patients receive particle therapy [16], even though it is believed that between 15% and 50% would benefit from it [11, 15]. For certain disease sites, this number may be even higher [11].

1.2 The need for accurate range prediction in particle therapy

One of the major advantages of particle therapy is its capacity to considerably decrease the radiation dose delivered to the tissue around the target volume [11]. Specifically, it can achieve a 50–70% dose reduction to normal tissue without lessening the dose to the tumor target volume that would be delivered by photon radiotherapy [11, 17]. This benefit of proton and light ion therapy derives from the favorable energy deposition properties of charged particles and their finite range [18, 19]. To properly exploit these physical characteristics, accurate prediction of the particle range within the body, derived from the stopping power ratio relative to water (SPR), is crucial for treatment planning [20, 21].

Pretreatment computed tomography (CT) imaging, which provides quantitative and anatomical information for treatment planning, is a necessary part of, and affects, the entire radiotherapy chain. In order to predict the finite beam range of charged particles, the treatment planning system (TPS) requires a CT scan of each patient. In current clinical practice, image data is acquired by using single-energy CT (SECT) systems. Yet clinical treatment planning that utilizes SECT-based systems can result in considerable range prediction uncertainties due to the heuristic conversion of CT numbers (CTN) from X-ray attenuation to ion SPR [22, 23]. CTN-to-SPR conversion has limited material differentiation because there is no one-to-one relationship (i.e., bijection) between CTN and SPR [19, 22]. Distinct materials with different SPR may have identical CTN in SECT-based images and vice versa [21]. Furthermore, the translation from CTN to SPR is not patient-specific; that is, the possible intra- and inter-patient variability is not covered by a CTN-to-SPR conversion [22]. Inter-patient variability arises from differences in density and elemental composition [24] (e.g., the calcium content of bone differs between children and adults [25]). There are also large deviations in the case of non-tissue materials (e.g., metals or implants), since the latter are generally not tissue-equivalent. Therefore, in such cases, the heuristic CTN-to-SPR conversion is of limited use [22]. The influence of the currently clinically used CTN-to-SPR conversion has been estimated to be the dominant factor contributing up to 2% to the overall particle range estimation uncertainty of 3.5% [20]. Thus, converting CTN to SPR may result in a range uncertainty of up to 3 mm in a typical treatment situation [26]. Because of the steep dose gradient at the distal edge of each beam, treatment planning and

delivery uncertainties can profoundly impact the delivered dose [27]. Small errors may lead to underdosing the tumor volume and overdosing surrounding critical structures [23]. Uncertainties in particle range prediction are accounted for by incorporating safety margins (i.e., extending the treatment volume) into treatment planning, which results in higher doses being delivered to healthy tissues; consequently, the physical advantages of particle therapy in comparison to photon radiotherapy in cancer treatment are not fully exploited. Therefore, reducing the range uncertainties in patient tissues resulting from conventional CTN-to-SPR conversion based on SECT imaging is crucial to improve clinical practice [22].

The use of dual-energy CT (DECT) was first proposed in the 1970s [28] to reduce the uncertainties in particle range prediction of the SECT-based approach [29]. However, for many years, there was no suitable way to implement the technique to acquire quantitative patient image data, and it was not until 2006 that DECT was clinically introduced for diagnostic imaging [30], providing material- and energy-selective image data [31]. Since then, a large number of studies have suggested several promising ways that DECT might be applied within the whole radiotherapy chain. These potential benefits include tumor staging and delineation, tumor and normal tissue characterization, metal artifact reduction (MAR), and dose calculation [22, 32, 33]. DECT imaging, which acquires CT data over two different X-ray spectra, may improve SPR prediction in clinical practice by using DECT-based material characterization [19].

To date, five technical approaches have been developed to acquire DECT image data, each possessing unique features and limitations that need to be considered when they are applied: dual-source CT (DSCT), sequential acquisition CT (SACT), fast kVp-switching CT (KVSCT), split-filter CT (SFCT), and dual-layer spectral CT (DLCT) [34, 35]. Both theoretical and experimental studies have already shown that DECT methods can improve the accuracy of SPR prediction over the conventional methods based on SECT [22, 32, 33, 36–39]. To date, most studies on DECT-based SPR prediction have been performed using DSCT or SACT [33]. DLCT imaging is a more recent technique that uses a single-source, dual-layer detector-based approach [40]. One advantage that DLCT offers in comparison to other DECT imaging techniques is that it simultaneously acquires energy-selective data by means of two detector layers with different spectral sensitivities, thus enabling projection domain-based material decomposition. Preliminary studies on DLCT imaging, which were conducted mainly on a theoretical basis, have shown promising results, particularly in the ability of DLCT to provide SPR prediction [41, 42].

There are continuing efforts using other methods to deal with range uncertainties in particle therapy. These efforts include, for example, pretreatment SPR estimation with particle CT, as well as range verification with a prompt gamma camera, positron emission tomography (PET), or ultrasound imaging [33, 36, 43–49]. Every one of these technologies has its own potential and challenges [33]. Of all these currently available technologies, DECT and particle CT are the sole methods that offer more accurate tissue characterization than SECT for particle therapy [33]. Up until now, DECT is the only technique that has made it into routine clinical practice [50].

1.3 Aim of the thesis

The main motivation of this thesis has been to investigate what improvements in particle range prediction are possible with DECT imaging, which may allow a reduction in safety margins and therefore less healthy tissue to be irradiated, while maintaining a conformal target dose.

The aim of this thesis has been to investigate the physical and clinical potential of DLCT imaging for dose calculation in particle therapy. This thesis has investigated whether DLCT may improve particle range prediction, what its potential advantages and challenges are, and how it could be clinically implemented for particle therapy treatment planning to address the limitations of the conventional SECT-based approach in SPR prediction. The following aspects have been included:

- An evaluation of the potential of DLCT for dose calculation in particle therapy treatment planning using tissue-equivalent materials, anthropomorphic phantoms, and non-tissue materials

- A retrospective patient study of the use of DLCT in proton, helium, and carbon ion beam therapy treatment planning for brain tumors

- An investigation of DECT-based particle therapy treatment planning for patients with dental implant and restoration materials

1.4 Structure of the thesis

In this thesis, chapter 2 reviews the principles of particle therapy and gives an overview of CT imaging for use in particle therapy. Chapter 3 gives a thematic overview of the three publications from the thesis and contains the published papers. A discussion of the results is presented in chapter 4. The conclusions are summarized in chapter 5. The appendix contains the supplementary material of the three publications.

2

Fundamentals and Background

This chapter provides an overview of the fundamentals underlying the research in this thesis. Section 2.1 covers the physical principles of particle therapy, followed by an overview of the basics of X-ray CT imaging and its use for treatment planning in particle therapy in section 2.2.

2.1 Principles of particle therapy

The goal of radiotherapy is to accurately deliver a dose distribution to the target volume while sparing as much as possible surrounding healthy tissue and critical structures [8]. In 1946, Robert R. Wilson first pointed out the dosimetric advantages of ion beams over photon radiotherapy [51]. Treatment of patients began with protons in 1954 [52], with helium ions in 1957, and with heavier ions in 1975 at the Lawrence Berkeley National Lab (LBL, USA) [53].

Charged particle beams, such as proton, helium ion, and carbon ion beams, have physical and biological advantages in cancer treatment over conventional photon irradiation [54, 55]. Unlike X-rays, charged particles are characterized by an inverse depth-dose profile, that is, the energy deposition is lower in the entrance channel, then steeply increases and precipitously falls off towards the end of the particle range in the so-called Bragg peak (Figure 2.1a) [43, 56]. The Bragg peak for monoenergetic ion beams, accelerated with a cyclotron or synchrotron, is very narrow. To cover the entire target volume longitudinally, however, what is required is a spread-out Bragg peak (SOBP), which can be achieved by superimposing beams of different energies (Figure 2.1b) [55]. Yet, in clinical application, the beams must be spread not only longitudinally to create a SOBP but also laterally and then shaped so that the high-dose regions are conformed to the target volume [16]. The beams can be spread and shaped by electro-mechanical means, specifically with either a passive scattering technique or an active spot scanning technique, which uses magnetic scanning of pencil beams of a set of initial energies to provide intensity-modulated particle therapy (IMPT) [16, 57].

The depth-dose characteristics of charged particles can be exploited to substantially reduce doses to normal tissue that is proximal or distal to the target volume, an advantage over treatment with photons (Figure 2.2) [17]. Achieving these reductions may make it possible to escalate tumor doses while substantially sparing normal tissue, which may improve local control and survival while reducing toxicity and improving quality of life [16].

5

(a) Bragg peak for different ion beams

(b) Spread-out Bragg peak for ion beams
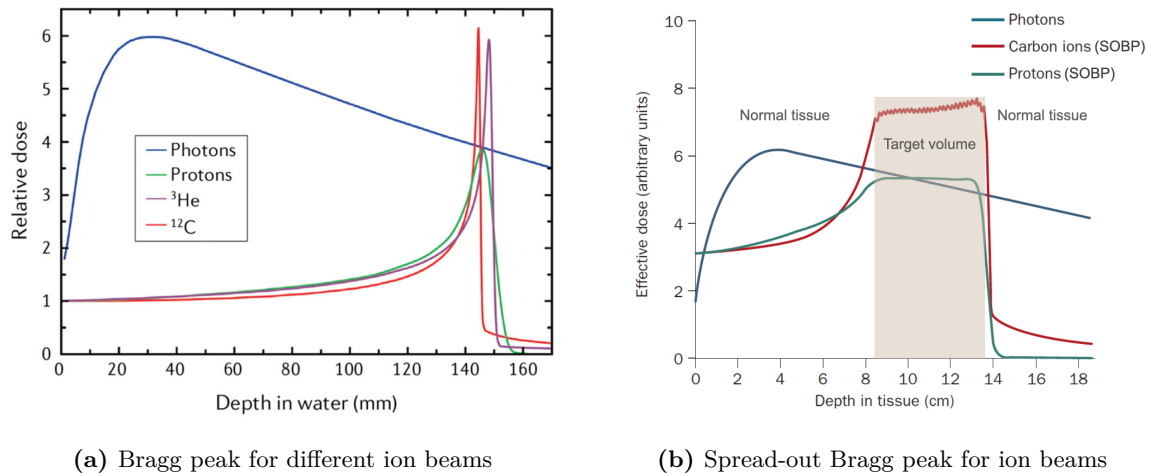
Figure 2.1: Depth-dose distribution of charged particles compared to photons. (a) Depth-dose profiles of photons and high-energy charged particles. The depth-dose curve for photons is calculated for a 21 MeV linear accelerator. The energies of the ion beams (^{1}H at 148 MeV, [3]He at 170 MeV/u, ^{12}C at 270 MeV/u) correspond to approximately the same range. (b) For clinical target volumes, a spread-out Bragg peak (SOBP) is used to apply a constant biologically effective dose within the tumor. Figure (a) adapted from [58] and (b) adapted from [55].


Figure 2.2: Comparison of dose distributions in an 11-year-old male patient with medulloblastoma from cranio-spinal irradiation using photon radiotherapy and particle therapy. Due to the comparatively low energy deposition before the dose maximum and the steep distal fall-off, proton therapy leads to a dose reduction in heart, lung, mediastinum, and intestine. Figure adapted from [59].

In addition to the physical characteristics of charged particles that allow for a higher degree of conformity, charged particles also have biological advantages that may allow for better tumor control [60, 61]. Ion beams are characterized by an increased relative biological effectiveness (RBE, defined as the ratio of photon to ion dose that produces the same biological effect [55]) that increases with linear energy transfer (LET, defined as the amount of energy loss per unit length of the particle's track, usually expressed in keV/μm [56]). The increased RBE results in 1 Gy delivered by ions being more biologically effective than 1 Gy delivered by photons [54, 62]. In current clinical practice, protons are assumed to have a constant RBE of 1.1 and thus a 10% higher biological effectiveness than photons [16, 53]. The RBE of carbon ions, by contrast, ranges from 3 to 5, depending on physical and biological parameters [60–62]. The variability in RBE must therefore be taken into consideration in treatment planning [62]. Given the increased RBE of high LET ion beams in the SOBP, together with other radiobiological advantages of charged particles, particle therapy can be more effective than photon irradiation in radioresistant tumors such as chordomas or chondrosarcomas of the skull base [8, 56, 62]. Compared to photon radiation, high LET radiation is also expected to have a reduced oxygen enhancement ratio (OER, defined as the ratio of radiation doses that produce the same cell survival under hypoxic and oxic conditions, respectively [55]), because radioresistance to photons is often induced by hypoxia. In addition, carbon ions may be able to induce stronger immune responses, though this is still under investigation in preclinical research [63, 64].

2.1.1 Interactions of charged particles with matter

At the energies used clinically in particle therapy (50–250 MeV/u for protons and helium ions, 90–430 MeV/u for carbon ions [53]), charged particles interact with matter predominantly via (1) Coulomb interactions with atomic electrons, (2) Coulomb interactions with nuclei, and (3) nuclear interactions (Figure 2.3) [16, 65]. The following describes each of these mechanisms.

(a) Inelastic scattering   **(b)** Elastic scattering   **(c)** Nuclear interactions
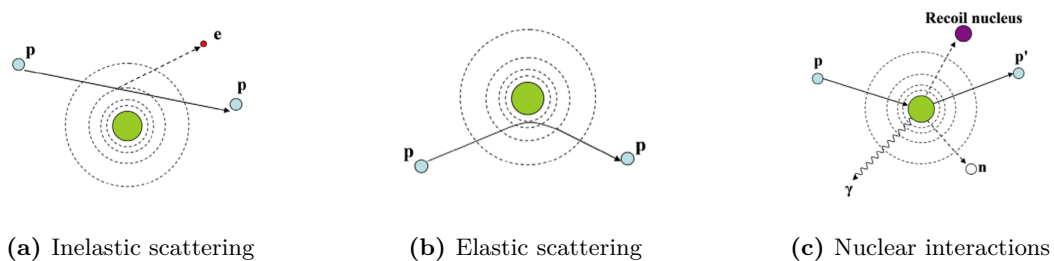
Figure 2.3: Schematic depiction of proton interaction mechanisms in matter: (a) energy loss through inelastic Coulomb interactions with electrons, (b) deflection of the proton trajectory via repulsive elastic Coulomb scattering with nucleus, (c) removal of primary proton and creation of secondary particles through non-elastic nuclear interaction (p: proton, e: electron, n: neutron, γ: gamma rays). Figure adapted from [66].

Energy loss

As they propagate through matter, charged particles interact mainly with atomic electrons through inelastic Coulomb interactions, by which they continuously lose energy (Figure 2.3a) [43]. In such interactions, incident particles collide with atomic electrons, causing excitation and ionization of the target atoms. The rate of particle energy loss increases with decreasing velocity. Monoenergetic charged particles will thus travel a well-defined distance in a uniform medium, losing energy at an increasing rate as they slow down before coming to rest [16]. Because protons and heavier ions are much heavier than electrons, they will not deviate appreciably from their original direction as a result of their interactions with electrons [16]. The stopping power $S(E)$ (expressed in MeV/cm) of charged particle beams describes the energy loss dE per unit path length dx in a medium. For incident charged particles with masses significantly greater than that of electrons, $S(E)$ is described analytically by the Bethe-Bloch equation [67–70]:

$$S = -\left\langle \frac{\mathrm{d}E}{\mathrm{d}x} \right\rangle = 4\pi N_A r_e^2 m_e c^2 \rho \frac{Z}{A} \frac{z^2}{\beta^2} \left[\ln\left(\frac{2m_e c^2 \gamma^2 \beta^2}{I} \right) - \beta^2 - \frac{\delta}{2} - \frac{C}{Z} \right] \tag{2.1}$$

where N_A is the Avogadro constant ($\approx 6.022 \cdot 10^{23}$ mol^{-1}), r_e is the classical electron radius ($\approx 2.812 \cdot 10^{-13}$ cm), m_e is the electron mass (≈ 0.511 MeV/c^2), ρ is the mass density of the medium, Z is the atomic number of the medium, A is the mass number of the medium (in g/mol), z is the charge of the projectile ($z = 1$ for protons, $z = 2$ for helium ions, and $z = 6$ for carbon ions), β is the velocity of the projectile v relative to the speed of light c, $\gamma = (1 - \beta^2)^{-\frac{1}{2}}$ is the Lorentz factor, I is the mean excitation energy of the medium (in MeV), $\delta/2$ is a density correction term, and C/Z is a shell correction term. The last two correction terms in the Bethe-Bloch equation take into consideration relativistic theory and quantum mechanics and must be included in calculations that involve very high or very low particle energies [66].

The relation $S(E) \propto v^{-2}$ makes it evident that the increase of energy loss for charged particles in matter is a function of decreasing particle velocity [43]. The Bethe-Bloch equation, together with the statistical nature of the Coulomb interactions for an ensemble of charged particles, gives the characteristic depth-dose curve for a monoenergetic beam of charged particles (Figure 2.1a) [18]. This means that charged particle beams lead to relatively low doses in the entrance channel in front of the tumor. The maximum dose is reached at the Bragg peak, which is then followed by a precipitous dose fall-off at the distal end near the finite penetration depth [71].

In radiation oncology, the absorbed dose D (expressed in units of Gray: 1 Gy = 1 J/kg) is defined as the mean energy dϵ deposited by the ionizing radiation either directly by the primary ions or by secondary particles in a mass element dm [53]:

$$D = \frac{\mathrm{d}\epsilon}{\mathrm{d}m} \tag{2.2}$$

In most situations, secondary electron equilibrium prevails, which means that the energy carried in and out of a volume of interest by secondary electrons is, on average, equal. Assuming this,

and disregarding nuclear interactions, the dose deposited in a thin slice of absorber material of mass density ρ by a fluence Φ of monoenergetic charged particles is proportional to the mean energy loss of the particle beam per unit path length [53]:

$$D = \frac{\Phi}{\rho} \left\langle \frac{\mathrm{d}E}{\mathrm{d}x} \right\rangle \tag{2.3}$$

Multiple Coulomb scattering

As ions slow down and pass close to target nuclei, and if the distance of approach is not too small, they may be deflected due to elastic Coulomb repulsion (Figure 2.3b) [16]. Although each deflection may be small, the deflections accumulate, a process known as multiple Coulomb scattering, which in turn can result in substantial lateral spreading of protons [16]. Yet lateral spreading is relatively small for heavier ions in particle therapy [72]. For example, protons scatter laterally about three times as much as carbon ions at a depth of 15 cm [58]. This relatively small lateral deflection of light ions when they penetrate a medium is clinically relevant for treatments near an organ-at-risk (OAR) [53]. The statistical distribution of the scattering angles of a pencil beam of particles behind a thick absorber is described by Molière's theory [73–75] and approximated by Highland with reasonable accuracy [76, 77].

Nuclear interactions

While primary charged particles can lose energy via Coulomb interactions with electrons or undergo track deflections due to Coulomb interactions with nuclei, there is also a small but finite probability that they will directly interact with atomic nuclei through elastic, inelastic, or non-elastic nuclear interactions (Figure 2.3c) [43]. The probability of nuclear interactions occurring increases with the energy of the ions and with the atomic number of the target nucleus [16]. It is estimated that up to 20% of protons of the highest energies in the therapeutic range are subject to nuclear interactions along their path [16].

In elastic collisions, the incident projectile scatters off the target nucleus and the total kinetic energy is conserved [16]. In the case of inelastic nuclear interactions, the collision of the projectile and the target results in excitation of the target nucleus and nuclear de-excitation with emission of secondary radiation (e.g., by emission of a prompt gamma ray).

In non-elastic collisions, the projectile particle enters the nucleus, and the characteristics of the nuclei are changed [43]. The target nucleus absorbs some of the energy, and the collision results in fragmentation of the target and/or, in the case of projectiles heavier than protons, fragmentation of the projectile into lighter projectile fragments [58, 66]. In proton therapy, only target fragmentation occurs, which results predominantly in secondary protons or neutrons [65]. Recoil nuclei and the heavier fragments are essentially absorbed at the point of interaction [72]. Nevertheless, scattered protons and especially secondary neutrons can travel comparatively long distances and create a low dose envelope [16]. In light ion therapy, fragmentation substantially reduces the fluence of the primary ions; for example, in a typical carbon ion therapy treatment,

only 50% of the ions actually reach a deep tumor, while the others undergo fragmentation [58, 65]. The projectile fragments have a velocity and direction similar to the primary ions, yet a lower charge and consequently a longer range [65]. They produce a dose tail after the Bragg peak, unlike protons [58].

Ongoing research is investigating the feasibility of using the distribution of prompt gamma rays or the short-lived radioisotopes ^{11}C and ^{15}O for *in vivo* range verification during particle therapy treatment delivery [78, 79].

2.1.2 Range of particles

The range of a particle beam is defined as the depth in a medium where half of the particles of a beam have stopped [66, 80]. For a monoenergetic particle beam of initial energy E, the range R of ions under the assumption of a continuous slowing down approach (CSDA) can be calculated by integrating the inverse of the stopping power over energy [72, 81]:

$$R(E) = \int_0^E S(E')^{-1}\mathrm{d}E' \tag{2.4}$$

In the case of a monoenergetic proton beam, the depth where 50% of the protons have come to rest coincides with the 80% fall-off position [20].

Statistical fluctuations in the interactions of ions with the electrons of the target atoms lead to small variations in the energy loss rates of individual ions, which is also called energy straggling [82]. This energy straggling further results in a variation in the range, which is called range straggling, which leads to the measured Bragg peak being broadened [66, 72]. The range straggling is inversely proportional to the square root of the particle mass [53]. In comparison to proton beams, the Bragg peak is narrower in the beam direction for carbon ion beams (Figure 2.1a) [72]. Additionally, range straggling increases with the penetration depth in a given material, leading to Bragg peaks of larger width and smaller height for higher initial energy [53]. Thus, the range is an average quantity that characterizes a beam, not individual particles [66].

2.1.3 Stopping power ratio

Treatment planning in particle therapy requires the stopping power ratio of a medium relative to water (water is denoted by the subscript w), which is approximated by the Bethe-Bloch equation (equation 2.1) without correction terms [83]:

$$\mathrm{SPR} = \frac{\left\langle \frac{\mathrm{d}E}{\mathrm{d}x} \right\rangle}{\left\langle \frac{\mathrm{d}E}{\mathrm{d}x} \right\rangle_\mathrm{w}} = \frac{\rho_\mathrm{e}}{\rho_\mathrm{e,w}} \cdot \frac{\ln\left(\frac{2m_\mathrm{e}c^2\beta^2}{I(1-\beta^2)} \right) - \beta^2}{\ln\left(\frac{2m_\mathrm{e}c^2\beta^2}{I_\mathrm{w}(1-\beta^2)} \right) - \beta^2} \tag{2.5}$$

Here, ρ_e refers to the electron density of the medium while $\rho_\mathrm{e,w}$ denotes the electron density of water. Similarly, I and I_w stand respectively for the mean excitation energies of the medium and water.

Within the typical energy range of therapeutic beams, SPR prediction is minimally dependent on energy [84]. Consequently, it is standard to neglect the energy dependence and to calculate the SPR of each tissue at a fixed particle kinetic energy [85]. Thus, the SPR for a given tissue depends only on two material-dependent parameters: the electron density relative to water (RED, $\rho_e/\rho_{e,w}$) and the *I*-value. The RED of a composite material can be calculated from the mass density ρ as follows [83]:

$$\frac{\rho_e}{\rho_{e,w}} = \frac{\rho \sum\limits_{i} w_i \frac{Z_i}{A_i}}{\rho_w \sum\limits_{j \in w} w_j \frac{Z_j}{A_j}} \tag{2.6}$$

In the sums, for element i in the object, w_i is the elemental weight fraction, Z_i is the atomic number, and A_i is the mass number. The sum in the numerator runs over the chemical elements in the object (note that tissues typically consist of elements of a low atomic number, e.g., H, C, O, and Ca), whereas $j \in w$ in the sum in the denominator denotes the elements present in water (i.e., H and O). The *I*-value for a compound material can be calculated using the Bragg additivity rule [70]:

$$\ln(I) = \frac{\sum\limits_{i} w_i \frac{Z_i}{A_i} \ln(I_i)}{\sum\limits_{i} w_i \frac{Z_i}{A_i}} \tag{2.7}$$

Here, I_i is the mean excitation energy of element i in the material. The values for I_i are given in tables 2.8 and 2.11 of the International Commission on Radiation Units and Measurements (ICRU) Report No. 49 [86]. The *I*-value of the tissue can be calculated from the effective atomic number (EAN) [37].

2.1.4 Treatment planning

Treatment planning in radiotherapy aims to calculate the optimal dose distribution by accounting for dose conformity, healthy tissue sparing, and robustness against uncertainties [43, 87]. Treatment planning relies on planning CT images of the patient that allow delineation of the target volume as well as OARs. Since CT image data lack soft tissue contrast [88], additional imaging modalities such as magnetic resonance imaging (MRI) or PET are often used to provide additional anatomical or functional information. The ICRU Reports No. 50 and 62 define the target volumes for which the dose is to be prescribed [89, 90]. The gross tumor volume (GTV) refers to the macroscopic tumor visible on the planning CT. The clinical target volume (CTV), an extension of the GTV, comprises infiltrating tumor cells which may not be visible on conventional image datasets that are employed in treatment planning. The planning target volume (PTV) is a geometric concept that is introduced into treatment planning in order to account for uncertainties in both treatment planning and delivery and thus ensure the delivery of the prescribed dose to the CTV. The size of these margins is determined on the basis of international recommendations and site-specific experience and may vary for different treatment techniques.

Different analytical models have been developed to determine the effect that systematic and random errors in treatment planning and delivery have on the coverage of the CTV. The most widely used model is the van Herk formula for margin determination [91]. The van Herk formula suggests setting the size of the PTV margin equal to 2.5 times the standard deviation of systematic errors plus 0.7 times the standard deviation of random errors [91]. This procedure, originally developed for photon radiotherapy, can also be used for particle therapy, provided that the uncertainty in the particle range specific to each beam is included in the calculation [43].

2.1.5 Sources and consequences of range uncertainties

The well-defined range is the main physical advantage of charged particles in radiotherapy (Figure 2.4a) [43]. Yet, as a consequence of the precipitous dose fall-off at the distal edge of the Bragg peak, uncertainties in range prediction can profoundly affect the actual dose distribution applied (Figure 2.4b) [43]. Thus, dose deposition in particle therapy is more sensitive to uncertainties than photon radiotherapy [16]. Range uncertainties can lead to systematic underestimation or overestimation of the ion range, resulting in beam undershoot or overshoot effects [23]. The uncertainties can affect several facets of a treatment, including target coverage, dose homogeneity, dose conformation, and OAR doses [23]. Range uncertainty is probably the primary challenge that inhibits particle therapy from being able to maximize healthy tissue sparing [43]. Ideally, the range of the beam in human tissue could be accurately predicted. However, as a result of uncertainties in treatment planning and delivery, the delivered beam range often differs from the predicted beam range. In photon therapy, density heterogeneity in the beam path leads to a dose reduction of a few percent. Yet for a SOBP field in particle therapy, the same calculation uncertainty might lead to dose changes of up to 100% in extreme cases as a consequence of the precipitous dose fall-off at the distal edge of the SOBP [43].

The various sources of range uncertainty in particle therapy and their contribution to the margin can be summarized [20] as those that are independent of dose calculation: uncertainties related to beam delivery (measurement uncertainty in water for commissioning, beam reproducibility [23]) and to patient setup and anatomical changes (setup errors [92], inter-fractional anatomical and physiological changes, intra-fractional organ motion [93]); and those that are dependent on dose calculation: uncertainties related to physics (image-based range prediction, namely the underlying CT imaging and conversion of CTN to SPR [26]) and to biological effects (RBE approximations [94, 95]). Treatment planning errors systematically affect all fractions of a treatment, in contrast to statistical deviations. Statistical deviations include, for example, patient positioning errors, which, under normal fractionation conditions, fluctuate around zero between fractions [43]. The largest uncertainty in range prediction comes from current image-based range prediction [21], which contributes up to 2% to the overall range uncertainty of 3.5% [20].

Several strategies have been established at each step in the radiotherapy chain to account for and minimize the impact of uncertainties on treatment outcomes. Ongoing investigations aim

(a) Nominal situation

(b) Situation with range uncertainty
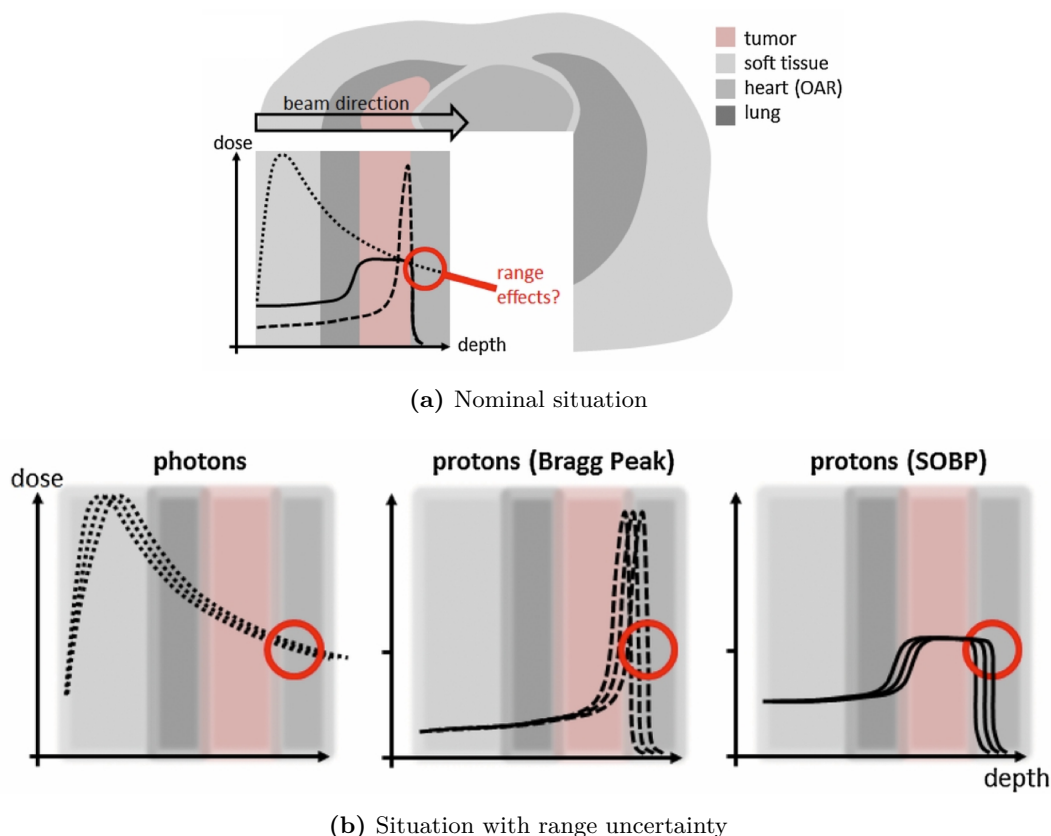
Figure 2.4: Schematic illustration of the influence of range uncertainties in photon and proton therapy. (a) Nominal situation for which the treatment plan was created (dotted line: photon depth-dose curve; dashed line: monoenergetic proton depth-dose curve (Bragg peak); straight line: proton spread out Bragg peak (SOBP) for coverage of the entire tumor). (b) Effect of range uncertainty on the depth-dose curves. Tissue variations in the beam direction affect the particle range, either increasing it in the case of a lower density medium (e.g., air) or decreasing it in the case of a higher density medium (e.g., bone), potentially resulting in underdosing the tumor and overdosing healthy tissue. The photon depth-dose distribution is only slightly affected by tissue variations. Range uncertainty does not apply to photon radiotherapy. Figure adapted from [43].

to better understand the consequences of the various uncertainties in particle therapy and to reduce these uncertainties [16], by means of, for example: adaptive radiotherapy [96], image guidance [97], further study of the biological properties of ion beams, and development of novel methods to improve the accuracy of image-based range prediction [33].

Range uncertainties are accounted for by adding safety margins to the treatment volume to ensure full coverage of the treatment volume. Thus, particle range uncertainty directly impacts the size of the PTV and, consequently, the ability of particle therapy to spare an OAR located near the CTV. Currently there is no consensus concerning the size of the margins, though clinics often employ a margin that amounts to 3.5% of the predicted range, plus an absolute value, typically of about 1 mm [20]. This leads to a considerable amount of healthy tissue receiving the full treatment dose, which increases the risk of side effects and reduces the therapeutic window. For example, a range margin of 3.5% + 1 mm causes a substantial overshoot of 8 mm for a 20 cm

(a) Safety margins currently applied **(b)** 2 mm margin reduction, 27% volume reduction
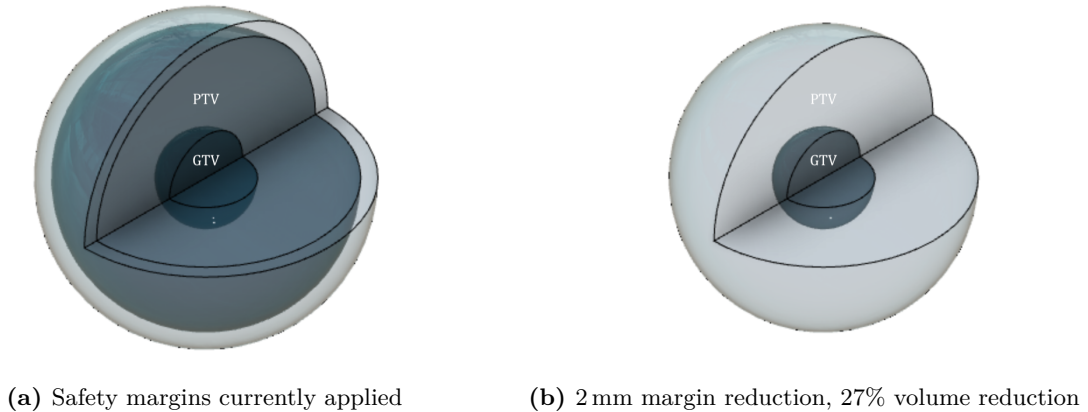
Figure 2.5: Schematic depiction of the influence of margins on volume for a spherical gross tumor volume (GTV) (dark gray) with an isotropic margin resulting in an extended planning target volume (PTV) (lighter gray). The clinical target volume (CTV) is not shown. Reducing the margin by 2 mm (10%) results in a 27% reduction in irradiated volume and substantial sparing of healthy tissue.

range field in soft tissue [20]. Therefore, in order to obtain optimal safety margins in particle therapy, it is necessary to minimize, but also to quantify as accurately as possible, particle range uncertainty. For IMPT, in addition to employing margins, robust optimization methods can be used that incorporate uncertainties directly into the IMPT optimization problem [98].

Improved range prediction, however, could lead to a reduction in safety margins, thus decreasing the volume of irradiated normal tissue. Reducing the irradiated volume of normal tissue increases its tolerance and allows higher doses to be delivered to the target tissue [99]. Increasing the dose to the target tissue will result in a higher tumor control probability (TCP) [99]. Reducing the treatment volume correspondingly makes it possible to irradiate less normal tissue and therefore leads to a lower normal tissue complication probability (NTCP) [99]. For example, a 2 mm reduction in the safety margin for a spherical tumor brings about a 27% reduction in the volume of irradiated surrounding tissue (Figure 2.5).

Improved range prediction could also enhance confidence in the application of beam directions that take greater advantage of the steep gradient at the distal edge to spare critical structures and that also require shorter path lengths through normal tissue [43]. Thus improving dose conformity to the target volume and reducing normal tissue irradiation could consequently enable more dose escalation while adequately sparing healthy tissue [43]. These potential improvements underscore the desirability of accurate range prediction.

2.2 Use of computed tomography in particle therapy

A necessary element of treatment planning for particle therapy is a 3D representation of the internal anatomy of the patient. X-ray CT is the primary imaging modality for radiotherapy treatment planning, especially for dose calculation [36]. This is mainly due to the achievable submillimeter resolution with high geometric accuracy of the object to be treated, the quantitative

nature of the CT measurements, and the short acquisition times, in the order of seconds. Conventional CT imaging acquires data with a single X-ray energy spectrum and produces a cross-sectional map of the X-ray attenuation of a patient's tissues [100]. This method was first proposed and technically implemented by Godfrey Hounsfield [28]. Later, Godfrey Hounsfield and Allan Cormack were jointly awarded the 1979 Nobel Prize in Physiology or Medicine for the development of CT [101].

While the dose exposure of a CT scan varies widely depending on the image acquisition protocols and the organ site being imaged, the effective dose of, for example, a CT brain examination is nowadays typically in the range of 1–2 mSv in adults [102].

2.2.1 Principles of CT imaging

According to Lambert-Beer's law, the intensity I of a polychromatic X-ray spectrum with initial intensity I_0 after a running length d through a heterogeneous object with energy-dependent, spatially varying attenuation coefficients $\mu(E, \lambda)$ is described by the following equation [103]:

$$I(d) = \int_0^{E_{\max}} I_0(E) \cdot e^{-\int_0^d \mu(E,\lambda)\mathrm{d}\lambda} \mathrm{d}E \tag{2.8}$$

The attenuation coefficient μ at an energy E and a spatial position λ along the beam path describes the probability of photon interactions with matter per unit path length. Based on this information, analytical or iterative image reconstruction algorithms determine the individual attenuation coefficient of each volume element (voxel) within the field-of-view (FOV).

Interactions of photons with matter

The attenuation coefficient varies with the mass density and the stoichiometric composition of the material being scanned, along with the energy of the interacting photon. Generally, μ can be described as the product of the electron density (ρ_e) (expressed in electrons/cm^3) and the photon attenuation cross section per electron (σ_e) (expressed in cm^2/electron) [104]:

$$\mu(E, Z) = \rho_e \cdot \sigma_e(E, Z) = \rho_e \cdot \left(\sigma_{e,\mathrm{photo}}(E, Z) + \sigma_{e,\mathrm{Rayleigh}}(E, Z) + \sigma_{e,\mathrm{Compton}}(E) \right) \tag{2.9}$$

For the energy range typically used in diagnostic radiology (30–150 keV), human tissue cross sections depend on three photon interaction processes [103]: photoelectric effect with $\sigma_{e,\mathrm{photo}} \propto Z^4/E^3$, Rayleigh or coherent scattering with $\sigma_{e,\mathrm{Rayleigh}} \propto Z^2/E^2$, Compton effect or incoherent scattering with $\sigma_{e,\mathrm{Compton}}$ described by the Klein-Nishina formula [105]. One further interaction with matter, namely pair production, arises only for $E > 1.022$ MeV. The probability of each interaction process varies with energy E and atomic number Z. In the case of tissues, body fluids, and other materials in the human body, the Compton effect is the dominant process within the diagnostic energy window for CT [103].

(a) Full CTN range

(b) Zoom in on soft tissue region
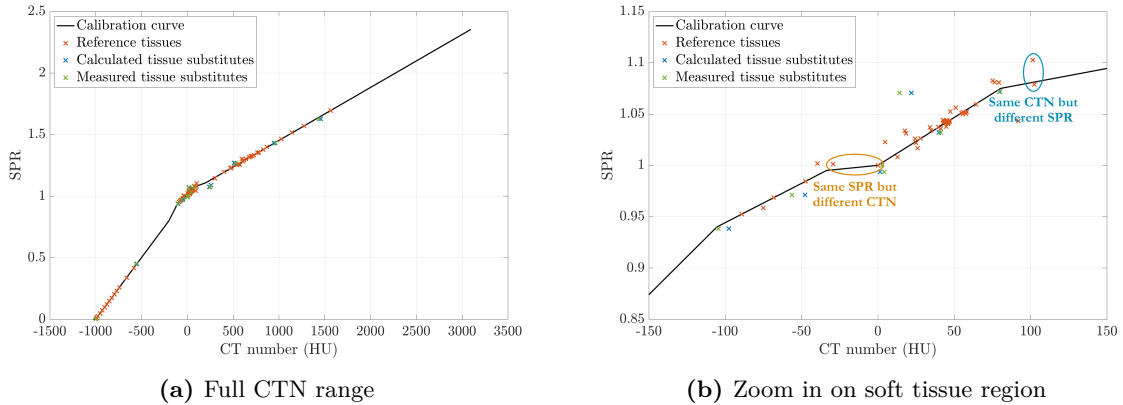
Figure 2.6: CT number (CTN) to stopping power ratio (SPR) conversion curve based on single-energy CT (SECT) using the stoichiometric calibration procedure. (a) Full CTN range and (b) zoom in on soft tissue region showing that the calibration is not unique.

Hounsfield scale

Since the linear attenuation coefficient is proportional to electron density (equation 2.9), the contrast in CT mainly results from the density differences between organs. CTN, displayed as gray values on a CT image, represent the relative difference in the linear attenuation coefficient of a tissue compared to water at a given energy, multiplied by 1000 and are expressed in Hounsfield units (HU) [106]:

$$\text{CTN} = \frac{\mu_{\text{tissue}} - \mu_{\text{water}}}{\mu_{\text{water}}} \cdot 1000 \tag{2.10}$$

Here, μ_{tissue} is the attenuation coefficient of the tissue and μ_{water} is the attenuation coefficient of water. By convention, CT systems are calibrated so that the CTN of water is 0 HU and the CTN of air is -1000 HU [106]. Fatty tissues have lower densities than water and CTN in the range of -100 to -70 HU, whereas most soft tissues are slightly denser than water, having values in the range of 20 to 70 HU [107]. Cortical bone reaches CTN of up to 2000 HU [107]. Due to the 12-bit encoding, the CTN scale ranges from -1024 to $+3071$ HU, adequately covering all human tissues. Artificially introduced materials of very high density, such as dental fillings, metal prostheses, or undiluted contrast media (e.g., in the area of the access vein), may not always be represented accurately in terms of their geometry and density, because CTN above 3071 HU are cut off and entered in the image as 3071 HU [107].

2.2.2 Stopping power ratio prediction from single-energy CT

Range prediction in clinical practice is based on a SECT scan of the patient. The CTN acquired are converted either voxel-wise into SPR for analytical dose calculation [83] or into mass densities and elemental compositions of tabulated human tissues for Monte Carlo-based dose calculation [108]. Both types of dose calculation require a bilinear heuristic conversion known as the Hounsfield look-up table (HLUT) (Figure 2.6a), which can be generated by empirical

calibration [109] or stoichiometric calibration [83]. These conversion procedures depend on a fit of data that are either experimentally acquired from tissue-equivalent materials or derived from tabulated human tissues. The basic methodology of CTN-to-SPR conversion has remained unchanged since the pioneering years of clinical particle therapy [36]. Yet the conversion process introduces errors because SECT does not offer sufficient information to accurately estimate tissue-specific quantities necessary for particle therapy treatment planning. The heuristic CTN-to-SPR conversion curve is inherently ambiguous due to the different physical interaction mechanisms involved: X-rays for imaging and ions for treatment. The values of both SPR and mass density depend on the RED and EAN of the tissue and thus are not fully proportional to the X-ray attenuation measured in the CT acquisition. Therefore, the CTN-to-SPR conversion curve has certain limitations [22]:

- The calibration is not unique, as two materials may have the same CTN but different SPR, and vice versa (Figure 2.6b). Therefore, there is no consistent one-to-one relationship (i.e., bijection) between CTN and SPR for different tissues and materials [19].

- A HLUT is static and not patient-specific, disregarding intra- and inter-patient variability in tissue composition [110]. Such variability includes, for example, differences in age, sex, and pathology, which cannot be adequately covered by a generic HLUT.

- Non-tissue materials, such as tooth fillings or surgical implants, often deviate greatly from the HLUT and may therefore introduce errors in the dose distribution [111].

- Scanner- and protocol-specific calibration curves are defined somewhat arbitrarily. CT imaging and CTN-to-SPR conversion protocols vary widely between centers, which leads to inter-center variations in dose calculation and potentially confounds the results of multi-center studies [36]. A consensus guideline for the specification of the HLUT has only recently been established [112].

It remains a major challenge to reduce uncertainty in CT-based prediction of SPR and range [36]. The main reason for range uncertainty in treatment planning—which has remained at about 3.5% of the absolute range, practically unchanged for decades—is the heuristic and indirect character of CTN-to-SPR conversion [36]. One potentially promising solution to better characterize tissue quantities from CT image acquisitions is to replace SECT imaging with DECT imaging [22].

2.2.3 Dual-energy CT

First introduced in the 1970s [113–117], DECT is an imaging technique that became clinically applicable in 2006 with the introduction of a first-generation DSCT system [30, 118] and provides both anatomical and tissue composition information in the form of energy-selective or material-selective images [32, 34].

In SECT imaging using a single X-ray energy spectrum, materials with different elemental compositions can exhibit the same CTN value [31]. Consequently, it can be challenging to

differentiate and classify different tissue types and contrast agents. By using two different X-ray spectra, DECT provides an additional attenuation measurement over a different energy spectrum [31]. As a result, the two different tissues will in all likelihood not have the same CTN for both energy spectra and the tissues can thus be differentiated. Using the two attenuation coefficient maps from two different effective energy spectra, it is possible to express the image in terms of fractions of two basis materials [119], such as water and bone, or in terms of different pairs of physical parameters, such as RED and EAN.
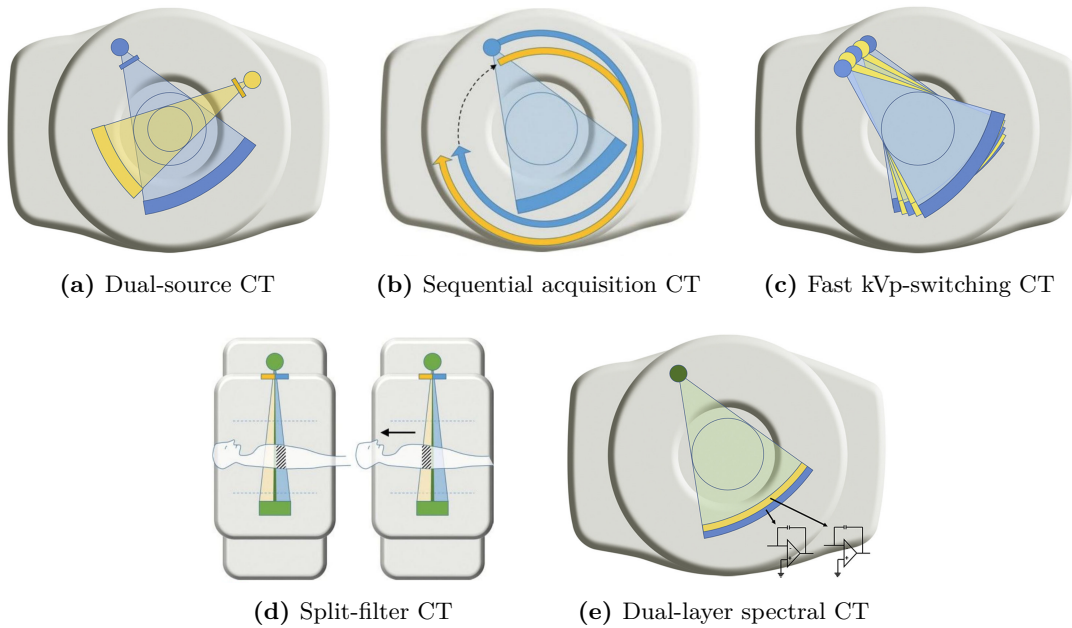
Clinical applications

DECT can be used to improve material differentiation. For example, it is able to differentiate kidney stones into uric acid and non-uric acid (i.e., calcium-containing) stones [120]; to distinguish gout from pseudo-gout; to differentiate silicone breast implants from dense soft tissue; and to remove bone from images, which improves visualization of contrast-enhanced vessels and organs [31]. DECT can also be used to enhance material characterization by creating the following: quantitative iodine and virtual non-contrast-enhanced maps for contrast-enhanced images; quantitative calcium and virtual non-calcium maps; virtual monoenergetic images to enhance tissue contrast and reduce metal artifacts; quantitative perfused blood volume images to improve pulmonary embolism detection; and RED and EAN maps for radiotherapy applications [31].

Dual-energy CT techniques

As of 2023, in clinical practice, there are multiple ways to acquire DECT data, including dual-source CT, dual-spiral or sequential acquisition CT, fast kVp-switching CT, split-filter CT, and dual-layer spectral CT (Figure 2.7) [35]. DSCT uses two X-ray tubes producing different voltages with an angular offset of approximately 90° and two detectors to achieve dual-energy acquisition and data processing [30]. SACT scans the entire volume sequentially at two different tube potentials [121]. KVSCT uses a single X-ray tube that alternates rapidly between high and low tube potentials multiple times within the same rotation [122]. SFCT uses a two-material filter at the output of the tube, which results in the separation of the beam along the longitudinal axis into low- and high-energy spectra, which are detected by their respective halves of the detector [123]. DLCT employs a single X-ray tube paired with a dual-layer detector that detects two energy levels simultaneously, with each layer having maximum sensitivity at different energies [124–128].

The different technical implementations share a similar basic physical principle. For DECT data acquisition, there are two main requirements: a sufficient difference in photon energies between the two CT image acquisitions, and a minimal time interval between the two CT acquisitions, which ideally occur at the same time [129]. The requirement concerning sufficient energy difference controls noise levels in the post-processed images to ensure acceptable image quality for diagnosis, and the requirement pertaining to the time interval ensures minimal

(a) Dual-source CT   **(b)** Sequential acquisition CT   **(c)** Fast kVp-switching CT

(d) Split-filter CT   **(e)** Dual-layer spectral CT

Figure 2.7: Schematic illustration of different dual-energy CT (DECT) techniques. Yellow represents the low-energy spectrum and blue represents the high-energy spectrum. Figure adapted from [35].

registration errors between the images from the two CT acquisitions [129]. All DECT platforms perform the same basic physical task of material decomposition during post-processing [129].

The strengths and limitations of the various currently available DECT acquisition techniques have been expounded on in previous work [22, 31, 34, 35, 39] and are summarized in Table 2.1 with a focus on particle therapy treatment planning applications. The choice of the most suitable DECT technique depends on the purpose of the application (e.g., presence of motion, body site) and the relative effect of various parameters (e.g., tube current modulation, impact of scattering, spectral separation) [22], and so it is difficult to give a general recommendation [126].

Stopping power ratio prediction from dual-energy CT

The use of DECT for treatment planning in particle therapy was first proposed in 1977 [29] and rediscovered in 2009 [130, 131]. In 2010, it was demonstrated that DECT could estimate SPR more accurately than SECT [37]. Since then, several mathematical models have been proposed [37, 111, 132–149] to convert DECT image data into SPR maps that can be used as input for a TPS. This thesis has aimed to investigate the potential of DECT, specifically DLCT, to reduce the uncertainties related to ion beam range prediction.

Table 2.1: Comparison of different dual-energy CT (DECT) acquisition techniques with a focus on particle therapy treatment planning. Table adapted from publication I [126].

Technical features	Dual-source CT	Sequential acquisition CT	Fast kVp-switching CT	Split-filter CT	Dual-layer spectral CT
Spectral mode	spectral mode preselection, prospective results generation	spectral mode preselection, prospective results generation	spectral mode preselection, prospective results generation	spectral mode preselection, prospective results generation	no special mode, pro- and retrospective results generation
Acquisition mode	dedicated dual-energy	dedicated dual-energy	dedicated dual-energy	dedicated dual-energy	implicit dual-energy
Temporal coherence	high (quarter rotation angular offset)	low (large offset)	high (nearly perfect alignment)	medium (half collimation offset)	perfect alignment
Spatio-temporal resolution	full capabilities	full capabilities	limited capabilities (impaired spatial resolution)	full capabilities	full capabilities
Availability of dose modulation	yes (individual tube current modulation)	yes (individual tube current modulation)	no (no tube current modulation)	yes (tube current modulation)	yes (tube current modulation)
Spectral separation	very high (with additional tin filtration)	very high	medium ("smearing of spectra" due to finite kV-switching times)	low	medium
Cross-scatter occurrence	between source–detector systems	no	no	between detector rows (halves) separated by the system's central vertical plane	between detector layers
Field-of-view	limited (up to 350 mm)	full	full	full	full
Time-resolved respiratory imaging	practicable with post-processing phase matching	practicable with post-processing phase matching	practicable with post-processing phase matching	practicable with post-processing phase matching	no technical limitations
Contrast-enhanced imaging	multi-phase (arterial and venous phases)	restricted to late or delayed phase	multi-phase (arterial and venous phases)	restricted to late or delayed phase	multi-phase (arterial and venous phases)
Spectral decomposition	image-based material decomposition	image-based material decomposition	projection-based material decomposition	image-based material decomposition	projection-based material decomposition

Publications

The thesis is presented in a cumulative format in accordance with the guidelines of the Department of Physics and Astronomy of Heidelberg University. The thesis includes three manuscripts published in internationally recognized, peer-reviewed journals. The publications are referenced by Roman numerals. I am the first author of publications I, II, and III. None of the publications has been used in other dissertations.

List of publications:

- **Publication I**
  Friderike K. Longarino, Antonia Kowalewski, Thomas Tessonnier, Stewart Mein, Benjamin Ackermann, Jürgen Debus, Andrea Mairani, Wolfram Stiller. Potential of a Second-Generation Dual-Layer Spectral CT for Dose Calculation in Particle Therapy Treatment Planning. *Frontiers in Oncology* (2022) 12:853495. DOI: 10.3389/fonc.2022.853495
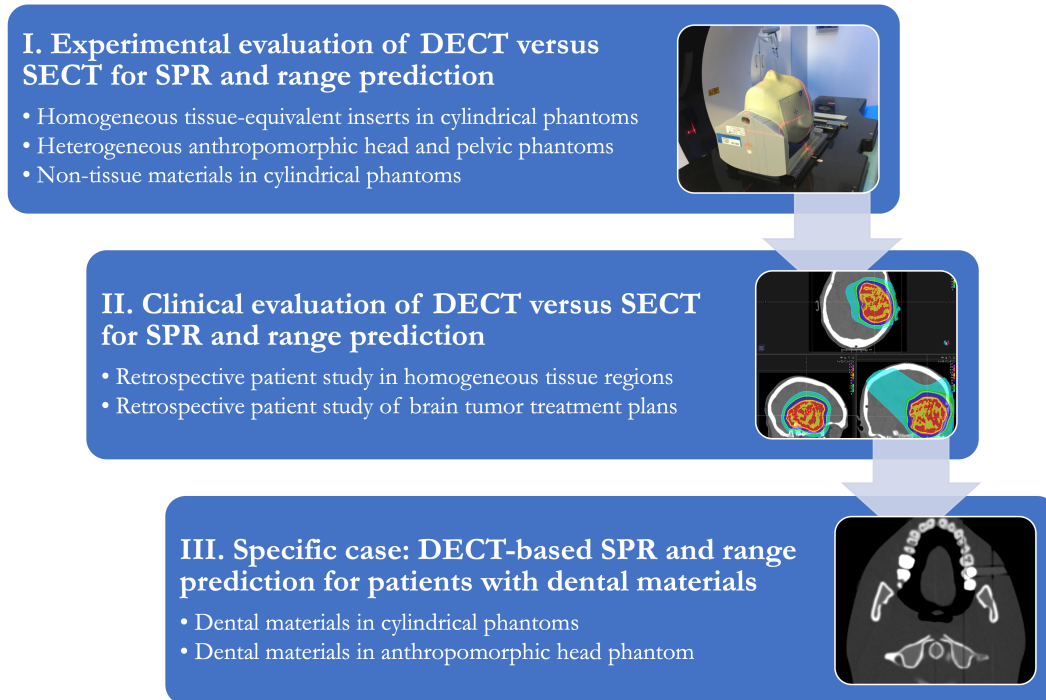
- **Publication II**
  Friderike K. Longarino, Thomas Tessonnier, Stewart Mein, Semi B. Harrabi, Jürgen Debus, Wolfram Stiller, Andrea Mairani. Dual-layer spectral CT for proton, helium, and carbon ion beam therapy planning of brain tumors. *Journal of Applied Clinical Medical Physics* (2022) 23(1):e13465. DOI: 10.1002/acm2.13465

- **Publication III**
  Friderike K. Longarino, Christopher Herpel, Thomas Tessonnier, Stewart Mein, Benjamin Ackermann, Jürgen Debus, Franz Sebastian Schwindling, Wolfram Stiller, Andrea Mairani. Dual-energy CT-based stopping power prediction for dental materials in particle therapy. *Journal of Applied Clinical Medical Physics* (2023) 24(8):e13977. DOI: 10.1002/acm2.13977

3.1 Thematic overview

Clinical treatment planning requires accurate beam range prediction in order to optimize targeted dose delivery in particle therapy. In this thesis, DLCT was investigated experimentally and clinically as a potential technique for obtaining patient-specific SPR estimates and for improving particle range prediction, an improvement that would minimize the uncertainty in the beam range and allow for reduced safety margins in the patient. To this end, the potential of DLCT

Figure 3.1: Thematic overview of the three publications.

as an alternative to SECT for improved SPR prediction was investigated in three different experimental settings and clinical scenarios. First, the potential of DLCT versus SECT for dose calculation in particle therapy treatment planning was investigated using tissue-equivalent material inserts, anthropomorphic phantoms, and non-tissue materials. Second, the clinical impact of using DLCT versus SECT for particle therapy treatment planning of brain tumors was analyzed in a retrospective patient study. Third, DECT-based SPR prediction for patients with dental materials, a specific case in particle therapy, was investigated. A thematic overview of the publications is shown in Figure 3.1. The main findings of the publications are briefly stated below. The original manuscripts can be found in sections 3.2 to 3.4, and supplementary material for each publication is included in the appendix.

Publication I investigated the use of a second-generation DLCT system (Spectral CT 7500, Philips Healthcare) as an alternative to conventional SECT for SPR prediction. To evaluate DLCT-based SPR prediction, a comprehensive workflow for particle therapy treatment planning was established based on quantitative measurements of RED and EAN using the Bethe equation (Figure 3.2). DLCT-based SPR prediction accuracy was evaluated in the case of tissue-equivalent materials and common non-tissue implant materials. In each instance, it was found that, in comparison to SECT, DLCT reduced the uncertainty in SPR predictions. The relative mean deviation from measured SPR values for tissue-equivalent materials was 1.6% in the case of SECT and 0.7% in the case of DLCT. The accuracy in SPR remained unaffected by the CT acquisition settings, reconstruction parameters, or the size and type of the phantom. For DLCT-based proton,
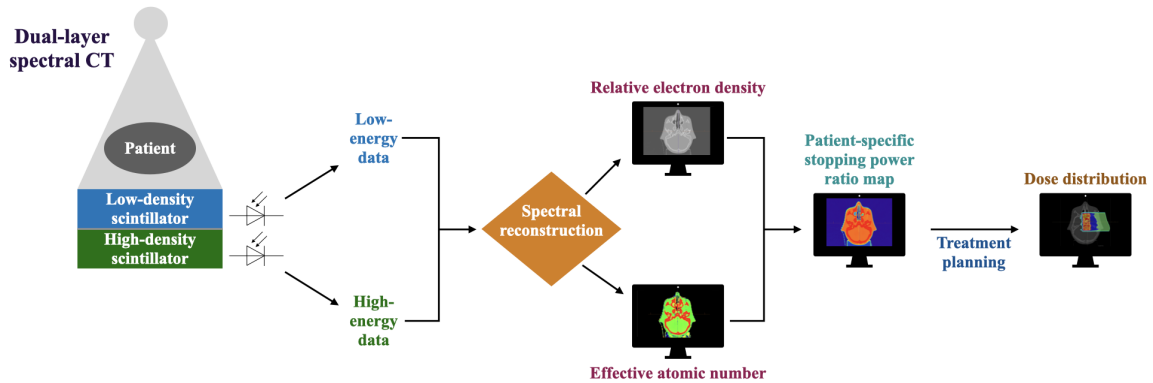
Figure 3.2: Principle of predicting stopping power ratio (SPR) for particle therapy treatment planning based on dual-layer spectral CT (DLCT). A dual-layer detector that detects two energy spectra enables the simultaneous acquisition of low- and high-energy data, which then allows for material decomposition in the projection-space domain. The data are reconstructed and processed to obtain spectral images, such as relative electron density (RED) and effective atomic number (EAN), to predict SPR and plan particle therapy treatments.

helium, and carbon ion beam therapy treatment planning, end-to-end tests were performed with anthropomorphic, geometrically complex head and pelvic phantoms in clinical-like settings. In these end-to-end tests, where ionization chamber array measurements were used as a reference, 3D gamma passing rates were observed to be higher for the DLCT-predicted dose distributions than for the SECT-predicted dose distributions, which indicated that SPR prediction with DLCT outperformed the conventional SECT standard. Additionally, the DLCT-based range prediction was demonstrated to be highly accurate in that the measured evaluation layers at the distal edge and their predicted positions were within 1 mm of each other. The investigation showed that, compared to SECT systems currently used in clinics, DLCT systems can result in a closer agreement between the planned and delivered dose in particle therapy.

Publication II evaluated DLCT-based SPR prediction for treatment planning with proton, helium, and carbon ion beams for brain tumors. A clinical comparison between DLCT- and SECT-based SPR prediction was conducted in anatomical regions of homogeneous as well as heterogeneous tissues. The study assessed the feasibility and clinical viability of using DLCT-based SPR prediction for particle therapy treatment planning. The study included eight patients who were scanned by using DLCT for diagnostic purposes. Four different treatment plans for simulated target volumes in various regions of the brain were devised for each patient. The DLCT- and SECT- based approaches showed mean SPR differences of approximately 1% for homogeneous anatomical regions. In treatment plans optimized for heterogeneous anatomy, investigations at the distal fall-off revealed relative (absolute) proton range shifts of 0.6% (0.4 mm) in the mean and up to 4.4% (2.1 mm). Additionally, 12% of the OARs evaluated in the studied cohort demonstrated differences in mean or maximum dose of over 0.5 Gy(RBE) and up to 6.8 Gy(RBE) over the entire treatment. The range shifts and dose differences in OARs that were

observed between DLCT- and SECT-based treatment plans were similar in the case of proton, helium, and carbon ion beams. In most cases studied (75$^{\text{th}}$ percentile), range estimates based on DLCT and SECT were within 0.6 mm. Nevertheless, clinically relevant deviations in range prediction between DLCT and SECT were observed in heterogeneous anatomical sites, inviting continued investigation in larger and more diverse cohorts. The findings of this study suggest that the use of DLCT in treatment planning may be beneficial for patients with brain tumors.

Publication III investigated DECT-based SPR prediction for head and neck particle therapy for patients with dental implant and restoration materials, a not infrequent, yet challenging scenario. Dental materials of uncertain stoichiometric composition can substantially impair particle therapy planning because of the associated uncertainties in SPR prediction. This study investigated the use of two DECT techniques, namely DLCT and SACT, to profile the characteristics of and offset the potential problems caused by commonly used dental materials during particle therapy treatment planning. The radiological material parameters of ten dental materials were determined. DECT- and SECT-based SPR predictions of dental materials were compared. The following abbreviations were used in this study: SECT-based SPR prediction with SACT at 140 kV$_{\text{p}}$ (SE-140-SACT), DECT-based SPR prediction with SACT using a DirectSPR implementation (DE-DirectSPR-SACT), DECT-based SPR prediction with SACT using the RhoZ-method (DE-RhoZ-SACT), SECT-based SPR prediction with DLCT at 120 kV$_{\text{p}}$ (SE-120-DLCT), and DECT-based SPR prediction with DLCT using the RhoZ-method (DE-RhoZ-DLCT). Overall, in comparison to SECT, DECT was found to reduce the SPR prediction uncertainty in dental materials, though the usefulness of DECT methods was impaired when applied to materials containing elements of a high atomic number. DECT-based treatment planning for helium ion therapy in an anthropomorphic head phantom with a removable tooth containing lithium disilicate showed that DECT-based techniques predicted similar ranges for beams unobstructed by dental material. In the case of ion beams that passed through the lithium disilicate restoration, SPR prediction based on DE-DLCT, which employs a projection-based method, most closely agreed with the measured reference data, with a range deviation of 0.2 mm. Thus, the management of certain dental implant and restoration materials may be improved by DECT-based SPR prediction, leading to increased accuracy in dose prediction.

In sum, the studies have demonstrated the ability of DLCT to directly predict patient-specific SPR and the feasibility of its use in treatment planning with proton, helium, and carbon ion beams. DLCT was more accurate than SECT in predicting SPR in tissue-equivalent materials, anthropomorphic phantoms, and non-tissue materials. A retrospective patient study demonstrated the potential benefit of using DLCT in treatment planning for brain tumors. In the case of patients with dental implant and restoration materials, predicting SPR based on DECT may improve dental management for patients undergoing head and neck particle therapy. Further clinical studies in larger patient cohorts and other treatment regions will further quantify the potential benefits of DLCT and estimate the potential reduction in range uncertainty, which could lead to smaller safety margins for high-precision particle therapy.

3.2 Publication I

Potential of a Second-Generation Dual-Layer Spectral CT for Dose Calculation in Particle Therapy Treatment Planning

---

Authors:	Friderike K. Longarino, Antonia Kowalewski, Thomas Tessonnier, Stewart Mein, Benjamin Ackermann, Jürgen Debus, Andrea Mairani, Wolfram Stiller
Publication status:	Published 20 April 2022
Journal reference:	*Frontiers in Oncology* (2022) 12:853495
DOI:	10.3389/fonc.2022.853495
Copyright:	© 2022 Longarino, Kowalewski, Tessonnier, Mein, Ackermann, Debus, Mairani and Stiller. This is an open-access article distributed under the terms of the Creative Commons Attribution License (CC BY). The use, distribution or reproduction in other forums is permitted, provided the original author(s) and the copyright owner(s) are credited and that the original publication in this journal is cited, in accordance with accepted academic practice. No use, distribution or reproduction is permitted which does not comply with these terms. No changes have been made.
Contribution:	FL and AK contributed equally to this work and are co-first authors of this publication. FL, AK, AM, and WS conceptualized the study. FL, AK, AM, and WS developed the methodology. Data was acquired and analyzed by FL, AK, and BA and interpreted by FL, AK, SM, TT, AM, and WS. FL and AK wrote the original draft of the manuscript and prepared all graphics. FL, AK, SM, TT, BA, JD, AM, and WS contributed to the review and editing of the final manuscript. JD, AM, and WS provided supervision.

Potential of a Second-Generation Dual-Layer Spectral CT for Dose Calculation in Particle Therapy Treatment Planning

Friderike K. Longarino [1,2,3†], Antonia Kowalewski [2,4,5†], Thomas Tessonnier [6], Stewart Mein [2,4,6,7,8], Benjamin Ackermann [6], Jürgen Debus [1,2,6,7,8,9], Andrea Mairani [2,6,8,10*‡] and Wolfram Stiller [11*‡]

[1] Clinical Cooperation Unit Radiation Oncology, German Cancer Research Center (DKFZ), Heidelberg, Germany, [2] Department of Radiation Oncology, Heidelberg University Hospital, Heidelberg, Germany, [3] Department of Physics and Astronomy, Heidelberg University, Heidelberg, Germany, [4] Translational Radiation Oncology, German Cancer Research Center (DKFZ), Heidelberg, Germany, [5] Department of Physics, Simon Fraser University, Burnaby, BC, Canada, [6] Heidelberg Ion Beam Therapy Center (HIT), Heidelberg, Germany, [7] Heidelberg Institute of Radiation Oncology (HIRO), National Center for Radiation Research in Oncology (NCRO), Heidelberg, Germany, [8] National Center for Tumor Diseases (NCT), Heidelberg, Germany, [9] German Cancer Consortium (DKTK), Core Center Heidelberg, Heidelberg, Germany, [10] Medical Physics, National Center of Oncological Hadrontherapy (CNAO), Pavia, Italy, [11] Diagnostic and Interventional Radiology (DIR), Heidelberg University Hospital, Heidelberg, Germany

In particle therapy treatment planning, dose calculation is conducted using patient-specific maps of tissue ion stopping power ratio (SPR) to predict beam ranges. Improving patient-specific SPR prediction is therefore essential for accurate dose calculation. In this study, we investigated the use of the Spectral CT 7500, a second-generation dual-layer spectral computed tomography (DLCT) system, as an alternative to conventional single-energy CT (SECT) for patient-specific SPR prediction. This dual-energy CT (DECT)-based method allows for the direct prediction of SPR from quantitative measurements of relative electron density and effective atomic number using the Bethe equation, whereas the conventional SECT-based method consists of indirect image data-based prediction through the conversion of calibrated CT numbers to SPR. The performance of the Spectral CT 7500 in particle therapy treatment planning was characterized by conducting a thorough analysis of its SPR prediction accuracy for both tissue-equivalent materials and common non-tissue implant materials. In both instances, DLCT was found to reduce uncertainty in SPR predictions compared to SECT. Mean deviations of 0.7% and 1.6% from measured SPR values were found for DLCT- and SECT-based predictions, respectively, in tissue-equivalent materials. Furthermore, end-to-end analyses of DLCT-based treatment planning were performed for proton, helium, and carbon ion therapies with anthropomorphic head and pelvic phantoms. 3D gamma analysis was performed with ionization chamber array measurements as the reference. DLCT-predicted dose distributions revealed higher passing rates compared to SECT-predicted dose distributions. In the DLCT-based treatment plans, measured distal-edge evaluation layers were within 1 mm of their

predicted positions, demonstrating the accuracy of DLCT-based particle range prediction. This study demonstrated that the use of the Spectral CT 7500 in particle therapy treatment planning may lead to better agreement between planned and delivered dose compared to current clinical SECT systems.

1 INTRODUCTION

The central goal of modern radiotherapy is the delivery of maximum radiation dose to tumors while minimizing radiation dose to healthy surrounding tissue. Particle therapy offers promising advancements in this regard [1], thanks to the favourable depth-dose curve of charged particles compared to conventional photon beams (X-rays) [2]. However, to take full advantage of the benefits of particle therapy, it is essential to have precise, accurate, and patient-specific predictions of particle ranges within the body [3]. For clinical treatment planning, predicted particle ranges are calculated from ion stopping power ratio (SPR) maps, which are in turn derived from patient computed tomography (CT) data. At present, CT numbers (CTNs) from single-energy CT (SECT) images are converted to SPR values using a generic, empirically validated conversion function called a Hounsfield look-up table (HLUT) (**Supplementary Figure 1**). This approach to SPR prediction is a main source of beam range uncertainty, as HLUTs do not account for degeneracies between CTN and SPR values, nor for variability in tissue composition between patients [4–8].

Recently, dual-energy CT (DECT), clinically introduced for diagnostic imaging in 2006 [9], has been investigated as an alternative to SECT. In DECT, two CT data sets are acquired using different X-ray spectra, enabling the generation of relative electron density (ED) and effective atomic number (EAN) maps [10]. From ED and EAN data, SPR values can be calculated through the Bethe equation without the need for a pre-defined HLUT [10, 11]. Both theoretical [5, 10] and experimental [5, 12–22] studies have shown DECT to improve SPR prediction accuracy over SECT. Several imaging techniques and modalities exist to achieve DECT results, including dual-spiral, dual-source, rapid kV switching, twin-beam, and dual-layer technologies [7] (**Supplementary Tables 1, 2**). Of these, dual-layer spectral CT (DLCT) employs a double-layer detector to simultaneously acquire high- and low-energy X-ray data [23]. This avoids exposing the patient to additional radiation [21], and achieves synchronicity between the low- and high-energy data acquisitions over the full scan field-of-view, facilitating the imaging of moving organs [24].

At present, the SPR prediction accuracy of DLCT has only been investigated using the Philips IQon Spectral CT (Philips Healthcare, Best, The Netherlands) [21, 22, 24–27]. Here, we investigate the SPR prediction accuracy of the new Philips Spectral CT 7500 (Philips Healthcare, Best, The Netherlands), commissioned at the Heidelberg University Hospital (Germany) for diagnostic use in February 2021 and officially released in May

2021. This scanner offers advantages over the Philips IQon Spectral CT, including a new high-performance patient table, a larger (anatomical) detector coverage enabling a greater number of simultaneously acquired slices per rotation (up to 256 versus 128), and a larger bore size (**Supplementary Table 3**). The large bore size of 800 mm allows for easier access to patients, and better accommodation of patient accessories and obese patients. Furthermore, the Philips Spectral CT 7500 allows the generation of spectral results at 100, 120, and 140 kV_P.

We seek to validate the Philips Spectral CT 7500 for particle therapy treatment planning by conducting a thorough analysis of its SPR prediction accuracy for both tissue-equivalent materials and common non-tissue implants. To our knowledge, this is the first study conducted on second-generation DLCT systems (i.e., Spectral CT 7500) and here we focus specifically on applications to particle therapy. We employed the same methodology as in the relevant publications on the first-generation system [22, 25, 27] in order to allow for direct comparability to results from prior studies. Furthermore, we perform end-to-end analyses for proton, helium ion, and carbon ion therapies with anthropomorphic head and pelvic phantoms.

2 MATERIALS AND METHODS

2.1 CT Image Acquisition and Reconstruction

All images were acquired using the Philips Spectral CT 7500 scanner (Philips Healthcare, Best, The Netherlands) at the Heidelberg University Hospital with a standardized head or body protocol at 120 kV_P. The image acquisition settings and reconstruction parameters for head and body protocols are specified in **Supplementary Table 4**, and are based on current state-of-the-art clinical protocols used for particle therapy planning at the Heidelberg Ion Beam Therapy Center (HIT, Germany). Both SECT and DLCT image data are automatically generated from the same raw data set for each acquisition on the Spectral CT 7500 scanner, enabling a direct comparison of the two techniques.

Image reconstruction was performed using the iDose^4 algorithm at levels 0, 3, and 6 (Philips Healthcare, Best, The Netherlands). The iDose^4 algorithm uses a hybrid iterative reconstruction technique to reduce image noise, and has levels ranging from 0 to 6, where higher levels correspond to greater noise reduction. In this context, an iDose^4 level of 0 corresponds to conventional filtered back-projection image reconstruction. For imaging of metallic materials, the Philips orthopedic metal

artifact reduction algorithm (O-MAR) (Philips Healthcare, Best, The Netherlands) was also applied.

2.2 SPR Prediction and Validation in Geometric Phantoms

The SPR prediction accuracy of the Philips Spectral CT 7500 scanner was first investigated using a number of custom cylindrical polymethyl methacrylate (PMMA) phantoms with tissue-equivalent inserts spanning the range of clinically relevant CTNs (**Figure 1**). Five PMMA phantoms were used to simulate different patient sizes: two one-bore cylinders of height 46.0 cm and radius 5.0 cm ("LCT", "long cylinder thin") and 8.0 cm ("LC", "long cylinder"), two nine-bore cylinders of height 10.0 cm and radius 8.0 cm ("SC", "short cylinder") and 16.0 cm ("SCB", "short cylinder big"), and a roughly human-shaped pelvis. Thirteen tissue-equivalent cylindrical inserts (Gammex Electron Density CT Phantom 467, Gammex-RMI, Middleton, WI, USA) of height 7.0 cm and radius 1.4 cm were used as bore inserts: cortical bone, CB2 50%, CB2 30%, inner bone, muscle, brain, adipose, true water, liver, solid water, breast, bone mineral, and lung. Reference SPR values of these inserts were determined experimentally at HIT by measuring the range shift of a carbon ion beam in a water absorber (Peakfinder Water Column, PTW-Freiburg, Freiburg, Germany). Carbon ions were used for the measurement due to their sharper Bragg peak, reduced lateral scattering, and reduced range straggling compared to protons (22). The inserts were placed in the phantoms in specific configurations to minimize artifacts caused by the high-density bone-equivalent inserts (14).

Furthermore, a selection of materials commonly found in non-tissue implants were scanned for SPR prediction. The metals aluminum and titanium and a carbon/PEEK-titanium composite (icotec ag, Altstätten, Switzerland) were imaged in the LC phantom, along with the special materials PMMA, TECAFORM® and TECAPEEK® (Ensinger GmbH, Nufringen, Germany), and Teflon™ (The Chemours Company, Wilmington, DE, USA). In addition, PALACOS® R + G bone cement (Heraeus, Hanau, Germany) was imaged in a water bath.

2.2.1 Calculation of Predicted SPR Values Based on Quantitative DLCT Data

Predicted SPR values were calculated from DLCT-generated ED and EAN maps using the Bethe equation neglecting higher order correction terms (11), as described in Faller et al. (22). The mean excitation energy (I-value) of the tissue was calculated from EAN data using the method outlined in Yang et al. (10). The I-value of water was set to 78.73 eV, consistent with the values proposed by Bär et al. (28) and the International Commission on Radiation Units and Measurements (29). A fixed particle kinetic energy of 100 MeV per nucleon was assumed, as recommended by Inaniwa & Kanematsu (30), since the energy dependence of SPR prediction is minimal in the therapeutic range (31).

2.2.2 Calculation of Predicted SPR Values Based on Conventional SECT Image Data

For each of the two imaging protocols (head and body), an HLUT was generated from 120 kV$_P$ SECT image data acquired
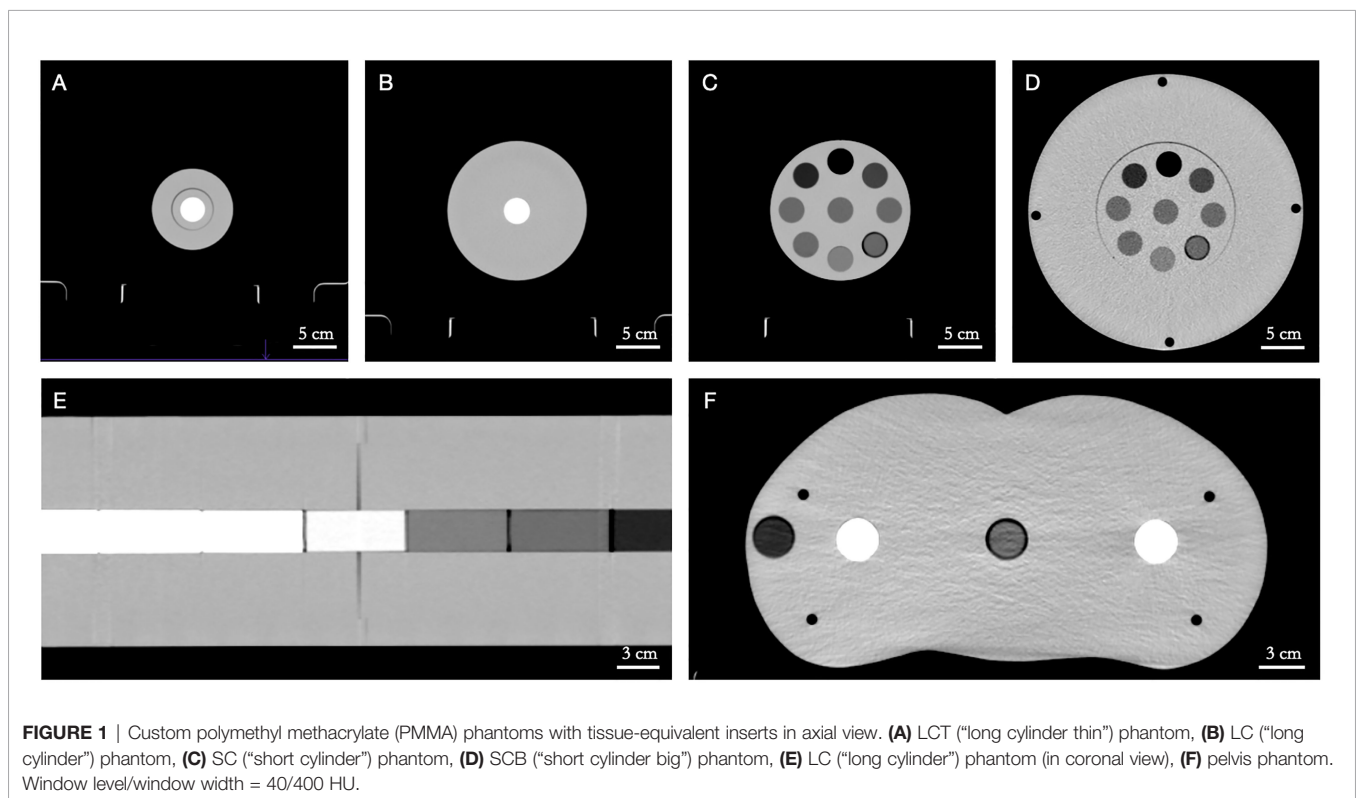
FIGURE 1 | Custom polymethyl methacrylate (PMMA) phantoms with tissue-equivalent inserts in axial view. **(A)** LCT ("long cylinder thin") phantom, **(B)** LC ("long cylinder") phantom, **(C)** SC ("short cylinder") phantom, **(D)** SCB ("short cylinder big") phantom, **(E)** LC ("long cylinder") phantom (in coronal view), **(F)** pelvis phantom. Window level/window width = 40/400 HU.

using the given protocol. A two-parameter stoichiometric parametrization (11, 32) was applied to generate the HLUT, following the current clinical protocol at HIT (33). The generated HLUT was then used to convert CTNs to SPR values (**Supplementary Figure 1**).

2.2.3 Assessment of DLCT- and SECT-Based SPR Predictions

Predicted SPR values of cylindrical phantom inserts were extracted for analysis using circular regions-of-interest (ROIs) with a size of ~70% of the inserts' cross-sectional diameters. This strategy avoided possible artifacts caused by gradient effects to the surrounding PMMA near the insert–phantom boundary. ROI slices towards both ends of the inserts were also excluded for similar reasons. Predicted SPR values of the PALACOS® R + G bone cement, imaged in a water bath, were extracted for analysis using a similar method, where ROIs were evaluated at cross-sectional locations along the longest axis of the bone cement sample.

The agreement of predicted SPR values (SPR_{pre}) with reference values (SPR_{ref}) was quantified using relative residuals, defined as

$$relative\ residual = \frac{SPR_{pre} - SPR_{ref}}{SPR_{ref}} \cdot 100\ \%$$

For each phantom–protocol combination, the mean overall relative residual was computed using the formula

$$mean\ overall\ relative\ residual = \frac{1}{N}\sum_{i=1}^{N}|relative\ residual|$$

Additionally, for each phantom–protocol combination, the root-mean-square error (RMSE) and Pearson's correlation coefficient (r) between predicted and reference SPR values were determined, using the formulas

$$RMSE = \sqrt{\frac{1}{N}\sum_{i=1}^{N}\left(SPR_{pre,i} - SPR_{ref,i}\right)^2}$$

and

$$r = \frac{\sum_{i=1}^{N}(SPR_{ref,i} - \overline{SPR_{ref}})(SPR_{pre,i} - \overline{SPR_{pre}})}{\sqrt{\sum_{i=1}^{N}(SPR_{ref,i} - \overline{SPR_{ref}})^2}\sqrt{\sum_{i=1}^{N}(SPR_{pre,i} - \overline{SPR_{pre}})^2}}$$

respectively. In both cases, N is the number of cylindrical inserts in a given phantom. In the Pearson's correlation coefficient formula, the bars represent arithmetic means.

Finally, predicted SPR values were fitted to reference values using linear regression, with parameters α and δ:

$$SPR_{pre} = \alpha \cdot SPR_{ref} + \delta$$

Pearson's correlation coefficient (r) and linear regression fitting parameters (α and δ) were used to quantify the agreement of DLCT- and SECT-based SPR predictions with measured reference values.

2.2.4 Evaluation of DLCT-Based Mass Density Calculation

We implemented and evaluated the DEEDZ-MD method proposed by Saito (34) to derive mass density (ρ) from DLCT data. ρ was calculated from DLCT-based ED (ρ_e) and EAN (Z_{eff}) values, with the EAN of water being $Z_{eff,w}$:

$$\rho = \rho_e + \rho_e\sum_{n=0}^{2}e_n\left\{\left(\frac{Z_{eff}}{Z_{eff,w}}\right)^m - 1\right\}^n$$

The value of m was set to 3.3, as determined in Saito & Sagara (35), and the same human tissue-specific parameters (e_n) as obtained in Saito (34) were employed.

2.3 Treatment Planning and Dosimetric Validation With Anthropomorphic Head and Pelvic Phantoms

The clinical benefits of SPR prediction based on DLCT data were investigated and compared with the currently applied SECT approach by using tissue-equivalent anthropomorphic head (Proton Therapy Dosimetry Head, Model 731-HN) and pelvic (Virtual Human Male Pelvis Phantom, Model 801-P) phantoms (Computerized Imaging Reference Systems, Inc. (CIRS), Norfolk, VA, USA).

Treatment planning optimizations with a dose grid of 1 mm were performed with RayStation Treatment Planning System v10 (RaySearch Laboratories AB, Stockholm, Sweden), using the Monte-Carlo dose engine for proton beams and the pencil beam dose engine for helium and carbon ion beams (**Figure 2**). The target position for each anthropomorphic phantom was selected such that it was located underneath multiple different tissue-equivalent layers, in order to test the various range prediction methods in heterogenous conditions. For the head phantom, an 8 x 8 x 3 cm^3 target volume located at the mid-head was optimized for a physical dose of 1 Gy (**Figure 2A**). For the pelvic phantom, two target types were optimized for a physical dose of 1 Gy: a prostate-like geometry of 52 cm^3 (**Figure 2B**) and a 6 x 6 x 6 cm^3 target volume (**Figure 2C**).

Treatment planning was initially performed with a conventional clinically-employed SECT scanner (SOMATOM Confidence, Siemens Healthcare GmbH, Erlangen, Germany) with a CT resolution of 0.977 x 0.977 x 1 mm^3 (head)/0.977 x 0.977 x 2 mm^3 (pelvis). Following plan optimization, forward dose calculations were performed on two additional (image) datasets from the Philips Spectral CT 7500: one using the SECT approach and one using the DLCT approach for SPR prediction.

Dosimetric measurements were acquired at HIT with the OCTAVIUS® 1000SRS P (PTW, Freiburg, Germany) prototype 2D ionization chamber array detector for proton, helium ion, and carbon ion beam treatment plans, as described in previous works (36). For both phantoms, measurements were performed in the high-dose area and at different positions along the distal edge. For the head phantom, irradiation was performed using the gantry at an angle of 0° with the half-head phantom placed on top of the OCTAVIUS® detector (**Supplementary Figure 2A**). For the pelvic phantom, irradiation was performed using the horizontal beam line with the half-pelvic phantom placed in front of the OCTAVIUS® detector (**Supplementary Figure 2B**).
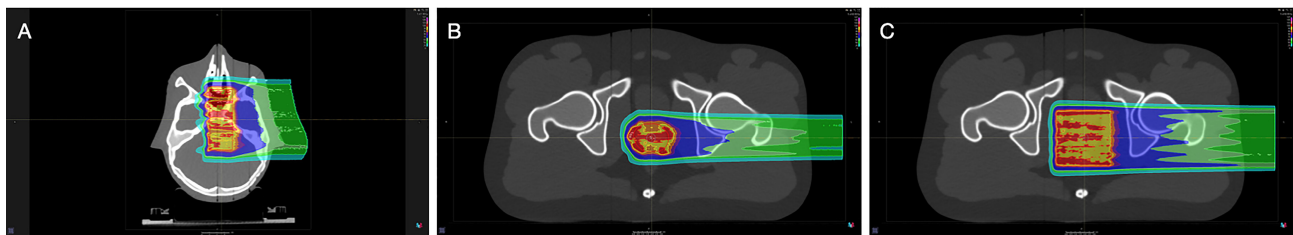
FIGURE 2 | Proton therapy treatment plans designed with the RayStation Treatment Planning System. **(A)** Head phantom with an 8 x 8 x 3 cm^3 target volume, **(B)** pelvic phantom with a prostate-like target volume of 52 cm^3, **(C)** pelvic phantom with a 6 x 6 x 6 cm^3 target volume.

Dose distributions were compared using a 3D gamma analysis (37) for local calculation with a passing criterion of 3%/1.5 mm using a low dose cut-off of 5% of the maximum dose.

3 RESULTS

3.1 CT Image Acquisition and Reconstruction

CT (image) data acquired using the head and body protocols produced similarly accurate SPR predictions (**Supplementary Tables 5**, **6**). As such, all reports of SPR prediction accuracy for the remainder of the study are based on CT images acquired using the body protocol, unless otherwise specified.

Similarly, the iDose^4 level used in image reconstruction was found to have no significant effect on the accuracy and standard deviation of predicted SPR values (**Supplementary Tables 5**, **6**). Therefore, all results reported for the remainder of the study are based on CT (image) data reconstructed using iDose^4 level 0 (that is, with minimum additional iterative post-processing), unless otherwise specified.

3.2 SPR Prediction and Assessment in Geometric Phantoms

For tissue surrogates, SPR values predicted using DLCT were consistently closer to reference values than SPR values predicted using SECT in all five phantoms (**Figure 3**; **Tables 1**, **2**). Pearson's correlation coefficient (r) and linear regression fitting parameters (α and δ) confirmed higher agreement between measured and DLCT-predicted SPR values compared to SECT-predicted SPR values (**Tables 1**, **2**). For consistency over all tissue-equivalent inserts, we focus solely on the LCT, LC, SC, and SCB phantoms for the remainder of the study, as not all inserts were imaged in the pelvis phantom.

For the LCT phantom, DLCT-based SPR prediction had a mean overall relative residual of 0.7% (range: [-0.3, 1.4]%) while SECT-based SPR prediction had a mean overall relative residual of 1.8% (range: [-5.7, 5.3]%) (**Figure 3A**). For the LC phantom, DLCT-based SPR prediction had a mean overall relative residual of 0.7% (range: [-1.4, 1.6]%) while SECT-based SPR prediction had a mean overall relative residual of 1.5% (range: [-5.3, 4.7]%) (**Figure 3B**). For the SC phantom, DLCT-based

SPR prediction had a mean overall relative residual of 0.6% (range: [-1.1, 1.5]%) while SECT-based SPR prediction had a mean overall relative residual of 1.5% (range: [-5.2, 4.3]%) (**Figure 3C**). Finally, for the SCB phantom, DLCT-based SPR prediction had a mean overall relative residual of 0.7% (range: [-1.2, 1.8]%) while SECT-based SPR prediction had a mean overall relative residual of 1.7% (range: [-4.3, 3.5]%) (**Figure 3D**). Across all four phantoms, the average mean overall relative residual was 0.7% for DLCT-based SPR prediction and 1.6% for SECT-based SPR prediction.
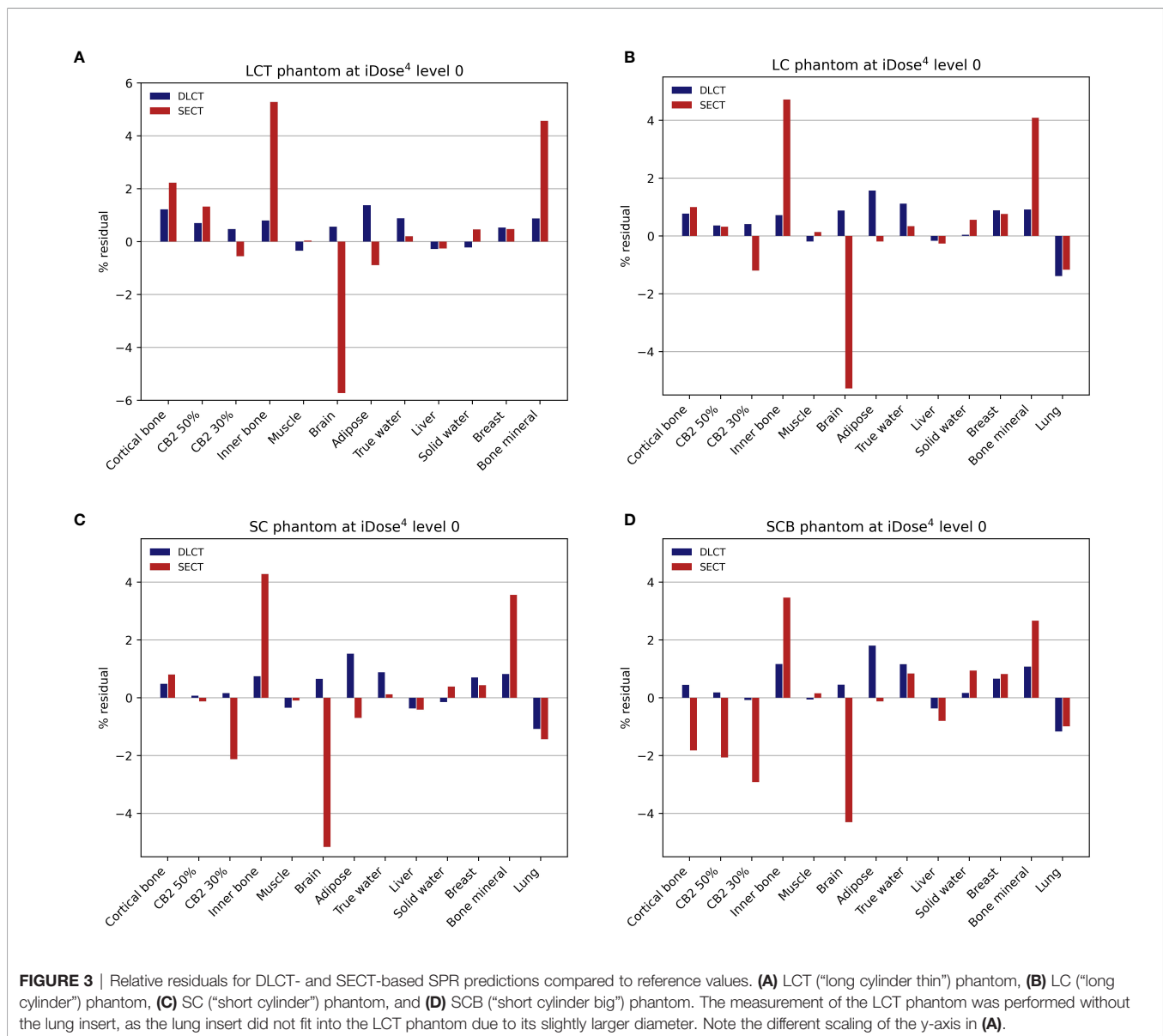
Accuracies of DLCT- and SECT-based SPR predictions across different non-tissue implant materials are listed in **Table 3**. DLCT substantially outperformed SECT in predicting SPR values for all non-tissue materials. For the metals aluminium and titanium, SPR prediction accuracy was similar with and without the metal artifact reduction algorithm O-MAR. The HLUT derived in the SECT-based approach is shown together with the eight non-tissue implant materials in **Supplementary Figure 1**.

Experimental validation of the DEEDZ-MD method for determining mass density was performed using the tissue-equivalent inserts in the SC phantom, yielding a relative mean deviation of -1.4% compared to the vendor's provided mass density data (Gammex Electron Density CT Phantom 467, Gammex-RMI, Middleton, WI, USA).

For the SC phantom, the effect of lowering the tube current-time product on SPR prediction accuracy was also investigated. The tube current-time product was lowered from 300 mAs to 250 mAs and 200 mAs with no adverse effect on the SPR prediction accuracy and its standard deviation. Increasing the tube voltage from 120 kV$_p$ to 140 kV$_p$ while using a tube current-time product of 200 mAs resulted in approximately the same volume CT dose index (CTDI$_{vol}$) as for the standard clinical protocol. DLCT-based SPR prediction using these CT acquisition settings (140 kV$_p$/200 mAs) had a mean overall relative residual of 0.6%, which is equal to that of the 120 kV$_p$/300 mAs protocol.

3.3 Treatment Planning and Dosimetric Validation With Anthropomorphic Head and Pelvic Phantoms

3D gamma analysis (3%/1.5 mm) using local calculation between SECT- and DLCT-based dose distributions and dosimetric measurements acquired with the OCTAVIUS$^{®}$

FIGURE 3 | Relative residuals for DLCT- and SECT-based SPR predictions compared to reference values. **(A)** LCT ("long cylinder thin") phantom, **(B)** LC ("long cylinder") phantom, **(C)** SC ("short cylinder") phantom, and **(D)** SCB ("short cylinder big") phantom. The measurement of the LCT phantom was performed without the lung insert, as the lung insert did not fit into the LCT phantom due to its slightly larger diameter. Note the different scaling of the y-axis in **(A)**.

ionization chamber array using the anthropomorphic head phantom revealed substantial agreement between measured and calculated dose distributions (**Tables 4**, **5**). For all three ion types, DLCT-based dose distributions showed higher 3D gamma passing rates compared to SECT-based dose distributions.

For the head phantom, the 3D gamma passing rates (3%/1.5 mm) were 98.8% (^{1}H), 97.9% (^{4}He), and 97.0% (^{12}C) using DLCT for the high-dose area of the target volume. For DLCT, the measured distal position of the 72% (^{1}H)/55% (^{4}He)/53% (^{12}C) dose level of the target volume was within 1 mm of the predicted distal position of the respective dose level with 3D gamma passing rates (3%/1.5 mm) of 97.4% (^{1}H), 84.6% (^{4}He), and 86.5% (^{12}C) (**Table 4**).

For the pelvic phantom, the 3D gamma passing rates (3%/1.5 mm) were 99.3% (^{1}H), 99.4% (^{4}He), and 99.5% (^{12}C)

using DLCT for the high-dose area of the prostate-like geometry and 98.1% (^{1}H), 99.4% (^{4}He), and 93.7% (^{12}C) for the high-dose area of the cubic target volume. For DLCT, the measured distal position of the 64% (^{1}H)/63% (^{4}He)/80% (^{12}C) dose level of the cubic target volume was within 1 mm of the predicted distal position of the respective dose level with 3D gamma passing rates (3%/1.5 mm) of 99.9% (^{1}H), 91.1% (^{4}He), and 97.6% (^{12}C) (**Table 5**).

4 DISCUSSION

4.1 Key Findings
In this study, we performed a thorough analysis of the use of the Philips Spectral CT 7500 DLCT system for SPR prediction in particle therapy treatment planning. For this purpose, we

TABLE 1 | Accuracy of DLCT-based SPR predictions across five different PMMA phantoms: LCT ("long cylinder thin") phantom, LC ("long cylinder") phantom, SC ("short cylinder") phantom, SCB ("short cylinder big") phantom, and a roughly human-shaped pelvis.

Phantom	LCT	LC	SC	SCB	Pelvis
Mean overall relative residual	0.688	0.725	0.613	0.675	0.816
RMSE	0.0093	0.0084	0.0056	0.0067	0.0116
r	0.9996	0.9998	0.9998	0.9997	0.9998
α	1.018	1.011	1.005	1.004	0.984
δ	-0.014	-0.006	-0.002	0.000	0.010

The table shows the mean overall relative residual, root-mean-square error (RMSE), Pearson's correlation coefficient (r), and linear regression fitting parameters (α and δ).

TABLE 2 | Accuracy of SECT-based SPR predictions across five different PMMA phantoms: LCT ("long cylinder thin") phantom, LC ("long cylinder") phantom, SC ("short cylinder") phantom, SCB ("short cylinder big") phantom, and a roughly human-shaped pelvis.

Phantom	LCT	LC	SC	SCB	Pelvis
Mean overall relative residual	1.833	1.538	1.514	1.685	0.859
RMSE	0.0307	0.0255	0.0243	0.0245	0.0101
r	0.9908	0.9956	0.9958	0.9962	0.9996
α	1.046	1.012	1.007	0.965	1.003
δ	-0.044	-0.009	-0.008	0.033	-0.005

The table shows the mean overall relative residual, root-mean-square error (RMSE), Pearson's correlation coefficient (r), and linear regression fitting parameters (α and δ).

TABLE 3 | Accuracy of SECT- and DLCT-based SPR predictions across different non-tissue materials.

Material	Relative residual SECT	Relative residual DLCT
Aluminium	-7.5	6.9
Carbon/PEEK-titanium composite	-16.8	1.0
Palacos bone cement	45.0	8.1
PMMA	-6.7	1.3
Tecaform	-13.7	2.2
Tecapeek	-11.0	1.7
Teflon	-19.8	4.4
Titanium	-28.0	18.4

experimentally verified DLCT-based SPR prediction accuracy and its impact on dose calculation in particle therapy planning with a Spectral CT 7500 scanner using tissue surrogates and non-tissue implant materials as well as anthropomorphic head and pelvic phantoms. To our knowledge, this is the first study to investigate this second-generation DLCT system for application in particle therapy. Moreover, this study presents the first dosimetric validation of DECT-based dose prediction using anthropomorphic phantoms for helium and carbon ion treatment plans. It is important to investigate DECT-based SPR prediction for helium and carbon ions since the impact of range uncertainty for these ion beams may lead to sizeable biological dose deviation, given the sharp gradients of linear energy transfer (LET) and relative biological effectiveness (RBE) end-of-range [38].

For tissue-equivalent materials, DLCT exhibited greater SPR prediction power, in general, compared to SECT with mean overall relative residuals of 0.6–0.7% for DLCT-based predictions and 1.5–1.8% for SECT-based predictions (**Figure 3**; **Tables 1**, **2**). Ranges represent the variability introduced by four different phantom geometries.

Furthermore, there are individual differences in the tissue-equivalent inserts, as discussed in Faller et al. [22]. The larger residuals of SECT-based SPR predictions for certain tissue-equivalent inserts (i.e., bone mineral, brain, and inner bone substitutes) (**Figure 3**) may in part result from differences between the elemental composition of the tissue surrogate inserts and their real tissue counterparts [39].

In clinical practice, many complicating factors to straight-forward SPR prediction exist, such as the presence of artifact-inducing implants in patients. Therefore, we also validated the use of DLCT for SPR prediction in eight common non-tissue implant materials. DLCT again outperformed SECT, although relative residuals for both approaches were significantly greater than those for tissue-equivalent materials: 1.0–18.4% for DLCT-based predictions, and -6.7%–45.0% for SECT-based predictions (**Table 3**). To illustrate the importance of SPR prediction for non-tissue implant materials, we consider the example of PALACOS® R + G bone cement. This common component of artificial joints is made mostly of PMMA and zirconium dioxide. Despite the presence of zirconium dioxide, a high-atomic-number material, the SPR of PALACOS® R + G

TABLE 4 | 3D gamma passing rates (3%/1.5 mm) using local calculation between SECT- and DLCT-based dose distributions and dosimetric measurements acquired with the OCTAVIUS® ionization chamber array using the anthropomorphic head phantom.

3D gamma passing rate in %

¹H			⁴He			¹²C		
Measurement position	SECT	DLCT	Measurement position	SECT	DLCT	Measurement position	SECT	DLCT
High-dose area, position A	98.6	98.8	High-dose area, position A	97.8	97.9	High-dose area, position A	96.9	97.0
High-dose area, position B	95.8	97.7	High-dose area, position B	95.7	99.4	92% dose fall-off	88.9	97.0
87% dose fall-off	92.3	99.6	72% dose fall-off	87.7	94.8	70% dose fall-off	75.7	78.3
72% dose fall-off	93.5	97.4	55% dose fall-off	81.5	84.6	53% dose fall-off	80.4	86.5

Four different depths were investigated, with two of the depths for ¹H and ⁴He being in the high-dose area (positions A and B), while the second depth for ¹²C was already in the dose fall-off.

TABLE 5 | 3D gamma passing rates (3%/1.5 mm) using local calculation between SECT- and DLCT-based dose distributions and dosimetric measurements acquired with the OCTAVIUS® ionization chamber array using the anthropomorphic pelvic phantom.

3D gamma passing rate in %

¹H			⁴He			¹²C		
Measurement position	SECT	DLCT	Measurement position	SECT	DLCT	Measurement position	SECT	DLCT
High-dose area (prostate-like geometry)	97.2	99.3	High-dose area (prostate-like geometry)	99.4	99.4	High-dose area (prostate-like geometry)	99.3	99.5
High-dose area, position A (cubic target volume)	95.7	98.1	High-dose area, position A (cubic target volume)	99.4	99.4	High-dose area, position A (cubic target volume)	93.3	93.7
95% dose fall-off (cubic target volume)	81.8	100.0	95% dose fall-off (cubic target volume)	83.2	94.3	High-dose area, position B (cubic target volume)	92.6	98.1
83% dose fall-off (cubic target volume)	85.9	100.0	81% dose fall-off (cubic target volume)	83.0	92.0	94% dose fall-off (cubic target volume)	94.8	97.9
64% dose fall-off (cubic target volume)	86.9	99.9	63% dose fall-off (cubic target volume)	82.0	91.1	80% dose fall-off (cubic target volume)	96.7	97.6

For the cubic target volume, four different depths were investigated, with two of the depths for ¹²C being in the high-dose area (positions A and B), while the second depth for ¹H and ⁴He was already in the dose fall-off.

is relatively low. The resulting uncertainty in SPR prediction can lead to a particle range deviation of several millimeters when using SECT-based treatment planning. Even if DECT is not implemented for quantitative SPR prediction in clinical practice, spectral image data could still be used to better differentiate between normal tissues and non-tissue implant materials and to help identify properties relating to the stopping power of non-tissue implant materials for contouring and SPR override. For example, using known ED and EAN data sets of commonly used implant materials, comparisons can be performed to quantify relevant physical properties to predict stopping power for unknown materials.

Furthermore, we used the Philips Spectral CT 7500 to experimentally validate the DEEDZ-MD method for determining mass density proposed by Saito (34). Our results showed a mean deviation of -1.4% from the reference value, which is similar to the -1.34% deviation reported by Saito (34). Future work may be dedicated to exploring treatment planning possibilities using mass density data.

We also found a result which suggests that tube current-time product can be lowered by 100 mAs in a simple geometric PMMA phantom without adverse effects on SPR prediction accuracy. Minimizing CT acquisition dose is an important component of CT research, particularly in fields with large pediatric contingents, such as particle therapy.

Finally, we demonstrated the feasibility of using the Philips Spectral CT 7500 to improve particle range prediction by irradiating anthropomorphic head and pelvic phantoms. We showed that dose distributions of DLCT-based treatment plans showed greater agreement with ionization chamber-measured dose distributions than dose distributions of SECT-based treatment plans for proton, helium ion, and carbon ion beams (**Tables 4**, **5**).

4.2 Comparison to Previous Work

DLCT-based SPR prediction accuracy was previously investigated at HIT using many of the same phantoms and tissue-equivalent inserts as in this study, but with the Philips IQon Spectral CT (22) (**Supplementary Table 2**). DLCT-based SPR prediction in that study yielded mean overall relative residuals of 0.6–0.9%, compared to the 0.6–0.7% reported here. These results indicate that the SPR prediction accuracy of the Philips Spectral CT 7500 is on par with that of the Philips IQon Spectral CT. However, the Philips Spectral CT 7500 provides numerous other advantages over the Philips IQon Spectral CT (**Supplementary Table 3**).

A related study using the Philips IQon Spectral CT reported similar SPR prediction accuracy results using mono-energetic images and the same inserts for calibration and evaluation (RMSE=0.6%) (25). Moreover, DLCT-based SPR prediction in this study showed similar accuracy compared to other DECT

systems for SPR prediction (12–14, 40). The SPR values of certain non-tissue implant materials used in this work have been previously investigated using dual-source CT (14). The DLCT functionality of the Philips Spectral CT 7500 yielded a similar SPR prediction accuracy as the dual-source CT in this previous study.

4.3 Clinical Relevance

As CT technology continues to improve, scanners with DECT capabilities are becoming increasingly available—they are already used for diagnostic purposes at many healthcare facilities. The application of DECT to particle therapy treatment planning could potentially improve patient outcomes. For example, inaccuracies in SPR prediction for pediatric proton therapy planning arising from SECT calibration curves based on adult male tissues may be avoided with DECT (41). Furthermore, SECT-based SPR prediction has been shown to introduce large inter-center variations in SPR, reaching up to 9% between different European institutions (42). Thus, DECT-based SPR prediction might offer more consistent SPR predictions between treatment centers or allow new particle therapy centers to begin treatment with greater confidence in SPR prediction. Moreover, recent work has demonstrated the benefits of even small reductions in range uncertainty to normal tissue complication probability (43), supporting that even small improvements in SPR prediction may be clinically beneficial.

4.4 Study Limitations and Future Work

This study demonstrated the feasibility of direct, patient-specific SPR prediction using existing clinical equipment and frameworks. However, in order to use DLCT for SPR prediction beyond a defined research environment, it will be necessary to devise and implement a complete workflow of certified medical products which does not currently exist. To start, SPR DICOM files could be provided as an on-demand spectral result directly from the Philips Spectral CT 7500 scanner instead of needing additional calculation steps using ED and EAN data.

The strengths and limitations of the different DECT or spectral CT acquisition techniques currently available have been described in previous works (7, 44–46) and are summarized in **Supplementary Table 1**, with a focus on applications to particle therapy treatment planning. Additionally, **Supplementary Table 2** lists selected publications on the different DECT or spectral CT acquisition techniques to provide an overview of the current state of research. The optimal DECT acquisition technique and hardware choice depends on the purpose of the application (e.g., body site, presence of motion) and the relative effect of various parameters (e.g., spectral separation, impact of scattering, tube current modulation) (7), which makes it difficult to give a general recommendation. Imaging with a dual-layer detector enables perfectly temporally and spatially aligned data sets. Moreover, DLCT imaging allows for tube current modulation, a full scan field-of-view coverage, and requires no special mode for DECT

acquisition. The dual-layer detector design also enables acquisition of dual-energy data at exactly the same phase of contrast enhancement. Furthermore, the DLCT technique facilitates projection-based material decomposition, allowing for better noise reduction and therefore potentially better material decomposition as compared to image-based methods (47). Nevertheless, spectral separation of DLCT systems is lower than that of source-based DECT systems (44), and spectral signal-to-noise ratio is comparable to that of other commercial DECT systems (48). In addition, DLCT systems carry the risk of cross-scatter occurring between detector layers (45).

In the future, particle CT might have the potential to further improve SPR prediction accuracies and serve as a ground-truth when comparing DECT-based SPR predictions (49). Thus far, precise SPR measurements using proton CT or helium CT are challenging to achieve, and provide a slightly lower SPR prediction accuracy compared to DECT (50).

While the tissue-equivalent materials used in this study are considered valid surrogates for biological tissues, they cannot fully represent the heterogeneity and variable composition of real tissues. Before DLCT-based SPR prediction can be implemented in clinical practice, more studies on biological tissue samples and *in vivo* systems need to be performed. In addition, measurements in this study were only performed with a male pelvic phantom, introducing a gender data gap. It would be desirable to perform similar measurements with a female pelvic phantom, but at the present time such a phantom does not exist. Furthermore, 4D treatment planning is important for radiotherapy treatments which require motion mitigation and/ or consideration during treatment, such as the thorax and the abdominal region. Future work could implement 4D DLCT-based SPR prediction and treatment planning. The large coverage of the Philips Spectral CT 7500 compared to the Philips IQon Spectral CT (80 mm versus 40 mm) (**Supplementary Table 3**) means that a larger portion of the patient anatomy is covered per gantry rotation of the CT system, leading to potential reduction in motion artifacts. Combining this feature with DLCT-based SPR prediction may enhance 4D CT planning in particle therapy for moving targets.

Finally, other beneficial characteristics of DECT should be investigated for all technical implementations available, including DLCT, to understand the full advantages of the technology. Beyond the computational aspects of DECT-based treatment planning discussed in this work, DECT imaging is expected to provide various opportunities to improve the accuracy of multiple parts of the radiotherapy chain. DECT has been suggested to improve image quality and reduce metal artifacts (51), to improve tumor staging, delineation, and characterization (52, 53), and to contribute to improved normal tissue characterization and personalized treatment through physiological quantification (46). Furthermore, DECT also shows potential for improved dose calculations for treatment modalities other than particle therapy, such as brachytherapy and conventional photon-based teletherapy (51). Finally, as briefly explored in this study and proposed by Albrecht et al. (54), DECT has the potential to reduce total

imaging dose. Future work might investigate these varied applications of DECT to radiotherapy.

DATA AVAILABILITY STATEMENT

The raw data supporting the conclusions of this article will be made available by the authors, without undue reservation.

AUTHOR CONTRIBUTIONS

Conceptualization, FL, AK, AM, and WS. Methodology, FL, AK, AM, and WS. Data acquisition and analysis, FL, AK, and BA. Interpretation, FL, AK, SM, TT, AM, and WS. Writing—original draft preparation, FL and AK. Writing—review and editing, FL, AK, SM, TT, BA, JD, AM, and WS. Supervision, JD, AM, and WS. All authors contributed to the article and approved the submitted version.

FUNDING

SUPPLEMENTARY MATERIAL

The Supplementary Material for this article can be found online at: https://www.frontiersin.org/articles/10.3389/fonc.2022.853495/full#supplementary-material

REFERENCES

1. Durante M, Orecchia R, Loeffler J. Charged-Particle Therapy in Cancer: Clinical Uses and Future Perspectives. *Nat Rev Clin Oncol* (2017) 14:483–95. doi: 10.1038/nrclinonc.2017.30

2. Bragg WH, Kleeman R. On the Ionization Curves of Radium. *London Edinburgh Dublin Philos Mag J Sci* (1904) 8(48):726–38. doi: 10.1080/14786440409463246

3. Paganetti H. Range Uncertainties in Proton Therapy and the Role of Monte Carlo Simulations. *Phys Med Biol* (2012) 57(11):R99–R117. doi: 10.1088/0031-9155/57/11/R99

4. Yang M, Zhu XR, Park PC, Titt U, Mohan R, Virshup G, et al. Comprehensive Analysis of Proton Range Uncertainties Related to Patient Stopping-Power-Ratio Estimation Using the Stoichiometric Calibration. *Phys Med Biol* (2012) 57(13):4095–115. doi: 10.1088/0031-9155/57/13/4095

5. Bär E, Lalonde A, Royle G, Lu H-M, Bouchard H. The Potential of Dual-Energy CT to Reduce Proton Beam Range Uncertainties. *Med Phys* (2017) 44(6):2332–44. doi: 10.1002/mp.12215

6. Wohlfahrt P, Möhler C, Stützer K, Greilich S, Richter C. Dual-Energy CT Based Proton Range Prediction in Head and Pelvic Tumor Patients. *Radiother Oncol* (2017) 125(3):526–33. doi: 10.1016/j.radonc.2017.09.042

7. Wohlfahrt P, Richter C. Status and Innovations in Pre-Treatment CT Imaging for Proton Therapy. *Br J Radiol* (2020) 93:20190590. doi: 10.1259/bjr.20190590

8. Wohlfahrt P, Möhler C, Troost EGC, Greilich S, Richter C. Dual-Energy Computed Tomography to Assess Intra- and Inter-Patient Tissue Variability for Proton Treatment Planning of Patients With Brain Tumor. *Int J Radiat Oncol Biol Phys* (2019) 105(3):504–13. doi: 10.1016/j.ijrobp.2019.06.2529

9. Flohr TG, McCollough CH, Bruder H, Petersilka M, Gruber K, Süß C, et al. First Performance Evaluation of a Dual-Source CT (DSCT) System. *Eur Radiol* (2006) 16(2):256–68. doi: 10.1007/s00330-005-2919-2

10. Yang M, Virshup G, Clayton J, Zhu XR, Mohan R, Dong L. Theoretical Variance Analysis of Single- and Dual-Energy Computed Tomography Methods for Calculating Proton Stopping Power Ratios of Biological Tissues. *Phys Med Biol* (2010) 55(5):1343–62. doi: 10.1088/0031-9155/55/5/006

11. Schneider U, Pedroni E, Lomax A. The Calibration of CT Hounsfield Units for Radiotherapy Treatment Planning. *Phys Med Biol* (1996) 41(1):111–24. doi: 10.1088/0031-9155/41/1/009

12. Hansen DC, Seco J, Sørensen TS, Petersen JBB, Wildberger JE, Verhaegen F, et al. A Simulation Study on Proton Computed Tomography (CT) Stopping Power Accuracy Using Dual Energy CT Scans as Benchmark. *Acta Oncol* (2015) 54(9):1638–42. doi: 10.3109/0284186X.2015.1061212

13. Hudobivnik N, Schwarz F, Johnson T, Agolli L, Dedes G, Tessonnier T, et al. Comparison of Proton Therapy Treatment Planning for Head Tumors With a Pencil Beam Algorithm on Dual and Single Energy CT Images. *Med Phys* (2016) 43(1):495–504. doi: 10.1118/1.4939106

14. Hünemohr N, Krauss B, Tremmel C, Ackermann B, Jäkel O, Greilich S. Experimental Verification of Ion Stopping Power Prediction From Dual Energy CT Data in Tissue Surrogates. *Phys Med Biol* (2014) 59(1):83–96. doi: 10.1088/0031-9155/59/1/83

15. Zhu J, Penfold SN. Dosimetric Comparison of Stopping Power Calibration With Dual-Energy CT and Single-Energy CT in Proton Therapy Treatment Planning. *Med Phys* (2016) 43(6):2845–54. doi: 10.1118/1.4948683

16. Bär E, Lalonde A, Zhang R, Jee K-W, Yang K, Sharp G, et al. Experimental Validation of Two Dual-Energy CT Methods for Proton Therapy Using Heterogeneous Tissue Samples. *Med Phys* (2018) 45(1):48–59. doi: 10.1002/mp.12666

17. Möhler C, Russ T, Wohlfahrt P, Elter A, Runz A, Richter C, et al. Experimental Verification of Stopping-Power Prediction From Single- and Dual-Energy Computed Tomography in Biological Tissues. *Phys Med Biol* (2018) 63(2):025001. doi: 10.1088/1361-6560/aaa1c9

18. Taasti VT, Michalak GJ, Hansen DC, Deisher AJ, Kruse JJ, Krauss B, et al. Validation of Proton Stopping Power Ratio Estimation Based on Dual Energy CT Using Fresh Tissue Samples. *Phys Med Biol* (2018) 63(1):015012. doi: 10.1088/1361-6560/aa952f

19. Wohlfahrt P, Möhler C, Richter C, Greilich S. Evaluation of Stopping-Power Prediction by Dual- and Single-Energy Computed Tomography in an Anthropomorphic Ground-Truth Phantom. *Int J Radiat Oncol Biol Phys* (2018) 100(1):244–53. doi: 10.1016/j.ijrobp.2017.09.025

20. Xie Y, Ainsley C, Yin L, Zou W, McDonough J, Solberg TD, et al. *Ex Vivo* Validation of a Stoichiometric Dual Energy CT Proton Stopping Power Ratio Calibration. *Phys Med Biol* (2018) 63(5):055016. doi: 10.1088/1361-6560/aaae91

21. Ates O, Hua C, Zhao L, Shapira N, Yagil Y, Merchant TE, et al. Feasibility of Using Post-Contrast Dual-Energy CT for Pediatric Radiation Treatment Planning and Dose Calculation. *Br J Radiol* (2020) 94(1118):20200170. doi: 10.1259/bjr.20200170

22. Faller FK, Mein S, Ackermann B, Debus J, Stiller W, Mairani A. Pre-Clinical Evaluation of Dual-Layer Spectral Computed Tomography-Based Stopping Power Prediction for Particle Therapy Planning at the Heidelberg Ion Beam Therapy Center. *Phys Med Biol* (2020) 65(9):095007. doi: 10.1088/1361-6560/ab735e

23. Große Hokamp N, Maintz D, Shapira N, Chang DH, Noël PB. Technical Background of a Novel Detector-Based Approach to Dual-Energy Computed Tomography. *Diagn Interv Radiol* (2020) 26(1):68–71. doi: 10.5152/dir.2019.19136

24. Hua C, Shapira N, Merchant TE, Klahr P, Yagil Y. Accuracy of Electron Density, Effective Atomic Number, and Iodine Concentration Determination With a Dual-Layer Dual-Energy Computed Tomography System. *Med Phys* (2018) 45(6):2486–97. doi: 10.1002/mp.12903

25. Landry G, Dörringer F, Si-Mohamed S, Douek P, Abascal JFPJ, Peyrin F, et al. Technical Note: Relative Proton Stopping Power Estimation From Virtual Monoenergetic Images Reconstructed From Dual-Layer Computed Tomography. *Med Phys* (2019) 46(4):1821–8. doi: 10.1002/mp.13404

26. Longarino FK, Tessonnier T, Mein S, Harrabi SB, Debus J, Stiller W, et al. Dual-Layer Spectral CT for Proton, Helium, and Carbon Ion Beam Therapy Planning of Brain Tumors. *J Appl Clin Med Phys* (2022) 23(1):e13465. doi: 10.1002/acm2.13465

27. Ohira S, Washio H, Yagi M, Karino T, Nakamura K, Ueda Y, et al. Estimation of Electron Density, Effective Atomic Number and Stopping Power Ratio Using Dual-Layer Computed Tomography for Radiotherapy Treatment Planning. *Physica Med* (2018) 56:34–40. doi: 10.1016/j.ejmp.2018.11.008

28. Bär E, Andreo P, Lalonde A, Royle G, Bouchard H. Optimized *I*-Values for Use With the Bragg Additivity Rule and Their Impact on Proton Stopping Power and Range Uncertainty. *Phys Med Biol* (2018) 63(16):165007. doi: 10.1088/1361-6560/aad312

29. International Commission on Radiation Units and Measurements (ICRU). Report 90: Key Data for Ionizing-Radiation Dosimetry: Measurement Standards and Applications. *J Int Comm Radiat Units Meas* (2014) 14(1):1–110. doi: 10.1093/jicru/ndw038

30. Inaniwa T, Kanematsu N. Effective Particle Energies for Stopping Power Calculation in Radiotherapy Treatment Planning With Protons and Helium, Carbon, and Oxygen Ions. *Phys Med Biol* (2016) 61(20):N542–50. doi: 10.1088/0031-9155/61/20/N542

31. International Commission on Radiation Units and Measurements (ICRU). Report 93: Prescribing, Recording, and Reporting Light Ion Beam Therapy. *J Int Comm Radiat Units Meas* (2016) 16(2):1–211. doi: 10.1093/jicru/ndy024

32. Schneider W, Bortfeld T, Schlegel W. Correlation Between CT Numbers and Tissue Parameters Needed for Monte Carlo Simulations of Clinical Dose Distributions. *Phys Med Biol* (2000) 45(2):459–78. doi: 10.1088/0031-9155/45/2/314

33. Telsemeyer J, Ackermann B, Ecker S, Jäkel O, Martišíková M. Experimental Verification of Ion Range Calculation in a Treatment Planning System Using a Flat-Panel Detector. *Phys Med Biol* (2014) 59(14):3737–47. doi: 10.1088/0031-9155/59/14/3737

34. Saito M. Quadratic Relation for Mass Density Calibration in Human Body Using Dual-Energy CT Data. *Med Phys* (2021) 48(6):3065–73. doi: 10.1002/mp.14899

35. Saito M, Sagara S. Simplified Derivation of Stopping Power Ratio in the Human Body From Dual-Energy CT Data. *Med Phys* (2017) 44(8):4179–87. doi: 10.1002/mp.12386

36. Mein S, Kopp B, Tessonnier T, Ackermann B, Ecker S, Bauer J, et al. Dosimetric Validation of Monte Carlo and Analytical Dose Engines With Raster-Scanning ^{1}H, ^{4}He, ^{12}C, and ^{16}O Ion-Beams Using an Anthropomorphic Phantom. *Physica Med* (2019) 64:123–31. doi: 10.1016/j.ejmp.2019.07.001

37. Low DA, Harms WB, Mutic S, Purdy JA. A Technique for the Quantitative Evaluation of Dose Distributions. *Med Phys* (1998) 25(5):656–61. doi: 10.1118/1.598248

38. Park SH, Kang JO. Basics of Particle Therapy I: Physics. *Radiat Oncol J* (2011) 29(3):135–46. doi: 10.3857/roj.2011.29.3.135

39. Gomà C, Almeida IP, Verhaegen F. Revisiting the Single-Energy CT Calibration for Proton Therapy Treatment Planning: A Critical Look at the Stoichiometric Method. *Phys Med Biol* (2018) 63(23):235011. doi: 10.1088/1361-6560/aaede5

40. Möhler C, Wohlfahrt P, Richter C, Greilich S. Range Prediction for Tissue Mixtures Based on Dual-Energy CT. *Phys Med Biol* (2016) 61(11):N268–75. doi: 10.1088/0031-9155/61/11/N268

41. Bär E, Collins-Fekete C-A, Rompokos V, Zhang Y, Gaze MN, Warry A, et al. Assessment of the Impact of CT Calibration Procedures for Proton Therapy Planning on Pediatric Treatments. *Med Phys* (2021) 48(9):5202–18. doi: 10.1002/mp.15062

42. Peters N, Wohlfahrt P, Dahlgren CV, de Marzi L, Ellerbrock M, Fracchiolla F, et al. Experimental Assessment of Inter-Centre Variation in Stopping-Power and Range Prediction in Particle Therapy. *Radiother Oncol* (2021) 163:7–13. doi: 10.1016/j.radonc.2021.07.019

43. Tattenberg S, Madden TM, Gorissen BL, Bortfeld T, Parodi K, Verburg J. Proton Range Uncertainty Reduction Benefits for Skull Base Tumors in Terms of Normal Tissue Complication Probability (NTCP) and Healthy Tissue Doses. *Med Phys* (2021) 48(9):5356–66. doi: 10.1002/mp.15097

44. McCollough CH, Leng S, Yu L, Fletcher JG. Dual- and Multi-Energy CT: Principles, Technical Approaches, and Clinical Applications. *Radiology* (2015) 276(3):637–53. doi: 10.1148/radiol.2015142631

45. McCollough CH, Boedeker K, Cody D, Duan X, Flohr T, Halliburton SS, et al. Principles and Applications of Multienergy CT: Report of AAPM Task Group 291. *Med Phys* (2020) 47(7):e881–912. doi: 10.1002/mp.14157

46. Kruis MF. Improving Radiation Physics, Tumor Visualisation, and Treatment Quantification in Radiotherapy With Spectral or Dual-Energy CT. *J Appl Clin Med Phys* (2022) 23(1):e13468. doi: 10.1002/acm2.13468

47. Maaß C, Baer M, Kachelrieß M. Image-Based Dual Energy CT Using Optimized Precorrection Functions: A Practical New Approach of Material Decomposition in Image Domain. *Med Phys* (2009) 36(8):3818–29. doi: 10.1118/1.3157235

48. Sellerer T, Noël PB, Patino M, Parakh A, Ehn S, Zeiter S, et al. Dual-Energy CT: A Phantom Comparison of Different Platforms for Abdominal Imaging. *Eur Radiol* (2018) 28(7):2745–55. doi: 10.1007/s00330-017-5238-5

49. Dedes G, Dickmann J, Niepel K, Wesp P, Johnson RP, Pankuch M, et al. Experimental Comparison of Proton CT and Dual Energy X-Ray CT for Relative Stopping Power Estimation in Proton Therapy. *Phys Med Biol* (2019) 64(16):165002. doi: 10.1088/1361-6560/ab2b72

50. Bär E, Volz L, Collins-Fekete C-A, Brons S, Runz A, Schulte RW, et al. Experimental Comparison of Photon Versus Particle Computed Tomography to Predict Tissue Relative Stopping Powers. *Med Phys* (2022) 49(1):474–87. doi: 10.1002/mp.15283

51. van Elmpt W, Landry G, Das M, Verhaegen F. Dual Energy CT in Radiotherapy: Current Applications and Future Outlook. *Radiother Oncol* (2016) 119(1):137–44. doi: 10.1016/j.radonc.2016.02.026

52. Toepker M, Czerny C, Ringl H, Fruehwald-Pallamar J, Wolf F, Weber M, et al. Can Dual-Energy CT Improve the Assessment of Tumor Margins in Oral Cancer? *Oral Oncol* (2014) 50(3):221–7. doi: 10.1016/j.oraloncology.2013.12.001

53. Wichmann JL, Nöske EM, Kraft J, Burck I, Wagenblast J, Eckardt A, et al. Virtual Monoenergetic Dual-Energy Computed Tomography: Optimization of Kiloelectron Volt Settings in Head and Neck Cancer. *Invest Radiol* (2014) 49(11):735–41. doi: 10.1097/RLI.0000000000000077

54. Albrecht MH, Scholtz JE, Kraft J, Bauer RW, Kaup M, Dewes P, et al. Assessment of an Advanced Monoenergetic Reconstruction Technique in Dual-Energy Computed Tomography of Head and Neck Cancer. *Eur Radiol* (2015) 25(8):2493–501. doi: 10.1007/s00330-015-3627-1

3.3 Publication II

Dual-layer spectral CT for proton, helium, and carbon ion beam therapy planning of brain tumors

Authors: Friderike K. Longarino, Thomas Tessonnier, Stewart Mein, Semi B. Harrabi, Jürgen Debus, Wolfram Stiller W, Andrea Mairani

Contribution: FL is the first author of this publication. FL, WS, and AM conceptualized the study. FL, TT, SH, WS, and AM developed the methodology. Data was acquired and analyzed by FL, TT, and AM and interpreted by FL, TT, SM, WS, and AM. FL wrote the original draft of the manuscript and prepared all graphics. FL, TT, SM, SH, JD, WS, and AM contributed to the review and editing of the final manuscript. JD, WS, and AM provided supervision.

RADIATION ONCOLOGY PHYSICS

Dual-layer spectral CT for proton, helium, and carbon ion beam therapy planning of brain tumors

Friderike K. Longarino[1,2,3] | Thomas Tessonnier[4] | Stewart Mein[2,4,5,6,7] | Semi B. Harrabi[2,4,6,7] | Jürgen Debus[1,2,4,6,7,8] | Wolfram Stiller[9] | Andrea Mairani[2,4,7,10]

[1] German Cancer Research Center (DKFZ), Clinical Cooperation Unit Radiation Oncology, Heidelberg, Germany

[2] Department of Radiation Oncology, Heidelberg University Hospital, Heidelberg, Germany

[3] Department of Physics and Astronomy, Heidelberg University, Heidelberg, Germany

[4] Heidelberg Ion Beam Therapy Center (HIT), Heidelberg, Germany

[5] German Cancer Research Center (DKFZ), Translational Radiation Oncology, Heidelberg, Germany

[6] National Center for Radiation Research in Oncology (NCRO), Heidelberg Institute of Radiation Oncology (HIRO), Heidelberg, Germany

[7] National Center for Tumor Diseases (NCT), Heidelberg, Germany

[8] Partner Site Heidelberg, German Cancer Consortium (DKTK), Heidelberg, Germany

[9] Diagnostic and Interventional Radiology (DIR), Heidelberg University Hospital, Heidelberg, Germany

[10] Medical Physics, National Centre of Oncological Hadrontherapy (CNAO), Pavia, Italy

Correspondence
Andrea Mairani and Wolfram Stiller, Department of Radiation Oncology, Heidelberg University Hospital, Im Neuenheimer Feld 400, 69120 Heidelberg, Germany.
Email:
andrea.mairani@med.uni-heidelberg.de;
wolfram.stiller@med.uni-heidelberg.de

Wolfram Stiller and Andrea Mairani contributed equally to this work.

Abstract

Pretreatment computed tomography (CT) imaging is an essential component of the particle therapy treatment planning chain. Treatment planning and optimization with charged particles require accurate and precise estimations of ion beam range in tissues, characterized by the stopping power ratio (SPR). Reduction of range uncertainties arising from conventional CT-number-to-SPR conversion based on single-energy CT (SECT) imaging is of importance for improving clinical practice. Here, the application of a novel imaging and computational methodology using dual-layer spectral CT (DLCT) was performed toward refining patient-specific SPR estimates.

A workflow for DLCT-based treatment planning was devised to evaluate SPR prediction for proton, helium, and carbon ion beam therapy planning in the brain. DLCT- and SECT-based SPR predictions were compared in homogeneous and heterogeneous anatomical regions. This study included eight patients scanned for diagnostic purposes with a DLCT scanner. For each patient, four different treatment plans were created, simulating tumors in different parts of the brain. For homogeneous anatomical regions, mean SPR differences of about 1% between the DLCT- and SECT-based approaches were found. In plans of heterogeneous anatomies, relative (absolute) proton range shifts of 0.6% (0.4 mm) in the mean and up to 4.4% (2.1 mm) at the distal fall-off were observed. In the investigated cohort, 12% of the evaluated organs-at-risk (OARs) presented differences in mean or maximum dose of more than 0.5 Gy (RBE) and up to

6.8 Gy (RBE) over the entire treatment. Range shifts and dose differences in OARs between DLCT and SECT in helium and carbon ion treatment plans were similar to protons.

In the majority of investigated cases (75th percentile), SECT- and DLCT-based range estimations were within 0.6 mm. Nonetheless, the magnitude of patient-specific range deviations between SECT and DLCT was clinically relevant in heterogeneous anatomical sites, suggesting further study in larger, more diverse cohorts. Results indicate that patients with brain tumors may benefit from DLCT-based treatment planning.

1 | INTRODUCTION

Radiotherapy using proton and light ion beams enables accurate and precise delivery of highly conformal dose distributions to the target volume while sparing normal tissues compared with conventional photon-based radiotherapy.[1,2] To properly exploit these physical characteristics, clinical application imposes high accuracy requirements in treatment planning and delivery.[3]

Successful treatment planning and optimization require precise estimations of the energy deposited along the penetration path and the finite beam range of charged particles, characterized by the stopping power ratio relative to water (SPR), to model radiation transport and interactions within a patient.[3] Pretreatment computed tomography (CT) imaging, providing anatomical and quantitative information for treatment planning, is an essential component of the radiotherapy treatment chain, and a topic of growing importance in ion beam therapy with relation to uncertainties in range prediction.[4,5] Compared with conventional photon-based therapy, the conversion of CT numbers to the relevant physical quantities for dose calculation within a treatment planning system (TPS) (i.e., relative electron density (ED) or SPR) is more critical in particle therapy due to the high precision required to predict the Bragg peak position.[5,6] Today, standard clinical protocols involve image data acquisition with single-energy CT (SECT) systems.[7] However, clinical treatment planning with SECT-based systems may be vulnerable to range prediction uncertainties due to generalized CT-number-to-SPR conversion, lacking patient-specificity,[6,8,9] with uncertainties reaching up to 3.5% between planned and delivered beam range.[6,9,10]

Uncertainties in particle range prediction are considered via incorporation of safety margins during treatment planning, e.g., via the robust optimization concept. For clinical CT-number-to-SPR calibration curves, also denoted Hounsfield look-up tables (HLUTs), there is no one-to-one correlation (i.e., bijection) between CT numbers and SPRs.[8] More specifically, two different materials with different compositions and physical properties (i.e., SPR) can exhibit identical CT numbers in SECT-based images and vice versa.[9] This nonbijectivity may be a source of systematic error between treatment planning and delivery[5] leading to enlarged margins and compromising the advantages of particle therapy over photon radiotherapy.

To mitigate the highlighted uncertainties arising during particle therapy treatment planning, dual-energy CT (DECT) systems, for acquisitions of two CT scans with different X-ray spectra, are becoming increasingly available and potentially offer an improved SPR prediction in the clinic[7,11–14] by making use of material-specific and/or material density images.[7,15] Since the clinical introduction of a first-generation dual-source CT system for diagnostic imaging,[16] a multitude of research studies identified various promising applications of DECT within the entire radiotherapy chain from tumor staging to delineation, tumor and normal tissue characterization, and dose calculations.[7]

Among the DECT acquisition methods available today, dual-layer spectral CT (DLCT), an approach combining a single X-ray source with a dual-layer detector, has been recently introduced into clinical practice.[17] Using two scintillator layers with different spectral sensitivities, DLCT enables simultaneous detection of two different energy levels for spectral imaging purposes, without the need to preselect specific CT protocols (e.g., different tube voltages).[18] In turn, more comprehensive image data acquisition and quantification regarding material compositions in the human body is feasible compared with SECT-based methods. Application of DLCT imaging and mathematical formalisms can yield direct patient-specific determination of SPR maps, which, in turn, may lead to improved agreement between planned and delivered ion beam treatments as opposed to indirect SECT-based SPR prediction. Moreover, unlike other published DECT-based methods, SPR prediction using DLCT imaging enables projection-based reconstruction[5] and directly makes use of the physical quantities ED and effective atomic number (EAN) provided by the DLCT scanner as spectral output data (without any need for further calibrations or

parametrizations) as input data for SPR prediction via the Bethe equation.

Substantial efforts have outlined and established treatment planning with other DECT acquisition methods[19]; however, to date, no study has presented investigations on the clinical feasibility of DLCT-based treatment planning from the perspective of patient delivery. Notably, the impact and comparison of using DLCT for treatment planning with different ions, such as helium (^{4}He) and carbon (^{12}C) ions, in addition to protons (^{1}H) have not yet been investigated in the literature. Prior to the clinical translation, an established clinical workflow and reliable benchmarks by means of quantitative DLCT imaging are needed for proper assessment. Previous works available in the literature present preclinical studies, illustrating the methodological development of SPR prediction with DLCT and experimental verification of the developed approach using tissue surrogates and anthropomorphic phantoms.[18,20–23] The data suggest a mean DLCT-based SPR prediction accuracy of 0.6% compared with measured SPR and 1 mm proton range prediction improvement in an anthropomorphic head phantom compared with SECT.[20] Nevertheless, thorough investigations on how these improvements affect the dose distribution in patients, as well as identification of which patient subgroups would benefit the most from DLCT, have yet to be performed.

This study aims to investigate DLCT imaging for proton, helium, and carbon ion beam range prediction in brain tumors. A clinical workflow for DLCT-based treatment planning is devised at the Heidelberg Ion Beam Therapy Center (HIT, Germany). Quantitative differences between SECT- and DLCT-based SPR prediction (interpatient and intrapatient) are assessed in various clinical scenarios. Furthermore, SPR prediction performance is evaluated to identify clinical cases that benefit from DLCT-based treatment planning in proton, helium, and carbon ion beam therapy.

2 | METHODS

2.1 | Patient cohort

The feasibility and accuracy of DLCT-based particle therapy planning were investigated in a group of eight randomly selected diagnostic radiological patients (age, 28–85 years) by analyzing previously acquired (i.e., for diagnostic purposes) DLCT image data of the head. Head cases were chosen for the investigation for two reasons: (i) They contain both a variety of homogeneous and heterogeneous anatomical treatment sites important for testing different clinical conditions, and the majority of patients at the HIT facility are treated for brain cancers and head and neck cancers. (ii) Image data acquired with a CT image acquisition and reconstruction protocol similar to that used for ion beam therapy planning at HIT were available only for head cases. More specifically, all other data sets were acquired with either contrast agent or exposure modulation, which prevents their use in this treatment planning study.

DLCT is not yet implemented in the clinical routine for ion beam therapy treatment planning at our institution. Therefore, to explore the DLCT modality, image data for patients who have undergone diagnostic procedures using the DLCT scanner were analyzed. Subsequently, DLCT image data were retrospectively derived on the IQon Spectral CT IntelliSpace Portal workstation. All imaging with the DLCT scanner was performed for clinical indications; hence, no scan was conducted explicitly for the purpose of this study. Anonymized patient records were obtained with informed consent following the Declaration of Helsinki. Clearance from the ethical review committee was not required for the retrospective nature of the study.

2.2 | Dual-layer spectral CT imaging technique

The DLCT imaging technique (IQon Spectral CT, Philips Healthcare, Best, The Netherlands) is based on two detector layers with different spectral sensitivities that detect high- and low-energy data simultaneously in time and space.[17] Low-energy photons from the X-ray spectrum are selectively absorbed by the top layer yttrium-based garnet scintillator, whereas high-energy photons pass through the top layer and are absorbed by the bottom layer gadolinium oxysulfide scintillator.[17] As a result, direct generation of quantitative spectral information (i.e., ED and EAN) is made possible on the full standard field-of-view of 500 mm for all performed scans, without the need of additional acquisitions or specific CT imaging protocols.[21] Such methods using spectral data allow determining volumetric SPR maps that are patient-specific and do not depend on generic CT-number-to-SPR conversions.[20]

2.3 | Image acquisition settings and reconstruction parameters

Image acquisitions were performed using the clinical protocol for adult head CT scans for diagnostics at our facility. The following acquisition settings were used: tube voltage of 120 kV$_p$, tube current-time product of 281 mAs (tube current modulation was deactivated), collimation of 64×0.625 mm, rotation time of 0.75 s, pitch of 0.39, CTDI$_{vol}$ of 48.1 mGy, slice thickness of 2 mm, and slice spacing of 1.5 mm. The reconstruction filter UB, a spectral level, and the hybrid-iterative reconstruction algorithm at iDose^4 level (scale: 0–6) of 3 were used. For each patient scan, on the IQon Spectral CT scanner, both a SECT and DLCT data set were derived.
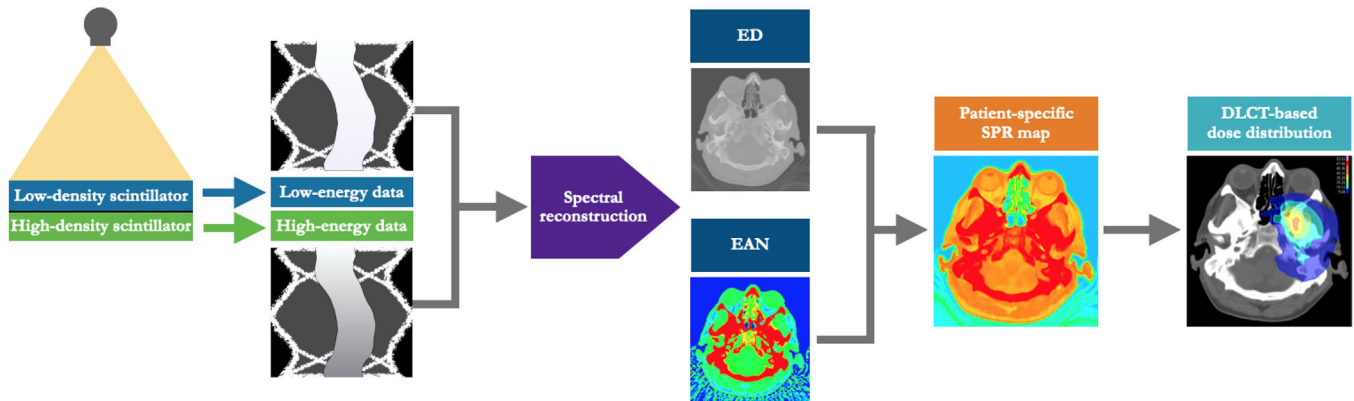
FIGURE 1 Principle of dual-layer spectral CT (DLCT)-based stopping power ratio relative to water (SPR) prediction for particle therapy treatment planning. Simultaneous acquisition of low- and high-energy data, with a detector made of two layers that simultaneously detect two energy levels, allows for projection-space spectral decomposition. After decomposition, the data are reconstructed and processed to obtain spectral images, i.e., relative electron density (ED) and effective atomic number (EAN), in order to predict SPR and to perform particle therapy treatment planning

2.4 | Methodology for performing DLCT data-based SPR prediction and treatment planning

To survey the feasibility of performing DLCT-based treatment planning, this study established a workflow for DLCT-based particle therapy treatment planning for potential clinical translation. For this purpose, DLCT-based treatment planning was designed and validated by first deriving 3D maps of SPR, followed by devising a methodology to perform DLCT-based dose calculation for particle therapy. The entire principle of DLCT data-based SPR prediction for treatment planning is shown in Figure 1.

For DLCT-based SPR prediction, the SPR was approximated with the Bethe formula, neglecting higher order correction terms.[10] Because SPR exhibits a minimal energy dependence in the therapeutic range,[24] a fixed kinetic energy of 100 MeV for all particle beams was assumed for SPR prediction. The approximation of a fixed value was based on previous work recommending an "effective energy" in SPR estimation of 100 MeV, whereby the uncertainties in energy dependence could be best compensated for clinical applications.[25] A mean excitation energy (*I*-value) for water of 78.73 eV was assigned,[26] consistent with previously reported results ((78 ± 2) eV).[27] The *I*-value of the tissue was approximated using a widely referenced parametric method converting EAN in *I*-value maps.[28] The exponent to derive EAN from the material-specific elemental composition weighted by the fraction of electrons associated with each element was 2.94, Philips' choice which is in correspondence to the Mayneord formula[29] and other publications.[21] For each DLCT image acquisition, processing of the raw spectral base image output yields 3D maps of ED and EAN, which in turn are used for SPR computation.[20] 3D maps of SPR were generated via an

in-house software that takes ED and EAN images and produces a corresponding SPR map that can be read by our clinically employed TPS. Up to now, the commercial TPS at our facility does not allow treatment planning based on SPR maps. However, this study established a workaround for implementing treatment planning based on DLCT-based SPR images with protons, helium, and carbon ions. For this purpose, we implemented an one-to-one conversion curve in the current CT number-to-SPR conversion definition required by the TPS and, subsequently, directly imported SPR images based on DLCT in the TPS.

For SECT-based SPR prediction, the clinical approach of our facility[30] based on a two-parameter stoichiometric method[10,31] was used to generate a CT protocol-specific HLUT (depicted in Supplementary Material (SM) S1), which was calibrated based on CT image data of body tissue surrogates (Gammex Electron Density CT Phantom 467, Gammex-RMI, Middleton, WI, USA) from the adult head scan protocol (cf. section 2.3).

2.5 | Assessment of DLCT data-based SPR prediction in head patients

In the first investigation, SPR predictions in homogeneous tissue regions were compared between SECT and DLCT image data sets. For each patient, circular regions-of-interest (ROIs) of equal size were placed in five reasonably homogeneous tissue regions, similar to Taasti et al.[13] (depicted in SM S2). The ROIs were placed at exactly the same position in the SECT and DLCT data sets. The brain was segmented by placing circular ROIs (covering an area of $\sim$100 mm^2, $\sim$640 voxels) in ten image slices in the homogeneous brain region above the level of the lateral ventricles. For the cranial bone

in the calvaria, ROIs (of ~50 mm^2, ~320 voxels) in ten slices in the upper part of the head were included in the analysis, from the top of the eyes upward. A circular ROI was placed in each eye (of ~100 mm^2, ~640 voxels) and in each lateral ventricle (of ~50 mm^2, ~320 voxels) in five consecutive slices, respectively. For the skull base bone, ROIs (of ~25 mm^2, ~160 voxels) in ten slices in the inferior part of the skull were included. Altogether, ~20 800 voxels were analyzed per patient in the SECT and DLCT data sets. Subsequently, the ROIs were evaluated quantitatively in terms of mean SPR using an image analysis software (syngo.via, version VB40A, Siemens Healthcare GmbH, Erlangen, Germany). Statistical analysis of SPR comparison between DLCT- and SECT-based methods is described in detail in SM S3.

## 2.6 | Assessment of DLCT data-based treatment planning in head patients

Following investigations of SECT- versus DLCT-based SPR predictions in homogeneous tissue regions (cf. section 2.5), a comparative patient planning study was performed to assess the performance of DLCT and identify which tumor sites would benefit the most from DLCT-based treatment planning. The treatment planning study was, wherever possible, conducted according to the recommendations of the Radiotherapy Treatment plannINg study Guidelines (RATING).[32] Proton treatment planning in six head patients from the patient cohort was evaluated. Two patients were excluded, because one patient wore earrings during image acquisition (evoking streak artifacts) and one patient had a hemicraniectomy that would have complicated treatment planning. For each patient, four different realistic treatment plans were created based on patient cases treated with proton therapy at HIT. Therefore, the number of simulated treatment plans was 24. Helium and carbon ion therapy planning was investigated in one patient (patient #1) to compare the impact of DLCT-based SPR predictions among different ions. Tumor characteristics (i.e., size, depth, location, etc.) were chosen to cover various clinical cases (astrocytoma, meningioma, oligodendroglioma, and pineal region tumor) with the details given in SM S4. For each investigated indication, a physician selected a clinically representative plan from our institution treated with proton beams to be referenced as a "template" for designing the simulated patients using the diagnostic DLCT-based images. Plan A was selected to evaluate a hypothetical planning target volume (PTV), with most of its volume situated in the brain, that would be treated with three beams. Plan B was created to cover a smaller hypothetical skull-based tumor with two nearly opposing beams. Compared with plan A, plan C covered a quite similar treatment volume, but would only be treated with two beams separated by 60°. Plan D was chosen for a centrally located tumor in the

brain with two nearly opposing fields. The PTV for each treatment plan was defined, and organs-at-risk (OARs) were contoured in the CT images using atlas-based segmentation.[33]

Treatment planning and optimization using multifield optimization with a dose grid of 0.2 cm were performed with RayStation TPS v10 (RaySearch Laboratories AB, Stockholm, Sweden) with the proton Monte-Carlo dose engine or with the pencil beam dose engine for helium and carbon ions. A fixed relative biological effectiveness (RBE) of 1.1 for protons was assumed. For helium ion therapy, the modified microdosimetric kinetic model (mMKM) was used.[34] In carbon ion therapy, the radiobiological local effect model (LEM) was employed.[35] Although the robust optimization concept is under investigation at HIT, it is not yet the clinical standard. Thus, we decided to use the PTV margin concept for optimization, consistent with our current clinical practice. Treatment planning was performed on the PTV with one extra energy layer in the distal margin, laterally with half a spot spacing. Intracranial OARs were delineated based on guidelines by Scoccianti et al.[36]: right and left eyes, optic chiasma, right and left cochlea, right and left hippocampus, brain, brainstem, pituitary gland, right and left inner ears, right and left mandibular condyles, right and left lens, right and left optic nerves, right and left lacrimal glands. The atlas-based segmentation was used for all OARs, but for several patients manual editing of some structures was still needed. For optimization, dose-volume parameters were defined as objectives. In a first step, objectives for the PTV and external contour were chosen: minimum dose to PTV of 95% of the prescribed dose, maximum dose to PTV of 103% of the prescribed dose, uniform dose to PTV of 100% of the prescribed dose, minimum dose of 98% of the prescribed dose to 98% of the volume, and dose fall-off at the external contour. In a second step, objectives for OARs were added according to the "template" treatment plans, whereby for each treatment plan different OARs were considered using the following optimization functions: dose-volume histogram (DVH) functions for OARs and Max EUD (equivalent uniform dose) functions, $a = 1$, corresponding to a mean dose constraint. PTV coverage was similar for proton, helium, and carbon ion treatment plans for comparisons between the different ions.

For each patient, treatment planning was performed on the SECT-based approach, as depicted in Figure 2. Plan acceptability was decided based on the clinical patient cases that were used as "template" treatment plans. Subsequently, the dose distributions were recalculated on DLCT-based SPR images using the same beam parameters without reoptimization.

Patient plans calculated with SECT and DLCT were then compared in terms of their range prediction and additional dose calculation features including PTV coverage and evaluation of dose differences to OARs. Differences in range prediction were analyzed with
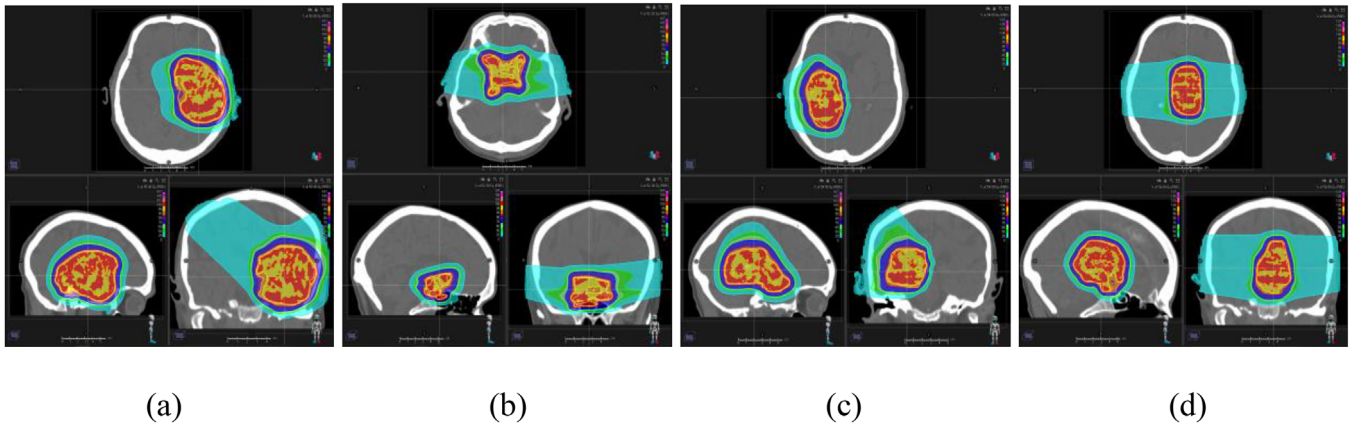
FIGURE 2 Proton treatment plan design for a study patient (patient #1) with RayStation treatment planning system (TPS) showing (a) plan A (astrocytoma), (b) plan B (meningioma), (c) plan C (oligodendroglioma), and (d) plan D (pineal region tumor)

line-dose profiles in beam direction (using RayStation TPS) and quantified by absolute range shifts at the distal range at 90% (R_{90}) and 80% (R_{80}) of prescribed dose ($\Delta R_{90} = | R_{90,SECT} - R_{90,DLCT} |$ and $\Delta R_{80} = | R_{80,SECT} - R_{80,DLCT} |$). For all patients and plans, five equidistant line-dose profiles (ten equidistant line-dose profiles for proton, helium, and carbon ion treatment plans in patient #1) per beam were evaluated inside each PTV (cf. Figure 5a). Relative range differences were calculated by dividing ΔR_{90} (ΔR_{80}) by $R_{90,DLCT}$ ($R_{80,DLCT}$):

$$\frac{\Delta R_{90}}{R_{90,DLCT}} = \frac{|R_{90,SECT} - R_{90,DLCT}|}{R_{90,DLCT}} \quad (1)$$

$$\frac{\Delta R_{80}}{R_{80,DLCT}} = \frac{|R_{80,SECT} - R_{80,DLCT}|}{R_{80,DLCT}} \quad (2)$$

To determine whether DLCT imaging had a significant effect on range prediction, a t test for two paired samples with a significance level of 5% was applied. In addition, the intrapatient (within a patient) and interpatient (between patients) variabilities of range shifts were calculated, which were defined in previous work as mean of the standard deviation and as standard deviation of the mean of patient-specific range shifts, respectively.[14] Dose distributions were compared using a 3D gamma analysis[37] for local calculation with a passing criterion of 1%/1 mm using a low dose cutoff of 5% of the maximum dose. Additionally, DVHs were compared in terms of absolute dose differences in the mean or maximum dose over the entire treatment (total dose) for each OAR, respectively. The target coverage was assessed by the PTV $D_{99\%}$ dose. The PTV is more sensitive to range shifts compared with the CTV, because changes in range directly impact the PTV coverage, but not necessarily the CTV.

3 | RESULTS

3.1 | Evaluation of DLCT data-based SPR prediction in head patients

Feasibility and accuracy of the DLCT-based SPR prediction were first investigated in homogeneous anatomical regions in a patient cohort. In Figure 3, the SPR prediction and relative differences between SPR maps derived using DLCT and SECT are plotted for patient #1. The largest SPR differences between DLCT and SECT were found in air-filled cavities and bone tissue, whereby the SPR differences were negative for air-filled cavities and positive for bones.

Quantitative analysis in specific tissue regions was performed per ROI for DLCT- and SECT-based SPR measurement. Figure 4 shows the median SPR value distributions for DLCT and SECT over all patients for the five ROIs. For all patients, mean SPR differences over five defined ROIs were positive, showing higher SPR estimates based on DLCT than on SECT (Table 1). The mean SPR difference was $(1.10 \pm 0.07)\%$ in brain, $(1.13 \pm 0.17)\%$ in cranial bone in the calvaria, $(0.69 \pm 0.06)\%$ in eyes, $(0.48 \pm 0.05)\%$ in lateral ventricles, and $(1.22 \pm 0.14)\%$ in skull base bone. The percentage difference ranged from 0.32% to 1.87% over all ROIs and was 0.87% in the median (cf. Table 1). The standard error of the mean in bony structures was higher than in brain, eyes, and lateral ventricles.

The performed t test rejected the null hypothesis at the 5% significance level, i.e., difference of mean SPR values for SECT and DLCT was nonzero. The SPR prediction based on DLCT was significantly different ($p < 0.05$) from the SPR prediction based on SECT. The mean relative difference in SPR prediction (δ_{SPR}) over the ROIs was 0.92%, with a standard error of the mean of 0.45%. The 95% confidence interval for SPR shifts was [0.88, 0.97]%.
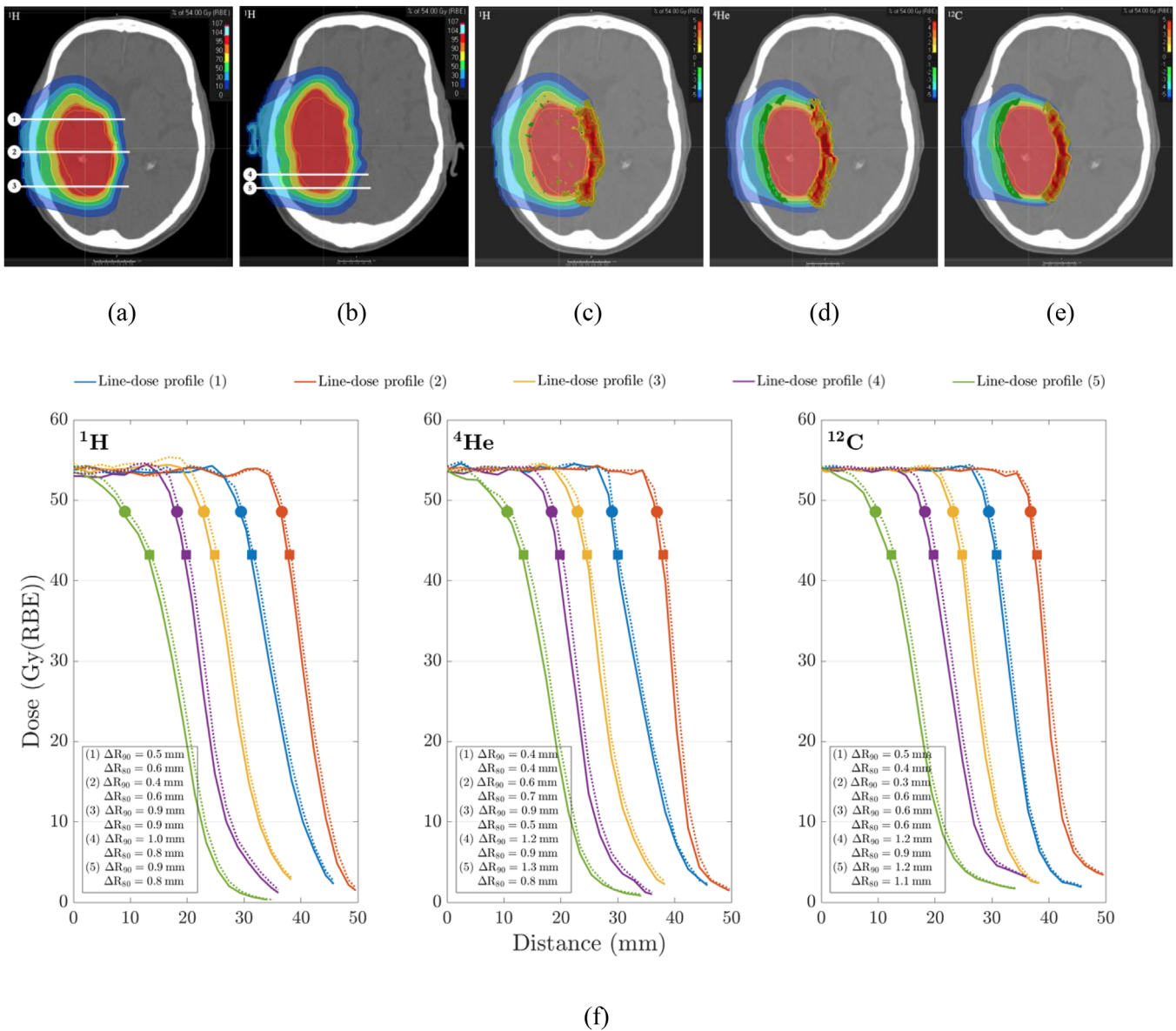
FIGURE 5 For a representative patient case, proton therapy dose distribution of plan C for patient #1 in two different axial slices (a, b), dose difference map superimposed on the dose distribution shown in (a) for protons (c), for helium ions (d), for carbon ions (e), and five representative line-dose profiles calculated on dual-layer spectral CT (DLCT) (solid line) and single-energy CT (SECT) (dotted line) for protons, helium, and carbon ions to quantify deviations in range prediction (f). The placement of the five line-dose profiles in (f) are illustrated in (a, b). The illustrated depth-dose curves indicate absolute range (R) differences between DLCT and SECT at R_{90} (marked with circles) and R_{80} (marked with squares)

3.2 | Evaluation of DLCT data-based treatment planning in head patients

Figure 5 shows exemplary proton therapy dose distributions and dose difference maps of patient #1 for protons, helium, and carbon ions as well as the corresponding line-dose profiles for DLCT- and SECT-based calculation of the depicted slices. Absolute and relative range shifts at 90% and 80% dose fall-off in proton treatment plans between the two SPR predictions are summarized in Figure 6. The plots in Figure 6 depict the results for (i)

each of the four plans combining the data for the six patients and (ii) each patient combining the data for the four plans using box plots to visualize the beam's eye view (BEV) range differences. For all patients, there was a statistically significant ($p < 0.05$) difference between the range predicted by SECT and DLCT. The shift of absolute (relative) range differences between SECT and DLCT lay in the interval [0.42, 0.47] mm ([0.54, 0.62]%) with a probability of 95%. Mean absolute range shift over 270 evaluated line-dose profiles in the virtual brain tumors between DLCT and SECT was (0.46 ± 0.32)
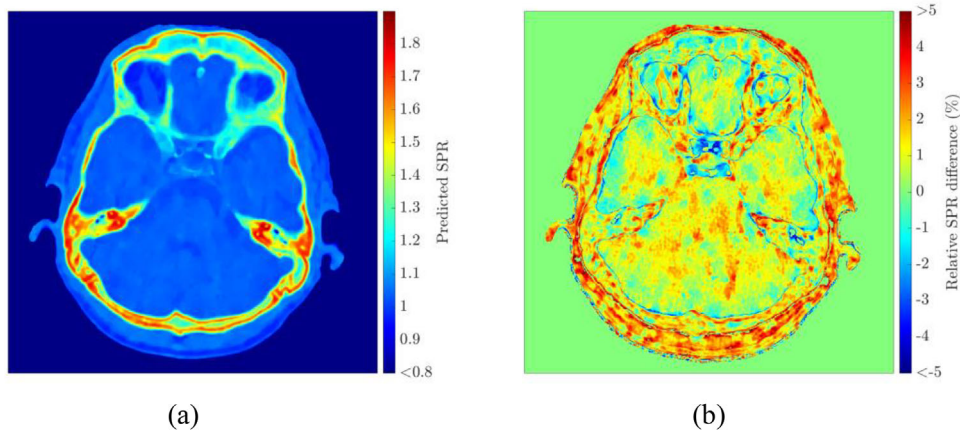
FIGURE 3 Axial plane of patient #1 showing predicted stopping power ratio (SPR) with dual-layer spectral CT (DLCT) images (a) and relative difference between SPR derived using DLCT and single-energy CT (SECT) (b)
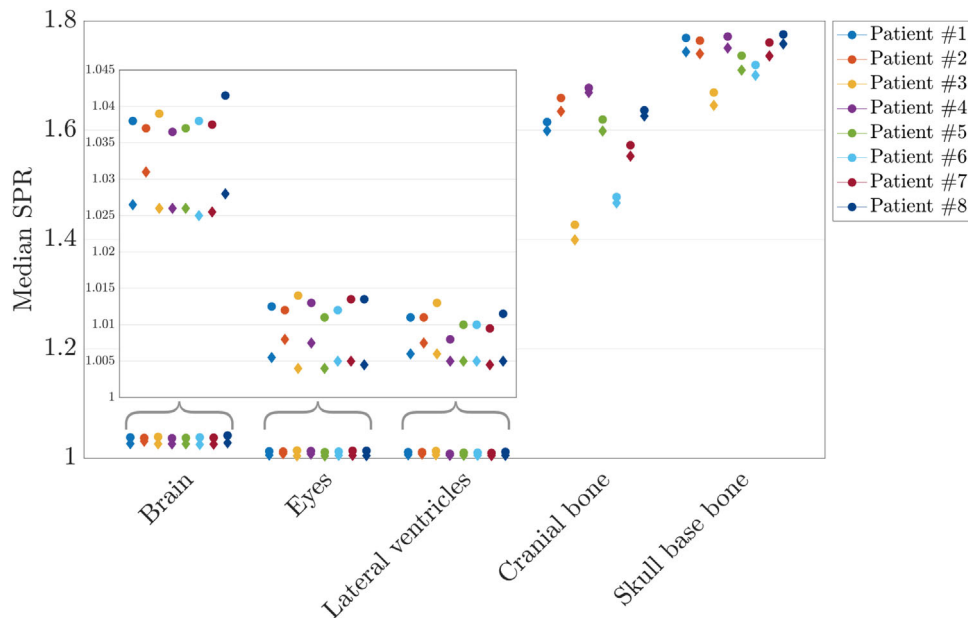
FIGURE 4 Median stopping power ratio (SPR) values predicted with dual-layer spectral CT (DLCT) (marked with circles) and single-energy CT (SECT) (marked with diamonds) over all investigated slices for all investigated regions-of-interest (ROIs) in each patient showing brain, eyes, lateral ventricles, cranial bone, and skull base bone. The subplot zooms in on the relevant SPR value region for brain, eyes, and lateral ventricles

mm at R_{90} and (0.42 ± 0.26) mm at R_{80}, with a maximum absolute range difference of 2.06 mm at R_{90} and of 1.47 mm at R_{80}. The range shift over both evaluated dose fall-off points was (0.44 ± 0.29) mm in the mean and with a median of 0.39 mm. The 25th percentile of the distribution was calculated to be 0.20 mm, and the 75th percentile of the distribution to be 0.59 mm. The relative differences are summarized in Table 2. The median relative range difference was 0.6% over all investigated treatment plans. Moreover, the intrapatient variability (cf. Figure 6d) of relative range shifts with a value of 0.44% was larger than the interpatient variability (cf. Figure 6c) of 0.07%. The differences between

intrapatient and interpatient variability are in part caused by considerably large differences between the chosen hypothetical treatment plans and, thus, differences in the traversed tissues in terms of tissue type and amount.

Figure 7 shows the absolute and relative range shifts for the four plans observed in patient #1 for the three ions (^{1}H, ^{4}He, and ^{12}C). The absolute range shift over both evaluated dose fall-off points was (0.58 ± 0.16) mm (^{1}H), (0.49 ± 0.19) mm (^{4}He), and (0.41 ± 0.17) mm (^{12}C) in the mean, and with a median of 0.60 mm (^{1}H), 0.40 mm (^{4}He), and 0.31 mm (^{12}C). The helium and carbon ion range shifts between SECT and DLCT were in line with those of protons, even though there are R_{90} or

TABLE 1 Stopping power ratio (SPR) difference for regions-of-interest (ROIs) in brain, cranial bone, eyes, lateral ventricles, and skull base bone

	SPR difference $\bar{\delta}_{SPR} \pm (\delta_{SPR})(\%)$				
Patient #	Brain	Cranial bone	Eyes	Lateral ventricles	Skull base bone
1	1.14 ± 0.09	1.28 ± 0.47	0.70 ± 0.13	0.47 ± 0.12	1.46 ± 0.54
2	0.68 ± 0.17	1.39 ± 0.16	0.38 ± 0.08	0.33 ± 0.08	1.14 ± 0.51
3	1.28 ± 0.13	1.87 ± 0.67	0.92 ± 0.05	0.64 ± 0.05	1.10 ± 0.47
4	1.02 ± 0.28	0.65 ± 0.24	0.50 ± 0.16	0.32 ± 0.14	1.24 ± 0.38
5	1.08 ± 0.06	0.96 ± 0.27	0.72 ± 0.11	0.57 ± 0.17	1.35 ± 0.37
6	1.21 ± 0.08	0.76 ± 0.30	0.64 ± 0.10	0.42 ± 0.17	1.08 ± 0.28
7	1.14 ± 0.16	1.49 ± 0.21	0.75 ± 0.16	0.50 ± 0.10	1.46 ± 0.32
8	1.22 ± 0.11	0.66 ± 0.09	0.89 ± 0.08	0.60 ± 0.12	0.92 ± 0.41
Median	1.16	1.07	0.69	0.50	1.25
Mean ± SEM	1.10 ± 0.07	1.13 ± 0.17	0.69 ± 0.06	0.48 ± 0.05	1.22 ± 0.14

Note: The arithmetic mean of the relative SPR difference ($\bar{\delta}_{SPR}$) is given along with the standard deviation ($s(\delta_{SPR})$) for each patient. Median and mean along with the standard error of the mean (SEM) over each ROI are indicated.

TABLE 2 Relative proton range differences given in percent ($\frac{\Delta R}{R_{DLCT}}$) (cf. Equations 1 and 2)

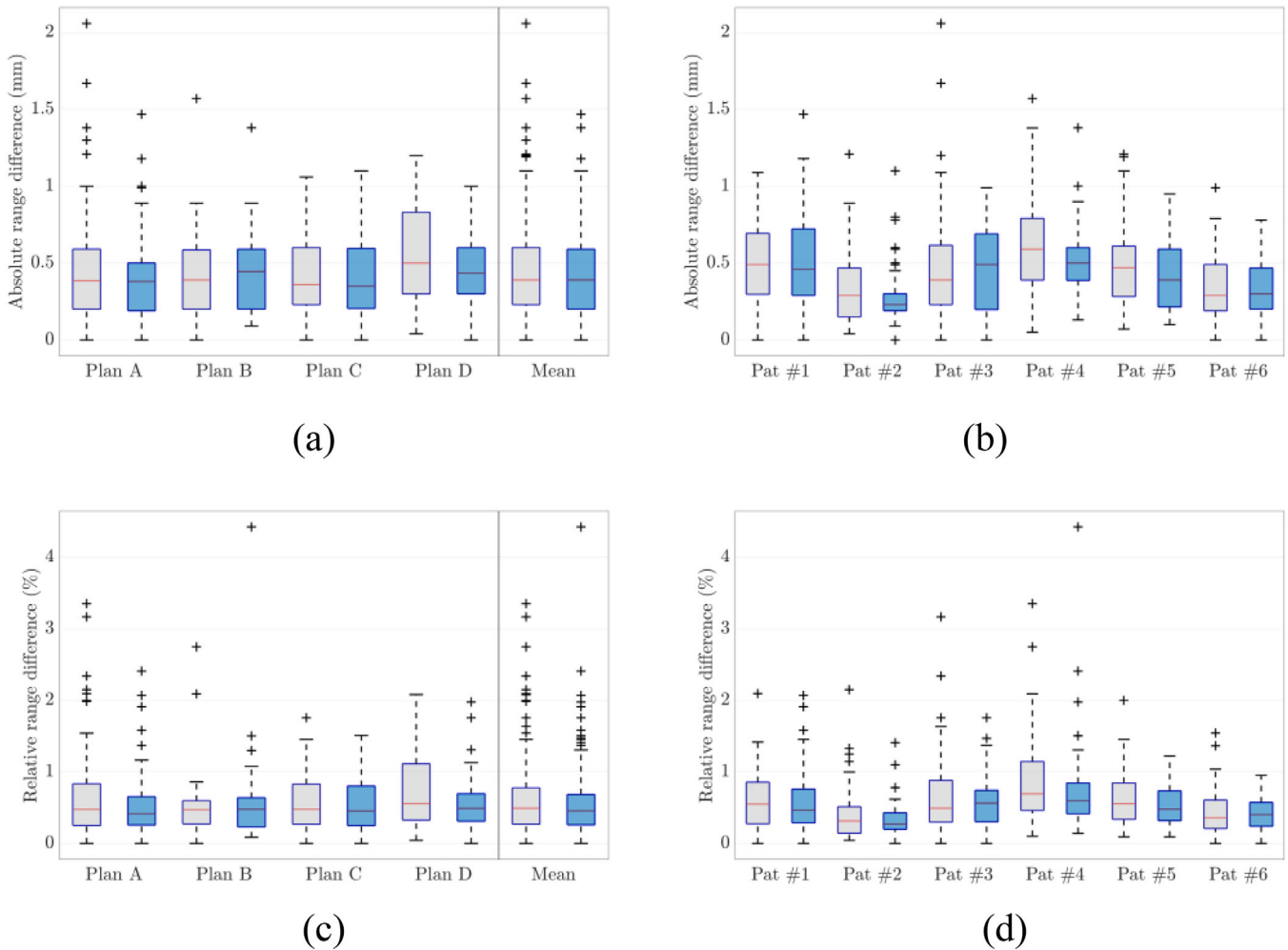|		Relative range differences (%)				
		Mean	25th Percentile	50th Percentile (median)	75th Percentile	100th Percentile
Plan A	R_{90}	0.66	0.25	0.48	0.83	3.35
	R_{80}	0.52	0.26	0.41	0.65	2.41
Plan B	R_{90}	0.50	0.27	0.47	0.60	2.75
	R_{80}	0.54	0.23	0.48	0.64	4.43
Plan C	R_{90}	0.58	0.27	0.48	0.83	1.76
	R_{80}	0.57	0.25	0.45	0.80	1.51
Plan D	R_{90}	0.70	0.33	0.56	1.11	2.08
	R_{80}	0.57	0.31	0.49	0.69	1.98
All plans	R_{90}	0.61	0.27	0.49	0.78	3.35
	R_{80}	0.55	0.26	0.46	0.68	4.43

R_{80} variations among the three particles in the individual plans.

The general agreement between DLCT- and SECT-based dose calculations was confirmed in the evaluation of the clinical patient treatment plans. 3D gamma analysis of the dose distributions revealed good agreement between DLCT- and SECT-based treatment planning with a mean 3D gamma local pass rate (1%/1 mm) of 97.3% over all patients and treatment plans, ranging from 96.4% (plan A) to 96.7% (plan D) to 97.7% (plan C) and 98.3% (plan B). Despite good agreement in 3D gamma analysis, there were differences between DLCT and SECT with regard to PTV coverage and dose to OARs.

In Figure 8, relevant dose differences are shown for all evaluated OARs in each patient and plan, respectively. In 12% of all evaluated OARs, the results indicated differ-ences in the mean or maximum ($D_{0.03cc}$) dose of more than 0.5 Gy (RBE) and differences up to 6.8 Gy (RBE) in the total plan. The average (and maximum) criterion was reached 46 (and 68) times over all patients and proton plans. DLCT-based recalculation of the SECT-optimized treatment plans showed a decrease in PTV coverage, as evaluated with the difference in PTV $D_{99\%}$, of 1.0% or 0.5 Gy (RBE) in the mean over all evaluated plans and patients (Table 3). With regard to the three ions, Table 3 indicates quite similar differences for [4]He and ^{12}C in PTV coverage between SECT and DLCT compared with [1]H. Figure 9 shows the DVH of plan C for an example patient (patient #1). In the optic chiasma (located close to the target dose fall-off), the maximum dose ($D_{0.03cc}$) was 49.71 Gy (RBE) for SECT-based and 47.06 Gy (RBE) for DLCT-based treatment planning, a decrease of 6%. A higher SPR value (as seen in bony
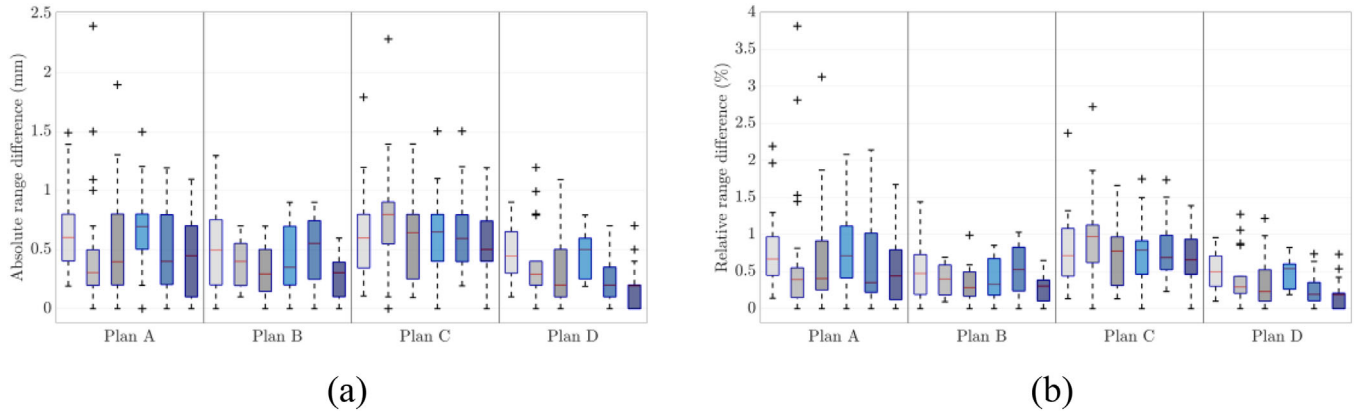
FIGURE 6 (a, b) Box plots showing deviations in beam's eye view (BEV) range (R) prediction between single-energy CT (SECT)- and dual-layer spectral CT (DLCT)-based proton treatment planning ($\Delta R = |R_{SECT} - R_{DLCT}|$). (c, d) Box plots showing relative differences in range prediction ($\frac{\Delta R}{R_{DLCT}}$) (cf. equations 1 and 2). On each box, the central mark (red) indicates the median, and the bottom and top edges of the box indicate the 25th and 75th percentiles, respectively. The whiskers extend to the most extreme data points (i.e., smallest observation $\geq$ lower quartile $- 1.5 \times$ interquartile range/largest observation $\leq$ upper quartile $+ 1.5 \times$ interquartile range), and the outliers are plotted individually using the $+$ symbol. In gray are the results depicted for R_{90}, and in blue are the results shown for R_{80}. (a, c) Analysis for each plan and (b, d) analysis for each patient (Pat)

structures and brain in Figure 4) leads to a shorter range, which resulted in a dose decrease in the optic chiasma in the given situation. The optic chiasma is a serial structure in which disabling any subunit causes the entire organ to fail.[38] In patient #1, differences in the mean or maximum dose of more than 0.5 Gy (RBE) over all evaluated OARs were observed in 13% for ^{1}H, in 9% for ^{4}He, and in 6% for ^{12}C. In the DVHs, the dose to distal OARs decreased using ^{4}He or ^{12}C, due to the sharper gradients of helium and carbon ions compared with protons (cf. Figure 5f). Therefore, the absolute dose differences to OARs between SECT and DLCT were also smaller compared with protons. Nevertheless, with a longer range using DLCT and sharper gradients, the dose there could be more than in the SECT plan; therefore, it is very patient-specific.

4 | DISCUSSION

This study evaluated the clinical relevance of DLCT-based SPR prediction for proton, helium, and carbon ion beam therapy treatment planning in the brain. A comprehensive workflow for DLCT-based ion beam therapy treatment planning was established (cf. section 2.4). Through a patient cohort study in homogeneous tissue regions and heterogeneous patient scenarios, DLCT- and SECT-based SPR differences and their dosimetric impact were investigated and compared. The clinical viability of DLCT-based SPR prediction and its feasibility for performing particle therapy treatment planning were assessed to justify its clinical use. Depending on the anatomical regions, SECT- and DLCT-based methods produced variant degrees of SPR prediction differences

(a)

(b)

FIGURE 7 (a) Box plot showing deviations in beam's eye view (BEV) range (R) prediction for the three ions (^{1}H, ^{4}He, ^{12}C) between single-energy CT (SECT)- and dual-layer spectral CT (DLCT)-based treatment planning ($\Delta R = |R_{SECT} - R_{DLCT}|$). (b) Box plots showing relative differences in range prediction ($\frac{\Delta R}{R_{DLCT}}$) (cf. equations 1 and 2). On each box, the central mark (red) indicates the median, and the bottom and top edges of the box indicate the 25th and 75th percentiles, respectively. The whiskers extend to the most extreme data points (i.e., smallest observation ≥ lower quartile − 1.5 × interquartile range/largest observation ≤ upper quartile + 1.5 × interquartile range), and the outliers are plotted individually using the + symbol. The plots show the analysis for each plan in patient #1. For each individual plan, the plots depict the results for ^{1}H (left), ^{4}He (middle), and ^{12}C (right). In gray shades are the results depicted for R_{90}, and in blue shades are the results shown for R_{80}
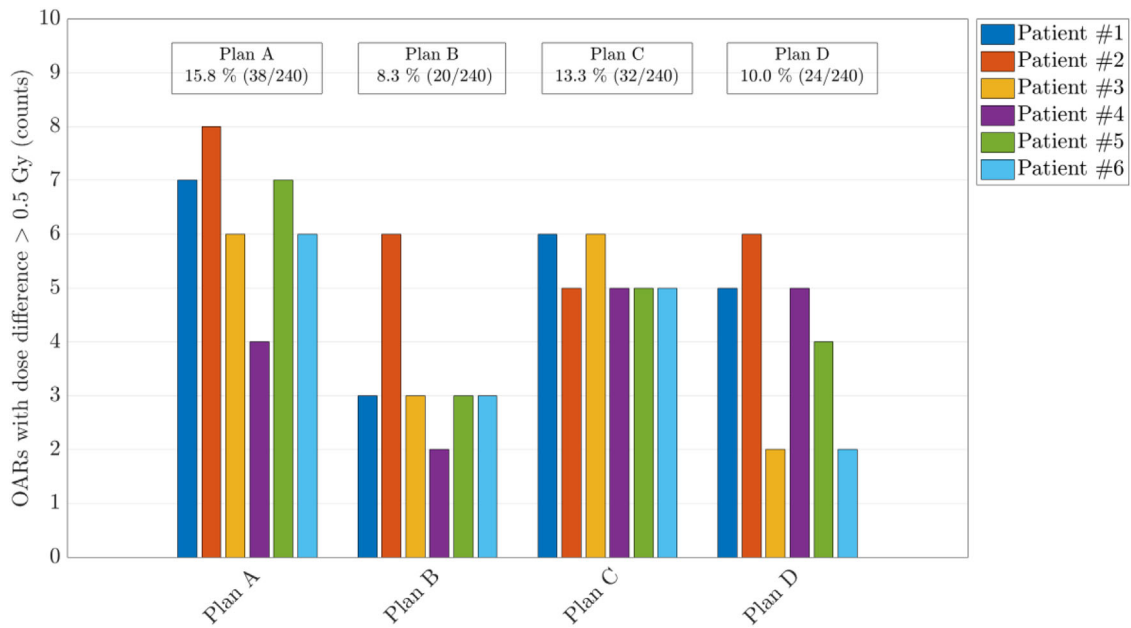
FIGURE 8 Dose differences in the mean or maximum dose of more than 0.5 Gy (RBE) in the total plan of all evaluated OARs (considering only proton treatment planning). Each color represents one of the six evaluated patients

in the studied patient cohort. Owing to the results from preclinical studies showing better SPR prediction with DLCT compared with SECT[18,20–23] and the observed differences in SPR prediction in this study, DLCT may be justifiably better for clinical practice in patient treatments where the beams intercept and traverse heterogeneous anatomical regions.

First, SPR differences in various homogeneous tissue regions were analyzed on a per-patient basis, and the determinants leading to the largest uncertainties were

identified and quantified. The relative SPR comparison in the patient cohort showed statistically significant SPR differences in all investigated anatomical regions between DLCT- and SECT-based methods. Furthermore, Table 1 shows the interpatient variability of SPR predictions. Bony tissues showed the largest deviation between DLCT and SECT of the investigated ROIs, potentially due to their high SPR values. The SPR differences of 1.1% to 1.2% seen in bone (cf. Table 1) could potentially imply a benefit in DLCT-based treatment
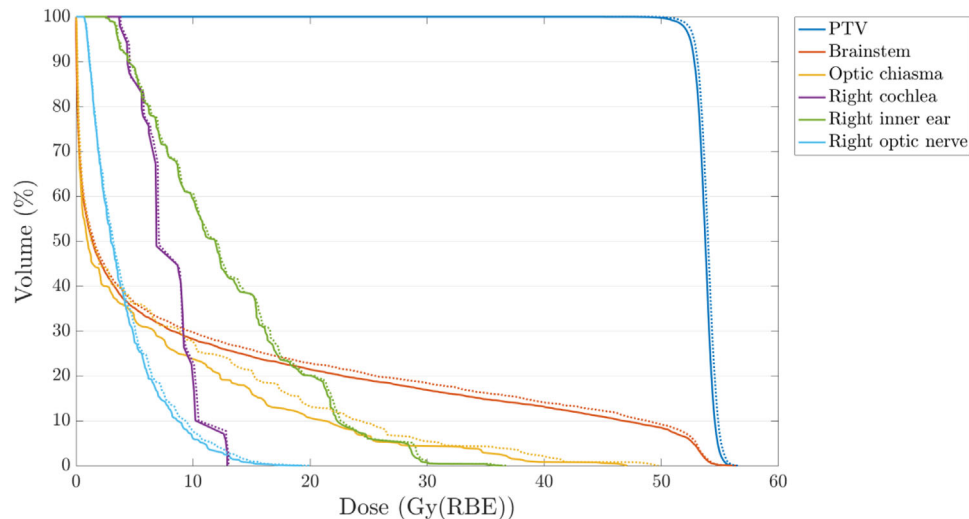
FIGURE 9 Representative DVH for patient #1, treatment plan C using protons, calculated on dual-layer spectral CT (DLCT) (solid line) and single-energy CT (SECT) (dotted line) data sets displaying all structures used for optimization

TABLE 3 Differences in planning target volume (PTV) coverage between single-energy CT (SECT) and dual-layer spectral CT (DLCT)

| | PTV coverage difference $\Delta D_{99\%}$ (Gy (RBE)) | | | |
Patient #	Plan A	Plan B	Plan C	Plan D
1 (^{1}H)	0.51	0.78	0.61	0.74
1 (^{4}He)	0.17	0.36	0.38	0.35
1 (^{12}C)	0.36	0.50	0.47	0.42
2	0.07	0.30	0.34	1.16
3	0.34	0.86	0.41	0.47
4	0.46	0.36	0.72	0.84
5	0.37	0.45	0.79	0.58
6	0.01	0.11	0.43	0.43
$\overline{\Delta D}_{99\%} \pm$ s($\Delta D_{99\%}$))	0.29 ± 0.21	0.48 ± 0.29	0.55 ± 0.18	0.70 ± 0.27

Note: Differences in PTV coverage between SECT- and DLCT-based dose calculations ($\Delta D_{99\%} = D_{99\%,SECT} - D_{99\%,DLCT}$) for each treatment plan and patient. The arithmetic mean ($\overline{\Delta D}_{99\%}$) in PTV coverage is indicated along with the standard deviation (s($\Delta D_{99\%}$)) for each plan (only proton treatment planning is included in the calculation).

planning, assuming a more accurate DLCT-based SPR prediction in patient anatomies. The SPR differences of about 1.1% in the brain, which is often the main tissue type in the beam, could also be of clinical relevance. For instance, SPR differences of 1%, i.e., translating into range differences of 1%, result in 1 mm range shift over 10 cm depth in the body. Beyond that, DLCT could be advantageous for tumors nearby critical OARs like the optical system or brainstem. Although the SPR differences were above 1% for ROIs uniformly composed of bony tissue or brain, median relative range deviations in the patient as a whole were 0.6%. The difference can be attributed to the dependence on anatomical target site and composition in treatment planning and the compounding effects of SPR prediction power of various heterogeneous tissues composed of bone and soft tissue.

Second, absolute and relative range differences and the dosimetric impact of DLCT-based SPR calculation in comparison with the SECT-based approach were carefully assessed. The influence of SPR uncertainty on patient dose uncertainty is not trivial and substantially case-dependent. Comparison of DLCT-based proton treatment plans of four brain tumor locations to the corresponding SECT plans showed considerable differences in SPR at voxel level and a mean relative range difference of about 0.6% at the distal fall-off were observed (cf. Table 2); in certain cases, the range shift might be of clinical relevance. The DVHs showed a decrease in the mean and maximum OAR dose using DLCT owing to the SPR difference between DLCT and SECT. The 25th and 75th percentiles varied from 0.23% to 1.11% across the six patients. Range shifts and dose differences in OARs between DLCT and SECT in helium and carbon ion treatment plans were similar to those of protons (cf. Figure 7). Despite the intrapatient and interpatient variability, the example cases showed clinically relevant range differences between SECT- and DLCT-based SPR predictions. Furthermore, the large intrapatient variation of range shifts illustrates that variation in range uncertainty depends on the anatomical structure and the beam path. In turn, the magnitude of improvement in range prediction with DLCT depends on the treatment location and its heterogeneity.

Similar studies have previously been performed comparing DECT- and SECT-based SPR estimation for patients with head tumors. The outcome in SPR prediction differences in homogeneous tissue regions is in line with a study of Taasti et al.,[13] who investigated

ROIs in the cranium, brain, and eyes. The results found in this study are also of the same order as recent studies using other DECT acquisition methods (e.g., consecutive scanning) or other DECT SPR prediction methods, showing that range differences of around 1 mm (1%) may be expected for the brain region.[13,14] The results from this work are likewise comparable with a study analyzing range shifts obtained in five head trauma patients with simulated base of skull tumors,[39] reporting median relative range differences of about 0.5%–1%. The median differences found in this study on DLCT-based range differences are similar to or slightly smaller than those observed in previous studies using other DECT acquisition methods; however, there exist rather high interpatient variabilities as well as larger differences for some patients. One should also take into consideration that the SECT-based prediction method applied in this study, using an HLUT divided into ten line segments, may be more methodologically demanding in the context of HLUT generation than in previous studies, that used an HLUT divided into three parts representing different tissue types along with different slopes of the respective line segments. A higher number of HLUT line segments might be already better suited for SPR prediction. A recent survey-based study revealed a large intercenter variability in HLUT definition, showing that the number of HLUT line segments varied widely between 2 and 11.[40] Hence, the applied HLUT in this study is at the upper end of the line segment number spectrum. In the context of range differences between DLCT and SECT observed in this study specifically, one must note that HIT implements highly refined treatment planning protocols that have evolved since facility start-up in 2009. Consequently, the facility has gained valuable experience in minimizing range uncertainty with the applied HLUT approach and demonstrated that such techniques can provide fairly accurate SPR estimation in controlled treatment scenarios. Nonetheless, benchmarking and comparison within the European Particle Therapy Network regarding CT calibrations using a standardized phantom showed large differences and intercenter variations in range reaching up to 2.9%.[41] Thus, direct DLCT-based SPR prediction could lead to reduced differences between centers or help new proton centers begin treatment with a greater confidence in range prediction.

As shown in the hypothetical treatment planning cases, even small discrepancies in the calculated SPR can result in significant changes in range, because they may accumulate over the entire beam path.[6] Thus, DLCT may lead to clinically relevant range shifts and subsequently dose differences, especially for tumors in challenging locations, e.g., tumors centrally located in the head, deep-seated, or treated with ion beams traversing a high amount of bony tissue. In turn, the range differences could enable reduced dose to normal tissue and OARs with benefits in PTV coverage (i.e., $D_{99\%}$ dose).

In particular, this study found differences in the mean or maximum dose of more than 0.5 Gy (RBE) in the total plan (cf. Figure 8) and mean differences in $D_{99\%}$ target dose of 0.5 Gy (RBE) (cf. Table 3). Variation in CTV coverage, however, might be even smaller and not clinically relevant. The current conservative safety margins and plan robustness may be reduced if the SPR can be calculated with greater confidence. Even if the observed range differences are below 1 mm in the median, there may be clinically significant differences for individual patients, as reported in the large intra- and interpatient variability (cf. Figure 6), which may be highly relevant for increasing personalized medicine considerations.[32] Recent work demonstrates the benefits in terms of normal tissue complication probability (NTCP) in mitigating range uncertainty even for smaller reductions.[42] The study showed that higher range differences might be expected for beams traversing heterogeneous tissues with SPR values that differ considerably compared with the SPR of water (e.g., bone tissue, air-filled cavities) (cf. Figure 4 and Table 1). Thereby, the accuracy of SPR in each voxel in the patient determines the accuracy of the range calculation. More different tissue types in the beam path can lead to larger deviations in range prediction (as already observed in previous studies[14]). Therefore, a patient-specific DLCT-based SPR prediction with high accuracy in each individual tissue type would be advisable. In particular, DLCT may be beneficial in complex cases; however, as of now it is difficult to identify in advance which patients would most benefit from DLCT-based treatment planning, and so the use of DLCT may be advisable for all patients. DLCT-based SPR calculation may even raise the possibility of using contrast agent during planning CT image acquisition[43] and may be beneficial in the presence of metal implants, surgical stabilizations, or other special materials (e.g., liquid embolic agents), or in the presence of image artifacts (e.g., produced by metal implants).[4]

To judge which of the two evaluated approaches is closer to reality, the respective SPR accuracy must be known.[14] For instance, precise range verification with prompt gamma imaging[44–46] or proton transmission imaging[47,48] could provide millimeter accuracy in range verification, but in its current state is not clinically widespread.[49] Thus, the accuracy of DLCT-based SPR prediction in patients has yet to be verified directly. Instead, SPR accuracy was demonstrated indirectly by translating the results shown in previous studies[18,20,22,23] to patient treatment planning. In tissue substitutes, predicted SPR values were within a mean accuracy of 0.6% compared with measured SPR and showed substantially better agreement with measured data compared with standard CT-number-to-SPR calibration with a mean deviation of 1.5%.[20] Beyond that, SPR prediction with DLCT outperformed the clinical SECT standard in a half-head anthropomorphic phantom with a range prediction improvement of 1 mm,[20]

when using a single beam directed through highly heterogeneous structures. A similar study acquired ground-truth measurements in an anthropomorphic head phantom showing better agreement between DECT and measured SPR compared with SECT.[50] The current study used two or three beam directions, directed through heterogeneous as well as relatively homogeneous tissue regions (e.g., brain). The order of magnitude of SPR prediction difference between DLCT and SECT in phantoms was similar to the examined patient cases in this study. Ideally, in this study, using a patient cohort, a ground-truth measurement for SPR would be referenced. However, this study aimed to evaluate whether clinically relevant SPR and therefore range deviations occurred between SECT and DLCT in a patient cohort, justifying whether more sophisticated image acquisition tools would be beneficial and may be considered for potential clinical implementation. As DLCT has been shown to be superior to SECT in tissue surrogates and an anthropomorphic phantom, the dissimilar results for DLCT and SECT observed in this patient study could imply that DLCT would improve the dose accuracy in ion beam therapy treatment planning.

In this study, the feasibility of direct patient-specific SPR prediction based on DLCT could be demonstrated using the existing clinical framework and equipment. Compared with other DECT techniques, DLCT imaging using a single X-ray source is not influenced by patient motion occurring within the time span of acquisition (e.g., breathing, swallowing, organ movements). At the same acquisition dose as conventional CT imaging, DLCT affords a comprehensive spectral data set for each patient, without the need for additional scans or deviations from the clinical protocols. Nevertheless, DLCT imaging has a limited spectral separation between the low- and high-energy data sets because the technique uses a single X-ray source.[15] Moreover, cross-scatter radiation between detector layers can occur.[17] Additionally, as a result of using the same tube current in both cases, noise level may differ between low- and high-energy images.[15] A discussion of uncertainties within the study can be found in SM S5.

Further studies may evaluate other anatomical sites (e.g., head and neck tumors) and beams traversing several tissue types and thicker bony structures (e.g., tumors in the pelvic region) as well as beams passing through the lungs (e.g., Hodgkin lymphoma). In brain tumor cases, ion beams penetrate mainly soft tissue. Within treatment fields of prostate cancer patients, we would expect substantially larger differences, as already observed by Wohlfahrt et al.[14] Although CT uncertainty can be incorporated into planning robustness optimization, this study followed the current clinical practice at HIT and applied the PTV margin concept. In additional studies, robust optimization might be conducted and compared with regard to dose differences in CTV and OARs, in order to assess the influence of robustly optimized treatment plans in combination with DLCT-based SPR prediction. Moreover, investigations of patients with real tumors in the brain and range measured in biological tissue samples are essential to confirm the clinical viability of DLCT-based range prediction. In particular, there exists a large intra- and interpatient variation of SPR shifts seen in this radiological patient cohort, which might also cause smaller or bigger range differences in other patient cases and should be further investigated in larger patient cohorts. Further studies with radio-oncological patient data and "real" clinical indications are important to carry out in order to show that the results may be generalizable and transferable to clinical routine. In spite of this, potential CT artifacts can also affect the accuracy of ion beam range prediction based on CT images, which are particularly severe in the presence of metallic implants.[6] Hence, the benefit of DLCT can be especially large in the case of nontissue materials such as implants or contrast agent, which in general are not appropriately covered by any conventional CT-number-to-SPR conversion.[19] Investigations of SPR precision for nontissue samples are foreseen. DLCT imaging may not only improve range prediction, but DLCT data sets could also help in characterizing the implant in terms of ED and EAN. Additional applications of DLCT in both photon radiotherapy and particle therapy are conceivable with more practical benefits, such as simplifying treatment planning workflow, reducing CT simulation time and radiation exposure as well as the anesthesia time for pediatric patients by performing dose calculation on postcontrast DLCT images.[43] Finally, evaluation of DLCT-based treatment planning in more patient cases for carbon and helium ion beam therapy is anticipated.

5 | CONCLUSIONS

This study performed the first analysis of DLCT-based SPR prediction in the brain. In homogeneous tissue regions, analysis suggests significant mean SPR differences between the DLCT-based and conventional SECT-based approaches of about 1%. In heterogeneous anatomical regions, mean proton range shifts in treatment plans between DLCT and the clinical standard of 0.6% were observed, with variations exceeding 4% of the total range. Range shifts between DLCT and SECT in helium and carbon ion treatment plans were similar to those of protons. In particular, DLCT is most advantageous in treatment plans where beams are traversing highly heterogeneous structures. Therefore, patient-specific DLCT-based SPR prediction may improve proton, helium, and carbon ion range calculation and eventually lead to reduced range uncertainty margins. In sum, the study demonstrated the feasibility of using DLCT imaging for proton, helium, and carbon ion beam therapy treatment planning and its ability to provide

patient-specific SPR prediction. Further clinical investigations using larger patient cohorts and examining other treatment regions will continue to focus on the inter- and intrapatient variability to realistically quantify the possible benefit of DLCT, and consequently to estimate the potential range uncertainty reduction resulting in smaller therapeutic margins for high-precision ion beam therapy.

AUTHOR CONTRIBUTIONS
Conceptualization, F.L., W.S., and A.M.; methodology, F.L., T.T., S.H., W.S., and A.M.; data acquisition and analysis, F.L., T.T., and A.M.; interpretation, F.L., T.T., S.M., W.S., and A.M.; writing—original draft preparation, F.L., T.T., and S.M.; writing—review and editing, F.L., T.T., S.M., S.H., J.D., W.S., and A.M.; supervision, J.D., W.S., and A.M.

CONFLICT OF INTEREST
The authors have no relevant conflicts of interest to disclose. W.S. is a member of the CT Advisory Board of Philips Medical Systems.

REFERENCES
1. Bortfeld TR, Loeffler JS. Three ways to make proton therapy affordable. *Nature*. 2017;549(7673):451-453.
2. Durante M, Orecchia R, Loeffler JS. Charged-particle therapy in cancer: clinical uses and future perspectives. *Nat Rev Clin Oncol*. 2017;14:483-495.
3. Baumann M, Krause M, Overgaard J, et al. Radiation oncology in the era of precision medicine. *Nat Rev Cancer*. 2016;16(4):234-249.
4. Paganetti H, Beltran C, Both S, et al. Roadmap: proton therapy physics and biology. *Phys Med Biol*. 2021;66(5):05RM01.
5. Wohlfahrt P, Richter C. Status and innovations in pre-treatment CT imaging for proton therapy. *Brit J Radiol*. 2020;93(1107):20190590.
6. Paganetti H. Range uncertainties in proton therapy and the role of Monte Carlo simulations. *Phys Med Biol*. 2012;57(11):R99-R117.
7. van Elmpt W, Landry G, Das M, Verhaegen F. Dual energy CT in radiotherapy: current applications and future outlook. *Radiother Oncol*. 2016;119(1):137-144.
8. Bär E, Lalonde A, Royle G, Lu H, Bouchard H. The potential of dual-energy CT to reduce proton beam range uncertainties. *Med Phys*. 2017;44(6):2332-2344.
9. Yang M, Zhu XR, Park PC, et al. Comprehensive analysis of proton range uncertainties related to patient stopping-power-ratio estimation using the stoichiometric calibration. *Phys Med Biol*. 2012;57(13):4095-4115.
10. Schneider U, Pedroni E, Lomax A. The calibration of CT Hounsfield units for radiotherapy treatment planning. *Phys Med Biol*. 1996;41(1):111-124.
11. Hünemohr N, Ackermann B, Jäkel O. Experimental verification of ion stopping power prediction from dual energy CT data in tissue surrogates. *Phys Med Biol*. 2014;59(1):83-96.
12. Möhler C, Wohlfahrt P, Richter C, Greilich S. Range prediction for tissue mixtures based on dual-energy CT. *Phys Med Biol*. 2016;61(11):N268-N275.

13. Taasti VT, Muren LP, Jensen K, et al. Comparison of single and dual energy CT for stopping power determination in proton therapy of head and neck cancer. *Phys Imag Radiat Oncol*. 2018;6:14-19.
14. Wohlfahrt P, Möhler C, Stützer K, Greilich S, Richter C. Dual-energy CT based proton range prediction in head and pelvic tumor patients. *Radiother Oncol*. 2017;125(3):526-533.
15. McCollough CH, Leng S, Yu L, Fletcher JG. Dual- and multi-energy CT: principles, technical approaches, and clinical applications. *Radiology*. 2015;276(3):637-653.
16. Flohr TG, McCollough CH, Bruder H, et al. First performance evaluation of a dual-source CT (DSCT) system. *Eur Radiol*. 2006;16(2):256-268.
17. McCollough CH, Boedeker K, Cody D, et al. Principles and applications of multienergy CT: report of AAPM Task Group 291. *Med Phys*. 2020;47(7):e881-e912.
18. Mei K, Ehn S, Oechsner M, et al. Dual-layer spectral computed tomography: measuring relative electron density. *Eur Radiol Exp*. 2018;2(1):1-9.
19. Wohlfahrt P, Möhler C, Hietschold V, et al. Clinical implementation of dual-energy CT for proton treatment planning on pseudo-monoenergetic CT scans. *Int J Radiat Oncol Biol Phys*. 2017;97(2):427-434.
20. Faller FK, Mein S, Ackermann B, Debus J, Stiller W, Mairani A. Pre-clinical evaluation of dual-layer spectral computed tomography-based stopping power prediction for particle therapy planning at the Heidelberg Ion Beam Therapy Center. *Phys Med Biol*. 2020;65(9):095007.
21. Hua C-H, Shapira N, Merchant TE, Klahr P, Yagil Y. Accuracy of electron density, effective atomic number, and iodine concentration determination with a dual-layer dual-energy computed tomography system. *Med Phys*. 2018;45(6):2486-2497.
22. Landry G, Dörringer F, Si-Mohamed S, et al. Technical note: relative proton stopping power estimation from virtual monoenergetic images reconstructed from dual-layer computed tomography. *Med Phys*. 2019;46(4):1821-1828.
23. Ohira S, Washio H, Yagi M, et al. Estimation of electron density, effective atomic number and stopping power ratio using dual-layer computed tomography for radiotherapy treatment planning. *Physica Med*. 2018;56:34-40.
24. International commission on radiation units and measurements: prescribing, recording, and reporting light ion beam therapy. ICRU Report No. 93. 2016. https://doi.org/10.1093/jicru/ndy024
25. Inaniwa T, Kanematsu N. Effective particle energies for stopping power calculation in radiotherapy treatment planning with protons and helium, carbon, and oxygen ions. *Phys Med Biol*. 2016;61(20):N542-N550.
26. Bär E, Andreo P, Lalonde A, Royle G, Bouchard H. Optimized I-values for use with the Bragg additivity rule and their impact on proton stopping power and range uncertainty. *Phys Med Biol*. 2018;63(16):165007.
27. International commission on radiation units and measurements. Key data for ionizing-radiation dosimetry: measurement standards and applications. ICRU Report No. 90. 2014. https://doi.org/10.1093/jicru/ndw043
28. Yang M, Virshup G, Clayton J, Zhu XR, Mohan R, Dong L. Theoretical variance analysis of single- and dual-energy computed tomography methods for calculating proton stopping power ratios of biological tissues. *Phys Med Biol*. 2010;55(5):1343-1362.
29. Mayneord WV. The significance of the Röntgen. *Acta Un Int Cancr*. 1937;2:271-282.
30. Telsemeyer J, Ackermann B, Ecker S, Jäkel O, Martišíková M. Experimental verification of ion range calculation in a treatment planning system using a flat-panel detector. *Phys Med Biol*. 2014;59(14):3737-3747.
31. Schneider W, Bortfeld T, Schlegel W. Correlation between CT numbers and tissue parameters needed for Monte Carlo

simulations of clinical dose distributions. *Phys Med Biol*. 2000;45(2):459-478.

32. Hansen CR, Crijns W, Hussein M, et al. Radiotherapy Treatment plannINg study Guidelines (RATING): a framework for setting up and reporting on scientific treatment planning studies. *Radiother Oncol*. 2020;153:67-78.

33. Delpon G, Escande A, Ruef T, et al. Comparison of automated atlas-based segmentation software for postoperative prostate cancer radiotherapy. *Front Oncol*. 2016;6:178.

34. Kopp B, Mein S, Tessonnier T, et al. Rapid effective dose calculation for raster-scanning 4He ion therapy with the modified microdosimetric kinetic model (mMKM). *Physica Med*. 2021;81:273-284.

35. Mairani A, Brons S, Cerutti F, et al. The FLUKA Monte Carlo code coupled with the local effect model for biological calculations in carbon ion therapy. *Phys Med Biol*. 2010;55(15):4273-4289.

36. Scoccianti S, Detti B, Gadda D, et al. Organs at risk in the brain and their dose-constraints in adults and in children: a radiation oncologist's guide for delineation in everyday practice. *Radiother Oncol*. 2015;114(2):230-238.

37. Low DA, Harms WB, Mutic S, Purdy JA. A technique for the quantitative evaluation of dose distributions. *Med Phys*. 1998;25(5):656-661.

38. Chang DS, Lasley FD, Das IJ, Mendonca MS, Dynlacht JR. Normal tissue radiation responses. *Basic Radiotherapy Physics and Biology*. Cham: Springer International Publishing; 2014:265-275.

39. Hudobivnik N, Schwarz F, Johnson T, et al. Comparison of proton therapy treatment planning for head tumors with a pencil beam algorithm on dual and single energy CT images. *Med Phys*. 2016;43(1):495-504.

40. Taasti VT, Bäumer C, Dahlgren CV, et al. Inter-centre variability of CT-based stopping-power prediction in particle therapy: survey-based evaluation. *Phys Imag Radiat Oncol*. 2018;6:25-30.

41. Peters N, Wohlfahrt P, Dahlgren CV, et al. Experimental assessment of inter-centre variation in stopping-power and range prediction in particle therapy. *Radiother Oncol*. 2021;163:7-13.

42. Tattenberg S, Madden TM, Gorissen BL, Bortfeld T, Parodi K, Verburg J. Proton range uncertainty reduction benefits for skull base tumors in terms of normal tissue complication probability (NTCP) and healthy tissue doses. *Med Phys*. 2021;48(9):5356-5366.

43. Ates O, Hua C-H, Zhao L, et al. Feasibility of using post-contrast dual-energy CT for pediatric radiation treatment planning and dose calculation. *Brit J Radiol*. 2020;94(1118):20200170.

44. Draeger E, Mackin D, Peterson S, et al. 3D prompt gamma imaging for proton beam range verification. *Phys Med Biol*. 2018;63(3):035019.

45. Hueso-González F, Rabe M, Ruggieri TA, Bortfeld T, Verburg JM. A full-scale clinical prototype for proton range verification using prompt gamma-ray spectroscopy. *Phys Med Biol*. 2018;63(18):185019.

46. Richter C, Pausch G, Barczyk S, et al. First clinical application of a prompt gamma based in vivo proton range verification system. *Radiother Oncol*. 2016;118(2):232-237.

47. Farace P, Righetto R, Meijers A. Pencil beam proton radiography using a multi-layer ionization chamber. *Phys Med Biol*. 2016;61(11):4078-4087.

48. Johnson RP. Review of medical radiography and tomography with proton beams. *Rep Prog Phys*. 2017;81(1):016701.

49. Parodi K. Latest developments in in-vivo imaging for proton therapy. *Brit J Radiol*. 2020;93(1107):20190787.

50. Wohlfahrt P, Möhler C, Richter C, Greilich S. Evaluation of stopping-power prediction by dual- and single-energy computed tomography in an anthropomorphic ground-truth phantom. *Int J Radiat Oncol Biol Phys*. 2018;100(1):244-253.

SUPPORTING INFORMATION

Additional supporting information may be found in the online version of the article at the publisher's website.

3.4 Publication III

Dual-energy CT-based stopping power prediction for dental materials in particle therapy

Authors: Friderike K. Longarino, Christopher Herpel, Thomas Tessonnier, Stewart Mein, Benjamin Ackermann, Jürgen Debus, Franz Sebastian Schwindling, Wolfram Stiller, Andrea Mairani

Contribution: FL is the first author of this publication. FL, CH, WS, and AM conceptualized the study. FL, CH, TT, WS, and AM developed the methodology. Data was acquired and analyzed by FL, TT, and BA and interpreted by FL, TT, WS, and AM. FL wrote the original draft of the manuscript and prepared all graphics. FL, CH, TT, SM, BA, JD, FS, WS, and AM contributed to the review and editing of the final manuscript. JD, FS, WS, and AM provided supervision.

RADIATION ONCOLOGY PHYSICS

Dual-energy CT-based stopping power prediction for dental materials in particle therapy

Friderike K. Longarino[1,2,3] | Christopher Herpel[4] | Thomas Tessonnier[5,6,7,8] | Stewart Mein[5,6,7,8] | Benjamin Ackermann[5] | Jürgen Debus[1,2,5,7,8,9] | Franz Sebastian Schwindling[4] | Wolfram Stiller[10] | Andrea Mairani[2,5,8,11]

[1]Clinical Cooperation Unit Radiation Oncology, German Cancer Research Center (DKFZ), Heidelberg, Germany

[2]Department of Radiation Oncology, Heidelberg University Hospital, Heidelberg, Germany

[3]Department of Physics and Astronomy, Heidelberg University, Heidelberg, Germany

[4]Department of Prosthodontics, Heidelberg University Hospital, Heidelberg, Germany

[5]Heidelberg Ion Beam Therapy Center (HIT), Heidelberg, Germany

[6]Translational Radiation Oncology, German Cancer Research Center (DKFZ), Heidelberg, Germany

[7]Heidelberg Institute of Radiation Oncology (HIRO), National Center for Radiation Research in Oncology (NCRO), Heidelberg, Germany

[8]National Center for Tumor Diseases (NCT), Heidelberg, Germany

[9]German Cancer Consortium (DKTK), Core Center Heidelberg, Heidelberg, Germany

[10]Diagnostic & Interventional Radiology (DIR), Heidelberg University Hospital, Heidelberg, Germany

[11]Medical Physics, National Center of Oncological Hadrontherapy (CNAO), Pavia, Italy

Correspondence
Wolfram Stiller, Diagnostic & Interventional Radiology (DIR), Heidelberg University Hospital, Im Neuenheimer Feld 420, 69120 Heidelberg, Germany.
Email: wolfram.stiller@med.uni-heidelberg.de

Andrea Mairani, Department of Radiation Oncology, Heidelberg University Hospital, Im Neuenheimer Feld 400, 69120 Heidelberg, Germany.
Email: andrea.mairani@med.uni-heidelberg.de

Abstract

Radiotherapy with protons or light ions can offer accurate and precise treatment delivery. Accurate knowledge of the stopping power ratio (SPR) distribution of the tissues in the patient is crucial for improving dose prediction in patients during planning. However, materials of uncertain stoichiometric composition such as dental implant and restoration materials can substantially impair particle therapy treatment planning due to related SPR prediction uncertainties. This study investigated the impact of using dual-energy computed tomography (DECT) imaging for characterizing and compensating for commonly used dental implant and restoration materials during particle therapy treatment planning. Radiological material parameters of ten common dental materials were determined using two different DECT techniques: sequential acquisition CT (SACT) and dual-layer spectral CT (DLCT). DECT-based direct SPR predictions of dental materials via spectral image data were compared to conventional single-energy CT (SECT)-based SPR predictions obtained via indirect CT-number-to-SPR conversion. DECT techniques were found overall to reduce uncertainty in SPR predictions in dental implant and restoration materials compared to SECT, although DECT methods showed limitations for materials containing elements of a high atomic number. To assess the influence on treatment planning, an anthropomorphic head phantom with a removable tooth containing lithium disilicate as a dental

material was used. The results indicated that both DECT techniques predicted similar ranges for beams unobstructed by dental material in the head phantom. When ion beams passed through the lithium disilicate restoration, DLCT-based SPR predictions using a projection-based method showed better agreement with measured reference SPR values (range deviation: 0.2 mm) compared to SECT-based predictions. DECT-based SPR prediction may improve the management of certain non-tissue dental implant and restoration materials and subsequently increase dose prediction accuracy.

1 | INTRODUCTION

Radiotherapy with protons or light ions can offer accurate and precise treatment delivery to cure tumors.[1] Head and neck tumors are among the indications for particle therapy, since it is able to reduce the volume of irradiated healthy tissues by more than 25% and thus more effectively spare organs-at-risk.[2] However, dental implant and restoration materials, which often exhibit uncertain stoichiometric composition, can be a source of larger uncertainty in the ion beam range.[2,3] For example, if metals are crossed by a proton beam, large differences between planned and delivered ranges with deviations up to several millimeters can occur in the patient, resulting in a dose deposition at an unexpected depth along the beam axis.[4,5] These range uncertainties can result from artifacts of dental implant and restoration materials on computed tomography (CT) treatment planning images for head and neck radiotherapy,[6] which are mainly caused by beam hardening and photon starvation and degrade the quantitative accuracy of CT numbers,[3] as well as from the CT-based estimation of stopping power ratio (SPR).[7] Since the SPR values are conventionally assigned from a heuristic CT-number-to-SPR conversion, which does not cover non-tissue implant materials,[8] errors in the treatment planning system (TPS)-calculated dose distribution can result. These systematic uncertainties may impact patient outcome in terms of local tumor control or normal tissue toxicity.[7]

To address the uncertainties arising from artifacts on CT images and the conventional CT-number-to-SPR conversion, different imaging techniques have been investigated. Over the past decade, dual-energy CT (DECT) systems have become increasingly available in the clinic. DECT generates image data from two x-ray acquisitions using differing energy ranges. It thus increases the available quantitative data and possibilities for material characterization compared to classical single-energy CT (SECT). Several different technical approaches for acquiring DECT image data have emerged with unique features and compromises to be balanced for each application,[9] comprising dual-source CT, sequential acquisition CT (SACT), twin-beam CT, fast kVp-switching CT, and dual-layer spectral CT (DLCT).[8–11] In various studies conducted with tissue surrogates or biological tissues as well as in patient analyses, DECT showed improved SPR prediction for particle therapy compared to SECT.[8,12–18] Besides human tissue, the usage of DECT in particle therapy planning may also be advantageous for non-tissue implant materials.[12,18]

For treating patients with dental implant and restoration materials, different avoidance strategies have been employed so far. For example, non-ideal beam geometries have been applied to avoid beam directions intersecting with a dental material, or treatment volumes have been modified to exclude dental materials. If such avoidance strategies are not feasible in certain cases, particle therapy may even be contraindicated.[19,20] Thus, the restrictions posed on treatment planning by dental materials could compromise treatment plan quality[20] and therapy outcome. Size, shape, material composition, relative electron density (RED), and effective atomic number (EAN) of dental materials are usually not characterized at the time of radiotherapy planning.[5] On the other hand, with an improved physical characterization of common dental materials and understanding of their dosimetric impact, it may become possible to use more conventional treatment planning strategies for accurately contoured dental materials.[19] This procedure may allow the optimizer to compensate for the materials themselves rather than simply avoiding dental materials.[20]

Previous investigations have employed various approaches to manage non-tissue implant materials. Imaging approaches, such as metal artifact reduction (MAR) methods, have been used to reduce CT imaging artifacts; other approaches have been applied to optimize treatment planning procedures, as, for example, when the required avoidance margin is determined in order to assure that the implant does not affect the dose distribution.[6,21–31] Evaluations have mostly been limited to photon therapy, even though some studies addressed dosimetric uncertainties for particle therapy.[6,20,24,29,31]

Recently, Hu et al. investigated common dental materials in terms of relative stopping power and 3D dose perturbation.[20] Thereby, all investigated dental materials substantially perturbed the dosimetry of pristine proton spots with respect to relative stopping power and spatial dose distribution.[20] Monte Carlo simulations and TPS dose calculations demonstrated good agreement with measurements, suggesting potential for proton treatments through dental materials given further investigation.[20] Because dental materials are a common scenario in particle therapy, further research is needed to improve treatment planning for patients with dental materials. In this context, DECT-based SPR prediction might be beneficial, but has not been sufficiently investigated hitherto.

This study examines the impact of using DECT imaging for particle therapy treatment planning in patients with dental materials regarding three aspects. (i) First, radiological material parameters of commonly used dental implant and restoration materials are determined with two different DECT techniques, using image-based (SACT) and projection-based (DLCT) methods. (ii) Second, through comparison of SECT- and DECT-based SPR predictions in phantoms with measured reference data, compensation of dental materials in particle therapy planning and feasibility of ion beam delivery are investigated. (iii) Third, DECT-based particle therapy treatment planning for head and neck cancer patients for one exemplary dental material is evaluated in a head phantom.

2 | MATERIALS AND METHODS

2.1 | Dental materials

Dental implant and restoration materials were selected in consultation with the institutional department of prosthodontics. Commonly used materials for fixed dental prostheses (cobalt-chrome, lithium disilicate, zirconium dioxide), core buildups/fillings (composite I), direct restorations/fillings (composite II), veneers/inlays/partial crowns (glass-ceramic), and dental implants (titanium, zirconium dioxide) were chosen for investigation. All these materials comprised elements of a high atomic number Z: cobalt-chrome ($Z_{Co} = 27$, $Z_{Cr} = 24$), composite I ($Z_{Ba} = 56$), composite II ($Z_{Yb} = 70$), glass-ceramic ($Z_Y = 39$), lithium disilicate ($Z_{Zn} = 30$, $Z_{Zr} = 40$), titanium ($Z_{Ti} = 22$), zirconium dioxide ($Z_{Zr} = 40$). Furthermore, we analyzed the single components of individualized 3D-printed tissue retraction devices (TRDs) used to protect healthy tissue from irradiation in head and neck radiotherapy.[32,33] TRDs consist of a fixation part (made of silicone material) and a tongue retraction part (made of polymethyl methacrylate [PMMA]). Samples were fabricated into cylinders with a diameter of 2.8 cm and a length of 1−2 cm (depending on the fabrication abil-

ities) (Figure 1). Thereby, samples of cobalt-chrome, composites, glass-ceramic, lithium disilicate, and zirconium dioxide were fabricated as an inner core with a diameter of 6−13 mm surrounded by PMMA due to manufacturing capabilities or the thickness of the materials. Additionally, a titanium insert from the Gammex 467 phantom (Gammex Electron Density CT Phantom 467, Gammex-RMI, Middleton, WI, USA) as well as an aluminum insert were used. Even though pure aluminum is not a dental material, it was chosen for investigation since it is a component of aluminum oxide ceramics, which are obsolete now but were previously used for dental restorations. Additionally, a pure metal ($Z_{Al} = 13$) might be of interest for other applications. For simplicity, aluminum is listed as dental material in this study. Details about the investigated materials can be found in Supplementary Table S1.

2.2 | DECT imaging techniques and CT image acquisition and reconstruction

Two different DECT imaging techniques available at the Heidelberg University Hospital were applied: a SACT scanner (SOMATOM Confidence, Siemens Healthcare GmbH, Erlangen, Germany) and a diagnostic DLCT scanner (Spectral CT 7500, Philips Healthcare, Best, The Netherlands).

SACT acquires the entire volume sequentially at two different tube potentials to generate dual-energy data with a single-source CT scanner. Hence, SACT image data can be acquired on any existing CT scanner; however, dedicated dual-energy acquisition modes are required. Due to the two sequential image acquisitions at two different tube potentials, SACT is able to provide very high spectral separation, but has a low temporal coherence (large offset). Material decomposition needs to be image-based.

DLCT uses a single x-ray tube paired with a double-layer detector that simultaneously detects projection-aligned high- and low-energy x-ray data. Each layer of the detector has a maximum sensitivity for different energy spectra. Thus, DLCT implicitly acquires dual-energy data without the need for a special mode, and allows for the pro- and retrospective generation of results with a perfect temporal and spatial alignment over the full field-of-view. However, medium spectral separation is expected to be achieved and cross-scatter between detector layers may occur. Projection-based material decomposition with implicit noise-reduction exploiting anti-correlated noise in both detector layers can be performed with DLCT imaging.

The image acquisition and reconstruction protocols for the two DECT techniques are based on current state-of-the-art clinical head protocols for treatment planning at the Heidelberg Ion Beam Therapy Center (HIT, Germany) (Supplementary Table S2). For SACT systems,
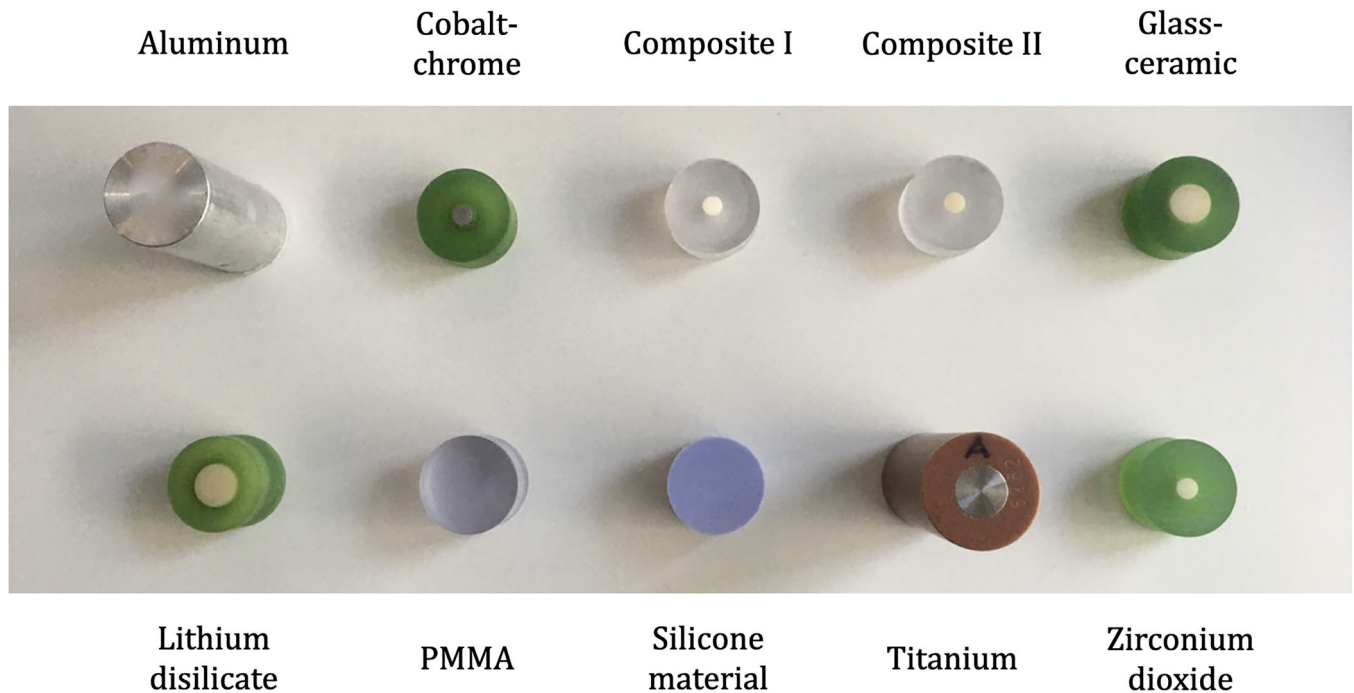
FIGURE 1 Cylindrical samples of investigated dental materials: aluminum, cobalt-chrome, composite I, composite II, glass-ceramic, lithium disilicate, polymethyl methacrylate (PMMA), silicone material, titanium, and zirconium dioxide. Some samples were fabricated as an inner core surrounded by PMMA (in green color or transparent).

dedicated DECT image acquisition and reconstruction protocols are necessary. For DLCT systems, the same protocol as for conventional imaging can be used to simultaneously obtain conventional and spectral image data. Additionally, for each SACT image acquisition, the Siemens iterative metal artifact reduction algorithm (iMAR) (Siemens Healthcare GmbH, Erlangen, Germany), and for each DLCT image acquisition, the Philips orthopedic metal artifact reduction algorithm (O-MAR) (Philips Healthcare, Best, The Netherlands) were applied,[29,34] since these MAR algorithms are directly implemented on the used clinical CT scanners.

2.3 | Investigation of radiological material parameters of dental materials

Image data of dental materials were acquired in a custom one-bore cylindrical phantom of 46.0 cm height and 8.0 cm radius made of PMMA to mimic beam hardening that occurs in a typical situation in the head. To ensure that no signal from one material interfered with the measurement signal from an adjacent material, a distance of 8 cm (detector width of the Spectral CT 7500) or 2 cm (detector width of the SOMATOM Confidence CT) was left between the individual dental materials in the phantom. The radiological material parameters CT number (CTN), RED, and EAN data provided by SACT and DLCT image data were quantified for initial characterization of the dental materials. RED and EAN datasets

were obtained from SACT acquisitions using the module syngo.CT DE Rho/Z in the syngo.via environment (Siemens Healthcare GmbH, Erlangen, Germany) and from DLCT acquisitions using Philips spectral software (Philips Healthcare, Best, The Netherlands). Circular regions-of-interest (ROIs) with a size of ∼70% of the inserts' cross-sectional diameters were placed in axial CT slices of each dental material. By using this method, possible artifacts that may arise due to gradient effects to the surrounding PMMA near the material–phantom boundary were avoided. For similar reasons, CT slices at both ends of the investigated materials were also excluded. The mean and standard deviation of the extracted values over all slices from each dental material were calculated.

Furthermore, the DEEDZ-MD method proposed by Saito[35] was used to calculate the mass density (MD, ρ) from DECT-based RED (ρ_e) and EAN (Z_{eff}) values, with $Z_{eff,w}$ being the EAN of water:

$$\rho = \rho_e + \rho_e \sum_{n=0}^{2} e_n \left\{ \left(\frac{Z_{eff}}{Z_{eff,w}} \right)^m - 1 \right\}^n \quad (1)$$

According to Saito and Sagara,[36] the value of m was set to 3.3, and the same human tissue-specific parameters (e_n) as obtained by Saito[35] were used. The DEEDZ-MD method was first experimentally validated for both DECT techniques using tissue-equivalent inserts (Gammex Electron Density CT Phantom 467,

Gammex-RMI, Middleton, WI, USA) and compared with MD data provided by the vendor (relative mean deviation of −1.2% [SACT] and −1.4% [DLCT]) before being applied to dental materials.

Besides, the severity of artifacts was qualitatively evaluated on a four-point scale[37]: 1, no; 2, mild; 3, moderate; 4, severe artifacts.

2.4 | Measurement and prediction of SPR values for dental materials

2.4.1 | Calculation of predicted SPR values based on quantitative DECT data

For DLCT imaging, RED and EAN data of the spectral results were used to calculate SPR values via the Bethe equation using an in-house program (denoted as DE-RhoZ-DLCT).[18] The mean excitation energy (I-value) was estimated from a piecewise linear fit to EAN using the method proposed by Yang et al.[38] The mean excitation energy of water was set to 78.73 eV, consistent with the values proposed by Bär et al.[39] and the ICRU Report 90.[40] Following the recommendation of Inaniwa and Kanematsu,[41] a fixed particle kinetic energy of 100 MeV per nucleon was assumed, because the energy dependence of SPR prediction in the therapeutic range is minimal.[42]

For SACT imaging, a DirectSPR implementation (Siemens Healthcare GmbH, Erlangen, Germany) in the syngo.via image-reconstruction software was employed (DE-DirectSPR-SACT).[43] In addition, RED and EAN data were obtained from the module syngo.CT DE Rho/Z were used to calculate SPR values via the same procedure as explained for DLCT imaging (referred to as DE-RhoZ-SACT).

Validation of SPR prediction for both DECT techniques (SACT and DLCT) and SPR prediction methods (DE-DirectSPR and DE-RhoZ) was performed using tissue-equivalent inserts (Gammex Electron Density CT Phantom 467, Gammex-RMI, Middleton, WI, USA) in a cylindrical PMMA phantom before applying DECT-based SPR prediction to dental materials. Relative mean deviation compared to measured SPR values was below 0.7% for DE-DirectSPR-SACT, DE-RhoZ-SACT, and DE-RhoZ-DLCT. Figure 2 illustrates the practical implementation of SECT and DECT approaches used in this study.

2.4.2 | Calculation of predicted SPR values based on conventional SECT image data

For the protocols of each of the two DECT techniques, a HLUT converting CTN to SPR values was generated. The clinically applied procedure using tissue-equivalent inserts (Gammex Electron Density CT Phantom 467,

Gammex-RMI, Middleton, WI, USA) was followed. For DLCT, the acquired 120 kV_p SECT image data was used (SE-120-DLCT), whereas for SACT, the HLUT was based on the 140 kV_p SECT image data (SE-140-SACT). The HLUTs were created based on the two-parameter stoichiometric parametrization,[44,45] following the current clinical protocol at HIT.[46]

2.4.3 | Measurement of SPR values

SPR values of all dental materials were determined experimentally at HIT by measuring, from each material of interest, the shift of a Bragg peak in a water absorber (Peakfinder Water Column, PTW-Freiburg, Freiburg, Germany) using carbon ions at 250.1 MeV/u. Carbon ions were used for the SPR measurements due to their sharper Bragg peak, reduced lateral scattering, and less range straggling compared to protons.[17] The measured SPR was calculated as:

$$SPR_{meas} = \frac{P_w - P_m}{d_m} \qquad (2)$$

Here, P_w denotes the mean of the depths in the water absorber corresponding to the fitted dose maximum, dose maximum, 90% distal dose, and 80% distal dose without a dental material sample present. P_m is the mean of the four depths with a dental material sample m intersecting the beam, and d is the thickness of the sample.

2.4.4 | Assessment of DECT- and SECT-based SPR predictions

Relative residuals were calculated to quantify the deviation between measured reference (SPR_{meas}) and SECT- or DECT-predicted SPR values (SPR_{CT}):

$$relative\ residual = \frac{SPR_{CT} - SPR_{meas}}{SPR_{meas}} \cdot 100\% \qquad (3)$$

2.5 | Assessment of treatment planning using DECT-based SPR prediction for ion beams with an anthropomorphic head phantom containing dental materials

To assess particle therapy treatment planning accuracy for patients with dental materials in clinical-like conditions, range prediction and dosimetric impact were evaluated using a tissue-equivalent anthropomorphic head phantom (Proton Therapy Dosimetry Head, Model 731-HN, Computerized Imaging Reference Systems, Inc. (CIRS), Norfolk, VA, USA). The model contains two removable pins that allow segments of molar tooth roots

(a)
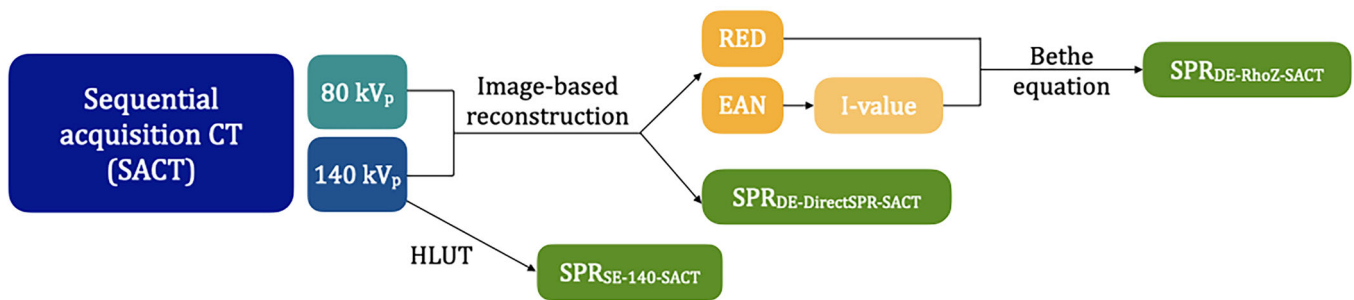
(b)
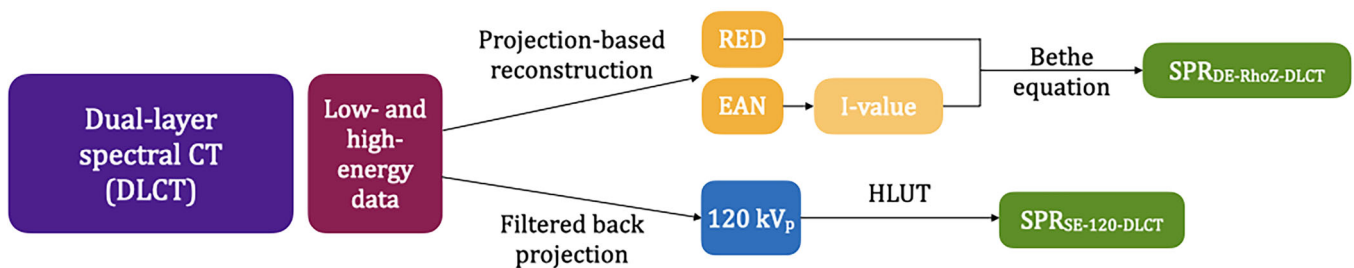
FIGURE 2 Practical implementation of (a) sequential acquisition CT (SACT) and (b) dual-layer spectral CT (DLCT) for single-energy CT (SECT)- and dual-energy CT (DECT)-based stopping power ratio (SPR) prediction using relative electron density (RED), effective atomic number (EAN), and mean excitation energy (I-value), or a Hounsfield look-up table (HLUT). SE-140-SACT, SECT-based SPR prediction with SACT at 140 kV$_p$; DE-DirectSPR-SACT, DECT-based SPR prediction with SACT using a DirectSPR implementation; DE-RhoZ-SACT, DECT-based SPR prediction with SACT using the RhoZ-method; SE-120-DLCT, SECT-based SPR prediction with DLCT at 120 kV$_p$; DE-RhoZ-DLCT, DECT-based SPR prediction with DLCT using the RhoZ-method.

to be exchanged. The segments are made of either tungsten or tissue-equivalent material. For this study, one of the teeth, located beneath different tissue-equivalent layers, was replaced with a dental restoration made of lithium disilicate. Lithium disilicate is a common dental material from Section 2.1 which was selected for further investigation in clinical-like conditions (Figure 3). Two different custom-made types of one of the replaceable teeth were fabricated: (a) spherical dental material with a diameter of 7 mm on a PMMA basis and (b) dental crown with a thickness of 1 mm on a PMMA basis. The head phantom was immobilized with a head cushion and an individualized thermoplastic mask, and the part of the mask surrounding the tooth was cut off.

Helium ions were chosen for the investigation of range and dose differences due to their intermediate physical properties between proton and carbon ion beams.[47] Helium ions have a sharper Bragg peak, less multiple Coulomb scattering, and reduced range straggling in comparison with protons, but a smaller fragmentation tail than carbon ions. Instead of optimizing a treatment plan for a specific target volume, one iso-energy layer

at 92.75 MeV/u was created with the RayStation TPS version 11B (RaySearch Laboratories AB, Stockholm, Sweden) using a pencil beam dose engine with a dose grid of 1 mm and spot spacing of 2 mm.

In all CT datasets, the PMMA basis and volume behind the dental material were manually delineated and overridden with the measured SPR value of PMMA (cf. Section 2.4.3). In an additional SE-140-SACT dataset, the dental material volume was delineated and overridden with the experimentally determined SPR value as well. Because the beam only passes through the experimentally determined overridden materials without passing any additional tissue-equivalent material, this material-specific dataset was then assumed to be the (measured) reference dataset to be compared with other CT datasets. Consequently, range differences that might occur between different CT datasets are only due to the dental restoration itself.

The iso-energy layer was initially calculated on the reference dataset. Following plan optimization, forward dose calculations were performed on five additional (image) datasets using the (A) SE-140-SACT (without material override of the dental material), (B)
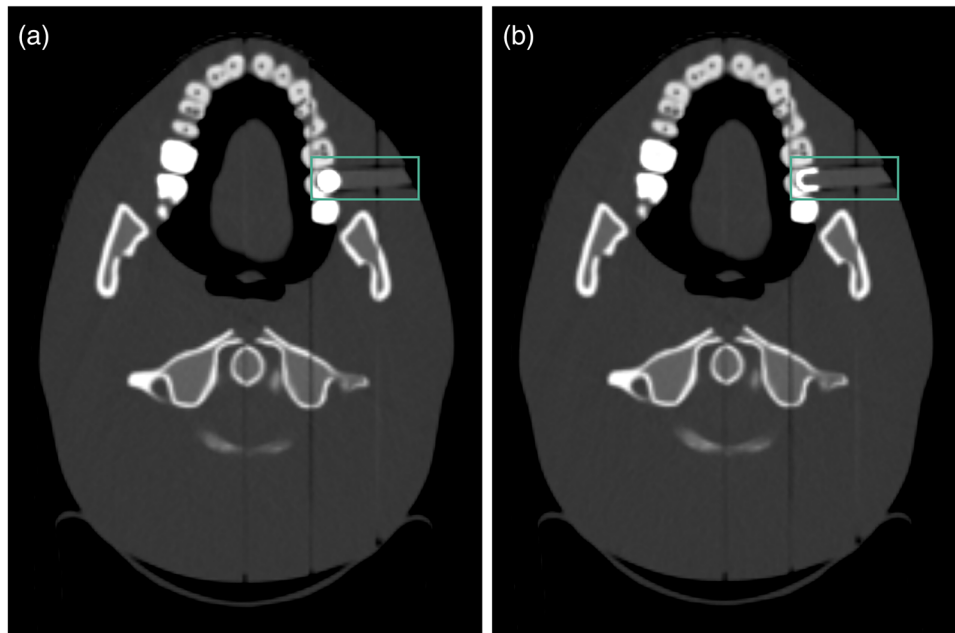
FIGURE 3 CT images of the anthropomorphic head phantom with a removable tooth in two different configurations: (a) spherical dental material and (b) dental crown.

DE-DirectSPR-SACT, (C) DE-RhoZ-SACT, (D) SE-120-DLCT, and (E) DE-RhoZ-DLCT approach.

SPR predictions from all CT datasets of the head phantom were analyzed with ROIs in the dental material (Figure 3a) as well as in the tooth dentin and tooth enamel. The dental material was compared to measured reference values acquired in Section 2.4.3 and the tooth dentin and tooth enamel were compared to measured values of 1.501 ± 0.003 and 1.763 ± 0.003 determined by Wohlfahrt et al.[16] Physical dose distributions calculated with SECT and DECT were then compared in terms of their range prediction to the (measured) reference dataset, respectively. Since range differences in the head phantom were analyzed and quantified in previous studies for beams unobstructed by dental material,[16–18] this study focused on evaluating range differences arising from the dental material. Differences in range prediction between (image) datasets and the reference dataset were analyzed with line-dose profiles in beam direction and quantified by absolute range shifts at the distal range at 80% (R_{80}) of prescribed dose ($\Delta R_{80} = R_{80,\text{Reference}} - R_{80,\text{CT}}$).

3 | RESULTS

3.1 | Determination of radiological material parameters of dental materials

The radiological parameters CTN, RED, EAN, MD, and artifact categories of the dental materials for the two DECT acquisition techniques are presented in Table 1. Dental materials containing an element of a high

atomic number (cobalt-chrome, composites I and II, glass-ceramic, lithium disilicate, titanium, and zirconium dioxide) saturated or nearly saturated CTN using SACT or DLCT and caused streak artifacts. RED, EAN, and MD values of TRD materials were similar for SACT and DLCT (relative deviation was <0.8% for RED, <3.0% for EAN, <1.5% for MD). However, RED, EAN, and thus also MD values differed for dental implant and restoration materials between SACT and DLCT because of their different (image- and projection-based) calculation methods.

3.2 | Measurement and prediction of SPR values for dental materials

Figure 4 presents SPR values of the investigated dental materials together with the respective CT acquisition technique (SACT and DLCT) and calculation method as well as measured SPR values, which are additionally listed in Supplementary Table S3. Comparison of SECT- and DECT-predicted SPR values are given in Table 2. For dental implant and restoration materials, SPR prediction accuracy using DECT techniques was overall closer to measured values than SECT, although DECT methods showed limitations for materials containing elements of a high atomic number. For TRD materials, DECT-based SPR prediction accuracy compared to measured SPR was <0.7% for PMMA and <2.3% for silicone material.

For SACT, the difference in SPR prediction between DE-DirectSPR-SACT and DE-RhoZ-SACT methods was minimal. Since the DE-RhoZ-SACT and DE-Direct

TABLE 1 Measured mean values and standard deviation of CT number (CTN), relative electron density (RED), effective atomic number (EAN), mass density (MD), and artifact category of dental materials for sequential acquisition CT (SACT) and dual-layer spectral CT (DLCT)

| Material	CTN_{SACT} (HU)	CTN_{DLCT} (HU)	RED_{SACT}	RED_{DLCT}	EAN_{SACT}	EAN_{DLCT}	MD_{SACT} (g/cm³)	MD_{DLCT} (g/cm³)	Artifact category
Aluminum	2047 ± 4	2279 ± 8	2.423 ± 0.002	2.331 ± 0.012	12.88 ± 0.05	13.00 ± 0.01	2.578 ± 0.002	2.485 ± 0.005	Mild
Cobalt-chrome	3030 ± 8	>3071	3.980 ± 0.006	4.049 ± 0.001	7.31 ± 0.05	16.00 ± 0.01	4.001 ± 0.005	4.516 ± 0.001	Severe
Composite I	3037 ± 4	>3071	3.898 ± 0.006	2.072 ± 0.088	7.79 ± 0.02	19.71 ± 0.49	3.929 ± 0.010	2.376 ± 0.088	Severe
Composite II	3026 ± 3	>3071	3.967 ± 0.007	4.049 ± 0.001	7.41 ± 0.03	16.00 ± 0.01	3.990 ± 0.006	4.516 ± 0.001	Severe
Glass-ceramic	2648 ± 6	>3071	3.282 ± 0.007	2.342 ± 0.003	10.38 ± 0.02	16.00 ± 0.01	3.382 ± 0.005	2.612 ± 0.003	Mild
Lithium disilicate	3069 ± 1	>3071	3.991 ± 0.022	2.583 ± 0.004	7.78 ± 0.11	17.00 ± 0.01	4.023 ± 0.024	2.919 ± 0.004	Mild
PMMA	127 ± 1	125 ± 2	1.154 ± 0.002	1.152 ± 0.001	6.38 ± 0.06	6.50 ± 0.55	1.155 ± 0.003	1.153 ± 0.001	No
Silicone material	431 ± 1	509 ± 3	1.268 ± 0.006	1.259 ± 0.002	10.68 ± 0.06	11.00 ± 0.01	1.311 ± 0.006	1.307 ± 0.001	No
Titanium	3069 ± 1	>3071	3.976 ± 0.013	4.026 ± 0.014	8.09 ± 0.09	16.00 ± 0.01	4.016 ± 0.013	4.490 ± 0.014	Moderate
Zirconium dioxide	3023 ± 7	>3071	4.000 ± 0.005	4.049 ± 0.001	7.18 ± 0.06	16.00 ± 0.01	4.018 ± 0.005	4.516 ± 0.001	Severe

Note: The CTN for SACT were determined on 140 kV_p image datasets. Since no extended HU scale was used, >3071 HU means that the CTN scale was saturated.

SPR-SACT algorithms rely on two image datasets acquired at 80 kV_p and 140 kV_p, it becomes difficult to achieve reliable quantitative DECT data if CTN of one or both of the 80 kV_p and 140 kV_p acquisitions are nearly or fully saturated (CTN $\geq$ 3071 HU) (cf. Table 1). This might cause the larger variations in SPR prediction compared to measured SPR values for cobalt-chrome, composites I and II, glass-ceramic, lithium disilicate, and titanium. Using the MAR algorithm iMAR showed no considerable difference in DECT-based SPR prediction within dental materials (deviation <0.2%).

For DLCT, DECT-based SPR predictions showed better agreement compared to measured SPR values than SECT-based SPR predictions for all dental materials (excluding composite II). DE-RhoZ-DLCT-predicted SPR for composite II showed a larger deviation than the other dental materials, which could result from a trace of the element ytterbium of a high atomic number. DECT-based SPR prediction accuracy for dental materials was similar with and without the MAR algorithm O-MAR (deviation <0.2%).

3.3 | Assessment of treatment planning using DECT-based SPR prediction for ion beams with an anthropomorphic head phantom containing dental materials

In the first part, range prediction differences for beams unobstructed by dental material were analyzed. As an initial validation, SECT-based predictions from both CT acquisition techniques (SACT and DLCT) were compared and showed similar range predictions with maximum differences <0.2 mm at R_{80} for beams unobstructed by dental material (Figure 5). These minor differences could be due to image registration and slightly different HLUTs of the two CT imaging protocols. Next, DE-DirectSPR-SACT predictions were investigated and confirmed range differences compared to SE-140-SACT-based SPR predictions. Since Wohlfahrt et al.[16] found that DirectSPR methods with a Siemens SACT scanner performed better than SECT-based SPR prediction methods in the CIRS anthropomorphic head phantom using validated ground truth SPR data, we also assumed that DE-DirectSPR-SACT predicts SPR values closer to the ground truth than SECT. The assumption that DE-DirectSPR-SACT outperforms SECT in the head phantom was confirmed by analyzing SPR values in the tooth dentin and tooth enamel (Table 3). Analyzed line-dose profiles revealed that both investigated DE-SACT approaches used in this study (DE-DirectSPR and DE-RhoZ) predicted similar ranges with small differences of <0.4 mm at R_{80}. As a following step, DE-DLCT range predictions were analyzed and found to be similar to DE-SACT for beams unobstructed by dental material with range differences between DE-SACT and DE-DLCT of <0.5 mm. Range differences
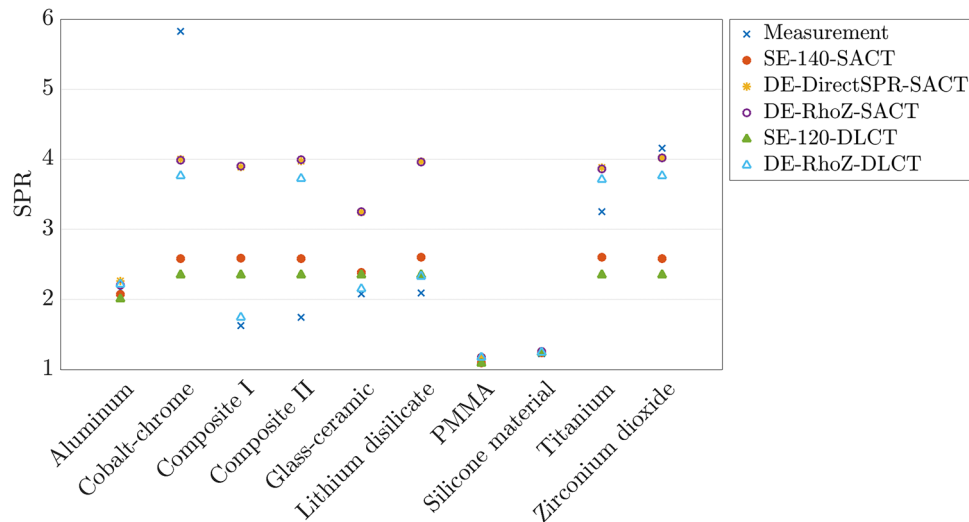
FIGURE 4 Stopping power ratio (SPR) values of the investigated dental materials predicted with sequential acquisition CT (SACT) and dual-layer spectral CT (DLCT). SE-140-SACT, SECT-based SPR prediction with SACT at 140 kV_p; DE-DirectSPR-SACT, DECT-based SPR prediction with SACT using a DirectSPR implementation; DE-RhoZ-SACT, DECT-based SPR prediction with SACT using the RhoZ-method; SE-120-DLCT, SECT-based SPR prediction with DLCT at 120 kV_p; DE-RhoZ-DLCT, DECT-based SPR prediction with DLCT using the RhoZ-method. Note that the markers of DE-DirectSPR-SACT are hidden by overlaying markers of DE-RhoZ-SACT.

might emerge from the two different DECT techniques (image- and projection-based methods), although small differences could also result from the image registration and image resolution. No systematic shift in one direction was observed. Thus, SECT and DECT predictions of the two CT acquisition techniques each showed to predict similar ranges in the head phantom (Figure 5). A previous study showed that DE-RhoZ-DLCT-predicted dose distributions revealed higher 3D gamma passing rates compared to SE-120-DLCT-predicted dose distributions for a helium ion therapy plan using the anthropomorphic head phantom.[18] Based on this, DE-RhoZ-DLCT SPR calculations were considered to be closer to the reference values—in alignment with the results that DE-DirectSPR-SACT outperforms SE-140-SACT.

In the second part, range prediction differences for ion beams passing through the dental material (Figure 3a) were analyzed. The lithium disilicate restoration had a smaller (more patient-realistic) diameter than the sample used in Section 3.2, which resulted in different SPR prediction accuracies (Tables 2 and 3). DE-SACT (DE-DirectSPR-SACT and DE-RhoZ-SACT) overestimated the SPR value of the lithium disilicate restoration (Table 3), which was already seen in Figure 4 and Table 2. This might result from partially saturated CTN in the 80 kV_p image datasets of the dental material. For this specific material, SECT-based SPR prediction was closer to the measured SPR value. Therefore, in its current status, DE-SACT-based SPR prediction for a lithium disilicate restoration may not be accurate enough for dose prediction in particle therapy. However, this also depends on the material, size, and shape of the dental restoration and how much of the dental material is

in the beam direction. The use of a lithium disilicate dental crown with a thickness of 1 mm on a PMMA basis (Figure 3b) resulted in an underestimation of the SPR value with DE-SACT due to beam hardening effects, but may lead to smaller overall range prediction errors due to the smaller diameter of the dental material. Projection-based SPR prediction for the lithium disilicate restoration using DE-RhoZ-DLCT was closer to the measured SPR than SE-120-DLCT (Table 3) and resulted in a remaining range deviation of 0.2 mm (SE-120-DLCT: 1.0 mm) at R_{80} compared to the reference dataset (Figure 5).

4 | DISCUSSION

4.1 | Key findings

In this study, we investigated the use of DECT-based particle therapy treatment planning for patients with dental implant and restoration materials, which is a common scenario in head and neck particle therapy. The reduction of dental material-induced effects is challenging, and is still an active research area because dental materials may negatively impact particle therapy treatment planning. Dental implant or restoration materials are composed of various materials such as cobalt-chrome, composites, glass-ceramic, lithium disilicate, titanium, and zirconium dioxide (Supplementary Table S1). In this study, DECT image acquisitions were performed with two different DECT techniques using SACT and DLCT scanners, each showing strengths and limitations for application in particle therapy. A comparison of different DECT acquisition techniques with a

TABLE 2 Relative residuals of dual-energy CT (DECT)- and single-energy CT (SECT)-predicted stopping power ratio (SPR) values of dental materials from measured SPR values in % using sequential acquisition CT (SACT) and dual-layer spectral CT (DLCT)

Material	SACT—Relative residuals			DLCT—Relative residuals	
	SPR_{SE-140}	$SPR_{DE-DirectSPR}$	$SPR_{DE-RhoZ}$	SPR_{SE-120}	$SPR_{DE-RhoZ}$
Aluminum	−3.08	5.98	2.93	−6.29	3.83
Cobalt-chrome	−55.68	−31.36	−31.56	−59.69	−35.43
Composite I	58.88	138.78	139.56	44.25	7.52
Composite II	47.88	127.68	128.78	34.58	113.38
Glass-ceramic	14.67	55.96	56.38	12.89	3.65
Lithium disilicate	24.39	89.79	89.44	12.24	11.53
PMMA	−6.57	0.49	0.68	−6.93	0.61
Silicone material	1.06	2.03	2.28	1.09	1.35
Titanium	−19.92	19.40	18.94	−27.74	14.17
Zirconium dioxide	−38.05	−3.31	−3.40	−43.58	−9.59

Abbreviations: SE-140-SACT, SECT-based SPR prediction with SACT at 140 kV_p; DE-DirectSPR-SACT, DECT-based SPR prediction with SACT using a DirectSPR implementation; DE-RhoZ-SACT, DECT-based SPR prediction with SACT using the RhoZ-method; SE-120-DLCT, SECT-based SPR prediction with DLCT at 120 kV_p; DE-RhoZ-DLCT, DECT-based SPR prediction with DLCT using the RhoZ-method.

focus on particle therapy treatment planning has been described in previous works[8–10,18] and is summarized in Section 2.2.

This study is the first to comprehensively investigate a full spectrum of common dental materials. Radiological material parameters CTN, RED, EAN, MD, and artifact categories of ten common dental materials currently applied in prosthetic and restorative dentistry and in radiotherapy-related tissue retraction were determined. CTN for most of the materials were larger than 3000 HU and some even saturated the CTN scale, causing mild to severe artifacts (Table 1).

Measured SPR values ranged from 1.169 (PMMA) to 5.823 (cobalt-chrome) (Figure 4 and Supplementary Table S3). For TRD materials, DECT can improve SPR prediction accuracy for particle therapy planning, resulting in remaining discrepancies of <0.7% for PMMA and <2.3% for silicone material (Table 2). In cases where TRDs lie in the beam path, dose delivered in tissue around TRDs can be more accurately predicted by using DECT.

For dental materials, DECT showed overall SPR predictions closer to measured SPR than SECT (Table 2). For cobalt-chrome (metal alloy), titanium (pure metal), and zirconium dioxide, which are materials made of elements of a high atomic number, both DE-SACT- and DE-DLCT-based SPR predictions seemed to reach a plateau at values around 3.9 (DE-SACT) and 3.7 (DE-DLCT) (Supplementary Table S3). These values seemed to be the current upper limit of the investigated DECT reconstruction methods. Furthermore, these elements do not only feature higher atomic numbers, but also high mass and electron densities relative to the natural elemental composition of the human body. The measured values displayed in Figure 4 indicate strong influence of (electron) density for these materials offering a potential explanation for the deviations between

measurements and CT imaging-based SPR prediction. Thus, it remained challenging to accurately predict SPR values of these materials exhibiting high SPR values. Yet, the use of DECT improved SPR prediction for cobalt-chrome, titanium, and zirconium dioxide compared to SECT. The two HLUTs applied have maximum SPR values of 2.602 (SE-140-SACT) and 2.347 (SE-120-DLCT), which led to an SPR underestimation of up to 60% for these dental materials using SECT (Table 2). For materials containing smaller amounts of elements of a high atomic number and/or high densities (composites I and II, glass-ceramic, and lithium disilicate), DE-SACT-based SPR prediction reached an SPR value of about 3.9 in most of the cases, leading to large deviations compared to measured SPR (Supplementary Table S3). This means that materials containing even small amounts of elements of a high atomic number and/or featuring high densities were overexpressed in the DECT reconstructions, except for glass-ceramic, where possibly smaller amounts of a high atomic number element (yttrium) were used. These elements led to high CTN for these materials and thus an overestimation of their SPR values using a HLUT compared to measured SPR. For these same materials, DE-DLCT-based SPR reconstruction seemed to predict SPR more accurately, except for composite II (Table 2 and Supplementary Table S3). The larger SPR deviation in composite II could be due to the element ytterbium of a high atomic number, resulting in an SPR value of about 3.7 as for a metal alloy.

Furthermore, DE-DirectSPR-SACT and DE-RhoZ-SACT methods showed similar SPR predictions (Table 2). Since DE-140-SACT using image-based methods relies on the 80 and 140 kV_p image datasets, it may be difficult to achieve reliable quantitative DECT data if CTN of one or both acquisitions are saturated or nearly saturated. For some materials (i.e., composites,
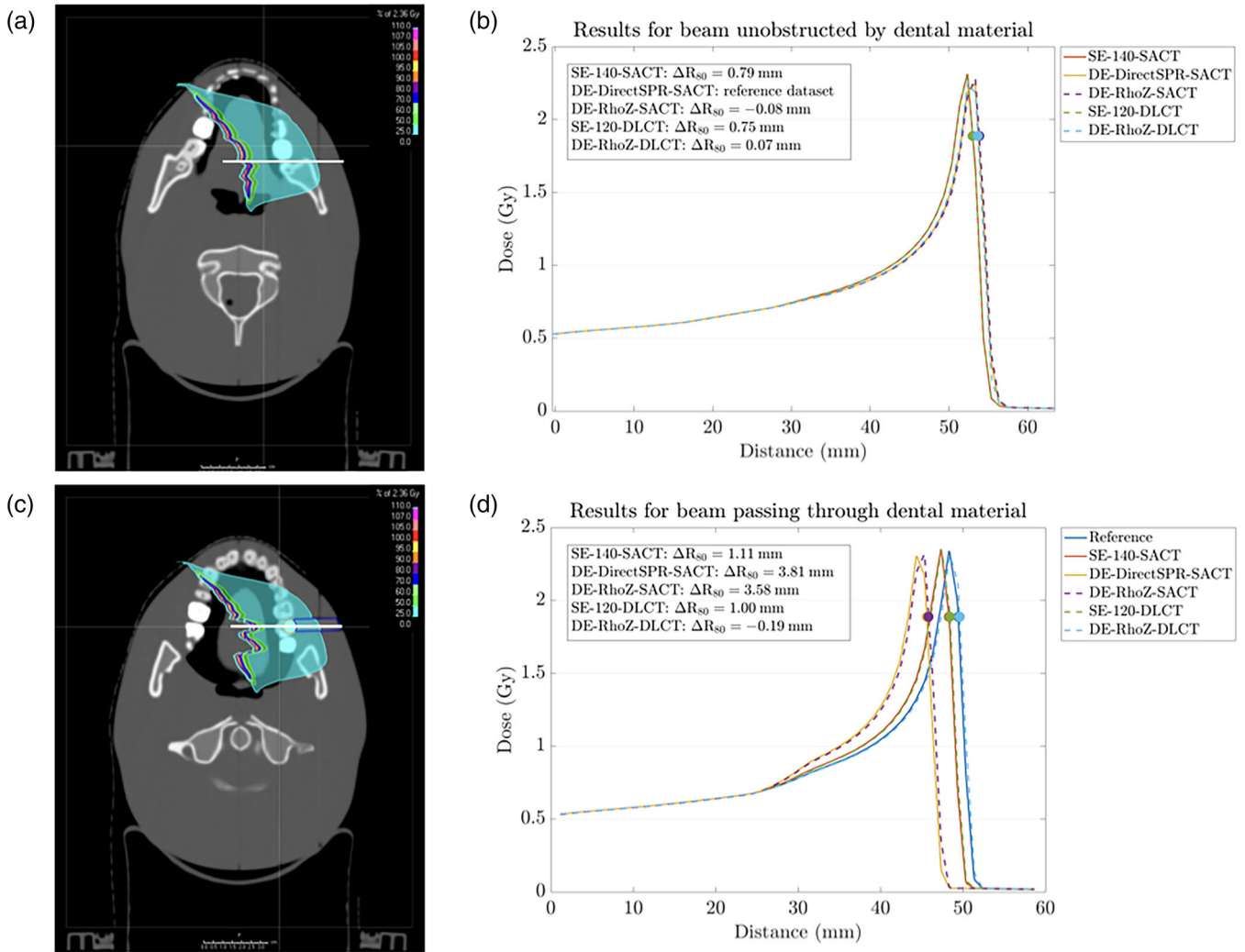
FIGURE 5 For two different axial CT slices, dose distribution for helium ions (a,c) and two representative line-dose profiles calculated on sequential acquisition CT (SACT) and dual-layer spectral CT (DLCT) to quantify deviations in range prediction (b,d) for a beam unobstructed by (a,b) or passing through (c,d) dental material. The placement of the line-dose profiles in (b,d) is illustrated in (a,c). The illustrated depth-dose curves indicate in beam's eye view absolute range (R) differences at R_{80} (marked with circles) between DE-DirectSPR-SACT and the other stopping power ratio (SPR) prediction methods in (b) and between the reference dataset and the different SPR prediction methods in (d). SE-140-SACT, SECT-based SPR prediction with SACT at 140 kV_p; DE-DirectSPR-SACT, DECT-based SPR prediction with SACT using a DirectSPR implementation; DE-RhoZ-SACT, DECT-based SPR prediction with SACT using the RhoZ-method; SE-120-DLCT, SECT-based SPR prediction with DLCT at 120 kV_p; DE-RhoZ-DLCT, DECT-based SPR prediction with DLCT using the RhoZ-method.

TABLE 3 Relative residuals of dual-energy CT (DECT)- and single-energy CT (SECT)-predicted stopping power ratio (SPR) values from measured SPR values in % using sequential acquisition CT (SACT) and dual-layer spectral CT (DLCT) in the anthropomorphic head phantom

Material	SACT—Relative residuals			DLCT—Relative residuals	
	SPR_{SE-140}	$SPR_{DE-DirectSPR}$	$SPR_{DE-RhoZ}$	SPR_{SE-120}	$SPR_{DE-RhoZ}$
Tooth dentin	1.53	−0.25	−0.33	1.53	−0.29
Tooth enamel	10.94	−0.58	−0.57	10.89	−0.97
Lithium disilicate restoration	10.91	35.04	34.27	8.42	0.22

Note: SPR values were determined in regions-of-interest (ROIs) in the tooth dentin, tooth enamel, and lithium disilicate restoration.
Abbreviations: SE-140-SACT, SECT-based SPR prediction with SACT at 140 kV_p; DE-DirectSPR-SACT, DECT-based SPR prediction with SACT using a DirectSPR implementation; DE-RhoZ-SACT, DECT-based SPR prediction with SACT using the RhoZ-method; SE-120-DLCT, SECT-based SPR prediction with DLCT at 120 kV_p; DE-RhoZ-DLCT, DECT-based SPR prediction with DLCT using the RhoZ-method.

glass-ceramic, lithium disilicate), SPR prediction accuracy might seem better with SECT compared to DECT. This is mainly tied to the fact that the HLUT used in our institution and in this study has a maximum SPR value of 2.602 when using SE-140-SACT, which may be incidentally closer to the measured value. However, other institutions might use a HLUT with a maximum SPR value of approximately 4, which might then cause a larger overestimation of SPR values for dental materials saturating the CTN scale from the measured values. Moreover, we found that the insert diameter had an impact on SPR prediction accuracy. For example, cobalt-chrome, composites, lithium disilicate, and zirconium dioxide didn't saturate the CTN scale anymore, when smaller insert diameters were fabricated and used. Thus, even smaller (more patient-realistic) sizes of dental materials may result in better DECT-based SPR predictions. DE-RhoZ-DLCT-based SPR prediction with a mean deviation of 9.7% (range: [−35.43, 14.17]%) was consistently closer to measured SPR values compared to SE-120-DLCT showing a mean deviation of 23.9% (range: [−59.69, 44.25]%) (Table 2, excluding composite II). In contrast to human tissue, however, for dental materials containing elements of a high atomic number (e.g., ytterbium or zirconium), accurate SPR predictions remain still challenging with current DECT techniques. In particular, the accuracy of RED and EAN maps can reach its limit for specific materials consisting of elements of a high atomic number. Previous works reported that already a small trace of an element of a high atomic number causes a substantial positive bias in RED using DECT.[48] As an example, a small amount of iodine in the thyroid was found to cause a positive bias in RED of about 1.1% for DE-SACT and 0.3% for DE-DLCT, which is most likely due to the larger influence of the photoelectric effect.[48] An increasing amount of a high atomic number element also increases the bias in RED, although DE-DLCT seems to be less affected than DE-SACT, which was confirmed by our data (Table 2). Therefore, an SPR overestimation as observed for almost all dental materials containing elements of a high atomic number (Table 2) is an inherent property of the investigated DECT-based SPR prediction methods as reported in previous studies.[16,48] Since the DE-RhoZ and DE-DirectSPR algorithms are implemented for the usual CTN range from −1024 HU to +3071 HU, an extended CTN scale doesn't provide additional information to improve SPR prediction. However, using an extended CTN scale may reveal more information about the dental material, including components and actual dimensions, that may be used to override the material with the proper SPR value. While current implementation does not seem to improve SPR prediction within dental materials, the use of MAR algorithms or virtual monoenergetic images may also reduce metal artifacts and improve structure delineation.[3,30] Altogether, DE-SACT- and DE-DLCT-based SPR prediction provide

improved SPR prediction accuracy compared to SECT for dental materials, especially for certain materials, for example, zirconium dioxide, and may improve treatment planning.

DECT-based particle therapy treatment planning for head and neck cancer patients was evaluated for one exemplary dental material in an anthropomorphic head phantom. In the tooth surrogates (tooth dentin and tooth enamel) of the head phantom where no dental implant or restoration material is present, DECT-based SPR predictions outperformed SECT (Table 3). SECT overestimated the SPR values of tooth dentin and tooth enamel compared to measured SPR values, whereas DECT slightly underestimated SPR values with deviations <1%. Since an SPR accuracy within 1% can be realistically reached using DECT in idealized situations,[11] the DECT-predicted SPR accuracy of the tooth surrogates was within the expected uncertainty. Moreover, the relative residuals of DECT-predicted SPR values were in the same order of magnitude as the uncertainty of the measured SPR values of the tooth surrogates (0.2%).[16] SECT-predicted SPR values may have overestimated measured SPR values because the CTN of the tooth surrogates are relatively high due to their elemental compositions, which convert to higher SPR values using a HLUT than expected from the measurements.

Assessment of treatment planning for helium ion beams with the anthropomorphic head phantom containing dental materials revealed that SECT- and DECT-based range predictions using SACT and DLCT were similar in the head phantom for beams unobstructed by dental material, respectively (Figure 5). Drawing on previous results from the same anthropomorphic head phantom using a validated ground truth SPR map,[16] we assumed that DECT-based SPR prediction is closer to the ground truth than SECT. However, an uncertainty of 1 mm has to be assumed due to the voxel size and from the manual delineation of the dental restoration. For the dental material, SECT- and DECT-based SPR predictions were compared to a reference dataset, which is based on the measured SPR value of lithium disilicate and therefore as accurate as the SPR measurement itself. When ion beams passed through the dental material, DE-SACT overestimated the SPR value of the lithium disilicate restoration with a relative deviation of about 35% compared to measured SPR (Table 3). Thus, current DE-DirectSPR-SACT SPR predictions may not be accurate enough for the specific material lithium disilicate at the moment. DE-RhoZ-DLCT with a relative deviation of 0.2% was closer to measured SPR than SE-120-DLCT (Table 3). Using projection-based DE-DLCT for patients with a lithium disilicate restoration showed better agreement with measured SPR than SECT (Figure 5) and may be used for future particle therapy treatment planning strategies.

In general, this study showed that, in its current state, image-based spectral reconstruction as used with SACT

may be limited in making quantitative statements for certain non-tissue dental materials, especially if the materials contain elements of a high atomic number, for example, composite II with ytterbium as investigated in Section 3.2. Projection-based spectral reconstruction may provide superior SPR prediction for some materials. However, the extent of improvement in dental management is largely dependent on the components, size, and shape of the material and therefore must be evaluated on a case-by-case basis to determine whether DECT-based SPR prediction is currently accurate enough for particle therapy treatment planning. The department of prosthodontics could preferentially use dental implant and restoration materials that are more suitable for DECT-based SPR prediction, if this is possible for the patient.

4.2 | Comparison to previous work

This study found that both subjective image quality and SPR prediction accuracy decreased for dental materials with higher densities (cobalt-chrome, composites, and zirconium dioxide). This is in line with previous works reporting that highly attenuating materials such as zirconium ($\rho \approx 6.5$ g/cm^3) or cobalt-chrome ($\rho \approx 8.5$ g/cm^3) cause more severe artifacts on CT image datasets, resulting in larger artifact index and lower image criteria scores compared to the artifacts caused by titanium ($\rho \approx 4.5$ g/cm^3).[49,50]

A previous study investigated a base metal, amalgam, lithium disilicate, and zirconia and observed substantial changes in proton range with respect to water for these materials.[20] The present study confirmed that ion beam range was affected by the lithium disilicate restoration in the head phantom and that current SECT-based SPR predictions don't provide sufficiently accurate range predictions in treatment planning (Table 3 and Figure 5). Compensating for the lithium disilicate restoration may be instead possible with projection-based DE-DLCT methods. For beams unobstructed by dental material in the anthropomorphic head phantom, the DE-RhoZ-SACT-determined SPR values for the tooth dentin of 1.496 ± 0.019 and tooth enamel of 1.753 ± 0.020 were comparable to the SPR results of 1.496 ± 0.011 and 1.869 ± 0.018 from a previous study,[16] although the SPR value for the dental enamel from this study was closer to the measured value.

4.3 | Clinical relevance

This study focused on the radiological and dosimetric effects of dental materials that are common in an aging population receiving radiotherapy. Despite sophisticated imaging technology, dental material-related effects on treatment planning remain a challenge in daily prac-

tice. In a previous study, a high incidence of over 70% of dental material artifacts was found on the planning CT image datasets of oral/oropharyngeal cancer patients.[51] The finite range of ion beams makes them more sensitive to planning uncertainties than photon beams; therefore, it is especially important to improve dental management for particle therapy.[5]

To our knowledge, this is the first study that comprehensively investigated and characterized common state-of-the-art dental implant and restoration materials using two different DECT techniques. To this end, radiological material parameters were determined and SPR values measured and compared between SECT and DECT techniques. For the investigated dental materials, measured SPR values can be assigned in treatment planning for patients with known, accurately contoured dental materials to account for uncertainties in SPR values. Moreover, robust optimization, using several CT image datasets (e.g., SECT, DECT, MAR, materials override…) of the patient and/or additional range uncertainty optimization parameters, may be applied to consider dental materials. In silico study using an anthropomorphic head phantom revealed that DE-DLCT-based SPR prediction for patients with lithium disilicate restorations may enable treatment planning despite the dental material. Thus, uncertainties in SPR prediction may be limitable and manageable using DECT.

4.4 | Study limitations and future work

This study investigated a representative selection of common dental materials. However, no amalgam samples were investigated, because the institutional department of prosthodontics no longer uses amalgam as a filling material, but elderly patients may still harbor amalgam. Moreover, no gold alloy was considered due to cost reasons. Finally, this study investigated two different DECT techniques (SACT and DLCT); however, other DECT techniques (e.g., dual-source CT, twin-beam CT, or fast kVp-switching CT) may change SPR prediction results. Using different dual-energy tube voltage combinations (e.g., 100 and 140 kV$_p$), for example, for SACT and dual-source CT may also influence results, but was not possible to employ with our CT scanner settings.

High-energy data acquired with photon-counting detector CT systems has been shown to reduce metal artifacts in reconstructions owing to reduced beam hardening.[52] With further development, photon-counting CT may offer the potential for improved SPR prediction and dose calculation for patients with dental materials.

In the future, dental implant and restoration materials which are often composed of various components could be manufactured with a lower amount of radiopaque material, which could be explored by vendors. Nevertheless, it will still be necessary to distinguish non-tissue dental materials from natural teeth in planar x-ray

imaging and CT image acquisitions. The discovery of new materials or compositions without elements of a high atomic number for usage in dentistry might reduce SPR prediction uncertainty in the future. Interdisciplinary collaborations are needed for the management of non-tissue dental materials. Institutional departments of prosthodontics might select dental implant and restoration materials that are more suitable for SPR prediction with SECT and DECT—depending on the available and used CT technology in a radiation therapy department.

Finally, other non-tissue implant materials in the body (e.g., spinal stabilization implants, hip prostheses, or silicone breast implants[53]) may also benefit from using DECT-based SPR prediction. For example, by using DECT, the SPR overestimation for PALACOS® R + G bone cement (Heraeus, Hanau, Germany) was reduced from 50% to less than 10%.[18] Future work might investigate other non-tissue implant materials in the human body using DECT imaging for particle therapy treatment planning.

5 | CONCLUSIONS

This study investigated DECT-based imaging for particle therapy treatment planning for patients with dental implant and restoration materials by using sequential acquisition and DLCT techniques. Radiological material parameters of ten common dental implant and restoration materials were determined. Overall, DECT-based SPR predictions of cylindrical inserts in a geometric phantom showed better agreement with measured reference data compared to SECT-based SPR predictions. DECT-based helium ion therapy treatment planning in an anthropomorphic head phantom with dental material indicated that DE-SACT and DE-DLCT predicted similar ranges for beams unobstructed by dental material. When ion beams passed through the lithium disilicate restoration, DE-DLCT-based SPR prediction using a projection-based method was closest to measured reference data resulting in a remaining range deviation of 0.2 mm. In sum, DECT-based SPR prediction may improve the management of non-tissue dental implant and restoration materials and subsequently compensate for them during particle therapy treatment planning. Further studies and interdisciplinary collaborations with departments of prosthodontics may assess other dental materials and techniques to further reduce SPR prediction uncertainty in dental materials. Prosthodontists stand to gain from such collaboration, for without it, particle therapy may require them to perform dental extractions for cancer patients with obstructive dental material,[5] which will have to be removed and then replaced with an alternative. Ongoing collaboration, however, would help to identify optimal materials for both prosthodontics and radio-oncology, thus incentivizing future research together to improve patient outcomes.

REFERENCES

1. Baumann M, Krause M, Overgaard J, et al. Radiation oncology in the era of precision medicine. *Nat Rev Cancer*. 2016;16(4):234-249. doi:10.1038/nrc.2016.18
2. Beddok A, Vela A, Calugaru V, et al. Proton therapy for head and neck squamous cell carcinomas: a review of the physical and clinical challenges. *Radiother Oncol*. 2020;147:30-39. doi:10.1016/j.radonc.2020.03.006
3. Rousselle A, Amelot A, Thariat J, et al. Metallic implants and CT artefacts in the CTV area: where are we in 2020? *Cancer Radiother*. 2020;24(6-7):658-666. doi:10.1016/j.canrad.2020.06.022
4. Verburg JM, Seco J. Dosimetric accuracy of proton therapy for chordoma patients with titanium implants. *Med Phys*. 2013;40(7):071727. doi:10.1118/1.4810942
5. Falek S, Regmi R, Herault J, et al. Dental management in head and neck cancers: from intensity-modulated radiotherapy with photons to proton therapy. *Support Care Cancer*. 2022;30:8377-8389. doi:10.1007/s00520-022-07076-5
6. Jäkel O, Reiss P. The influence of metal artefacts on the range of ion beams. *Phys Med Biol*. 2007;52(3):635-644. doi:10.1088/0031-9155/52/3/007
7. Paganetti H. Range uncertainties in proton therapy and the role of Monte Carlo simulations. *Phys Med Biol*. 2012;57(11):R99-117. doi:10.1088/0031-9155/57/11/R99
8. Wohlfahrt P, Richter C. Status and innovations in pretreatment CT imaging for proton therapy. *Br J Radiol*. 2020;93(1107):20190590. doi:10.1259/bjr.20190590
9. McCollough CH, Boedeker K, Cody D, et al. Principles and applications of multienergy CT: report of AAPM Task Group 291. *Med Phys*. 2020;47(7):e881-e912. doi:10.1002/mp.14157
10. Kruis MF. Improving radiation physics, tumor visualisation, and treatment quantification in radiotherapy with spectral or dual-energy CT. *J Appl Clin Med Phys*. 2022;23(1):e13468. doi:10.1002/acm2.13468

11. Yang M, Wohlfahrt P, Shen C, Bouchard H. Dual- and multi-energy CT for particle stopping-power estimation: current state, challenges and potential. *Phys Med Biol*. 2023;68(4):04TR01. doi:10.1088/1361-6560/acabfa

12. Hünemohr N, Krauss B, Tremmel C, Ackermann B, Jäkel O, Greilich S. Experimental verification of ion stopping power prediction from dual energy CT data in tissue surrogates. *Phys Med Biol*. 2014;59:83-96. doi:10.1088/0031-9155/59/1/83

13. Bär E, Lalonde A, Royle G, Lu HM, Bouchard H. The potential of dual-energy CT to reduce proton beam range uncertainties. *Med Phys*. 2017;44(6):2332-2344. doi:10.1002/mp.12215

14. Taasti VT, Michalak GJ, Hansen DC, et al. Validation of proton stopping power ratio estimation based on dual energy CT using fresh tissue samples. *Phys Med Biol*. 2017;63(1):015012. doi:10.1088/1361-6560/aa952f

15. Möhler C, Russ T, Wohlfahrt P, et al. Experimental verification of stopping-power prediction from single- and dual-energy computed tomography in biological tissues. *Phys Med Biol*. 2018;63(2):025001. doi:10.1088/1361-6560/aaa1c9

16. Wohlfahrt P, Möhler C, Richter C, Greilich S. Evaluation of stopping-power prediction by dual- and single-energy computed tomography in an anthropomorphic ground-truth phantom. *Int J Radiat Oncol Biol Phys*. 2018;100(1):244-253. doi:10.1016/j.ijrobp.2017.09.025

17. Faller FK, Mein S, Ackermann B, Debus J, Stiller W, Mairani A. Preclinical evaluation of dual-layer spectral computed tomography-based stopping power prediction for particle therapy planning at the Heidelberg Ion Beam Therapy Center. *Phys Med Biol*. 2020;65(9):095007. doi:10.1088/1361-6560/ab735e

18. Longarino FK, Kowalewski A, Tessonnier T, et al. Potential of a second-generation dual-layer spectral ct for dose calculation in particle therapy treatment planning. *Front Oncol*. 2022;12:853495. doi:10.3389/fonc.2022.853495

19. Oancea C, Luu A, Ambrožová I, Mytsin G, Vondráček V, Davídková M. Perturbations of radiation field caused by titanium dental implants in pencil proton beam therapy. *Phys Med Biol*. 2018;63(21):215020. doi:10.1088/1361-6560/aae656

20. Hu Y-H, Wan Chan Tseung HS, Mundy DW. Physical characterization of therapeutic proton delivery through common dental materials. *Med Phys*. 2022;49(5):2904-2913. doi:10.1002/mp.15602

21. Bamberg F, Dierks A, Nikolaou K, Reiser MF, Becker CR, Johnson TR. Metal artifact reduction by dual energy computed tomography using monoenergetic extrapolation. *Eur Radiol*. 2011;21(7):1424-1429. doi:10.1007/s00330-011-2062-1

22. Verburg JM, Seco J. CT metal artifact reduction method correcting for beam hardening and missing projections. *Phys Med Biol*. 2012;57(9):2803-2818. doi:10.1088/0031-9155/57/9/2803

23. Lin MH, Li J, Price RA Jr, Wang L, Lee CC, Ma CM. The dosimetric impact of dental implants on head-and-neck volumetric modulated arc therapy. *Phys Med Biol*. 2013;58(4):1027-1040. doi:10.1088/0031-9155/58/4/1027

24. Ager B, Mohamed A, Palmer MB, et al. Hounsfield unit correction for dental implant materials in intensity modulated proton therapy of head and neck cancer: a quality assurance benchmark study. *Int J Radiat Oncol Biol Phys*. 2014;90(1):S925-S926. doi:10.1016/j.ijrobp.2014.05.2620

25. Axente M, Paidi A, Von Eyben R, et al. Clinical evaluation of the iterative metal artifact reduction algorithm for CT simulation in radiotherapy. *Med Phys*. 2015;42(3):1170-1183. doi:10.1118/1.4906245

26. Huang JY, Followill DS, Howell RM, et al. Approaches to reducing photon dose calculation errors near metal implants. *Med Phys*. 2016;43(9):5117. doi:10.1118/1.4960632

27. Giantsoudi D, De Man B, Verburg J, et al. Metal artifacts in computed tomography for radiation therapy planning: dosimetric effects and impact of metal artifact reduction. *Phys Med Biol*. 2017;62(8):R49-R80. doi:10.1088/1361-6560/aa5293

28. Katsura M, Sato J, Akahane M, Kunimatsu A, Abe O. Current and novel techniques for metal artifact reduction at CT: practical guide for radiologists. *Radiographics*. 2018;38(2):450-461. doi:10.1148/rg.2018170102

29. Andersson KM, Dahlgren CV, Reizenstein J, Cao Y, Ahnesjö A, Thunberg P. Evaluation of two commercial CT metal artifact reduction algorithms for use in proton radiotherapy treatment planning in the head and neck area. *Med Phys*. 2018;45(10):4329-4344. doi:10.1002/mp.13115

30. Pettersson E, Bäck A, Björk-Eriksson T, Lindencrona U, Petruson K, Thilander-Klang A. Structure delineation in the presence of metal - A comparative phantom study using single and dual-energy computed tomography with and without metal artefact reduction. *Phys Imaging Radiat Oncol*. 2019;9:43-49. doi:10.1016/j.phro.2019.01.001

31. Fellin F, Artoni M, Righetto R, et al. An avoidance method to minimize dose perturbation effects in proton pencil beam scanning treatment of patients with small high-Z implants. *Phys Med Biol*. 2020;65(14):14NT01. doi:10.1088/1361-6560/ab9775

32. Herpel C, Schwindling FS, Held T, et al. Individualized 3D-printed tissue retraction devices for head and neck radiotherapy. *Front Oncol*. 2021;11:628743. doi:10.3389/fonc.2021.628743

33. Held T, Herpel C, Schwindling FS, et al. 3D-printed individualized tooth-borne tissue retraction devices compared to conventional dental splints for head and neck cancer radiotherapy: a randomized controlled trial. *Radiat Oncol*. 2021;16:75. doi:10.1186/s13014-021-01803-8

34. Puvanasuntharajah S, Fontanarosa D, Wille ML, Camps SM. The application of metal artifact reduction methods on computed tomography scans for radiotherapy applications: a literature review. *J Appl Clin Med Phys*. 2021;22(6):198-223. doi:10.1002/acm2.13255

35. Saito M. Quadratic relation for mass density calibration in human body using dual-energy CT data. *Med Phys*. 2021;48(6):3065-3073. doi:10.1002/mp.14899

36. Saito M, Sagara S. Simplified derivation of stopping power ratio in the human body from dual-energy CT data. *Med Phys*. 2017;44(8):4179-4187. doi:10.1002/mp.12386

37. Nagayama Y, Tanoue S, Oda S, et al. Metal artifact reduction in head CT performed for patients with deep brain stimulation devices: effectiveness of a single-energy metal artifact reduction algorithm. *AJNR Am J Neuroradiol*. 2020;41(2):231-237. doi:10.3174/ajnr.A6375

38. Yang M, Virshup G, Clayton J, Zhu XR, Mohan R, Dong L. Theoretical variance analysis of single- and dual-energy computed tomography methods for calculating proton stopping power ratios of biological tissues. *Phys Med Biol*. 2010;55(5):1343-1362. doi:10.1088/0031-9155/55/5/006

39. Bär E, Andreo P, Lalonde A, Royle G, Bouchard H. Optimized I-values for use with the Bragg additivity rule and their impact on proton stopping power and range uncertainty. *Phys Med Biol*. 2018;63(16):165007. doi:10.1088/1361-6560/aad312

40. International Commission on Radiation Units and Measurements (ICRU). Report 90: key data for ionizing-radiation dosimetry: measurement standards and applications. *J Int Comm Radiat Units Meas*. 2014;14(1):1-110. doi:10.1093/jicru/ndw038

41. Inaniwa T, Kanematsu N. Effective particle energies for stopping power calculation in radiotherapy treatment planning with protons and helium, carbon, and oxygen ions. *Phys Med Biol*. 2016;61(20):N542-N550. doi:10.1088/0031-9155/61/20/N542

42. International Commission on Radiation Units and Measurements (ICRU). Report 93: prescribing, recording, and reporting light ion beam therapy. *J Int Comm Radiat Units Meas*. 2016;16(2):1-211. doi:10.1093/jicru/ndy024

43. Peters N, Wohlfahrt P, Hofmann C, et al. Reduction of clinical safety margins in proton therapy enabled by the clinical implementation of dual-energy CT for direct stopping-power prediction.

Radiother Oncol. 2022;166:71-78. doi:10.1016/j.radonc.2021.11.002

44. Schneider U, Pedroni E, Lomax A. The calibration of CT Hounsfield units for radiotherapy treatment planning. *Phys Med Biol*. 1996;41(1):111-124. doi:10.1088/0031-9155/41/1/009

45. Schneider W, Bortfeld T, Schlegel W. Correlation between CT numbers and tissue parameters needed for Monte Carlo simulations of clinical dose distributions. *Phys Med Biol*. 2000;45(2):459-478. doi:10.1088/0031-9155/45/2/314

46. Telsemeyer J, Ackermann B, Ecker S, Jäkel O, Martišíková M. Experimental verification of ion range calculation in a treatment planning system using a flat-panel detector. *Phys Med Biol*. 2014;59(14):3737-3747. doi:10.1088/0031-9155/59/14/3737

47. Mairani A, Mein S, Blakely E, et al. Roadmap: helium ion therapy. *Phys Med Biol*. 2022;67(15):15TR02. doi:10.1088/1361-6560/ac65d3

48. Möhler C, Wohlfahrt P, Richter C, Greilich S. Methodological accuracy of image-based electron density assessment using dual-energy computed tomography. *Med Phys*. 2017;44(6):2429-2437. doi:10.1002/mp.12265

49. Chindasombatjaroen J, Kakimoto N, Murakami S, Madea Y, Furukawa S. Quantitative analysis of metallic artifacts caused by dental metals: comparison of cone-beam and multi-detector row CT scanners. *Oral Radiol*. 2011;27:114-120. doi:10.1007/s11282-011-0071-z

50. De Crop A, Casselman J, Van Hoof T, et al. Analysis of metal artifact reduction tools for dental hardware in CT scans of the oral cavity: kVp, iterative reconstruction, dual-energy CT, metal artifact reduction software: does it make a difference? *Neuroradiology*. 2015;57(8):841-849. doi:10.1007/s00234-015-1537-1

51. Richard P, Sandison G, Dang Q, Johnson B, Wong T, Parvathaneni U. Dental amalgam artifact: adverse impact on tumor visualization and proton beam treatment planning in oral and oropharyngeal cancers. *Pract Radiat Oncol*. 2015;5(6):e583-588. doi:10.1016/j.prro.2015.04.007

52. Richtsmeier D, O'Connell J, Rodesch PA, Iniewski K, Bazalova-Carter M. Metal artifact correction in photon-counting detector computed tomography: metal trace replacement using high-energy data. *Med Phys*. 2023;50(1):380-396. doi:10.1002/mp.16049

53. Chacko MS, Grewal HS, Wu D, Sonnad JR. Accuracy of proton stopping power estimation of silicone breast implants with single and dual-energy CT calibration techniques. *J Appl Clin Med Phys*. 2021;22(9):159-170. doi:10.1002/acm2.13358

SUPPORTING INFORMATION

Additional supporting information can be found online in the Supporting Information section at the end of this article.

How to cite this article: Longarino FK, Herpel C, Tessonnier T, et al. Dual-energy CT-based stopping power prediction for dental materials in particle therapy. *J Appl Clin Med Phys*. 2023;24:e13977.
https://doi.org/10.1002/acm2.13977

4
Discussion

4.1 Research focus

Range prediction is essential for accurate treatment planning in particle therapy and it is standardly based on SECT imaging. Yet SECT-based CTN-to-SPR conversion is one of the major sources of range uncertainty. Therefore, this thesis has aimed to improve SPR prediction by using DECT imaging. The potential of DLCT for SPR prediction was investigated under various experimental and clinical conditions and compared with the conventional SECT imaging method. To facilitate clinical applicability and to improve accuracy, the methodology established in this thesis for DLCT-based SPR prediction is patient-specific and direct and therefore does not require the heuristic and indirect SECT-based CTN-to-SPR conversion. This work has demonstrated that the use of DLCT can improve SPR prediction for accurate particle therapy treatment planning. Consequently, in comparison to the current clinical SECT method, DLCT-based range prediction results in a closer agreement between planned and delivered dose.

4.2 Overview and interpretation of key findings

4.2.1 Experimental evaluation of dual-energy CT versus single-energy CT for SPR and range prediction

In publication I, the accuracy of DLCT-based SPR prediction was experimentally evaluated and its impact on dose calculation in treatment planning for particle therapy was assessed by using tissue surrogates, anthropomorphic and geometrically complex head and pelvic phantoms, and non-tissue materials. For this purpose, a comprehensive workflow for DLCT-based SPR prediction and particle therapy treatment planning was established (Figure 3.2).

For homogeneous tissue-equivalent material inserts in cylindrical phantoms, predicted SPR values from DLCT-based maps of RED and EAN were within a mean accuracy of 0.7% in comparison with experimentally determined SPR and demonstrated considerably better agreement with measured data than SECT-based CTN-to-SPR conversion with a mean residual of 1.6% (Figure 3 and Tables 1, 2 in publication (publ.) I). In this investigation, cylindrical phantoms made of polymethyl methacrylate (PMMA) were used with radii ranging from 5 cm to 16 cm, which span the range that is clinically relevant for treatment sites including the head, neck, abdomen, and pelvis. In a PMMA phantom, the tube current-time product was found to be

reduced by 100 mAs, with no adverse effect on SPR prediction accuracy for tissue-equivalent material inserts. Such a reduction is relevant for minimizing CT dose, which is particularly important in areas with large pediatric contingents, such as particle therapy.

Experimentally, in heterogeneous anthropomorphic head and pelvic phantoms, DLCT showed improvements in SPR and range prediction compared to SECT. Range verification measurements in anthropomorphic phantoms were performed with protons, helium, and carbon ions. The analysis revealed that the dose distributions of the DLCT-based treatment plans were in better agreement with the dose distributions measured by the ionization chamber array, with substantially higher 3D gamma passing rates, than the SECT-based treatment plans (Tables 4, 5 in publ. I). DLCT-based range prediction was demonstrated to be highly accurate, as the measured evaluation layers at the distal edge and their predicted positions were within 1 mm of each other. The study presented the first dosimetric validation of dose calculation based on DECT using anthropomorphic phantoms for treatment planning with helium and carbon ion beams in addition to proton beams. The motivation for investigating DECT-based SPR prediction for helium and carbon ion beams is that the uncertainty in beam range can cause considerable deviations in biological dose due to the sharp gradients in LET and RBE end-of-range [150].

Many complicating factors in clinical practice make straightforward prediction of SPR difficult, including the presence of artifact-inducing implants in patients. For the common non-tissue materials evaluated, DLCT again performed better than SECT in predicting SPR. However, both approaches showed considerably higher relative residuals than those for tissue-equivalent materials. The DLCT-based predictions yielded residuals ranging from 1.0% to 18.4%, while the SECT-based predictions showed residuals ranging from -6.7% to 45.0% (Table 3 in publ. I). The importance of SPR prediction for non-tissue materials can be seen in the case of Palacos bone cement, which is commonly used in artificial joints and primarily made of PMMA and zirconium dioxide. Despite the high atomic number of zirconium, the bone cement's SPR value is low relative to tissue-equivalent materials with the same CTN. Consequently, uncertainty in SPR prediction can arise, which in turn can result in a particle range deviation of a few millimeters when SECT is used. However, when DECT was utilized, the SPR overestimation was reduced from 45% to below 10% in the case of Palacos bone cement. Even if DECT is not applied in clinical practice for SPR prediction, spectral image data can be employed to better distinguish normal tissue from non-tissue material and to identify SPR-related properties of non-tissue materials for contouring and SPR override.

4.2.2 Clinical evaluation of dual-energy CT versus single-energy CT for SPR and range prediction

In publication II, the clinical viability of DLCT-based SPR prediction was evaluated in treatment planning for therapy with proton, helium, and carbon ion beams in the brain. A patient cohort study examined homogeneous and heterogeneous tissue regions, in order to compare the differences in SPR that result from DLCT- and SECT-based methods, and to investigate

the ensuing dosimetric impact. In the patient cohort, the DLCT- and SECT-based methods produced varying degrees of differences in SPR prediction depending on the anatomical regions.

In homogeneous tissue regions, SPR values calculated with DLCT data showed statistically significant differences from SPR values derived from SECT images in all anatomical regions examined (Table 1 in publ. II). Bony tissues showed the largest deviation between DLCT and SECT among the investigated regions-of-interest (ROIs), which may be attributable to their high SPR values. Given that bones showed SPR differences ranging from 1.1% to 1.2%, DLCT-based treatment planning may be beneficial, provided that there is a more accurate DLCT-based prediction of SPR in patient anatomies. As for the brain, which, in treatment plans, is often the main tissue type in the beam path, the SPR differences amounted to about 1.1%, which could also be clinically relevant. For example, a SPR difference of 1% translates into a range difference of 1%, resulting in a 1 mm range shift over 10 cm depth in the body. Avoiding such range uncertainties is particularly important in the case of tumors located near critical OARs such as the brainstem or optic system. DLCT may therefore offer a special advantage in such scenarios.

In treatment plans for heterogeneous anatomical regions, the relative and absolute range differences between DLCT-based and SECT-based SPR predictions were evaluated and their corresponding dosimetric impact examined. The comparison between DLCT-based proton treatment plans and corresponding SECT plans for four brain tumor sites revealed considerable differences in SPR at the voxel level and relative (absolute) proton range shifts of 0.6% (0.4 mm) in the mean and up to 4.4% (2.1 mm) at the distal fall-off (Table 2 in publ. II); in certain cases, the range shifts could be clinically relevant. Among the evaluated OARs in the investigated cohort, 12% showed differences in the mean or maximum dose of more than 0.5 Gy(RBE) and up to 6.8 Gy(RBE) over the entire treatment. The range shifts and dose differences in OARs that were observed between DLCT- and SECT-based proton therapy treatment plans were similar to those found in helium and carbon ion treatment plans (Figure 7 in publ. II). This study has shown that the impact of SPR uncertainty on patient dose uncertainty is highly case-dependent. Although there was intra- and inter-patient variability, the sample cases revealed clinically relevant range differences between SECT- and DLCT-based predictions. Additionally, the large intra-patient variation in range shifts demonstrated that the variation in range uncertainty is dependent on the anatomical structure and the path of the beam. Consequently, the magnitude of improvement in range prediction when DLCT is used is contingent on the site of treatment and its heterogeneity.

4.2.3 Specific case: Dual-energy CT-based SPR and range prediction for patients with dental materials

Publication III investigated DECT-based treatment planning for head and neck particle therapy for patients with dental implant and restoration materials, a common yet challenging scenario. The reduction of dental material-induced effects remains an active area of research, as dental materials can adversely affect particle therapy treatment planning.

This study was the first to comprehensively investigate a full spectrum of state-of-the-art dental materials commonly used in prosthetic and restorative dentistry, as well as in radiotherapy-related tissue retraction. For the acquisition of DECT images, the study utilized two DECT techniques: image-based SACT and projection-based DLCT. Radiological material parameters were determined and SPR values were measured and compared to SECT and DECT techniques. The CTN values for most materials exceeded 3000 HU, with some even saturating the CTN scale, which caused mild to severe artifacts (Table 1 in publ. III).

As for the components of a tissue retraction device (TRD), it was found that DECT can enhance SPR prediction accuracy (Table 2 in publ. III). When a TRD is in the beam path, DECT can predict the dose delivered to the tissue surrounding the TRD more accurately.

In regard to dental materials, SPR predictions obtained via DECT were overall closer to the measured values compared to SPR predictions based on SECT (Table 2 in publ. III). Publication III extensively discusses the accuracy of SPR prediction methods for the various dental materials investigated, as well as the limitations observed in materials that contain elements of a high atomic number, which resulted in discrepancies between measurements and CT-based SPR prediction. In notable contrast to human tissues, it remains challenging to accurately predict SPR for dental materials that contain elements of a high atomic number (e.g., ytterbium) with current DECT techniques. Especially for materials containing elements of a high atomic number, RED and EAN maps may be of limited accuracy. It has been found that RED evinces a substantial positive bias when even a slight amount of an element of a high atomic number is present in DECT acquisitions [151]. For instance, a trace of iodine in the thyroid caused a positive bias in RED of about 1.1% for DE-SACT and 0.3% for DE-DLCT, most likely due to the greater impact of the photoelectric effect [151]. The bias in RED becomes greater as the amount of the element of a high atomic number increases. However, this bias seems to affect DE-DLCT less than DE-SACT, a finding that was confirmed in this study (Table 2 in publ. III). When such biases occur, DECT-based SPR prediction methods can lead to SPR overestimation [151, 152], a result that was observed for almost all dental materials containing elements of a high atomic number. In comparison to SECT, DE-SACT- and DE-DLCT-based SPR predictions overall improved SPR prediction accuracy for dental materials, particularly for certain materials such as zirconium dioxide, and may improve treatment planning.

As already noted, dental materials have a high CTN, and some even exceed the usual CTN scale. However, the current DE-RhoZ and DE-DirectSPR algorithms are implemented for the usual CTN range from -1024 HU to $+3071$ HU. Thus, extending the CTN scale does not currently provide additional information to enhance SPR prediction. Nevertheless, an extended CTN scale may reveal more information about the dental material, including its actual dimensions and components. Such information may be used to override the material with the proper SPR value. While SPR prediction for dental materials also does not seem to be improved by the current implementation of MAR algorithms or virtual monoenergetic images, the application of each may also reduce the effects of metal artifacts and enhance structure delineation [153, 154].

An anthropomorphic head phantom containing dental materials was used to evaluate treatment planning for helium ion beam therapy. Here, a DLCT scanner was applied for SECT and DECT-based SPR predictions, and the same was done with a SACT scanner. Range predictions for beams unobstructed by dental material were similar for both DECT techniques as well as for the two SECT methods (Figure 5 in publ. III). DECT-based SPR prediction was found to be closer to the ground truth than SECT in a previous study which used a validated ground truth SPR map and the same anthropomorphic phantom [152]. This result was then adopted as an assumption for the study conducted here. The study then evaluated the DECT- and SECT-based range predictions for ion beams when they passed through the dental material in the head phantom. In order to assess the accuracy of the respective predictions, they were compared to a reference dataset that was based on the measured SPR of lithium disilicate. In the case of DE-SACT, the SPR value of the lithium disilicate restoration was overestimated by about 35% compared to the measured SPR (Table 3 in publ. III). Thus, DE-DirectSPR-SACT SPR predictions may not be accurate enough for lithium disilicate at this time. In contrast, projection-based DE-RhoZ-DLCT showed a relative deviation of only 0.2% and thus was closer to the measured SPR than SE-120-DLCT (Table 3 and Figure 5 in publ. III). DE-DLCT may therefore be beneficial for treatment planning where a lithium disilicate restoration is present.

In sum, this study showed that image-based spectral reconstruction, as, for example, used in SACT, currently may not be able to make reliable quantitative statements about certain non-tissue dental materials, particularly when they are composed of elements of a high atomic number, e.g., composite II with ytterbium. In comparison, projection-based spectral reconstruction may enable more accurate SPR prediction for certain materials. Yet since the components, size, and shape of the material largely determines the extent of the improvement in dental management, each case needs to be evaluated individually to determine whether current DECT-based SPR prediction is accurate enough for particle therapy treatment planning. For the proper management of dental materials, interdisciplinary collaboration is essential. Depending on the CT technology that is employed in a radiotherapy department, departments of prosthodontics could, if possible for the patient, select dental implant and restoration materials that are better suited for SPR prediction with SECT and DECT.

4.3 Comparison to previous work

In publication I, DLCT-based SPR prediction for homogeneous tissue-equivalent material inserts showed similar SPR prediction accuracy compared to other DECT systems [19, 135, 136, 142, 145, 148, 155–161]. In such controlled situations, a SPR prediction accuracy of about 1% can be achieved [33]. The results of publication I are on par with the SPR prediction accuracy that was discovered in a previous study that used similar phantoms and tissue-equivalent inserts with the first-generation DLCT system (mean deviation=0.6%) [162]. Other studies using the first-generation DLCT system reported similar SPR prediction accuracy results for tissue-equivalent

inserts using monoenergetic images (RMSE=0.6%) [42] or using theoretical, non-experimentally determined values as a reference (mean error=0.3%) [41]. A recent study confirmed the accuracy of DLCT-based SPR prediction from monoenergetic images against theoretical reference SPR values (deviation <1%); the study also found a reduction in the deviation of water equivalent thickness from SECT to DLCT in animal tissue samples [163]. Certain non-tissue materials used in this thesis showed similar SPR prediction accuracy as DSCT in a previous study [136]. For other polymers, DECT has also been demonstrated to predict SPR more accurately than SECT [144, 164]. A previous study obtained ground truth measurements in an anthropomorphic head phantom and revealed considerably higher gamma passing rates with DECT compared to SECT [152], which is consistent with the results of this work, which showed improved SPR prediction with DLCT in anthropomorphic phantoms. The superiority of DECT over SECT was also confirmed in homogeneous [165–167] and heterogeneous [160, 168] animal tissue samples. After accounting for the various factors that contribute to uncertainty in clinical conditions, the overall range uncertainty for DECT-based SPR estimation has been estimated to be approximately 2% [33, 50, 159].

Studies related to publication II compared SPR prediction based on DECT and SECT in patients with head tumors. The DECT- and SECT-based differences in SPR prediction in homogeneous tissue regions, as discussed in publication II, are in line with a study that examined ROIs in the cranium, brain, and eyes [169]. The findings of publication II are also in the same order of magnitude as studies that used different DECT acquisition techniques (e.g., DSCT or SACT) and other DECT-based SPR prediction methods, which demonstrated that, for the brain region, range differences of about 1 mm (1%) can be expected [169, 170]. The results of publication II are also comparable to those of an investigation that examined the case of a head and neck cancer patient, where proton range differences between DECT and SECT were about 1 mm (0.5%) [171], and to the findings of a study of five head trauma patients with simulated skull base tumors, in which case the median relative range differences were about 0.5%–1% for different treatment plans [156]. Thus, the median differences in DLCT-based range differences observed in publication II were similar to or slightly smaller than the results of studies that used different DECT acquisition techniques; however, there was rather high inter-patient variability and large range differences were also found.

Publication III found a decrease in both SPR prediction accuracy and subjective image quality for higher density dental materials (cobalt-chrome, composites, and zirconium dioxide). These observations are consistent with studies which report that highly attenuating materials such as cobalt-chrome ($\rho \approx 8.5$ g/cm^3) or zirconium ($\rho \approx 6.5$ g/cm^3) result in more severe artifacts on CT image datasets, leading to lower image criteria scores and higher artifact index compared to the artifacts caused by titanium ($\rho \approx 4.5$ g/cm^3) [172, 173]. One investigation examined a base metal, zirconia, lithium disilicate, and amalgam and observed considerable changes in the proton range for these materials [174]. Publication III corroborated that beam range is affected when an ion beam passes through a lithium disilicate restoration and that SECT-based SPR prediction

does not provide sufficiently accurate range prediction. Yet it may be possible to offset the effect of a lithium disilicate restoration by utilizing projection-based DE-DLCT methods.

4.4 Clinical relevance

Despite the physical advantages of particle therapy over photon radiotherapy in cancer treatment, range uncertainties from SECT hinder exploiting the full potential of particle therapy. As demonstrated in publication I, applying DECT-based SPR prediction in treatment planning may improve patient outcomes in particle therapy by providing more accurate SPR predictions and, accordingly, decreasing deviations between the elemental compositions of tissues in cancer patients and those of reference tissues [33]. Furthermore, employing DECT for pediatric proton therapy can avoid SPR prediction inaccuracies that arise from using SECT-based calibration curves based on adult male tissue [175]. Since SECT-based SPR prediction has been demonstrated to result in large inter-center variations in SPR—up to 9% among different European institutions [176]—DECT-based SPR prediction may facilitate greater consistency in SPR predictions among treatment centers and enable new particle therapy centers to start treatment with higher confidence in SPR prediction.

As demonstrated in the simulated treatment planning scenarios in publication II, minor differences in the predicted SPR may lead to substantial range shifts, as the SPR differences can accumulate over the entire beam path [20]. As the range predictions vary between DLCT and SECT, DLCT may result in clinically relevant range shifts compared to SECT, which would consequently lead to dose differences. This may be particularly relevant for tumors in difficult locations, for example, tumors that are deep-seated in the body, located centrally in the head, or treated with ion beams that traverse a large volume of bony tissue. In the case of deep-seated tumors, DLCT may particularly improve range prediction accuracy, because in this scenario, a large amount of tissue including bone may be traversed, which may lead to larger range differences [162], as already observed in the case of prostate tumors [170]. In the case of brain tumors, publication II found differences of more than 0.5 Gy(RBE) in the mean or maximum dose of OARs in the total plan (Figure 8 in publ. II). Additionally, a mean difference of 0.5 Gy(RBE) was observed in $D_{99\%}$ target dose (Table 3 in publ. II). Yet, the variation in CTV coverage may be even smaller and thus clinically irrelevant. There may also be clinically significant variations for individual patients even if the observed range differences are less than 1 mm in the median, as demonstrated by the large intra- and inter-patient variability (Figure 6 in publ. II), which may have considerable potential to increase personalized medicine considerations [177]. Recent investigations have demonstrated the advantages of even small reductions in range uncertainty on NTCP [178], so even small improvements in SPR prediction can be clinically beneficial. Publication II also found that larger range differences between SECT and DLCT can result when beams pass through heterogeneous tissues whose SPR values are substantially different from the SPR of water (e.g., air-filled cavities, bony tissues) (Figure 4 and Table 1 in

publ. II). If SPR can be calculated more accurately, the current safety margins could potentially be reduced. A recent study demonstrated that there was a clinical advantage when the range uncertainty was reduced from 3% to 2% in robustly optimized DECT-based proton treatment planning for neuro-oncology patients, since this led to a dose reduction to at least one OAR in 89% of patients and a reduction in expected toxicity level in 44% of patients [179].

Publication III examined the radiological and dosimetric impact of dental materials that are commonly present in patients who are undergoing radiotherapy. Dental materials continue to pose a challenge in daily clinical practice, because, even though clinics employ advanced imaging technology, the effects of dental materials can compromise treatment planning. For example, one investigation found that dental material artifacts appeared on over 70% of planning CT image datasets for oral/oropharyngeal cancer patients [180]. Improving dental management for particle therapy is particularly important due to the finite range of ion beams, which means that they are more sensitive to planning uncertainties than photon beams [181]. To account for uncertainties in SPR values of the investigated dental implant and restoration materials, measured SPR values can be assigned in treatment planning for patients with known, accurately contoured dental materials. The uncertainties associated with dental materials could also be accounted for by applying robust optimization that uses multiple CT datasets (e.g., SECT, DECT, MAR, material override) and/or additional range uncertainty optimization parameters. This study demonstrated that, despite the presence of dental material, DLCT-based SPR prediction may enable treatment planning for patients with lithium disilicate restorations. Thus, the uncertainties associated with SPR prediction for dental materials may be limited and managed by employing DECT.

Overall, results such as these may be important to the development and evaluation of Digital Imaging and Communications in Medicine (DICOM) compliant SPR files that may be available as spectral results directly from DLCT scanners. Such a clinically available feature may be an important step to move beyond a defined research environment and to help other clinics in the use of DLCT for SPR prediction.

4.5 Strengths and limitations

By utilizing current clinical devices and frameworks, this thesis has demonstrated that it is feasible to directly predict patient-specific SPR by using DLCT. DLCT employs a double-layer detector that can simultaneously detect projection-aligned high- and low-energy X-ray data. Each detector layer has a maximum sensitivity for different energy spectra [124]. Consequently, DLCT is able to implicitly acquire dual-energy data. Since DLCT can be used without employing a special mode, it is possible to pro- and retrospectively generate dual-energy data that are perfectly aligned, temporally and spatially, over the full FOV [125]. DLCT imaging is not affected by patient motion during acquisition (e.g., breathing, swallowing, organ movement), unlike other DECT techniques (Table 2.1). Although DLCT systems are characterized by lower spectral separation than source-based DECT systems [34], which may constitute a limitation

of DLCT, the spectral signal-to-noise ratio is comparable to that of other commercial DECT systems [182]. Additionally, DLCT may be affected by cross-scatter between detector layers [31]. Nevertheless, DLCT imaging enables projection-based material decomposition with implicit noise reduction that exploits anti-correlated noise in the two detector layers.

Although the tissue-equivalent materials and anthropomorphic phantoms employed in this work are deemed to be valid surrogates for biological tissues and suitable for DECT-based range prediction comparisons [152, 183–185], they are not able to perfectly reflect the heterogeneity and variable composition of real tissues. Further studies on biological tissue samples and *in vivo* would therefore be desirable before DLCT-based SPR prediction can be widely clinically applied. Another possible limitation to this study is that the measurements were obtained solely with a male pelvic phantom, which introduces the potential problem of a gender data gap. Similar measurements using a female pelvic phantom would close this potentially problematic gap, but such a phantom does not currently exist.

Furthermore, while the dental materials examined constitute a representative sample of those commonly used in prosthodontics, it was not possible to investigate amalgam. This is because amalgam is no longer used as a filling material by the institutional department of prosthodontics. It should be borne in mind, though, that elderly patients may still harbor the material in their fillings. Gold alloys were also not included for cost reasons.

To determine whether SECT or DECT better reflects the actual SPR distribution in the retrospective patient study, it is necessary to know the corresponding SPR accuracy [170]. Without knowing the respective SPR accuracy, this study could only indirectly demonstrate the accuracy of DLCT-based SPR prediction in patients. One potential way to directly verify the accuracy would be to employ proton transmission imaging [186, 187] or prompt gamma imaging [188–190], which may be able to offer range verification with millimeter accuracy, but they are not currently widely available clinically [79]. Based on the results of publication I and other preclinical investigations that have demonstrated that DLCT surpasses SECT in SPR prediction [41, 42, 162, 163], and in view of the findings of publication II regarding differences in SPR prediction, it may be justifiably claimed that DLCT is to be clinically preferred for patient treatments where beams pass through heterogeneous anatomical regions.

Lastly, while the applied SPR prediction method [37] is considered a robust and accurate method for DECT-based SPR prediction [191], there are several other SPR prediction methods [33] that were not investigated in this work and could potentially enhance the predictions.

4.6 Possibilities for future research

This study has investigated a variety of experimental and clinical scenarios to test the ability of DECT to reduce the uncertainty in SPR estimation that results from using SECT. Further studies may evaluate other anatomical regions where beams have to traverse thicker bony structures and multiple tissue types—as occurs, for example, when treating tumors in the

pelvic region—or pass through the lungs, as in the case of Hodgkin lymphoma. Since this study was conducted in accordance with current clinical practice at the Heidelberg Ion Beam Therapy Center (HIT) and therefore applied the PTV margin concept, it did not incorporate CT uncertainty in robust optimization. Future studies might therefore apply robustly optimized treatment plans combined with DLCT-based SPR prediction to evaluate dose differences in the CTV and OARs. Additionally, to confirm the clinical viability of DLCT-based range prediction, it will be necessary to perform studies with radio-oncology patient data and clinical indications for particle therapy, alongside range measurements in biological tissue samples. Also, further study in larger patient cohorts is called for in light of the considerable intra- and inter-patient variations in SPR shifts.

It would also be beneficial to expand these findings to 4D treatment planning, which is crucial when motion needs to be considered and/or mitigated during radiotherapy treatments, as when tumors are located in the thoracic or abdominal regions [192, 193]. Future work may be able to reduce motion artifacts by utilizing 4D DLCT-based SPR prediction and treatment planning that uses the large coverage of 80 mm per gantry rotation of the second-generation DLCT system.

Publications I and III suggest that DLCT-based range prediction can be especially beneficial for non-tissue materials, and its impact on patient treatment plans invites further evaluation. DECT-based SPR prediction may also prove useful for other non-tissue implant materials such as hip prostheses, spinal stabilization implants, or silicone breast implants [194].

While the uncertainty in SPR estimation for dental materials may be mitigated better by DECT than by SECT, it may also be advantageous for vendors to consider manufacturing dental implant and restoration materials with a lower amount of radiopaque material. Specifically, it may be helpful if dentistry can employ materials that are not composed of elements of a high atomic number. Even if vendors make such changes, though, it will still be essential to be able to distinguish between natural teeth and non-tissue dental materials in CT imaging and planar X-rays. Interdisciplinary collaborations with departments of prosthodontics are necessary to evaluate dental materials and techniques that may lead to improvements in SPR prediction. Such collaboration is in the interest of prosthodontists, because, without it, they may have to extract dental material from cancer patients that inhibits particle therapy [181] and then replace it with an alternative. Interdisciplinary cooperation, though, could identify materials that are optimal for prosthodontics and radio-oncology, and thus improve patient outcomes.

Several studies have compared the five commercially available DECT techniques in terms of image quality for diagnostic purposes [182, 195]. As of yet, though, no study has directly compared the SPR prediction accuracy of all five DECT platforms [33]. In addition to DECT, triple-energy CT imaging could also be investigated more extensively to improve SPR prediction [196]. Furthermore, particle CT may be able to improve accuracy in SPR prediction and to serve as a reference in comparisons of DECT-based SPR predictions [45]. To date, it has been challenging to obtain accurate SPR measurements by means of proton CT or helium CT; in comparison to DECT, these methods offer slightly lower SPR prediction accuracy

[49]. MRI- or cone beam CT-based synthetic CT generation for range prediction is also under investigation. Additionally, CT systems with energy-resolving, photon-counting detectors have evinced advantages in comparison to energy-integrating CT detectors. Specifically, they offer higher spatial resolution and reduced image noise simultaneously [33, 197] and can reduce metal artifacts in reconstructions due to reduced beam hardening [198]. Despite having the potential to provide spectral data, photon-counting detector CT systems are just starting to become clinically available. As it continues to be developed, photon-counting CT may be able to improve patient dose calculation.

While dose calculation in DECT-based treatment planning has been investigated, it is expected that DECT imaging may offer several opportunities for enhancing the accuracy of other parts of the radiotherapy chain. It has been proposed that DECT may reduce metal artifacts and enhance image quality [32]; improve tumor staging, delineation, and characterization [199, 200]; and enable better normal tissue characterization and personalized treatment by means of physiological quantification [39]. DECT has further demonstrated potential to improve dose calculation in treatment modalities other than particle therapy, including external photon beam radiotherapy and brachytherapy [32]. Furthermore, DLCT may be applied in photon radiotherapy and particle therapy in ways that may offer other practical advantages. The application of DLCT may make it possible to, for example, simplify the treatment planning workflow; decrease CT simulation duration and radiation exposure by providing virtual non-contrast images [33, 201]; and require less time under anesthesia for pediatric patients since dose calculation can be performed on post-contrast DLCT images [202]. Finally, DECT has the potential to predict treatment response after neoadjuvant chemoradiation therapy for pancreatic cancer by calculating the extracellular volume fraction based on iodine maps [203]. Future work is encouraged to further explore these various applications of DECT in radiotherapy.

4.7 Importance of findings

The full physical potential of particle therapy has not yet been able to be exploited, due in no small part to beam range uncertainty [33]. This thesis, along with other investigations of DECT-based SPR and range prediction, has shown that SPR accuracy can be improved by using the additional information on material composition provided by two X-ray spectra in DECT, which is not possible with the clinical SECT standard. In various experimental and clinical scenarios—homogeneous tissue-equivalent materials, heterogeneous anthropomorphic phantoms, non-tissue materials, a treatment planning study for brain tumor patients, and the specific case of treatment planning for patients with dental materials—this thesis has demonstrated that using DLCT for treatment planning improves range prediction for high-precision particle therapy. The application of DLCT may allow the use of more suitable beam angles and reduced safety margins in particle therapy, thereby reducing target volumes and avoiding overtreatment of normal tissues, thus decreasing the probability of complications and late effects.

5

Conclusions

The availability of and demand for particle therapy is growing exponentially, as radiotherapy with protons or light ions is a highly precise form of cancer treatment [11]. The physical and biological properties of ion beams make particle therapy a clinically promising treatment option for critically localized and radioresistant tumors, where the precise application of escalated radiation doses is particularly important [8]. To fully exploit the physical advantages of ion beams, including efficient target coverage and OAR sparing, accurate range prediction, calculated from the SPR of tissues in the patient, is required [20, 22].

For particle therapy treatment planning, accurate range prediction is critical, and the current clinical standard is based on SECT imaging, but SECT-based CTN-to-SPR conversion is one of the major sources of range uncertainty [33]. Therefore, this thesis has aimed to improve SPR prediction using DECT imaging. DECT image data is generated by utilizing two X-ray spectra of different energy ranges; thus, DECT enables direct SPR prediction based on quantitative measurements of RED and EAN using the Bethe equation. By contrast, the SECT-based method relies on converting CTN to SPR, yet CTN acquired from X-ray attenuation cannot be used to accurately predict energy loss by ions, which makes the approach indirect. In this work, the physical and clinical potential of DLCT as an alternative to conventional SECT for improving SPR prediction has been (1) experimentally evaluated in homogeneous tissue-equivalent materials, heterogeneous and geometrically complex anthropomorphic phantoms, and non-tissue materials; (2) clinically analyzed for brain tumors in a retrospective patient study; and (3) experimentally investigated in the case of particle therapy treatment planning for patients with dental materials. To improve accuracy and to facilitate clinical applicability, the methodology established in this thesis for DLCT-based SPR prediction is physics-based, patient-specific, and direct and therefore does not require the heuristic, ambiguous, and indirect SECT-based CTN-to-SPR conversion. This work has demonstrated that the use of DLCT can improve SPR prediction for particle therapy treatment planning. Consequently, in comparison to the SECT method, DLCT-based range prediction results in a closer agreement between planned and delivered dose.

In the first part of the thesis, the relative mean deviation in SPR prediction for tissue-equivalent materials was reduced from 1.6% with SECT to 0.7% with DLCT compared to measured SPR values. For proton, helium, and carbon ion beam therapy treatment planning, end-to-end tests were performed with anthropomorphic head and pelvic phantoms. Using ionization chamber array measurements as a reference, 3D gamma passing rates were observed to be higher for

the DLCT-predicted dose distributions than for the SECT-predicted dose distributions. The DLCT-based range prediction was demonstrated to be highly accurate in that the measured evaluation layers at the distal edge were within 1 mm of their predicted positions. DLCT was also found to reduce the uncertainty in predicting SPR for non-tissue materials compared to SECT.

The second part of the thesis conducted a retrospective patient study to analyze DLCT-based SPR prediction in the brain. The DLCT- and SECT-based approaches showed mean SPR differences of approximately 1% in regions of homogeneous tissue. In treatment plans where beams traversed several, heterogeneous tissues, DLCT and SECT demonstrated mean proton range shifts of 0.6%, and variations that exceeded 4% of the total range were found. The range shifts that were observed between DLCT- and SECT-based treatment plans were similar in the case of proton, helium, and carbon ion beams. Therefore, when employing these three particles in radiotherapy, range calculation may be improved by using patient-specific DLCT-based SPR prediction.

In the third part of the thesis, DLCT and SACT were used to investigate DECT-based SPR prediction for patients with dental implant and restoration materials. Overall, in comparison to SECT-based SPR predictions, DECT-based SPR predictions of cylindrical dental material inserts showed better agreement with measured reference data. The usefulness of DECT methods was impaired, though, when applied to materials containing elements of a high atomic number. When applied to an anthropomorphic head phantom with dental material, DECT-based treatment planning using helium ions showed that DECT-based techniques predicted similar ranges for beams that were unobstructed by dental material. In the case of ion beams that passed through a lithium disilicate restoration, SPR prediction based on DLCT, which employs a projection-based method, most closely agreed with the measured reference data, with a range deviation of 0.2 mm. Therefore, SPR prediction based on DECT may be better able to offset the potential issues caused by dental implant and restoration materials during particle therapy treatment planning.

This thesis has demonstrated the use of DLCT to be a viable technique for pretreatment range prediction. In particular, DLCT imaging can improve the accuracy of SPR predictions for proton, helium, and carbon ion beam therapy compared to conventional SECT systems by using a projection-based calculation of RED and EAN. This is an important step in optimizing treatment planning for particle therapy. By facilitating the reduction of uncertainties in clinical range prediction to less than 1% in controlled experimental scenarios, DLCT offers the potential to reduce safety margins, thus allowing dose escalation to treat tumors more effectively while limiting toxicity. Further clinical investigation in other treatment regions and with larger patient cohorts will continue to explore the potential benefits of DLCT for particle therapy. Given the physics-based advantages of DECT-based SPR prediction for particle therapy, it may be advisable to apply this method more widely in clinical settings, as it can lead to higher treatment accuracy and better care for tumor patients.

List of Scientific Contributions

Journal articles

<u>Friderike K. Longarino</u>, Christopher Herpel, Thomas Tessonnier, Stewart Mein, Benjamin Ackermann, Jürgen Debus, Franz Sebastian Schwindling, Wolfram Stiller, Andrea Mairani. Dual-energy CT-based stopping power prediction for dental materials in particle therapy. *J Appl Clin Med Phys* (2023) 24(8):13977. DOI: 10.1002/acm2.13977

Thomas Tessonnier, Swantje Ecker, Judith Besuglow, Jakob Naumann, Stewart Mein, <u>Friderike K. Longarino</u>, Malte Ellerbrock, Benjamin Ackermann, Marcus Winter, Stephan Brons, Abdallah Qubala, Thomas Haberer, Jürgen Debus, Oliver Jäkel, Andrea Mairani. Commissioning of Helium Ion Therapy and the First Patient Treatment With Active Beam Delivery. *Int J Radiat Oncol Biol Phys* (2023) 116(4):935–948. DOI: 10.1016/j.ijrobp.2023.01.015

<u>Friderike K. Longarino</u>, Antonia Kowalewski, Thomas Tessonnier, Stewart Mein, Benjamin Ackermann, Jürgen Debus, Andrea Mairani, Wolfram Stiller. Potential of a Second-Generation Dual-Layer Spectral CT for Dose Calculation in Particle Therapy Treatment Planning. *Front Oncol* (2022) 12:853495. DOI: 10.3389/fonc.2022.853495

<u>Friderike K. Longarino</u>, Thomas Tessonnier, Stewart Mein, Semi B. Harrabi, Jürgen Debus, Wolfram Stiller, Andrea Mairani. Dual-layer spectral CT for proton, helium, and carbon ion beam therapy planning of brain tumors. *J Appl Clin Med Phys* (2022) 23(1):e13465. DOI: 10.1002/acm2.13465

<u>Friderike K. Faller</u>, Stewart Mein, Benjamin Ackermann, Jürgen Debus, Wolfram Stiller, Andrea Mairani. Pre-clinical evaluation of dual-layer spectral computed tomography-based stopping power prediction for particle therapy planning at the Heidelberg Ion Beam Therapy Center. *Phys Med Biol* (2020) 65(9):095007. DOI: 10.1088/1361-6560/ab735e

Conference contributions

Neha Koonjoo, Torben Hornung, Sheng Shen, <u>Friderike Longarino</u>, Susu Yan, Matthew Rosen, Thomas Bortfeld. Low field Breast and Chest Wall Imaging for MR guided Proton Therapy. *Toronto, ISMRM & ISMRT Annual Meeting & Exhibition* (2023).

<u>Friderike Longarino</u>, Thomas Tessonnier, Christopher Herpel, Stewart Mein, Benjamin Ackermann, Jürgen Debus, Franz Sebastian Schwindling, Thomas Bortfeld, Wolfram Stiller, Andrea Mairani. Dual-energy computed tomography for stopping power prediction in particle therapy. *Boston, Executive Committee on Research of Massachusetts General Hospital, Scientific Advisory Committee Virtual Poster Session* (2023).

<u>Friderike Longarino</u>, Antonia Kowalewski, Thomas Tessonnier, Stewart Mein, Benjamin Ackermann, Jürgen Debus, Wolfram Stiller, Andrea Mairani. Feasibility of a second-generation dual-layer spectral CT system for stopping power prediction and dose calculation in particle therapy. *Washington, DC, 64th American Association of Physicists in Medicine (AAPM) Annual Meeting & Exhibition* (2022).

<u>Friderike Faller</u>, Stewart Mein, Benjamin Ackermann, Wolfram Stiller, Andrea Mairani. Clinical impact of spectral CT-based stopping power prediction for particle therapy planning. *39th European Society for Radiotherapy and Oncology (ESTRO) Congress. Radiother Oncol* (2020) 152:S955–S956. DOI: 10.1016/S0167-8140(21)01744-8

<u>Friderike Faller</u>, Stewart Mein, Benjamin Ackermann, Markus Alber, Wolfram Stiller, Andrea Mairani. Dosimetric calibration and validation of spectral CT-based stopping power prediction for particle therapy planning. *Montréal, 19th International Conference on the Use of Computers in Radiation Therapy (ICCR)* (2019).
The poster received the 3rd prize in the ICCR Rising Stars Competition.

<u>Friderike Faller</u>, Stewart Mein, Benjamin Ackermann, Wolfram Stiller, Andrea Mairani. Dosimetric validation of spectral CT-based stopping power prediction for proton beams using an anthropomorphic head phantom. *Manchester, 58th Particle Therapy Co-Operative Group (PTCOG) Conference* (2019).

<u>Friderike Faller</u>, Benjamin Ackermann, Gregor Pahn, Markus Alber, Wolfram Stiller, Andrea Mairani. Calibration and validation of ion stopping power prediction with Philips IQon Spectral CT. *Milan, 38th European Society for Radiotherapy and Oncology (ESTRO) Congress. Radiother Oncol* (2019) 133:S558–S559. DOI: 10.1016/S0167-8140(19)31431-8

Bibliography

[1]   Wang H, Naghavi M, Allen C, et al. Global, regional, and national life expectancy, all-cause mortality, and cause-specific mortality for 249 causes of death, 1980–2015: a systematic analysis for the Global Burden of Disease Study 2015. *Lancet* (2016) 388(10053):1459–1544. DOI: 10.1016/S0140-6736(16)31012-1.

[2]   Sung H, Ferlay J, Siegel RL, et al. Global Cancer Statistics 2020: GLOBOCAN Estimates of Incidence and Mortality Worldwide for 36 Cancers in 185 Countries. *CA Cancer J Clin* (2021) 71(3):209–249. DOI: 10.3322/caac.21660.

[3]   Bray F, Laversanne M, Weiderpass E, et al. The ever-increasing importance of cancer as a leading cause of premature death worldwide. *Cancer* (2021) 127(16):3029–3030. DOI: 10.1002/cncr.33587.

[4]   World Health Organization. *Cancer*. Date of access: July 25, 2023. URL: https://www.who.int/news-room/fact-sheets/detail/cancer.

[5]   Weinstein IB and Case K. The History of Cancer Research: Introducing an AACR Centennial Series. *Cancer Res* (2008) 68(17):6861–6862. DOI: 10.1158/0008-5472.CAN-08-2827.

[6]   Crosby D, Bhatia S, Brindle KM, et al. Early detection of cancer. *Science* (2022) 375(6586):eaay9040. DOI: 10.1126/science.aay9040.

[7]   Palumbo MO, Kavan P, Miller Jr. WH, et al. Systemic cancer therapy: achievements and challenges that lie ahead. *Front Pharmacol* (2013) 4:57. DOI: 10.3389/fphar.2013.00057.

[8]   Christiansen H and Bremer M, eds. *Strahlentherapie und Radioonkologie aus interdisziplinärer Sicht*. 7th edition. Lehmanns Media: Berlin (2022).

[9]   Baumann M, Krause M, Overgaard J, et al. Radiation oncology in the era of precision medicine. *Nat Rev Cancer* (2016) 16:234–249. DOI: 10.1038/nrc.2016.18.

[10] Durante M, Orecchia R, and Loeffler JS. Charged-particle therapy in cancer: clinical uses and future perspectives. *Nat Rev Clin Oncol* (2017) 14:483–495. DOI: 10.1038/nrclinonc.2017.30.

[11] Yan S, Ngoma TA, Ngwa W, et al. Global democratisation of proton radiotherapy. *Lancet Oncol* (2023) 24(6):e245–e254. DOI: 10.1016/S1470-2045(23)00184-5.

[12] Kuhlthau KA, Pulsifer MB, Yeap BY, et al. Prospective Study of Health-Related Quality of Life for Children With Brain Tumors Treated With Proton Radiotherapy. *J Clin Oncol* (2012) 30(17):2079–2086. DOI: 10.1200/JCO.2011.37.0577.

[13] Particle Therapy Co-Operative Group. *Patient Statistics*. Date of access: July 25, 2023. URL: https://ptcog.site/index.php/patient-statistics-2.

[14] Particle Therapy Co-Operative Group. *Facilities in Operation.* Date of access: July 25, 2023. URL: https://ptcog.site/index.php/facilities-in-operation-public.

[15] Bortfeld TR and Loeffler JS. Three ways to make proton therapy affordable. *Nature* (2017) 549:451–453. DOI: 10.1038/549451a.

[16] Mohan R and Grosshans D. Proton therapy – Present and future. *Adv Drug Deliv Rev* (2017) 109:26–44. DOI: 10.1016/j.addr.2016.11.006.

[17] Lomax AJ, Bortfeld T, Goitein G, et al. A treatment planning inter-comparison of proton and intensity modulated photon radiotherapy. *Radiother Oncol* (1999) 51(3):257–271. DOI: 10.1016/S0167-8140(99)00036-5.

[18] Bragg WH and Kleeman R. On the ionization curves of radium. *London Edinburgh Dublin Philos Mag J Sci* (1904) 8(48):726–738. DOI: 10.1080/14786440409463246.

[19] Bär E, Lalonde A, Royle G, et al. The potential of dual-energy CT to reduce proton beam range uncertainties. *Med Phys* (2017) 44(6):2332–2344. DOI: 10.1002/mp.12215.

[20] Paganetti H. Range uncertainties in proton therapy and the role of Monte Carlo simulations. *Phys Med Biol* (2012) 57(11):R99–R117. DOI: 10.1088/0031-9155/57/11/R99.

[21] Yang M, Zhu XR, Park PC, et al. Comprehensive analysis of proton range uncertainties related to patient stopping-power-ratio estimation using the stoichiometric calibration. *Phys Med Biol* (2012) 57(13):4095–4115. DOI: 10.1088/0031-9155/57/13/4095.

[22] Wohlfahrt P and Richter C. Status and innovations in pre-treatment CT imaging for proton therapy. *Br J Radiol* (2020) 93(1107):20190590. DOI: 10.1259/bjr.20190590.

[23] Lomax AJ. Myths and realities of range uncertainty. *Br J Radiol* (2020) 93(1107):20190582. DOI: 10.1259/bjr.20190582.

[24] White DR, Widdowson EM, Woodard HQ, et al. The composition of body tissues. (II) Fetus to young adult. *Br J Radiol* (1991) 64(758):149–159. DOI: 10.1259/0007-1285-64-758-149.

[25] Wohlfahrt P, Möhler C, Troost EGC, et al. Dual-Energy Computed Tomography to Assess Intra- and Inter-Patient Tissue Variability for Proton Treatment Planning of Patients With Brain Tumor. *Int J Radiat Oncol Biol Phys* (2019) 105(3):504–513. DOI: 10.1016/j.ijrobp.2019.06.2529.

[26] Schaffner B and Pedroni E. The precision of proton range calculations in proton radiotherapy treatment planning: experimental verification of the relation between CT-HU and proton stopping power. *Phys Med Biol* (1998) 43(6):1579–1592. DOI: 10.1088/0031-9155/43/6/016.

[27] Knopf A, Parodi K, Bortfeld T, et al. Systematic analysis of biological and physical limitations of proton beam range verification with offline PET/CT scans. *Phys Med Biol* (2009) 54(14):4477–4495. DOI: 10.1088/0031-9155/54/14/008.

[28] Hounsfield GN. Computerized transverse axial scanning (tomography): Part 1. Description of system. *Br J Radiol* (1973) 46(552):1016–1022. DOI: 10.1259/0007-1285-46-552-1016.

[29] Goitein M. The measurement of tissue heterodensity to guide charged particle radiotherapy. *Int J Radiat Oncol Biol Phys* (1977) 3:27–33. DOI: 10.1016/0360-3016(77)90223-1.

[30] Flohr TG, McCollough CH, Bruder H, et al. First performance evaluation of a dual-source CT (DSCT) system. *Eur Radiol* (2006) 16(2):256–268. DOI: 10.1007/s00330-005-2919-2.

[31] McCollough CH, Boedeker K, Cody D, et al. Principles and applications of multienergy CT: Report of AAPM Task Group 291. *Med Phys* (2020) 47(7):e881–e912. DOI: 10.1002/mp.14157.

[32] van Elmpt W, Landry G, Das M, et al. Dual energy CT in radiotherapy: Current applications and future outlook. *Radiother Oncol* (2016) 119(1):137–144. DOI: 10.1016/j.radonc.2016.02.026.

[33] Yang M, Wohlfahrt P, Shen C, et al. Dual- and multi-energy CT for particle stopping-power estimation: current state, challenges and potential. *Phys Med Biol* (2023) 68(4):04TR01. DOI: 10.1088/1361-6560/acabfa.

[34] McCollough CH, Leng S, Yu L, et al. Dual- and Multi-Energy CT: Principles, Technical Approaches, and Clinical Applications. *Radiology* (2015) 276(3):637–653. DOI: 10.1148/radiol.2015142631.

[35] Forghani R, De Man B, and Gupta R. Dual-Energy Computed Tomography: Physical Principles, Approaches to Scanning, Usage, and Implementation: Part 1. *Neuroimaging Clin North Am* (2017) 27(3):371–384. DOI: 10.1016/j.nic.2017.03.002.

[36] Paganetti H, Beltran C, Both S, et al. Roadmap: proton therapy physics and biology. *Phys Med Biol* (2021) 66(5):05RM01. DOI: 10.1088/1361-6560/abcd16.

[37] Yang M, Virshup G, Clayton J, et al. Theoretical variance analysis of single- and dual-energy computed tomography methods for calculating proton stopping power ratios of biological tissues. *Phys Med Biol* (2010) 55(5):1343–1362. DOI: 10.1088/0031-9155/55/5/006.

[38] Landry G and Hua C-H. Current state and future applications of radiological image guidance for particle therapy. *Med Phys* (2018) 45(11):e1086–e1095. DOI: 10.1002/mp.12744.

[39] Kruis MF. Improving radiation physics, tumor visualisation, and treatment quantification in radiotherapy with spectral or dual-energy CT. *J Appl Clin Med Phys* (2022) 23(1):e13468. DOI: 10.1002/acm2.13468.

[40] Altman A and Carmi R. TU-E-210A-03: A Double-Layer Detector, Dual-Energy CT – Principles, Advantages and Applications. *Med Phys* (2009) 36(6):2750. DOI: 10.1118/1.3182434.

[41] Ohira S, Washio H, Yagi M, et al. Estimation of electron density, effective atomic number and stopping power ratio using dual-layer computed tomography for radiotherapy treatment planning. *Phys Med* (2018) 56:34–40. DOI: 10.1016/j.ejmp.2018.11.008.

[42] Landry G, Dörringer F, Si-Mohamed S, et al. Technical note: Relative proton stopping power estimation from virtual monoenergetic images reconstructed from dual-layer computed tomography. *Med Phys* (2019) 46(4):1821–1828. DOI: 10.1002/mp.13404.

[43] Knopf A-C and Lomax A. In vivo proton range verification: a review. *Phys Med Biol* (2013) 58(15):R131–R160. DOI: 10.1088/0031-9155/58/15/R131.

[44] Roellinghoff F, Benilov A, Dauvergne D, et al. Real-time proton beam range monitoring by means of prompt-gamma detection with a collimated camera. *Phys Med Biol* (2014) 59(5):1327–1338. DOI: 10.1088/0031-9155/59/5/1327.

[45] Dedes G, Dickmann J, Niepel K, et al. Experimental comparison of proton CT and dual energy x-ray CT for relative stopping power estimation in proton therapy. *Phys Med Biol* (2019) 64(16):165002. DOI: 10.1088/1361-6560/ab2b72.

[46] Ozoemelam I, van der Graaf E, van Goethem M-J, et al. Real-Time PET Imaging for Range Verification of Helium Radiotherapy. *Front Phys* (2020) 8:565422. DOI: 10.3389/fphy.2020.565422.

[47] Heymans SV, Carlier B, Toumia Y, et al. Modulating ultrasound contrast generation from injectable nanodroplets for proton range verification by varying the degree of superheat. *Med Phys* (2021) 48(4):1983–1995. DOI: 10.1002/mp.14778.

[48] Morozov A, Simões H, and Crespo P. Distal edge determination precision for a multi-slat prompt-gamma camera: A comprehensive simulation and optimization of the detection system. *Phys Med* (2021) 84:85–100. DOI: 10.1016/j.ejmp.2021.03.028.

[49] Bär E, Volz L, Collins-Fekete C-A, et al. Experimental comparison of photon versus particle computed tomography to predict tissue relative stopping powers. *Med Phys* (2022) 49(1):474–487. DOI: 10.1002/mp.15283.

[50] Peters N, Wohlfahrt P, Hofmann C, et al. Reduction of clinical safety margins in proton therapy enabled by the clinical implementation of dual-energy CT for direct stopping-power prediction. *Radiother Oncol* (2022) 166:71–78. DOI: 10.1016/j.radonc.2021.11.002.

[51] Wilson RR. Radiological Use of Fast Protons. *Radiology* (1946) 47(5):487–491. DOI: 10.1148/47.5.487.

[52] Tobias CA, Lawrence JH, Born JL, et al. Pituitary Irradiation with High-Energy Proton Beams: A Preliminary Report. *Cancer Res* (1958) 18(2):121–134.

[53] Schardt D, Elsässer T, and Schulz-Ertner D. Heavy-ion tumor therapy: Physical and radiobiological benefits. *Rev Mod Phys* (2010) 82(1):383–425. DOI: 10.1103/RevModPhys.82.383.

[54] Suit H, DeLaney T, Goldberg S, et al. Proton vs carbon ion beams in the definitive radiation treatment of cancer patients. *Radiother Oncol* (2010) 95(1):3–22. DOI: 10.1016/j.radonc.2010.01.015.

[55] Durante M and Loeffler J. Charged particles in radiation oncology. *Nat Rev Clin Oncol* (2010) 7:37–43. DOI: 10.1038/nrclinonc.2009.183.

[56] Schaub L, Harrabi SB, and Debus J. Particle therapy in the future of precision therapy. *Br J Radiol* (2020) 93(1114):20200183. DOI: 10.1259/bjr.20200183.

[57] Battistoni G, Mattei I, and Muraro S. Nuclear physics and particle therapy. *Adv Phys: X* (2016) 1(4):661–686. DOI: 10.1080/23746149.2016.1237310.

[58] Durante M, Debus J, and Loeffler JS. Physics and biomedical challenges of cancer therapy with accelerated heavy ions. *Nat Rev Phys* (2021) 3(12):777–790. DOI: 10.1038/s42254-021-00368-5.

[59] Stokkevåg CH, Engeseth G-M, Ytre-Hauge KS, et al. Estimated risk of radiation-induced cancer following paediatric cranio-spinal irradiation with electron, photon and proton therapy. *Acta Oncol* (2014) 53(8):1048–1057. DOI: 10.3109/0284186X.2014.928420.

[60] Amaldi U and Kraft G. Radiotherapy with beams of carbon ions. *Rep Prog Phys* (2005) 68(8):1861–1882. DOI: 10.1088/0034-4885/68/8/R04.

[61] Rackwitz T and Debus J. Clinical applications of proton and carbon ion therapy. *Semin Oncol* (2019) 46(3):226–232. DOI: 10.1053/j.seminoncol.2019.07.005.

[62] Karger CP, Glowa C, Peschke P, et al. The RBE in ion beam radiotherapy: In vivo studies and clinical application. *Z Med Phys* (2021) 31(2):105–121. DOI: 10.1016/j.zemedi.2020.12.001.

[63] Konings K, Vandevoorde C, Baselet B, et al. Combination Therapy With Charged Particles and Molecular Targeting: A Promising Avenue to Overcome Radioresistance. *Front Oncol* (2020) 10:128. DOI: 10.3389/fonc.2020.00128.

[64] Zhou H, Yang P, Li H, et al. Carbon ion radiotherapy boosts anti-tumour immune responses by inhibiting myeloid-derived suppressor cells in melanoma-bearing mice. *Cell Death Discov* (2021) 7:332. DOI: 10.1038/s41420-021-00731-6.

[65] Durante M and Paganetti H. Nuclear physics in particle therapy: a review. *Rep Prog Phys* (2016) 79(9):096702. DOI: 10.1088/0034-4885/79/9/096702.

[66] Newhauser WD and Zhang R. The physics of proton therapy. *Phys Med Biol* (2015) 60(8):R155–R209. DOI: 10.1088/0031-9155/60/8/R155.

[67] Bethe H. Zur Theorie des Durchgangs schneller Korpuskularstrahlen durch Materie. *Ann Phys* (1930) 397(3):325–400. DOI: 10.1002/andp.19303970303.

[68] Bloch F. Bremsvermögen von Atomen mit mehreren Elektronen. *Z Physik* (1933) 81:363–376. DOI: 10.1007/BF01344553.

[69] Bloch F. Zur Bremsung rasch bewegter Teilchen beim Durchgang durch Materie. *Ann Phys* (1933) 408(3):285–320. DOI: 10.1002/andp.19334080303.

[70] International Commission on Radiation Units and Measurements. *Stopping Powers for Electrons and Protons.* ICRU Report No. 37. 1984.

[71] Brown A and Suit H. The centenary of the discovery of the Bragg peak. *Radiother Oncol* (2004) 73(3):265–268. DOI: 10.1016/j.radonc.2004.09.008.

[72] Jäkel O. Physical advantages of particles: protons and light ions. *Br J Radiol* (2020) 93(1107):20190428. DOI: 10.1259/bjr.20190428.

[73] Molière G. Theorie der Streuung schneller geladener Teilchen I. Einzelstreuung am abgeschirmten Coulomb-Feld. *Z Naturforsch A* (1947) 2a(3):133–145. DOI: 10.1515/zna-1947-0302.

[74] Molière G. Theorie der Streuung schneller geladener Teilchen II. Mehr- und Vielfachstreuung. *Z Naturforsch A* (1948) 3a(2):78–97. DOI: 10.1515/zna-1948-0203.

[75] Bethe HA. Molière's Theory of Multiple Scattering. *Phys Rev* (1953) 89(6):1256–1266. DOI: 10.1103/PhysRev.89.1256.

[76] Highland VL. Some practical remarks on multiple scattering. *Nucl Instr Meth* (1975) 129(2):497–499. DOI: 10.1016/0029-554X(75)90743-0.

[77] Highland VL. Erratum: Some practical remarks on multiple scattering. *Nucl Instr Meth* (1979) 161:171.

[78] Parodi K and Polf JC. In vivo range verification in particle therapy. *Med Phys* (2018) 45(11):e1036–e1050. DOI: 10.1002/mp.12960.

[79] Parodi K. Latest developments in in-vivo imaging for proton therapy. *Br J Radiol* (2020) 93(1107):20190787. DOI: 10.1259/bjr.20190787.

[80] Kraan AC. Range Verification Methods in Particle Therapy: Underlying Physics and Monte Carlo Modeling. *Front Oncol* (2015) 5:150. DOI: 10.3389/fonc.2015.00150.

[81] Podgorsak EB. *Radiation physics for medical physicists.* 3rd edition. Springer: Cham (2016). DOI: 10.1007/978-3-319-25382-4.

[82] Ulmer W. Theoretical aspects of energy–range relations, stopping power and energy straggling of protons. *Rad Phys Chem* (2007) 76(7):1089–1107. DOI: 10.1016/j.radphyschem.2007.02.083.

[83] Schneider U, Pedroni E, and Lomax A. The calibration of CT Hounsfield units for radiotherapy treatment planning. *Phys Med Biol* (1996) 41(1):111–124. DOI: 10.1088/0031-9155/41/1/009.

[84] International Commission on Radiation Units and Measurements. *Prescribing, Recording, and Reporting Light Ion Beam Therapy.* ICRU Report No. 93. 2016.

[85] Inaniwa T and Kanematsu N. Effective particle energies for stopping power calculation in radiotherapy treatment planning with protons and helium, carbon, and oxygen ions. *Phys Med Biol* (2016) 61(20):N542–N550. DOI: 10.1088/0031-9155/61/20/N542.

[86] International Commission on Radiation Units and Measurements. *Stopping Powers and Ranges for Protons and Alpha Particles*. ICRU Report No. 49. 1993.

[87] Nystrom H, Jensen MF, and Nystrom PW. Treatment planning for proton therapy: what is needed in the next 10 years? *Br J Radiol* (2020) 93(1107):20190304. DOI: 10.1259/bjr.20190304.

[88] Chang AE, Matory YL, Dwyer AJ, et al. Magnetic resonance imaging versus computed tomography in the evaluation of soft tissue tumors of the extremities. *Ann Surg* (1987) 205(4):340–348. DOI: 10.1097/00000658-198704000-00002.

[89] International Commission on Radiation Units and Measurements. *Prescribing, Recording, and Reporting Photon Beam Therapy*. ICRU Report No. 50. 1993.

[90] International Commission on Radiation Units and Measurements. *Prescribing, Recording and Reporting Photon Beam Therapy (Supplement to ICRU 50)*. ICRU Report No. 62. 1999.

[91] van Herk M, Remeijer P, Rasch C, et al. The probability of correct target dosage: dose-population histograms for deriving treatment margins in radiotherapy. *Int J Radiat Oncol Biol Phys* (2000) 47(4):1121–1135. DOI: 10.1016/S0360-3016(00)00518-6.

[92] Lowe M, Albertini F, Aitkenhead A, et al. Incorporating the effect of fractionation in the evaluation of proton plan robustness to setup errors. *Phys Med Biol* (2015) 61(1):413. DOI: 10.1088/0031-9155/61/1/413.

[93] Bert C and Durante M. Motion in radiotherapy: particle therapy. *Phys Med Biol* (2011) 56(16):R113. DOI: 10.1088/0031-9155/56/16/R01.

[94] Paganetti H, Niemierko A, Ancukiewicz M, et al. Relative biological effectiveness (RBE) values for proton beam therapy. *Int J Radiat Oncol Biol Phys* (2002) 53(2):407–421. DOI: 10.1016/S0360-3016(02)02754-2.

[95] Paganetti H. Relative biological effectiveness (RBE) values for proton beam therapy. Variations as a function of biological endpoint, dose, and linear energy transfer. *Phys Med Biol* (2014) 59(22):R419. DOI: 10.1088/0031-9155/59/22/R419.

[96] Albertini F, Matter M, Nenoff L, et al. Online daily adaptive proton therapy. *Br J Radiol* (2020) 93(1107):20190594. DOI: 10.1259/bjr.20190594.

[97] Zhang M, Zou W, and Teo BK. Image guidance in proton therapy for lung cancer. *Transl Lung Cancer Res* (2018) 7(2):160–170. DOI: 10.21037/tlcr.2018.03.26.

[98] Unkelbach J and Paganetti H. Robust Proton Treatment Planning: Physical and Biological Optimization. *Sem Rad Onc* (2018) 28(2):88–96. DOI: 10.1016/j.semradonc.2017.11.005.

[99] Verellen D, Ridder M, Linthout N, et al. Innovations in image-guided radiotherapy. *Nat Rev Cancer* (2007) 7:949–960. DOI: 10.1038/nrc2288.

[100] Sodickson AD, Keraliya A, Czakowski B, et al. Dual energy CT in clinical routine: how it works and how it adds value. *Emerg Radiol* (2021) 28:103–117. DOI: 10.1007/s10140-020-01785-2.

[101] Di Chiro G and Brooks RA. The 1979 Nobel Prize in Physiology or Medicine. *Science* (1979) 206(4422):1060–1062. DOI: 10.1126/science.386516.

[102] Tan XM, Shah MTBM, Chong S-L, et al. Differences in radiation dose for computed tomography of the brain among pediatric patients at the emergency departments: an observational study. *BMC Emerg Med* (2021) 21:106. DOI: 10.1186/s12873-021-00502-7.

[103] Buzug T. *Computed Tomography. From Photon Statistics to Modern Cone-Beam CT.* 1st edition. Springer: Berlin, Heidelberg (2008). DOI: 10.1007/978-3-540-39408-2.

[104] Hawkes DJ and Jackson DF. An accurate parametrisation of the X-ray attenuation coefficient. *Phys Med Biol* (1980) 25(6):1167–1171. DOI: 10.1088/0031-9155/25/6/014.

[105] Klein O and Nishina Y. Über die Streuung von Strahlung durch freie Elektronen nach der neuen relativistischen Quantendynamik von Dirac. *Z Physik* (1929) 52:853–868. DOI: 10.1007/BF01366453.

[106] Fletcher JG, Leng S, Yu L, et al. Dealing with Uncertainty in CT Images. *Radiology* (2016) 279(1):5–10. DOI: 10.1148/radiol.2016152771.

[107] Schlegel W, Karger C, and Jäkel O, eds. *Medizinische Physik. Grundlagen – Bildgebung – Therapie – Technik.* 1st edition. Springer Spektrum: Berlin, Heidelberg (2018). DOI: 10.1007/978-3-662-54801-1.

[108] Schneider W, Bortfeld T, and Schlegel W. Correlation between CT numbers and tissue parameters needed for Monte Carlo simulations of clinical dose distributions. *Phys Med Biol* (2000) 45(2):459–478. DOI: 10.1088/0031-9155/45/2/314.

[109] Jäkel O, Jacob C, Schardt D, et al. Relation between carbon ion ranges and x-ray CT numbers. *Med Phys* (2001) 28(4):701–703. DOI: 10.1118/1.1357455.

[110] Woodard HQ and White DR. The composition of body tissues. *Br J Radiol* (1986) 59(708):1209–1218. DOI: 10.1259/0007-1285-59-708-1209.

[111] Wohlfahrt P, Möhler C, Hietschold V, et al. Clinical Implementation of Dual-energy CT for Proton Treatment Planning on Pseudo-monoenergetic CT scans. *Int J Radiat Oncol Biol Phys* (2017) 97(2):427–434. DOI: 10.1016/j.ijrobp.2016.10.022.

[112] Peters N, Taasti VT, Ackermann B, et al. Consensus guide on CT-based prediction of stopping-power ratio using a Hounsfield look-up table for proton therapy. *Radiother Oncol* (2023) 184:109675. DOI: 10.1016/j.radonc.2023.109675.

[113]   Phelps ME, Gado MH, and Hoffman EJ. Correlation of Effective Atomic Number and Electron Density with Attenuation Coefficients Measured with Polychromatic X Rays. *Radiology* (1975) 117(3):585–588. DOI: 10.1148/117.3.585.

[114]   Alvarez RE and Macovski A. Energy-selective reconstructions in X-ray computerised tomography. *Phys Med Biol* (1976) 21(5):733–744. DOI: 10.1088/0031-9155/21/5/002.

[115]   Alvarez R and Seppi E. A Comparison of Noise and Dose in Conventional and Energy Selective Computed Tomography. *IEEE Trans Nucl Sci* (1979) 26(2):2853–2856. DOI: 10.1109/TNS.1979.4330549.

[116]   Lehmann LA, Alvarez RE, Macovski A, et al. Generalized image combinations in dual kVp digital radiography. *Med Phys* (1981) 8(5):659–667. DOI: 10.1118/1.595025.

[117]   Kalender WA, Perman WH, Vetter JR, et al. Evaluation of a prototype dual-energy computed tomographic apparatus. I. Phantom studies. *Med Phys* (1986) 13(3):334–339. DOI: 10.1118/1.595958.

[118]   Johnson TRC, Krauß B, Sedlmair M, et al. Material differentiation by dual energy CT: initial experience. *Eur Radiol* (2007) 17:1510–1517. DOI: 10.1007/s00330-006-0517-6.

[119]   Jacobsen MC, Cressman ENK, Tamm EP, et al. Dual-Energy CT: Lower Limits of Iodine Detection and Quantification. *Radiology* (2019) 292(2):414–419. DOI: 10.1148/radiol.2019182870.

[120]   Fletcher JG, Takahashi N, Hartman R, et al. Dual-Energy and Dual-Source CT: Is There a Role in the Abdomen and Pelvis? *Radiol Clin North Am* (2009) 47(1):41–57. DOI: 10.1016/j.rcl.2008.10.003.

[121]   Millner MR, McDavid WD, Waggener RG, et al. Extraction of information from CT scans at different energies. *Med Phys* (1979) 6(1):70–71. DOI: 10.1118/1.594555.

[122]   Kalender WA, Perman WH, Vetter JR, et al. Evaluation of a prototype dual-energy computed tomographic apparatus. I. Phantom studies. *Med Phys* (1986) 13(3):334–339. DOI: 10.1118/1.595958.

[123]   Rutt B and Fenster A. Split-Filter Computed Tomography: A Simple Technique for Dual Energy Scanning. *J Comput Assist Tomogr* (1980) 4(4):501–509. DOI: 10.1097/00004728-198008000-00019.

[124]   Rassouli N, Etesami M, Dhanantwari A, et al. Detector-based spectral CT with a novel dual-layer technology: principles and applications. *Insights Imaging* (2017) 8:589–598. DOI: 10.1007/s13244-017-0571-4.

[125]   Große Hokamp N, Maintz D, Shapira N, et al. Technical background of a novel detector-based approach to dual-energy computed tomography. *Diagn Interv Radiol* (2020) 26:68–71. DOI: 10.5152/dir.2019.19136.

[126] Longarino FK, Kowalewski A, Tessonnier T, et al. Potential of a Second-Generation Dual-Layer Spectral CT for Dose Calculation in Particle Therapy Treatment Planning. *Front Oncol* (2022) 12:853495. DOI: 10.3389/fonc.2022.853495.

[127] Longarino FK, Tessonnier T, Mein S, et al. Dual-layer spectral CT for proton, helium, and carbon ion beam therapy planning of brain tumors. *J Appl Clin Med Phys* (2022) 23(1):e13465. DOI: 10.1002/acm2.13465.

[128] Longarino FK, Herpel C, Tessonnier T, et al. Dual-energy CT-based stopping power prediction for dental materials in particle therapy. *J Appl Clin Med Phys* (2023) 24(8):e13977. DOI: 10.1002/acm2.13977.

[129] Alkadhi H, Euler A, Maintz D, et al., eds. *Spectral Imaging. Dual-Energy, Multi-Energy and Photon-Counting CT*. 1st edition. Springer: Cham (2022). DOI: 10.1007/978-3-030-96285-2.

[130] Bazalova M, Carrier J-F, Beaulieu L, et al. Dual-energy CT-based material extraction for tissue segmentation in Monte Carlo dose calculations. *Phys Med Biol* (2008) 53(9):2439–2456. DOI: 10.1088/0031-9155/53/9/015.

[131] Beaulieu L, Bazalova M, Furstoss C, et al. SU-FF-T-408: Tissue Inhomogeneities in Monte Carlo Treatment Planning for Proton Therapy. *Med Phys* (2009) 36(6):2616–2616. DOI: 10.1118/1.3181890.

[132] Saito M. Potential of dual-energy subtraction for converting CT numbers to electron density based on a single linear relationship. *Med Phys* (2012) 39(4):2021–2030. DOI: 10.1118/1.3694111.

[133] Landry G, Seco J, Gaudreault M, et al. Deriving effective atomic numbers from DECT based on a parameterization of the ratio of high and low linear attenuation coefficients. *Phys Med Biol* (2013) 58(19):6851–6866. DOI: 10.1088/0031-9155/58/19/6851.

[134] Landry G, Parodi K, Wildberger JE, et al. Deriving concentrations of oxygen and carbon in human tissues using single- and dual-energy CT for ion therapy applications. *Phys Med Biol* (2013) 58(15):5029–5048. DOI: 10.1088/0031-9155/58/15/5029.

[135] Bourque AE, Carrier J-F, and Bouchard H. A stoichiometric calibration method for dual energy computed tomography. *Phys Med Biol* (2014) 59(8):2059–2088. DOI: 10.1088/0031-9155/59/8/2059.

[136] Hünemohr N, Krauss B, Tremmel C, et al. Experimental verification of ion stopping power prediction from dual energy CT data in tissue surrogates. *Phys Med Biol* (2014) 59(1):83–96. DOI: 10.1088/0031-9155/59/1/83.

[137] Hünemohr N, Paganetti H, Greilich S, et al. Tissue decomposition from dual energy CT data for MC based dose calculation in particle therapy. *Med Phys* (2014) 41(6):061714. DOI: 10.1118/1.4875976.

[138] van Abbema JK, van Goethem MJ, Greuter MJW, et al. Relative electron density determination using a physics based parameterization of photon interactions in medical DECT. *Phys Med Biol* (2015) 60(9):3825–3846. DOI: 10.1088/0031-9155/60/9/3825.

[139] Garcia LIR, Azorin JFP, and Almansa JF. A new method to measure electron density and effective atomic number using dual-energy CT images. *Phys Med Biol* (2016) 61(1):265–279. DOI: 10.1088/0031-9155/61/1/265.

[140] Han D, Siebers JV, and Williamson JF. A linear, separable two parameter model for dual energy CT imaging of proton stopping power computation. *Med Phys* (2016) 43(1):600–612. DOI: 10.1118/1.4939082.

[141] Lalonde A and Bouchard H. A general method to derive tissue parameters for Monte Carlo dose calculation with multi-energy CT. *Phys Med Biol* (2016) 61(22):8044–8069. DOI: 10.1088/0031-9155/61/22/8044.

[142] Möhler C, Wohlfahrt P, Richter C, et al. Range prediction for tissue mixtures based on dual-energy CT. *Phys Med Biol* (2016) 61(11):N268–N275. DOI: 10.1088/0031-9155/61/11/n268.

[143] Taasti VT, Petersen JBB, Muren LP, et al. A robust empirical parametrization of proton stopping power using dual energy CT. *Med Phys* (2016) 43(10):5547–5560. DOI: 10.1118/1.4962934.

[144] Zhu J and Penfold SN. Dosimetric comparison of stopping power calibration with dual-energy CT and single-energy CT in proton therapy treatment planning. *Med Phys* (2016) 43(6):2845–2854. DOI: 10.1118/1.4948683.

[145] Saito M and Sagara S. Simplified derivation of stopping power ratio in the human body from dual-energy CT data. *Med Phys* (2017) 44(8):4179–4187. DOI: 10.1002/mp.12386.

[146] Vilches-Freixas G, Létang JM, Ducros N, et al. Optimization of dual-energy CT acquisitions for proton therapy using projection-based decomposition. *Med Phys* (2017) 44(9):4548–4558. DOI: 10.1002/mp.12448.

[147] Zhang S, Han D, Politte DG, et al. Impact of joint statistical dual-energy CT reconstruction of proton stopping power images: Comparison to image- and sinogram-domain material decomposition approaches. *Med Phys* (2018) 45(5):2129–2142. DOI: 10.1002/mp.12875.

[148] Shen C, Li B, Chen L, et al. Material elemental decomposition in dual and multi-energy CT via a sparsity-dictionary approach for proton stopping power ratio calculation. *Med Phys* (2018) 45(4):1491–1503. DOI: 10.1002/mp.12796.

[149] Lee HHC, Park YK, Duan X, et al. Convolutional neural network based proton stopping-power-ratio estimation with dual-energy CT: a feasibility study. *Phys Med Biol* (2020) 65(21):215016. DOI: 10.1088/1361-6560/abab57.

[150] Park SH and Kang JO. Basics of particle therapy I: physics. *Radiat Oncol J* (2011) 29(3):135–146. DOI: 10.3857/roj.2011.29.3.135.

[151] Möhler C, Wohlfahrt P, Richter C, et al. Methodological accuracy of image-based electron density assessment using dual-energy computed tomography. *Med Phys* (2017) 44(6):2429–2437. DOI: 10.1002/mp.12265.

[152] Wohlfahrt P, Möhler C, Richter C, et al. Evaluation of Stopping-Power Prediction by Dual- and Single-Energy Computed Tomography in an Anthropomorphic Ground-Truth Phantom. *Int J Radiat Oncol Biol Phys* (2018) 100(1):244–253. DOI: 10.1016/j.ijrobp.2017.09.025.

[153] Rousselle A, Amelot A, Thariat J, et al. Metallic implants and CT artefacts in the CTV area: Where are we in 2020? *Cancer Radiother* (2020) 24(6):658–666. DOI: 10.1016/j.canrad.2020.06.022.

[154] Pettersson E, Bäck A, Björk-Eriksson T, et al. Structure delineation in the presence of metal – A comparative phantom study using single and dual-energy computed tomography with and without metal artefact reduction. *Phys Imaging Radiat Oncol* (2019) 9:43–49. DOI: 10.1016/j.phro.2019.01.001.

[155] Hansen DC, Seco J, Sørensen TS, et al. A simulation study on proton computed tomography (CT) stopping power accuracy using dual energy CT scans as benchmark. *Acta Oncol* (2015) 54(9):1638–1642. DOI: 10.3109/0284186X.2015.1061212.

[156] Hudobivnik N, Schwarz F, Johnson T, et al. Comparison of proton therapy treatment planning for head tumors with a pencil beam algorithm on dual and single energy CT images. *Med Phys* (2016) 43(1):495–504. DOI: 10.1118/1.4939106.

[157] Michalak G, Taasti VT, Krauss B, et al. A comparison of relative proton stopping power measurements across patient size using dual- and single-energy CT. *Acta Oncol* (2017) 56(11):1465–1471. DOI: 10.1080/0284186X.2017.1372625.

[158] Almeida IP, Landry G, Dedes G, et al. Evaluating Clinical Stopping Power Estimation from a Radiotherapy Dual Energy CT Scanner. *Acta Phys Pol B* (2017) 48(10):1619–1623. DOI: 10.5506/APhysPolB.48.1619.

[159] Li B, Lee HC, Duan X, et al. Comprehensive analysis of proton range uncertainties related to stopping-power-ratio estimation using dual-energy CT imaging. *Phys Med Biol* (2017) 62(17):7056–7074. DOI: 10.1088/1361-6560/aa7dc9.

[160] Xie Y, Ainsley C, Yin L, et al. Ex vivo validation of a stoichiometric dual energy CT proton stopping power ratio calibration. *Phys Med Biol* (2018) 63(5):055016. DOI: 10.1088/1361-6560/aaae91.

[161] Zhang S, Han D, Williamson JF, et al. Experimental implementation of a joint statistical image reconstruction method for proton stopping power mapping from dual-energy CT data. *Med Phys* (2019) 46(1):273–285. DOI: 10.1002/mp.13287.

[162] Faller FK, Mein S, Ackermann B, et al. Pre-clinical evaluation of dual-layer spectral computed tomography-based stopping power prediction for particle therapy planning at the Heidelberg Ion Beam Therapy Center. *Phys Med Biol* (2020) 65(9):095007. DOI: 10.1088/1361-6560/ab735e.

[163] Moskvin VP, Pirlepesov F, Yan Y, et al. Accuracy of stopping power ratio calculation and experimental validation of proton range with dual-layer computed tomography. *Acta Oncol* (2022) 61(7):864–868. DOI: 10.1080/0284186X.2022.2069477.

[164] Taasti VT, Høye EM, Hansen DC, et al. Technical Note: Improving proton stopping power ratio determination for a deformable silicone-based 3D dosimeter using dual energy CT. *Med Phys* (2016) 43(6):2780–2784. DOI: 10.1118/1.4948677.

[165] Möhler C, Russ T, Wohlfahrt P, et al. Experimental verification of stopping-power prediction from single- and dual-energy computed tomography in biological tissues. *Phys Med Biol* (2018) 63(2):025001. DOI: 10.1088/1361-6560/aaa1c9.

[166] Taasti VT, Michalak GJ, Hansen DC, et al. Validation of proton stopping power ratio estimation based on dual energy CT using fresh tissue samples. *Phys Med Biol* (2018) 63(1):015012. DOI: 10.1088/1361-6560/aa952f.

[167] Niepel KB, Stanislawski M, Wuerl M, et al. Animal tissue-based quantitative comparison of dual-energy CT to SPR conversion methods using high-resolution gel dosimetry. *Phys Med Biol* (2021) 66(7):075009. DOI: 10.1088/1361-6560/abbd14.

[168] Bär E, Lalonde A, Zhang R, et al. Experimental validation of two dual-energy CT methods for proton therapy using heterogeneous tissue samples. *Med Phys* (2018) 45(1):48–59. DOI: 10.1002/mp.12666.

[169] Taasti VT, Muren LP, Jensen K, et al. Comparison of single and dual energy CT for stopping power determination in proton therapy of head and neck cancer. *Phys Imaging Radiat Oncol* (2018) 6:14–19. DOI: 10.1016/j.phro.2018.04.002.

[170] Wohlfahrt P, Möhler C, Stützer K, et al. Dual-energy CT based proton range prediction in head and pelvic tumor patients. *Radiother Oncol* (2017) 125(3):526–533. DOI: 10.1016/j.radonc.2017.09.042.

[171] Almeida IP, Schyns LEJR, Vaniqui A, et al. Monte Carlo proton dose calculations using a radiotherapy specific dual-energy CT scanner for tissue segmentation and range assessment. *Phys Med Biol* (2018) 63(11):115008. DOI: 10.1088/1361-6560/aabb60.

[172] Chindasombatjaroen J, Kakimoto N, Murakami S, et al. Quantitative analysis of metallic artifacts caused by dental metals: comparison of cone-beam and multi-detector row CT scanners. *Oral Radiol* (2011) 27(2):114–120. DOI: 10.1007/s11282-011-0071-z.

[173] De Crop A, Casselman J, van Hoof T, et al. Analysis of metal artifact reduction tools for dental hardware in CT scans of the oral cavity: kVp, iterative reconstruction, dual-energy CT, metal artifact reduction software: does it make a difference? *Neuroradiology* (2015) 57(8):841–849. DOI: 10.1007/s00234-015-1537-1.

[174] Hu Y-H, Wan Chan Tseung HS, and Mundy DW. Physical characterization of therapeutic proton delivery through common dental materials. *Med Phys* (2022) 49(5):2904–2913. DOI: 10.1002/mp.15602.

[175] Bär E, Collins-Fekete C-A, Rompokos V, et al. Assessment of the impact of CT calibration procedures for proton therapy planning on pediatric treatments. *Med Phys* (2021) 48(9):5202–5218. DOI: 10.1002/mp.15062.

[176] Peters N, Wohlfahrt P, Dahlgren CV, et al. Experimental assessment of inter-centre variation in stopping-power and range prediction in particle therapy. *Radiother Oncol* (2021) 163:7–13. DOI: 10.1016/j.radonc.2021.07.019.

[177] Hansen CR, Crijns W, Hussein M, et al. Radiotherapy Treatment plannINg study Guidelines (RATING): A framework for setting up and reporting on scientific treatment planning studies. *Radiother Oncol* (2020) 153:67–78. DOI: 10.1016/j.radonc.2020.09.033.

[178] Tattenberg S, Madden TM, Gorissen BL, et al. Proton range uncertainty reduction benefits for skull base tumors in terms of normal tissue complication probability (NTCP) and healthy tissue doses. *Med Phys* (2021) 48(9):5356–5366. DOI: 10.1002/mp.15097.

[179] Taasti VT, Decabooter E, Eekers D, et al. Clinical benefit of range uncertainty reduction in proton treatment planning based on dual-energy CT for neuro-oncological patients. *Br J Radiol* (2023) 96(1149):20230110. DOI: 10.1259/bjr.20230110.

[180] Richard P, Sandison G, Dang Q, et al. Dental amalgam artifact: Adverse impact on tumor visualization and proton beam treatment planning in oral and oropharyngeal cancers. *Pract Radiat Oncol* (2015) 5(6):e583–e588. DOI: 10.1016/j.prro.2015.04.007.

[181] Falek S, Regmi R, Herault J, et al. Dental management in head and neck cancers: from intensity-modulated radiotherapy with photons to proton therapy. *Support Care Cancer* (2022) 30(10):8377–8389. DOI: 10.1007/s00520-022-07076-5.

[182] Sellerer T, Noël PB, Patino M, et al. Dual-energy CT: a phantom comparison of different platforms for abdominal imaging. *Eur Radiol* (2018) 28(7):2745–2755. DOI: 10.1007/s00330-017-5238-5.

[183] Schaly B, Varchena V, Au P, et al. Evaluation of an anthropomorphic male pelvic phantom for image-guided radiotherapy. *Rep Med Imaging* (2009) 2:69–78. DOI: 10.2147/RMI.S6114.

[184] Li H, Dolly S, Chen H-C, et al. A comparative study based on image quality and clinical task performance for CT reconstruction algorithms in radiotherapy. *J Appl Clin Med Phys* (2016) 17(4):377–390. DOI: 10.1120/jacmp.v17i4.5763.

[185] Grevillot L, Stock M, Palmans H, et al. Implementation of dosimetry equipment and phantoms at the MedAustron light ion beam therapy facility. *Med Phys* (2018) 45(1):352–369. DOI: 10.1002/mp.12653.

[186] Farace P, Righetto R, and Meijers A. Pencil beam proton radiography using a multilayer ionization chamber. *Phys Med Biol* (2016) 61(11):4078–4087. DOI: 10.1088/0031-9155/61/11/4078.

[187] Johnson RP. Review of medical radiography and tomography with proton beams. *Rep Prog Phys* (2018) 81(1):016701. DOI: 10.1088/1361-6633/aa8b1d.

[188] Draeger E, Mackin D, Peterson S, et al. 3D prompt gamma imaging for proton beam range verification. *Phys Med Biol* (2018) 63(3):035019. DOI: 10.1088/1361-6560/aaa203.

[189] Hueso-González F, Rabe M, Ruggieri TA, et al. A full-scale clinical prototype for proton range verification using prompt gamma-ray spectroscopy. *Phys Med Biol* (2018) 63(18):185019. DOI: 10.1088/1361-6560/aad513.

[190] Richter C, Pausch G, Barczyk S, et al. First clinical application of a prompt gamma based in vivo proton range verification system. *Radiother Oncol* (2016) 118(2):232–237. DOI: 10.1016/j.radonc.2016.01.004.

[191] Lee HHC, Li B, Duan X, et al. Systematic analysis of the impact of imaging noise on dual-energy CT-based proton stopping power ratio estimation. *Med Phys* (2019) 46(5):2251–2263. DOI: 10.1002/mp.13493.

[192] Wohlfahrt P, Troost EGC, Hofmann C, et al. Clinical Feasibility of Single-Source Dual-spiral 4D Dual-Energy CT for Proton Treatment Planning Within the Thoracic Region. *Int J Radiat Oncol Biol Phys* (2018) 102(4):830–840. DOI: 10.1016/j.ijrobp.2018.06.044.

[193] Ohira S, Wada K, Hirata T, et al. Clinical implementation of contrast-enhanced four-dimensional dual-energy computed tomography for target delineation of pancreatic cancer. *Radiother Oncol* (2018) 129(1):105–111. DOI: 10.1016/j.radonc.2018.01.012.

[194] Chacko MS, Grewal HS, Wu D, et al. Accuracy of proton stopping power estimation of silicone breast implants with single and dual-energy CT calibration techniques. *J Appl Clin Med Phys* (2021) 22(9):159–170. DOI: 10.1002/acm2.13358.

[195] Jacobsen MC, Schellingerhout D, Wood CA, et al. Intermanufacturer Comparison of Dual-Energy CT Iodine Quantification and Monochromatic Attenuation: A Phantom Study. *Radiology* (2018) 287(1):224–234. DOI: 10.1148/radiol.2017170896.

[196] Kim Y, Kim JS, and Cho S. Feasibility study of using triple-energy CT images for improving stopping power estimation. *Nucl Eng Technol* (2023) 55(4):1342–1349. DOI: 10.1016/j.net.2022.12.018.

[197] Lell MM and Kachelrieß M. Recent and Upcoming Technological Developments in Computed Tomography: High Speed, Low Dose, Deep Learning, Multienergy. *Investig Radiol* (2020) 55(1):8–19. DOI: 10.1097/RLI.0000000000000601.

[198] Richtsmeier D, O'Connell J, Rodesch P-A, et al. Metal artifact correction in photon-counting detector computed tomography: metal trace replacement using high-energy data. *Med Phys* (2023) 50(1):380–396. DOI: 10.1002/mp.16049.

[199] Toepker M, Czerny C, Ringl H, et al. Can dual-energy CT improve the assessment of tumor margins in oral cancer? *Oral Oncol* (2014) 50(3):221–227. DOI: 10.1016/j.oraloncology. 2013.12.001.

[200] Wichmann JL, Nöske E-M, Kraft J, et al. Virtual Monoenergetic Dual-Energy Computed Tomography: Optimization of Kiloelectron Volt Settings in Head and Neck Cancer. *Investig Radiol* (2014) 49(11):735–741. DOI: 10.1097/RLI.0000000000000077.

[201] Lalonde A, Xie Y, Burgdorf B, et al. Influence of intravenous contrast agent on dose calculation in proton therapy using dual energy CT. *Phys Med Biol* (2019) 64(12):125024. DOI: 10.1088/1361-6560/ab1e9d.

[202] Ates O, Hua C-H, Zhao L, et al. Feasibility of using post-contrast dual-energy CT for pediatric radiation treatment planning and dose calculation. *Br J Radiol* (2021) 94(1118):20200170. DOI: 10.1259/bjr.20200170.

[203] Noid G, Godfrey G, Hall W, et al. Predicting Treatment Response From Extracellular Volume Fraction for Chemoradiation Therapy of Pancreatic Cancer. *Int J Radiat Oncol Biol Phys* (2023) 115(3):803–808. DOI: 10.1016/j.ijrobp.2022.09.084.
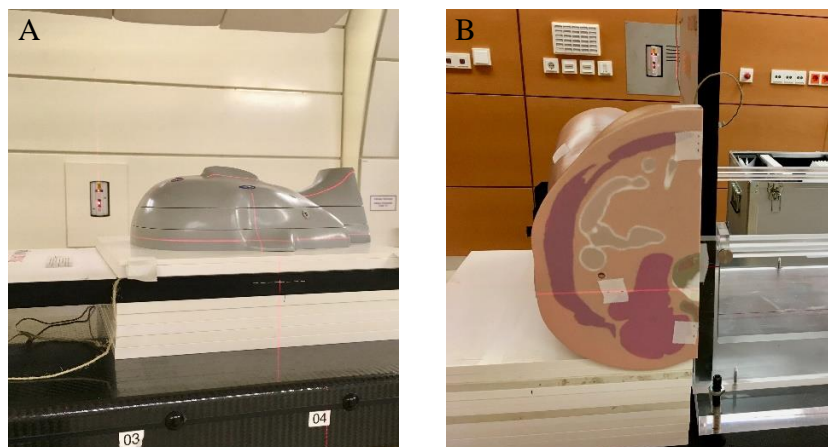
Appendix

Supplementary material for publication 1

Supplementary Material

1 Supplementary Figures and Tables
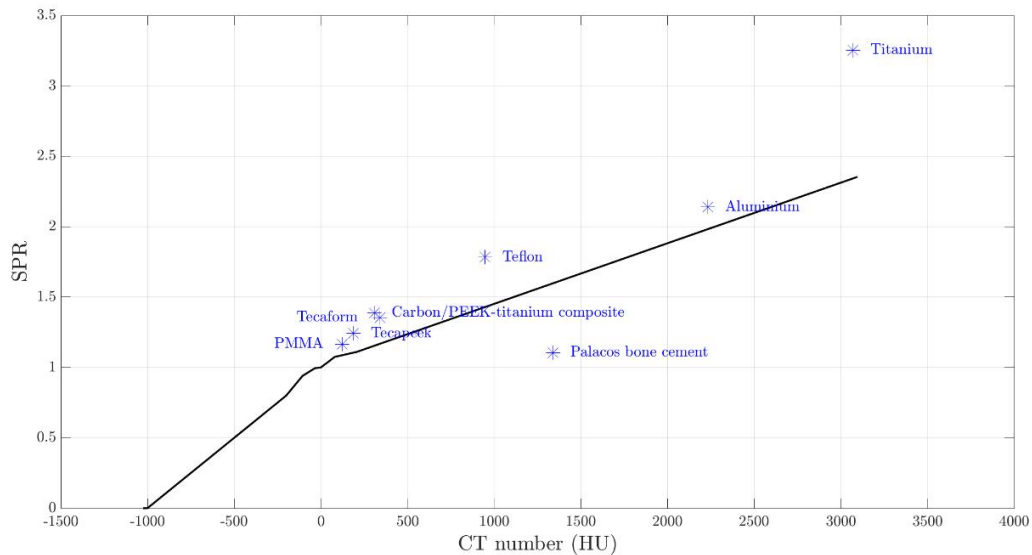
Supplementary Figure 1. Single-energy CT (SECT)-based CT-number-to-stopping-power-ratio (SPR) calibration curve, or Hounsfield look-up table (HLUT), together with the eight non-tissue implant materials used in this study.

Supplementary Figure 2. Dosimetric measurements with anthropomorphic head and pelvic phantoms. For the head phantom (A), irradiation was performed using the gantry at an angle of 0° with the half-head phantom placed on top of the OCTAVIUS® detector. For the pelvic phantom (B), irradiation was performed using the horizontal beam line with the half-pelvic phantom placed in front of the OCTAVIUS® detector.

Technical features	Dual-source CT	Dual-spiral	Fast tube voltage switching	Twin-beam	Dual-layer detector	Photon-counting CT
Spectral mode	spectral mode preselection, prospective results generation	spectral mode preselection, prospective results generation	spectral mode preselection, prospective results generation	spectral mode preselection, prospective results generation	no special mode, pro- and retrospective results generation	no special mode, pro- and retrospective results generation
Acquisition mode	dedicated dual-energy	dedicated dual-energy	dedicated dual-energy	dedicated dual-energy	implicit dual-energy	implicit multi-energy
Temporal coherence	high (quarter rotation angular offset)	low (large offset)	high (nearly perfect alignment)	medium (half collimation offset)	perfect alignment	perfect alignment
Spatio-temporal resolution	full capabilities	full capabilities	limited capabilities (impaired spatial resolution)	full capabilities	full capabilities	full capabilities (superior spatial resolution)
Availability of dose modulation	yes (individual tube current modulation)	yes (individual tube current modulation)	no (no tube current modulation)	yes (tube current modulation)	yes (tube current modulation)	yes (tube current modulation)
Spectral separation	very high (with additional tin filtration)	very high	medium ("smearing of spectra" due to finite kV-switching times)	low	medium	high
Cross-scatter occurrence	between source–detector systems	no	no	between detector rows (halves) separated by the system's central vertical plane	between detector layers	no
Field-of-view	limited (up to 350 mm)	full	full	full	full	full

Time-resolved respiratory imaging	feasible with phase matching in post-processing	feasible with phase matching in post-processing	feasible with phase matching in post-processing	feasible with phase matching in post-processing	no technical limitations	no technical limitations
Contrast-enhanced imaging	multi-phase (arterial and venous)	limited to late or delayed phase	multi-phase (arterial and venous)	limited to late or delayed phase	multi-phase (arterial and venous)	multi-phase (arterial and venous)
Spectral decompo-sition	image-based material decomposition	image-based material decomposition	projection-based material decomposition	image-based material decomposition	projection-based material decomposition	projection-based material decomposition

Supplementary Table 1. Comparison of different dual-energy or spectral CT acquisition techniques with a focus on particle therapy treatment planning. Note that despite having the potential to provide spectral data, CT systems with energy-resolving, photon-counting detectors are just starting to become clinically available but do not yet see widespread use.

	Dual-source CT	Dual-spiral	Fast tube voltage switching	Twin-beam	Dual-layer detector	Photon-counting CT
Theoretical studies	• [4] Bär et al (2017)					• [27] Taasti et al (2018)
Phantom studies (phantoms with simplified geometries or anthropo-morphic phantoms)	• [2] Almeida et al (2018) • [4] Bär et al (2017) • [5] Bär et al (2018) • [7] Bourque et al (2014) • [10] Hansen et al (2015) • [11] Hudobivnik et al (2016) • [12] Hünemohr et al (2014) • [15] Li et al (2017) • [17] Michalak et al (2017) • [23] Saito et al (2017) • [29] Wohlfahrt et al (2018)	• [1] Almeida et al (2017) • [2] Almeida et al (2018) • [8] Chacko et al (2021) • [19] Mossahebi et al (2020) • [24] Shen et al (2018) • [33] Zhang et al (2019) • [34] Zhu & Penfold (2016)	• [21] Ohira et al (2022)	• [2] Almeida et al (2018)	• [9] Faller et al (2020) • [13] Landry et al (2019) • [20] Ohira et al (2018)	• [14] Lee et al (2021)
Biological tissue sample studies (homo-geneous or hetero-geneous tissue samples)	• [5] Bär et al (2018) • [18] Möhler et al (2018) • [25] Taasti et al (2017)	• [25] Taasti et al (2017) • [32] Xie et al (2018)		• [25] Taasti et al (2017)		• [27] Taasti et al (2018)

| Patient studies | • [6] Bär et al (2021)
 • [11] Hudobivnik et al (2016)
 • [26] Taasti et al (2018) | • [2] Almeida et al (2018)
 • [22] Peters et al (2021)
 • [26] Taasti et al (2018)
 • [28] Wohlfahrt et al (2017)
 • [30] Wohlfahrt et al (2018)
 • [31] Wohlfahrt et al (2019) | • [3] Ates et al (2021)
 • [16] Longarino et al (2022) |

Supplementary Table 2. Selected publications of different dual-energy or spectral CT acquisition techniques currently available with a focus on particle therapy treatment planning. Note: The table is in alphabetical order and might not be exhaustive.

[1] Almeida et al (2017): Siemens SOMATOM Definition Open AS
[2] Almeida et al (2018): Siemens SOMATOM Force, Siemens SOMATOM Confidence RT Pro, Siemens SOMATOM Definition Edge
[3] Ates et al (2021): Philips IQon Spectral CT
[4] Bär et al (2017): Siemens SOMATOM Definition Flash
[5] Bär et al (2018): Siemens SOMATOM Definition Flash
[6] Bär et al (2021): Siemens SOMATOM Definition Flash
[7] Bourque et al (2014): Siemens SOMATOM Definition Flash
[8] Chacko et al (2021): Siemens SOMATOM Confidence RT Pro
[9] Faller et al (2020): Philips IQon Spectral CT
[10] Hansen et al (2015): Siemens SOMATOM Definition Flash
[11] Hudobivnik et al (2016): Siemens SOMATOM Force
[12] Hünemohr et al (2014): Siemens SOMATOM Definition Flash
[13] Landry et al (2019): Philips IQon Spectral CT
[14] Lee et al (2021): Energy-differentiation-type 64-channel cadmium telluride (CdTe) radiation line sensor module (C10413, Hamamatsu, Japan)
[15] Li et al (2015): Siemens SOMATOM Force
[16] Longarino et al (2022): Philips IQon Spectral CT
[17] Michalak et al (2017): Siemens SOMATOM Force
[18] Möhler et al (2018): Siemens SOMATOM Definition Flash
[19] Mossahebi et al (2020): Siemens SOMATOM Definition Edge
[20] Ohira et al (2018): Philips IQon Spectral CT
[21] Ohira et al (2022): GE Healthcare Revolution HD
[22] Peters et al (2021): Siemens SOMATOM Definition AS
[23] Saito et al (2017): Siemens SOMATOM Definition Flash
[24] Shen et al (2018): GE Healthcare LightSpeed QX/i
[25] Taasti et al (2017): Siemens SOMATOM Definition AS, Siemens SOMATOM Definition Flash, Siemens SOMATOM Force, Siemens SOMATOM Definition Edge
[26] Taasti et al (2018): Siemens SOMATOM Definition Flash, Philips Brilliance Big Bore
[27] Taasti et al (2018): Siemens research SOMATOM CounT
[28] Wohlfahrt et al (2017): Siemens SOMATOM Definition AS
[29] Wohlfahrt et al (2018): Siemens SOMATOM Definition AS
[30] Wohlfahrt et al (2018): Siemens SOMATOM Definition AS
[31] Wohlfahrt et al (2019): Siemens SOMATOM Definition AS
[32] Xie et al (2018): Siemens SOMATOM Sensation Open
[33] Zhang et al (2019): Philips Brilliance Big Bore
[34] Zhu & Penfold (2016): Philips Brilliance Big Bore

Feature	Spectral CT 7500	IQon Spectral CT
Generator power	120 kW	120 kW
Maximum detector collimation	128×0.625 mm	64×0.625 mm
Coverage (per rotation)	80 mm	40 mm
Minimum gantry rotation time	0.27 s	0.27 s
Maximum scannable range (axial)	2000 mm	2100 mm
Bore size	800 mm	700 mm
Conventional reconstruction time	iDose[4]: 93% of reference protocols under 1 minute	iDose[4]: majority of reference protocols under 1 minute
Spectral reconstruction time	1–2 minutes for the majority of cases	3–5 minutes for the majority of cases
Spectral temporal resolution	Simultaneous in the same time and space	Simultaneous in the same time and space
Spectral kV_p stations	100, 120, 140	120, 140

Supplementary Table 3. Comparison of the Philips Spectral CT 7500 [35] and IQon Spectral CT [36] scanners.

Protocol	Tube voltage (kV_p)	Tube current-time product (mAs)	Colli-mation (mm)	Rotation time (s)	Pitch	$CTDI_{vol}$ (mGy)	Slice thickness and spacing (mm)	Recon-struction filter
Head	120	300	64×0.625	0.5	0.8	47.2	1.5	UB
Body	120	300	128×0.625	0.5	0.8	23.2	2.0	B

Supplementary Table 4. Image acquisition settings and reconstruction parameters for head and body protocols.

Phantom	LC				SC			
Protocol	Head	Body			Head	Body		
iDose^4 level	0	0	3	6	0	0	3	6
Mean overall relative residual	0.728	0.725	0.723	0.724	0.761	0.613	0.579	0.605
RMSE	0.0086	0.0084	0.0085	0.0084	0.0089	0.0056	0.0056	0.0057
r	0.9998	0.9998	0.9998	0.9998	0.9998	0.9998	0.9998	0.9998
α	1.016	1.011	1.011	1.001	1.015	1.005	1.005	1.005
δ	–0.012	–0.006	–0.006	–0.006	–0.010	–0.002	–0.001	–0.002

Supplementary Table 5. Accuracy of dual-layer spectral CT (DLCT)-based stopping power ratio (SPR) predictions across head and body protocols and iDose^4 levels 0, 3, and 6 for the LC ("long cylinder") phantom and SC ("short cylinder") phantom.

Phantom	LC				SC			
Protocol	Head	Body			Head	Body		
iDose^4 level	0	0	3	6	0	0	3	6
Mean overall relative residual	1.514	1.538	1.540	1.537	1.515	1.514	1.523	1.516
RMSE	0.0246	0.0255	0.0256	0.0256	0.0240	0.0243	0.0244	0.0243
r	0.9958	0.9956	0.9956	0.9956	0.9959	0.9958	0.9958	0.9958
α	1.009	1.012	1.012	1.012	1.005	1.007	1.008	1.008
δ	–0.009	–0.009	–0.009	–0.009	–0.007	–0.008	–0.008	–0.008

Supplementary Table 6. Accuracy of single-energy CT (SECT)-based stopping power ratio (SPR) predictions across head and body protocols and iDose^4 levels 0, 3, and 6 for the LC ("long cylinder") phantom and SC ("short cylinder") phantom.

2 References

[1] Almeida IP, Landry G, Dedes G, Patel R, Pankuch M, Coutrakon G et al. Evaluating clinical stopping power estimation from a radiotherapy dual energy CT scanner. Acta Phys Pol B (2017) 48(10):1619-1623. doi:10.5506/APhysPolB.48.1619

[2] Almeida IP, Schyns LEJR, Vaniqui A, van der Heyden B, Dedes G, Resch AF et al. Monte Carlo proton dose calculations using a radiotherapy specific dual-energy CT scanner for tissue segmentation and range assessment. Phys Med Biol (2018) 63(11):115008. doi: 10.1088/1361-6560/aabb60

[3] Ates O, Hua CH, Zhao L, Shapira N, Yagil Y, Merchant TE et al. Feasibility of using post-contrast dual-energy CT for pediatric radiation treatment planning and dose calculation. Br J Radiol (2021) 94(1118):20200170. doi: 10.1259/bjr.20200170

[4] Bär E, Lalonde A, Royle G, Lu HM, Bouchard H. The potential of dual-energy CT to reduce proton beam range uncertainties. Med Phys (2017) 44(6):2332-2344. doi: 10.1002/mp.12215

[5] Bär E, Lalonde A, Zhang R, Jee KW, Yang K, Sharp G et al. Experimental validation of two dual-energy CT methods for proton therapy using heterogeneous tissue samples. Med Phys (2018) 45(1):48-59. doi: 10.1002/mp.12666

[6] Bär E, Collins-Fekete CA, Rompokos V, Zhang Y, Gaze MN, Warry A et al. Assessment of the impact of CT calibration procedures for proton therapy planning on pediatric treatments. Med Phys (2021) 48(9):5202-5218. doi: 10.1002/mp.15062

[7] Bourque AE, Carrier JF, Bouchard H. A stoichiometric calibration method for dual energy computed tomography. Phys Med Biol (2014) 59(8):2059-2088. doi: 10.1088/0031-9155/59/8/2059

[8] Chacko MS, Grewal HS, Wu D, Sonnad JR. Accuracy of proton stopping power estimation of silicone breast implants with single and dual-energy CT calibration techniques. J Appl Clin Med Phys (2021) 22(9):159-170. doi: 10.1002/acm2.13358

[9] Faller FK, Mein S, Ackermann B, Debus J, Stiller W, Mairani A. Pre-clinical evaluation of dual-layer spectral computed tomography-based stopping power prediction for particle therapy planning at the Heidelberg Ion Beam Therapy Center. Phys Med Biol (2020) 65(9):095007. doi: 10.1088/1361-6560/ab735e

[10] Hansen DC, Seco J, Sørensen TS, Petersen JB, Wildberger JE, Verhaegen F et al. A simulation study on proton computed tomography (CT) stopping power accuracy using dual energy CT scans as benchmark. Acta Oncol (2015) 54(9):1638-1642. doi: 10.3109/0284186X.2015.1061212

[11] Hudobivnik N, Schwarz F, Johnson T, Agolli L, Dedes G, Tessonnier T et al. Comparison of proton therapy treatment planning for head tumors with a pencil beam algorithm on dual and single energy CT images. Med Phys (2016) 43(1):495-504. doi: 10.1118/1.4939106

[12] Hünemohr N, Krauss B, Tremmel C, Ackermann B, Jäkel O, Greilich S. Experimental verification of ion stopping power prediction from dual energy CT data in tissue surrogates. Phys Med Biol (2014) 59(1):83-96. doi: 10.1088/0031-9155/59/1/83

[13] Landry G, Dörringer F, Si-Mohamed S, Douek P, Abascal JFPJ, Peyrin F et al. Technical Note: Relative proton stopping power estimation from virtual monoenergetic images reconstructed from dual-layer computed tomography. Med Phys (2019) 46(4):1821-1828. doi: 10.1002/mp.13404

[14] Lee SH, Sunaguchi N, Nagao A, Hirano Y, Sakurai H, Kano Y et al. Calculation of Stopping-Power Ratio from Multiple CT Numbers Using Photon-Counting CT System: Two- and Three-Parameter-Fitting Method. Sensors (2021) 21(4):1215. doi: 10.3390/s21041215

[15] Li B, Lee HC, Duan X, Shen C, Zhou L, Jia X et al. Comprehensive analysis of proton range uncertainties related to stopping-power-ratio estimation using dual-energy CT imaging. Phys Med Biol (2017) 62(17):7056-7074. doi: 10.1088/1361-6560/aa7dc9

[16] Longarino FK, Tessonnier T, Mein S, Harrabi SB, Debus J, Stiller W et al. Dual-layer spectral CT for proton, helium, and carbon ion beam therapy planning of brain tumors. J Appl Clin Med Phys (2022) 23(1):e13465. doi: 10.1002/acm2.13465

[17] Michalak G, Taasti V, Krauss B, Deisher A, Halaweish A, McCollough C. A comparison of relative proton stopping power measurements across patient size using dual- and single-energy CT. Acta Oncol (2017) 56(11):1465-1471. doi: 10.1080/0284186X.2017.1372625

[18] Möhler C, Russ T, Wohlfahrt P, Elter A, Runz A, Richter C et al. Experimental verification of stopping-power prediction from single- and dual-energy computed tomography in biological tissues. Phys Med Biol (2018) 63(2):025001. doi: 10.1088/1361-6560/aaa1c9

[19] Mossahebi S, Sabouri P, Chen H, Mundis M, O'Neil M, Maggi P et al. Initial Validation of Proton Dose Calculations on SPR Images from DECT in Treatment Planning System. Int J Part Ther (2020) 7(2):51-61. doi: 10.14338/IJPT-XX-000XX.1

[20] Ohira S, Washio H, Yagi M, Karino T, Nakamura K, Ueda Y et al. Estimation of electron density, effective atomic number and stopping power ratio using dual-layer computed tomography for radiotherapy treatment planning. Physica Medica (2018) 56:34-40. doi: 10.1016/j.ejmp.2018.11.008

[21] Ohira S, Imai Y, Koike Y, Ono S, Ueda Y, Miyazaki M et al. Evaluation of Stopping Power Ratio Calculation Using Dual-energy Computed Tomography With Fast Kilovoltage Switching for Treatment Planning of Particle Therapy. In Vivo (2022) 36(1):103-110. doi: 10.21873/invivo.12681

[22] Peters N, Wohlfahrt P, Hofmann C, Möhler C, Menkel S, Tschiche M et al. Reduction of clinical safety margins in proton therapy enabled by the clinical implementation of dual-energy CT for direct stopping-power prediction. Radiother Oncol (2021) 166:71-78. doi: 10.1016/j.radonc.2021.11.002

[23] Saito M, Sagara S. Simplified derivation of stopping power ratio in the human body from dual-energy CT data. Med Phys (2017) 44(8):4179-4187. doi: 10.1002/mp.12386

[24] Shen C, Li B, Chen L, Yang M, Lou Y, Jia X. Material elemental decomposition in dual and multi-energy CT via a sparsity-dictionary approach for proton stopping power ratio calculation. Med Phys (2018) 45(4):1491-1503. doi: 10.1002/mp.12796

[25] Taasti VT, Michalak GJ, Hansen DC, Deisher AJ, Kruse JJ, Krauss B et al. Validation of proton stopping power ratio estimation based on dual energy CT using fresh tissue samples. Phys Med Biol (2017) 63(1):015012. doi: 10.1088/1361-6560/aa952f

[26] Taasti VT, Muren LP, Jensen K, Petersen JBB, Thygesen J, Tietze A et al. Comparison of single and dual energy CT for stopping power determination in proton therapy of head and neck cancer. Phys Imaging Radiat Oncol (2018) 6:14-19. doi: 10.1016/j.phro.2018.04.002

[27] Taasti VT, Hansen DC, Michalak GJ, Deisher AJ, Kruse JJ, Muren LP et al. Theoretical and experimental analysis of photon counting detector CT for proton stopping power prediction. Med Phys (2018) 45(11):5186-5196. doi: 10.1002/mp.13173

[28] Wohlfahrt P, Möhler C, Stützer K, Greilich S, Richter C. Dual-energy CT based proton range prediction in head and pelvic tumor patients. Radiother Oncol (2017) 125(3):526-533. doi: 10.1016/j.radonc.2017.09.042

[29] Wohlfahrt P, Möhler C, Richter C, Greilich S. Evaluation of Stopping-Power Prediction by Dual- and Single-Energy Computed Tomography in an Anthropomorphic Ground-Truth Phantom. Int J Radiat Oncol Biol Phys (2018) 100(1):244-253. doi: 10.1016/j.ijrobp.2017.09.025

[30] Wohlfahrt P, Troost EGC, Hofmann C, Richter C, Jakobi A. Clinical Feasibility of Single-Source Dual-spiral 4D Dual-Energy CT for Proton Treatment Planning Within the Thoracic Region. Int J Radiat Oncol Biol Phys (2018) 102(4):830-840. doi: 10.1016/j.ijrobp.2018.06.044

[31] Wohlfahrt P, Möhler C, Troost EGC, Greilich S, Richter C. Dual-Energy Computed Tomography to Assess Intra- and Inter-Patient Tissue Variability for Proton Treatment Planning of Patients With Brain Tumor. Int J Radiat Oncol Biol Phys (2019) 105(3):504-513. doi: 10.1016/j.ijrobp.2019.06.2529

[32] Xie Y, Ainsley C, Yin L, Zou W, McDonough J, Solberg TD et al. Ex vivo validation of a stoichiometric dual energy CT proton stopping power ratio calibration. Phys Med Biol (2018) 63(5):055016. doi: 10.1088/1361-6560/aaae91

[33] Zhang S, Han D, Williamson JF, Zhao T, Politte DG, Whiting BR et al. Experimental implementation of a joint statistical image reconstruction method for proton stopping power mapping from dual-energy CT data. Med Phys (2019) 46(1):273-285. doi: 10.1002/mp.13287

[34] Zhu J, Penfold SN. Dosimetric comparison of stopping power calibration with dual-energy CT and single-energy CT in proton therapy treatment planning. Med Phys (2016) 43(6):2845-2854. doi: 10.1118/1.4948683

[35] Philips. Spectral CT 7500 (2021). URL: https://www.usa.philips.com/healthcare/product/728333/spectral-ct-7500-philips-all-new-spectral-detector-ct-750 [accessed November 22, 2021]

[36] Philips. IQon Spectral CT (2021). URL: https://www.usa.philips.com/healthcare/product/HCNOCTN284/iqon-spectral-ct-certainty-lives-in-layers [accessed November 22, 2021]

Supplementary material for publication 2

Dual-layer spectral CT for proton, helium and carbon ion-beam therapy planning of brain tumors

SUPPLEMENTARY MATERIAL

S1 Single-energy CT-based Hounsfield look-up table

The Hounsfield look-up table (HLUT) derived in the single-energy CT (SECT)-based approach is shown in figure 1.
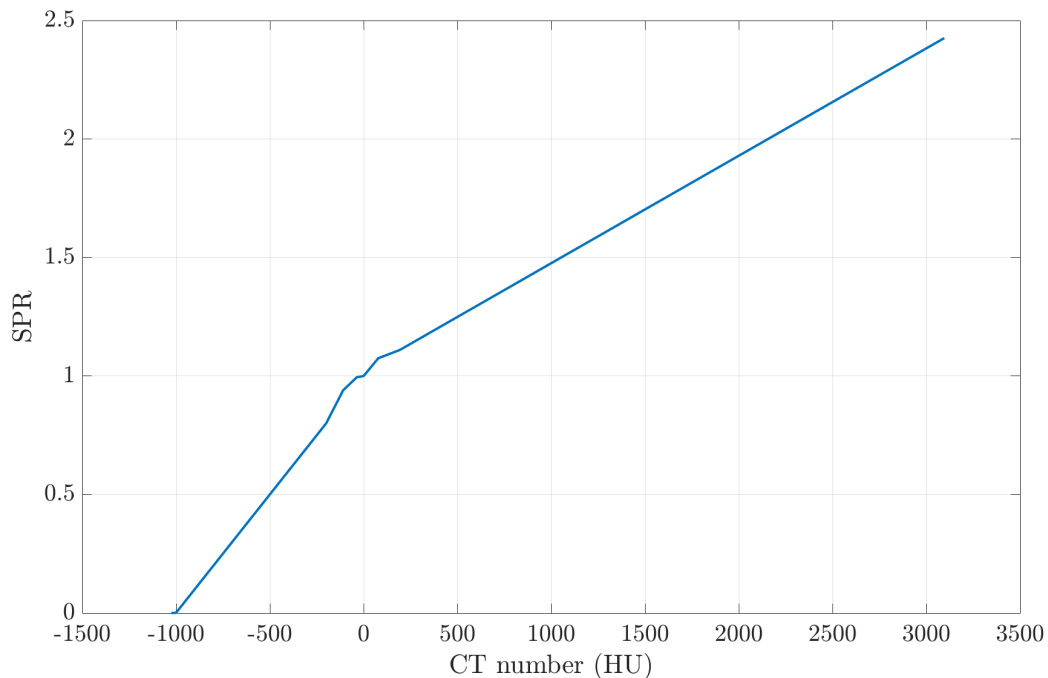

Figure 1: Single-energy CT (SECT)-based CT-number-to-stopping-power-ratio (SPR) calibration curve, or Hounsfield look-up table (HLUT), used in this study.

S2 Stopping power ratio predictions in homogeneous tissue regions

Figure 2 depicts representative regions-of-interest (ROIs) for stopping power ratio relative to water (SPR) predictions in relatively homogeneous tissue regions.
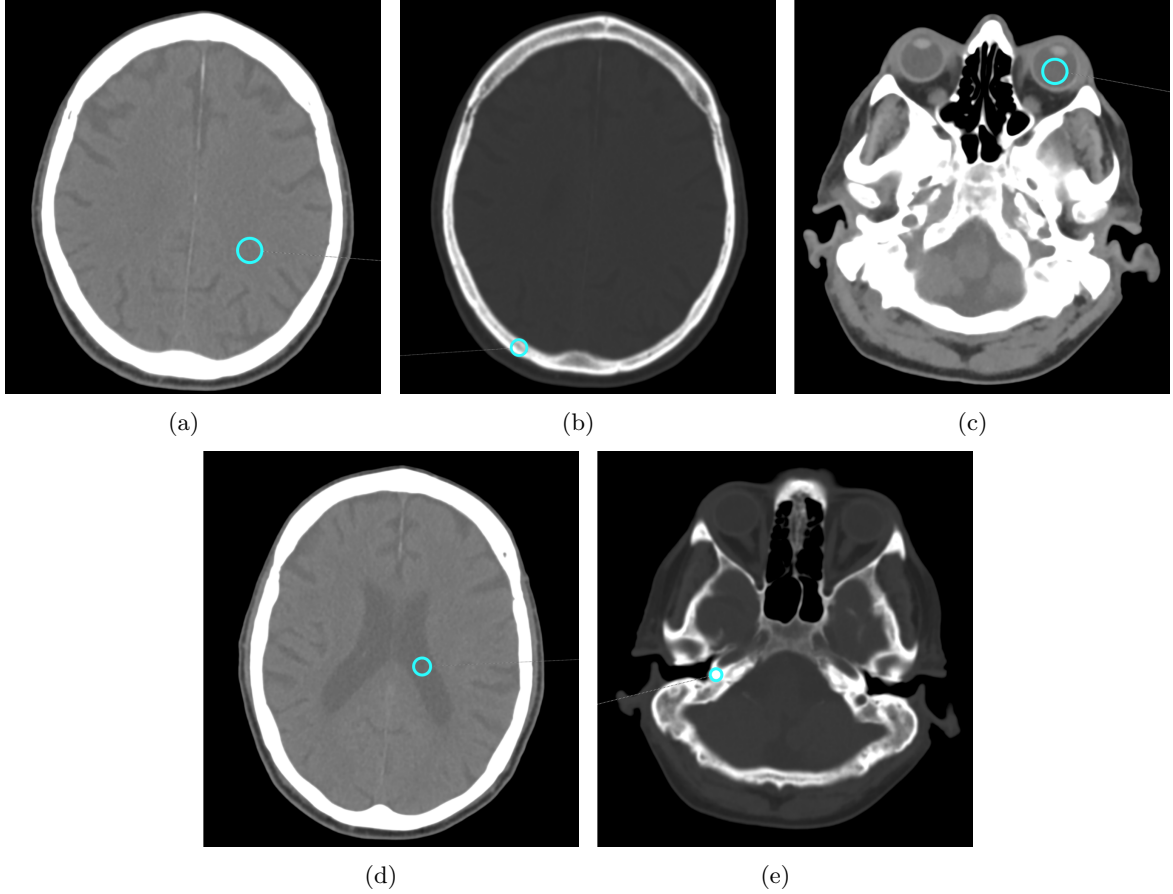
Figure 2: Representative regions-of-interest (ROIs) for a study patient (patient #1) showing brain (a), cranial bone (b), eyes (c), lateral ventricles (d), and skull base bone (e). Brain, eyes, and lateral ventricles are shown in a soft tissue window (window width: 400 HU, window center: 40 HU), whereas cranial bone and skull base bone are displayed in a bone window (window width: 1500 HU, window center: 450 HU).

S3 Analysis of dual-layer spectral CT data-based stopping power ratio prediction in head patients

SPR difference maps were generated by subtracting the SECT- from the dual-layer spectral CT (DLCT)-based SPR map and taken relative to the SPR in the DLCT-based SPR maps (DLCT was used as reference analogous to previous studies). Statistical analysis of SPR comparison between DLCT- and SECT-based methods was conducted on a per-patient basis. The absolute SPR deviation over each ROI ($SPR_{DLCT} - SPR_{SECT}$) was taken relative to the SPR value in the DLCT-based SPR map, respectively, similarly to Taasti et al. [1]:

$$\delta_{SPR} = \frac{\Delta SPR}{SPR_{DLCT}} \cdot 100\ \% = \frac{SPR_{DLCT} - SPR_{SECT}}{SPR_{DLCT}} \cdot 100\ \% \tag{1}$$

The standard deviation over n investigated slices was calculated, respectively:

$$s(\delta_{SPR}) = \sqrt{\frac{\sum_{i=1}^{n}(\delta_{SPR,i} - \overline{\delta}_{SPR})^2}{n-1}} \tag{2}$$

Here, $\bar{\delta}_{SPR}$ is the arithmetic mean of the n values $\delta_{SPR,1}, ..., \delta_{SPR,n}$. The standard error of the mean (SEM) describes the variability of mean SPR difference over all patients:

$$\text{SEM}(\bar{\delta}_{SPR}) = \frac{s(\delta_{SPR})}{\sqrt{n}} \cdot 100 \ \% \tag{3}$$

To test whether the difference of the mean SPR values for SECT and DLCT was non-zero, a t-test for two paired samples was performed. The significance level was set to 5 %. The 95 %-confidence interval gave the range of values in which the population parameter lay with a probability of 95 %.

S4 Treatment plan characteristics

Table 1 summarizes the treatment plan characteristics for the four plans assessed in this study.

Table 1: Treatment plan characteristics. The table summarizes basic details for the planning target volume (PTV), prescription in relative biological effectiveness (RBE)-weighted dose, and setup for each plan. The chosen ion type is protons, helium or carbon ions with a horizontal beam angle for each plan. The couch angle is given for each beam. The number of treatment fields (i.e. couch angles) varies depending on tumor position.

	Basic details			Prescription	Setup
Plan	Tumor type	Volume of PTV (cm^3)	Dose (Gy(RBE))	Description	Couch angles (°)
A	Astrocytoma	170	50.4	28 × 1.8 Gy(RBE)	220 | 310 | 350
B	Meningioma	31	52.2	29 × 1.8 Gy(RBE)	190 | 350
C	Oligodendroglioma	182	54.0	30 × 1.8 Gy(RBE)	175 | 235
D	Pineal region tumor	73	54.0	30 × 1.8 Gy(RBE)	185 | 355

S5 Discussion of uncertainties within the study

Preceding works suggest that a systematic mean SPR bias in the irradiated volume translates directly into a mean range bias of roughly the same magnitude [2]. Similar to prior works, our study scrutinized relative ion range shifts, as opposed to absolute range predictions, and subsequent differences in dose distributions. Several uncertainty factors in SPR prediction can be classified in three different categories [3]. The first category includes imaging uncertainties (beam hardening effects [3], scanner calibration and homogeneity [4], noise [5], presence of sharp radiodensity gradients [6]). The second category involves modelling uncertainties (relative electron density (ED) and effective atomic number (EAN) accuracy, mean excitation energy (I-value) of the medium determination [7]). Uncertainties in performing DLCT data-based SPR prediction would hamper the predictions; however, ED and EAN accuracy and I-value of the medium determination were already studied and validated in previous work [8, 9, 10, 11]. Besides, several other SPR prediction methods from spectral data available in literature that were not applied in this study might further improve the predictions. The third category comprises other uncertainties (neglection of SPR energy dependence, I-value of water uncertainty). Prior studies researched into the SPR energy dependence [12] and I-value of water uncertainty [7, 13]; the optimal results found in these works were employed in this study (cf. section 2.4). The influence of the three different uncertainty categories on SPR prediction, and hence the estimated dose, depends also on the body region.

References

[1] V. T. Taasti, L. P. Muren, K. Jensen, J. B. B. Petersen, J. Thygesen, A. Tietze, C. Grau, and D. C. Hansen, "Comparison of single and dual energy CT for stopping power determination in proton therapy of head and neck cancer," *Phys. Imag. Radiat. Oncol.*, vol. 6, pp. 14–19, 2018.

[2] P. Wohlfahrt, C. Möhler, K. Stützer, S. Greilich, and C. Richter, "Dual-energy CT based proton range prediction in head and pelvic tumor patients," *Radiother. Oncol.*, vol. 125, no. 3, pp. 526–533, 2017.

[3] B. Li, H. C. Lee, X. Duan, C. Shen, L. Zhou, X. Jia, and M. Yang, "Comprehensive analysis of proton range uncertainties related to stopping-power-ratio estimation using dual-energy CT imaging," *Phys. Med. Biol.*, vol. 62, no. 17, pp. 7056–7074, 2017.

[4] H. Paganetti, "Range uncertainties in proton therapy and the role of Monte Carlo simulations," *Phys. Med. Biol.*, vol. 57, no. 11, pp. R99–R117, 2012.

[5] H. H. C. Lee, B. Li, X. Duan, L. Zhou, X. Jia, and M. Yang, "Systematic analysis of the impact of imaging noise on dual-energy CT-based proton stopping power ratio estimation," *Med. Phys.*, vol. 46, no. 5, pp. 2251–2263, 2019.

[6] T. Kairn, S. B. Crowe, P. Fogg, and J. V. Trapp, "The appearance and effects of metallic implants in CT images," *Australas. Phys. Eng. Sci. Med.*, vol. 36, no. 2, pp. 209–217, 2013.

[7] V. De Smet, R. Labarbe, F. Vander Stappen, B. Macq, and E. Sterpin, "Reassessment of stopping power ratio uncertainties caused by mean excitation energies using a water-based formalism," *Med. Phys.*, vol. 45, no. 7, pp. 3361–3370, 2018.

[8] F. K. Faller, S. Mein, B. Ackermann, J. Debus, W. Stiller, and A. Mairani, "Pre-clinical evaluation of dual-layer spectral computed tomography-based stopping power prediction for particle therapy planning at the Heidelberg Ion Beam Therapy Center," *Phys. Med. Biol.*, vol. 65, no. 9, p. 095007, 2020.

[9] G. Landry, F. Dörringer, S. Si-Mohamed, P. Douek, J. F. P. J. Abascal, F. Peyrin, I. P. Almeida, F. Verhaegen, I. Rinaldi, K. Parodi, and S. Rit, "Technical Note: Relative proton stopping power estimation from virtual monoenergetic images reconstructed from dual-layer computed tomography," *Med. Phys.*, vol. 46, no. 4, pp. 1821–1828, 2019.

[10] K. Mei, S. Ehn, M. Oechsner, F. K. Kopp, D. Pfeiffer, A. A. Fingerle, F. Pfeiffer, S. E. Combs, J. J. Wilkens, E. J. Rummeny, and P. B. Noël, "Dual-layer spectral computed tomography: measuring relative electron density," *Eur. Radiol. Exp.*, vol. 2, no. 1, pp. 1–9, 2018.

[11] S. Ohira, H. Washio, M. Yagi, T. Karino, K. Nakamura, Y. Ueda, M. Miyazaki, M. Koizumi, and T. Teshima, "Estimation of electron density, effective atomic number and stopping power ratio using dual-layer computed tomography for radiotherapy treatment planning," *Physica Medica*, vol. 56, pp. 34–40, 2018.

[12] T. Inaniwa and N. Kanematsu, "Effective particle energies for stopping power calculation in radiotherapy treatment planning with protons and helium, carbon, and oxygen ions," *Phys. Med. Biol.*, vol. 61, no. 20, pp. N542–N550, 2016.

[13] E. Bär, P. Andreo, A. Lalonde, G. Royle, and H. Bouchard, "Optimized I-values for use with the Bragg additivity rule and their impact on proton stopping power and range uncertainty," *Phys. Med. Biol.*, vol. 63, no. 16, p. 165007, 2018.

Supplementary material for publication 3

Dual-energy CT-based stopping power prediction for dental materials in particle therapy

Supplementary Material

Supplementary Table 1. Dental materials investigated in the study with their main components, main application field, and manufacturing details.

Material type	Main components	Main application field	Manufacturing process	Product, Manufacturer
Aluminum	Al	Pure metal, component of aluminum oxide ceramics	CAD/CAM milling	Custom-made
Cobalt-chrome	CoCr	Fixed dental prostheses	CAD/CAM milling, casting	Colado CAD CoCr4, Ivoclar
Composite I	Mixture of dimethacrylates, silicates, ceramics, initiators, stabilizers	Core buildups, fillings	Manual layering and light-curing	Rebilda DC, VOCO
Composite II	Mixture of dimetracrylates, inorganic fillers, copolymer, ytterbium fluoride, initiators, stabilizers, pigments	Direct restorations, fillings	Manual layering and light-curing	Tetric EvoCeram, Ivoclar
Glass-ceramic	Mixture of leucite $KAlSi_2O_6$, fluorapatite $Ca_5(PO_4)_3F$, oxyapatite $NaY_9(SiO_4)_8O_2$	Veneers, inlays, partial crowns	Conventional layering	IPS Style Ceram, Ivoclar
Lithium disilicate	$Li_2O_5Si_2$	Fixed dental prostheses	CAD/CAM milling, press technology	IPS e.max Press, Ivoclar
Polymethyl methacrylate (PMMA)	$C_5H_8O_2$	Tissue retraction devices	3D-printing	V-print splint, VOCO
Silicone material	Mixture of silicone polymers and fillers with platinum catalyst	Tissue retraction devices	Dental impression taking	Silicone impression material: Flexitime Putty, Kulzer; Sealing silicone: Mucopren Silicone sealant, Kettenbach
Titanium	Ti	Dental implants	Casting, prefabricated	Gammex Electron Density CT Phantom 467, Gammex-RMI
Zirconium dioxide	ZrO_2	Fixed dental prostheses, dental implants	CAD/CAM milling	IPS e.max ZirCAD, Ivoclar

Supplementary Table 2. Image acquisition settings and reconstructions parameters of head protocols for sequential acquisition CT (SACT) and dual-layer spectral CT (DLCT). Tube current modulation was deactivated. Please note the different reference diameters for $CTDI_{vol}$ of the two protocols resulting from the different protocol setting options. For DLCT, an iDose[4] level of 0 was applied (Philips Healthcare, Best, The Netherlands), which corresponds to conventional filtered back-projection image reconstruction.

Protocol	DECT tech-nique	Tube voltage (kV_p)	Tube current-time product (mAs)	Collima-tion (mm)	Rotation time (s)	Pitch	$CTDI_{vol}$ (mGy)	Slice thick-ness and spacing (mm)	Recon-struc-tion filter
Head	SACT	80/140	247/58	2 x 32 x 0.6	0.5	0.55	11.1/12.7 (32 cm $CTDI_{vol}$ diameter)	1.5/1.5	Qr40f
Head	DLCT	120	300	64 x 0.625	0.5	0.8	47.2 (16 cm $CTDI_{vol}$ diameter)	1.5/1.5	UB

Supplementary Table 3. Dental materials investigated in the study with measured, single-energy CT (SECT)- and dual-energy CT (DECT)-predicted stopping power ratio (SPR) values using sequential acquisition CT (SACT) and dual-layer spectral CT (DLCT). No uncertainty (or 0) was reported for certain materials for SE-120-DLCT because the CTN were saturated, resulting in a maximum SPR value. SE-140-SACT: SECT-based SPR prediction with SACT at 140 kV_p; DE-DirectSPR-SACT: DECT-based SPR prediction with SACT using a DirectSPR implementation; DE-RhoZ-SACT: DECT-based SPR prediction with SACT using the RhoZ-method; SE-120-DLCT: SECT-based SPR prediction with DLCT at 120 kV_p; DE-RhoZ-DLCT: DECT-based SPR prediction with DLCT using the RhoZ-method.

Material	Measured SPR	SACT			DLCT	
		SPR_{SE-140}	$SPR_{DE-DirectSPR}$	$SPR_{DE-RhoZ}$	SPR_{SE-120}	$SPR_{DE-RhoZ}$
Aluminum	2.140 ± 0.002	2.074 ± 0.003	2.268 ± 0.003	2.203 ± 0.022	2.006 ± 0.008	2.222 ± 0.008
Cobalt-chrome	5.823 ± 0.002	2.581 ± 0.008	3.997 ± 0.010	3.985 ± 0.026	2.347 ± 0.000	3.760 ± 0.001
Composite I	1.627 ± 0.001	2.585 ± 0.004	3.885 ± 0.009	3.898 ± 0.006	2.347 ± 0.000	1.749 ± 0.077
Composite II	1.744 ± 0.002	2.579 ± 0.003	3.971 ± 0.010	3.990 ± 0.006	2.347 ± 0.000	3.722 ± 0.015
Glass-ceramic	2.079 ± 0.002	2.384 ± 0.006	3.242 ± 0.006	3.251 ± 0.006	2.347 ± 0.000	2.155 ± 0.004
Lithium disilicate	2.091 ± 0.001	2.601 ± 0.001	3.968 ± 0.052	3.961 ± 0.070	2.347 ± 0.000	2.332 ± 0.009
PMMA	1.169 ± 0.001	1.092 ± 0.001	1.175 ± 0.003	1.177 ± 0.005	1.088 ± 0.002	1.176 ± 0.002
Silicone material	1.229 ± 0.003	1.242 ± 0.001	1.254 ± 0.007	1.257 ± 0.004	1.242 ± 0.003	1.246 ± 0.002
Titanium	3.248 ± 0.002	2.601 ± 0.001	3.878 ± 0.005	3.863 ± 0.008	2.347 ± 0.000	3.708 ± 0.061
Zirconium dioxide	4.160 ± 0.001	2.577 ± 0.007	4.022 ± 0.005	4.018 ± 0.033	2.347 ± 0.000	3.761 ± 0.001

Acknowledgments

I would like to express my heartfelt gratitude to all those who supported me professionally and personally throughout this thesis. Without the kindness and encouragement of so many people around me, I would not have managed to complete this journey. The following list is not exhaustive, but I am no less grateful to those whom I cannot mention here.

First of all, I would like to thank Prof. Dr. Dr. Jürgen Debus for giving me the opportunity to carry out my thesis work in the Clinical Cooperation Unit Radiation Oncology at the German Cancer Research Center (DKFZ), the Department of Radiation Oncology at the Heidelberg University Hospital (UKHD), and the Heidelberg Ion Beam Therapy Center (HIT). His invaluable guidance and support were crucial for the completion of this project. I especially thank Prof. Dr. Michael Hausmann who provided insightful feedback throughout the project and kindly accepted to act as second referee for my dissertation. I would also like to express my deep gratitude to Prof. Dr. Amir Abdollahi for his reliably astute advice and contagious enthusiasm. I owe a debt of gratitude as well to the DKFZ International PhD Program, which provided the funding that made this work possible.

I would further like to express my special appreciation for and sincere gratitude to my supervisor, Prof. Dr. Andrea Mairani, for supporting and encouraging me with his passion for research, his commitment to our group's work, as well as his inspiring knowledge, ideas, and continual guidance.

I would also like to offer my gratitude to PD Dr. Wolfram Stiller for his consistent feedback, help, and expert advice on theoretical and practical aspects of CT imaging. Thanks additionally to the RTT team for aiding me in conducting numerous CT scans.

Thank you also to Dr. Christopher Herpel and Prof. Dr. Sebastian Schwindling for supporting the project with dental materials and to Dr. Semi Harrabi for providing a clinical perspective.

Additional special thanks are due to Annette Groß and Rosi Vay-Meyer for their kind assistance in dealing with administrative and organizational challenges. I am especially grateful to Claudia Rittmüller for helping me navigate the administrative complexity of the multiple organizations involved.